
COLUMBIA

ACCIDENT INVESTIGATION BOARD



Note: Volumes II – VI contain a number of conclusions and recommendations, several of which were adopted by the Board in Volume I. The other conclusions and recommendations drawn in Volumes II – VI do not necessarily reflect the opinion of the Board, but are included for the record. When there is conflict, Volume I takes precedence.

REPORT VOLUME V
APPENDIX G.13
OCTOBER 2003



On the Front Cover

This was the crew patch for STS-107. The central element of the patch was the microgravity symbol, μg , flowing into the rays of the Astronaut symbol. The orbital inclination was portrayed by the 39-degree angle of the Earth's horizon to the Astronaut symbol. The sunrise was representative of the numerous science experiments that were the dawn of a new era for continued microgravity research on the International Space Station and beyond. The breadth of science conducted on this mission had widespread benefits to life on Earth and the continued exploration of space, illustrated by the Earth and stars. The constellation Columba (the dove) was chosen to symbolize peace on Earth and the Space Shuttle Columbia. In addition, the seven stars represent the STS-107 crew members, as well as honoring the original Mercury 7 astronauts who paved the way to make research in space possible. The Israeli flag represented the first person from that country to fly on the Space Shuttle.



On the Back Cover

This emblem memorializes the three U.S. human space flight accidents – Apollo 1, Challenger, and Columbia. The words across the top translate to: "To The Stars, Despite Adversity – Always Explore"

The Board would like to acknowledge the hard work and effort of the following individuals in the production of Volumes II – VI.

Maj. Gen. John L. Barry	Executive Director to the Chairman
Dennis R. Jenkins	Investigator and Liaison to the Board
Lt. Col. Donald J. White	Technical Editor
Lt. Col. Patrick A. Goodman	Technical Editor
Joshua M. Limbaugh	Layout Artist
Joseph A. Reid	Graphic Designer
Christine F. Cole	Administrative Assistant
Jana T. Schultz	Administrative Assistant
Lester A. Reingold	Lead Editor
Christopher M. Kirchhoff	Editor
Ariel H. Simon	Assistant Editor
Jennifer L. Bukvics	Lead Project Manager
Donna J. Fudge	Senior Paralegal, Group II Coordinator
Susan M. Plott	Project Supervisor, Group III Coordinator
Ellen M. Tanner	Project Supervisor
Matthew J. Martin	Government Relations Consultant
Frances C. Fisher	ANSER Liaison

Limited First Printing, October 2003, by the
Columbia Accident Investigation Board

Subsequent Printing and Distribution by the
National Aeronautics and Space Administration
and the
Government Printing Office
Washington, D.C.

VOLUME I

PART ONE	THE ACCIDENT
Chapter 1	The Evolution of the Space Shuttle Program
Chapter 2	<i>Columbia's</i> Final Flight
Chapter 3	Accident Analysis
Chapter 4	Other Factors Considered
PART TWO	WHY THE ACCIDENT OCCURRED
Chapter 5	From <i>Challenger</i> to <i>Columbia</i>
Chapter 6	Decision Making at NASA
Chapter 7	The Accident's Organizational Causes
Chapter 8	History as Cause: <i>Columbia</i> and <i>Challenger</i>
PART THREE	A LOOK AHEAD
Chapter 9	Implications for the Future of Human Space Flight
Chapter 10	Other Significant Observations
Chapter 11	Recommendations
PART FOUR	APPENDICES
Appendix A	The Investigation
Appendix B	Board Member Biographies
Appendix C	Board Staff

VOLUME II

	CAIB TECHNICAL DOCUMENTS CITED IN THE REPORT
	Reader's Guide to Volume II
Appendix D.a	Supplement to the Report
Appendix D.b	Corrections to Volume I of the Report
Appendix D.1	STS-107 Training Investigation
Appendix D.2	Payload Operations Checklist 3
Appendix D.3	Fault Tree Closure Summary
Appendix D.4	Fault Tree Elements – Not Closed
Appendix D.5	Space Weather Conditions
Appendix D.6	Payload and Payload Integration
Appendix D.7	Working Scenario
Appendix D.8	Debris Transport Analysis
Appendix D.9	Data Review and Timeline Reconstruction Report
Appendix D.10	Debris Recovery
Appendix D.11	STS-107 Columbia Reconstruction Report
Appendix D.12	Impact Modeling
Appendix D.13	STS-107 In-Flight Options Assessment
Appendix D.14	Orbiter Major Modification (OMM) Review
Appendix D.15	Maintenance, Material, and Management Inputs
Appendix D.16	Public Safety Analysis
Appendix D.17	MER Manager's Tiger Team Checklist
Appendix D.18	Past Reports Review
Appendix D.19	Qualification and Interpretation of Sensor Data from STS-107
Appendix D.20	Bolt Catcher Debris Analysis

VOLUME III

OTHER TECHNICAL DOCUMENTS

	Reader's Guide to Volume III
Appendix E.1	CoFR Endorsements
Appendix E.2	STS-107 Image Analysis Team Final Report
Appendix E.3	An Assessment of Potential Material Candidates for the "Flight Day 2"
	Radar Object Observed during the NASA Mission STS-107
Appendix E.4	Columbia Early Sighting Assessment Team Final Report

VOLUME IV

OTHER TECHNICAL DOCUMENTS

	Reader's Guide to Volume IV
Appendix F.1	Water Absorption by Foam
Appendix F.2	Follow the TPS
Appendix F.3	MADS Sensor Data
Appendix F.4	ET Cryoinsulation
Appendix F.5	Space Shuttle STS-107 Columbia Accident Investigation, External Tank Working Group Final Report – Volume 1

VOLUME V

OTHER SIGNIFICANT DOCUMENTS

	Reader's Guide to Volume V
Appendix G.1	Requirements and Procedures for Certification of Flight Readiness
Appendix G.2	Appendix R, Space Shuttle Program Contingency Action Plan
Appendix G.3	CAIB Charter, with Revisions
Appendix G.4	Group 1 Matrix Brief on Maintenance, Material, and Management
Appendix G.5	Vehicle Data Mapping (VDM) Team Final Report, Jun 13, 2003
Appendix G.6	SRB Working Group Presentation to CAIB
Appendix G.7	Starfire Team Final Report, Jun 3, 2003
Appendix G.8	Using the Data and Observations from Flight STS-107... Exec Summary
Appendix G.9	Contracts, Incentives, and Safety/Technical Excellence
Appendix G.10	Detailed Summaries: Rogers Commission Report, ASAP Report, SIAT Report
Appendix G.11	Foam Application and Production Chart
Appendix G.12	Crew Survivability Report

Appendix G.13	Aero/Aerothermal/Thermal/Structures Team Final Report, Aug 6, 2003
---------------	--

VOLUME VI

TRANSCRIPTS OF BOARD PUBLIC HEARINGS

	Reader's Guide to Volume VI
Appendix H.1	March 6, 2003 Houston, Texas
Appendix H.2	March 17, 2003 Houston, Texas
Appendix H.3	March 18, 2003 Houston, Texas
Appendix H.4	March 25, 2003 Cape Canaveral, Florida
Appendix H.5	March 26, 2003 Cape Canaveral, Florida
Appendix H.6	April 7, 2003 Houston, Texas
Appendix H.7	April 8, 2003 Houston, Texas
Appendix H.8	April 23, 2003 Houston, Texas
Appendix H.9	May 6, 2003 Houston, Texas
Appendix H.10	June 12, 2003 Washington, DC



Reader's Guide to Volume V

Volume V of the Report contains appendices that were not cited in Volume I. These consist of documents produced by NASA and other organizations, which were provided to the Columbia Accident Investigation Board in support of its inquiry into the February 1, 2003 destruction of the Space Shuttle *Columbia*. The documents are compiled in this volume in the interest of establishing a complete record, but they do not necessarily represent the views of the Board. Volume I contains the Board's findings, analysis, and recommendations. The documents in Volume V are also contained in their original color format on the DVD disc in the back of Volume II.

THIS PAGE INTENTIONALLY LEFT BLANK



Volume V

Appendix G.13

Aero/Aerothermal/Thermal/Structures Team Final Report, Aug 6, 2003

This Appendix contains NSTS-37398 Aero/Aerothermal/Thermal/Structures Team Final Report in Support of the *Columbia* Accident Investigation, 6 August 2003.

THIS PAGE INTENTIONALLY LEFT BLANK

NSTS-37398



**Aero/Aerothermal/Thermal/Structures Team
Final Report**
**in support of the
Columbia Accident Investigation**

August 6, 2003

Submitted by

Original signature obtained

Pam Madera, USA
Team Lead

Original signature obtained

Steve Labbe, NASA JSC
Aerodynamics

Original signature obtained

Joe Caram, NASA JSC
Aerothermodynamics

Original signature obtained

Chris Madden, NASA JSC
Thermal

Original signature obtained

Mike Dunham, Boeing
Stress, Loads and
Dynamics



Contributing Authors - Aerodynamics

Karen Bibb, NASA Langley Research Center
Greg Brauckmann, NASA Langley Research Center
Olman Carvajal, Boeing-Houston
Kevin Dries, NASA Johnson Space Center
Randy Lillard, NASA Johnson Space Center
Ramadas K. Prabhu, LESC-Hampton
Karuna Rajagopal, Boeing-Huntington Beach
James Reuther, NASA Ames Research Center
William I. Scallion, NASA Langley Research Center
Jeff Stone, Boeing-Huntington Beach

Contributing Authors – Aerothermodynamics

Steve Alter, NASA Langley Research Center
Steve Barson, Boeing Rocketdyne Propulsion and Power
Maria Bobskill, Ph. D. , NASA Langley Research Center
Stan Bouslog, Lockheed Martin
Katie Boyles, NASA Johnson Space Center
Kevin Bowcut, Ph. D., Boeing Huntington Beach
Charles Campbell, NASA Johnson Space Center
Steve Fitzgerald, NASA Johnson Space Center
Michail Gallis, Ph. D., Sandia National Laboratories
Peter Gnoffo, Ph. D. , NASA Langley Research Center
Scott Halloran, Boeing Rocketdyne Propulsion and Power
Tom Horvath, NASA Langley Research Center
Randy Lillard, NASA Johnson Space Center
Joe Olejniczak Ph. D., NASA Ames Research Center

Tom Paul, Lockheed Martin
Jeff Payne, Sandia National Laboratories
Don Picetti, Boeing Huntington Beach
Karuna Rajagopal, Ph. D., Boeing Huntington Beach
James Reuther, Ph. D, NASA Ames Research Center
Joe Ruf, NASA Marshall Space Flight Center
Greg Schunk, NASA Marshall Space Flight Center
John Sharp, NASA Marshall Space Flight Center
Joel Stolfus, NASA Johnson Space Center White Sands Test Facility
Ricky Thompson, NASA Langley Research Center
K. C. Wang, Boeing Houston
Vince Zoby, NASA Langley Research Center

Contributing Authors - Thermal

Donald Curry, NASA Johnson Space Center
Steven Del Papa, NASA Johnson Space Center
Ronald Lewis, NASA Johnson Space Center
Dan Newswander, NASA Johnson Space Center
Don Picetti, Boeing Huntington Beach
Alvaro Rodriguez, NASA Johnson Space Center

Contributing Authors – Stress

Jason Adair, BNA-Houston
Charles Park, BNA- Huntington Beach
Paul Parker, BNA-Houston
Shawn Sorenson, BNA-Houston

Table of Contents

Executive Summary.....	1
1 INTRODUCTION.....	2
2 PURPOSE & SCOPE.....	2
3 METHODOLOGY.....	3
4 AERODYNAMICS.....	5
4.1 Introduction.....	5
4.1.1 Team Objectives.....	5
4.1.2 Nominal Orbiter Aerodynamic Entry Flight Overview.....	5
4.1.3 Chronology of Investigation – Test & Analysis.....	5
4.1.4 Approach / Processes – Methodology to Achieve Objectives.....	6
4.2 Aerodynamic Extraction.....	11
4.2.1 Atmospheric Model.....	11
4.2.2 GSFC/DAO Upper Atmospheric Wind Model.....	12
4.2.3 Aerodynamic Increment Extraction Results.....	12
4.2.4 Correlation to Working Scenario.....	13
4.3 Damage Assessment Aero.....	23
4.3.1 Wind Tunnel Testing.....	23
4.3.2 Damage Assessment Using Computational Fluid Dynamics.....	42
4.4 Application of Data to the Working Scenario.....	85
4.4.1 Correlation of CFD & WTT – Results by Timeline Section.....	85
4.4.2 Damage Progression Theory and Supporting Aero.....	92
4.5 Summary – conclusions & observations.....	110
4.6 References – Aerodynamics.....	111
4.7 Appendices – Aerodynamics.....	112
4.7.1 Aerodynamic Definitions, Coordinate Systems and References.....	112
4.7.2 Surface Pressure Entry Data Evaluation.....	116
4.7.3 Wind Tunnel Test Matrix – Comprehensive Listing.....	119
4.7.4 FELISA Inviscid CFD - Comments and Additional Analysis.....	122
4.7.5 OVERFLOW CFD Analysis of Leaside Flow field Interactions.....	127
4.7.6 Aerodynamic Investigation using CART3D CFD Analysis.....	134
4.7.7 Aerodynamic Investigation using USA CFD Analysis.....	142
4.7.8 CFD Tools:.....	142
5 AEROTHERMODYNAMICS.....	146
5.1 Introduction.....	146
5.1.1 Team Objective.....	146
5.1.2 Aerothermodynamics Overview –Orbiter Perspective.....	146
5.1.3 Approach to Determining Required Environments.....	147
5.2 Orbiter External Aerothermodynamic Environments (Nominal & Damaged Configurations).....	148
5.2.1 Orbiter OML/Skin Flight Data Observations.....	148
5.2.2 Orbiter Certified Body Point Heating Methodology.....	160
5.2.3 Wind Tunnel Testing.....	171
5.2.4 Computational Fluid Dynamics (CFD) and Direct Simulation Monte Carlo (DSMC).....	195
5.2.5 Application of External Environments Data to the Working Scenario.....	271

5.3	Damaged Orbiter Internal Aerothermodynamic Environments	282
5.3.1	Process of Determining Internal Aerothermodynamic Environments	282
5.3.2	External/Internal Environments – Engineering Analysis	287
5.3.3	Plume Model Development	297
5.3.4	Effects of Burning Aluminum	325
5.3.5	Coupled Venting and Thermal Model of Wing	330
5.3.6	3D CFD & DSMC of Wing Leading Edge Cavity	363
5.3.7	Application of Data to the Working Scenario	466
5.4	Aerothermodynamic Environments Summary	482
5.5	References	485
5.6	Appendix for Aerothermodynamics	493
5.6.1	Engineering Tools	493
5.6.2	Wind Tunnel Facilities & Measurement Techniques	493
5.6.3	CFD/DSMC Tools	495
5.6.4	Hypersonic Boundary Layer Transition Effective Trip Height Calculation	501
5.6.5	STS-107 End of Mission (EOM) 3 Pre-Entry Trajectory	503
6	THERMAL	510
6.1	Panel 8/9 Spar & Clevis Thermal Analysis	510
6.1.1	Damaged Tee-seal	511
6.2	Spar Burn Through Analysis	512
6.3	Wheel Well Thermal Analysis	512
6.4	Wire Bundle Burn-Through Tests	514
6.5	Wire Bundle Burn-Through Thermal Analysis	517
6.5.1	Tee-seal scenario	519
6.6	Orbiter Sidewall Bondline Thermal Analysis	519
6.7	Damaged Wing Leading Edge Coupled Aero-Thermal-Structural Analysis	520
6.8	Chin Panel Temperature Anomaly	522
6.9	Truss Tube Thermal Analysis	522
6.10	RCC Knife Edge Tests	523
6.11	Leading Edge Reinforced Carbon-Carbon (RCC) Hole Growth Thermal Analysis	525
7	STRESS	577
7.1	Panel 9 Spar Strain Gauge Evaluation	577
7.1.1	Analysis Objective	577
7.1.2	Analytical Approach	578
7.1.3	Model Description	578
7.1.4	Thermal Profiles	579
7.1.5	Results	582
7.1.6	Conclusions	584
7.2	1040 Spar Strain Gauge Evaluation	587
7.2.1	Analysis Objective	587
7.2.2	Analysis Inputs, Models, Assumptions, and Approach	587
7.2.3	Results	590
7.2.4	Conclusions	592
7.3	Overall Wing MADS Evaluation	593
7.3.1	Analysis Objective	593
7.3.2	Analysis Inputs, Models, Assumptions, and Approach	593
7.3.3	Results	594
7.3.4	Conclusions	597
7.4	Accelerometer Evaluation	597
7.4.1	Ascent	597
7.4.2	Descent	611
7.4.3	Summary	618
7.5	Feasible Wing Deformation Prior to Loss of Signature	619
7.5.1	Analysis Objective	619
7.5.2	OV-102 Wing Finite Element Model	619
7.5.3	Load Cases	620

7.5.4	Analytical Procedure	621
7.5.5	Analysis Results	625
7.5.6	Conclusions	637
7.6	Stress Appendix	638
7.7	Reference – MADS PCM Installation Drawings	652
8	CONCLUSIONS	653
9	CREDITS	655
10	Acknowledgements	656
	References	656
	Appendix A - Acronyms and Abbreviations	658
	Appendix B - Team Member List & Biographies	661

Executive Summary

The Aerodynamic/Aerothermodynamic/Thermal/Structures (AATS) Team was formed by the Orbiter Vehicle Engineering Working Group (OVEWG) to assist in the STS-107 Columbia Accident Investigation. The primary objective of this team was to provide an analytical basis for a most probable damage scenario for the STS-107 entry. This team was not chartered with the task of defining how the initial damage was incurred.

The approach used by the AATS Team was to postulate the approximate location and extent of damage experienced by Columbia during entry. The team would then formulate analyses or tests that would emulate the vehicle aerodynamic, thermal, or structural responses to the postulated hardware damage. The results of the analyses or tests were compared to anomalous MADS and OI measured data or off-nominal aerodynamic increments associated with the STS-107 entry to determine if the postulated damage condition was feasible. Results were then integrated to ensure that the postulated damage condition could be supported across the technical disciplines. Where appropriate to ensure consistency, corresponding analysis of damage conditions were completed for the ascent phase of flight. Finally, postulated damage conditions were evaluated to ensure that they would not conflict with the condition of recovered hardware or other flight data.

The AATS Team efforts were primarily focused on postulated damage conditions starting at entry interface (EI) and extending to approximately 615 seconds from EI. Evaluations of off-nominal indications during this time frame were expected to provide the best insight into identifying the initial damage condition. An evaluation of damage conditions consistent with aerodynamic increments just prior to loss of signal (LOS) was conducted for completeness.

The culmination of multiple analyses substantiates a most probable entry damage scenario that begins with damage to the wing leading edge reinforced carbon-carbon (RCC) prior to EI. Analyses indicate that the initial damage was consistent with a breach in the lower portion of RCC panel 8. The breach can be described as an aperture with an area equivalent to that of a six to ten inch diameter hole. From the beginning of the entry profile, hot gas was ingested into the wing leading edge cavity behind the RCC panels. The flow of hot gas into the cavity was disturbed by complex internal geometry increasing both the local pressure in the cavity and the heating of local surfaces. The increase in RCC cavity pressure and internal flow patterns increased flow out of the vents located at the top of the cavity. By approximately EI+340 seconds from EI, the vent paths were increased slightly due to thermal degradation. Flow out of the upper vents resulted in a disturbance of flow on the leeside of the vehicle, thereby displacing the strake and canopy vortices and temporarily reducing heating to the left sidewall and left Orbital Maneuver System (OMS) pod. Heating of local surfaces inside the RCC cavity eventually resulted in burn through of the wing leading edge spar by approximately EI plus 487 seconds. The transverse momentum of the flow of hot gas entering the RCC cavity was redirected as the flow impinges on RCC ribs and spanner beam hardware and insulation. As a result, the plume entering the intermediate wing was directed normal from the spar toward the main landing gear compartment wall. The impingement of the plume in this region resulted in burning of the four OI/MADS wire bundles, burn through of the main landing gear compartment wall, and burn through of the upper wing skin. Burn through of the main landing gear compartment wall resulted in an abnormal temperature rise of main landing gear components in the wheel well due to convective heating. Increased outer mold line heating of the left sidewall and OMS pod can be explained by redirection of the wing leading edge windward flow to the leeside through either a severely damaged and/or missing upper RCC carrier panel(s), severely damaged or missing full RCC panel (e.g. panel 9), or damaged upper wing just aft of the wing leading edge. These damage conditions are also consistent with anomalous aerodynamic increments between EI+500 to EI+600 seconds. Damage in the left wing cavity continued to progress until loss of signal. This damage resulted in a significant depression being formed on the lower surface of the left wing due to burn through of intermediate wing truss tubes and compromised structural strength associated with heating internal to the wing. The depression in the lower wing resulted in external flow patterns that effectively increased the lift and drag on the left wing resulting in the positive rolling moment and negative yawing moment just prior to loss of signal. This report details the tests and analyses results that lend credence to this damage progression as a plausible explanation of Columbia's final moments of flight.

1 INTRODUCTION

The AATS Team was formed by the Orbiter Vehicle Engineering Working Group (OVEWG) to aid the NASA community in the investigation of the STS-107 accident. The team was formed with members from various organizations and technical disciplines throughout the NASA and contractor communities. The team was organized with sub-team leads for each significant technical area as shown in Figure 1.1. A short biography of team leads and a list of team members can be found in Appendix B of this report.

This report summarizes the analyses performed by the AATS Team to support scenario development and to address actions levied and/or requests made by the Columbia Accident Investigation Board, OVEWG, and other teams supporting the investigation.

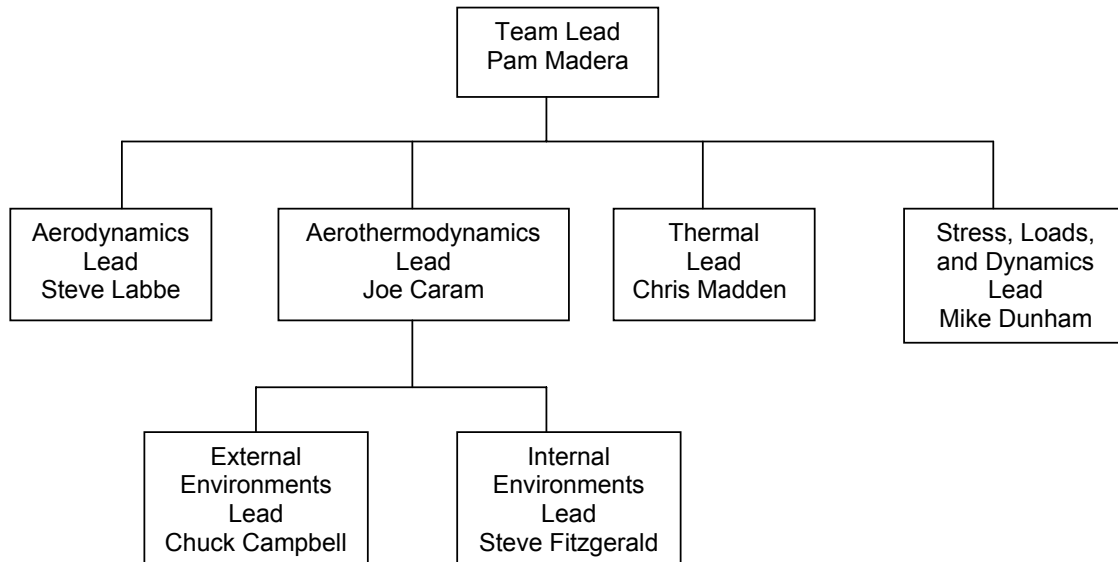


Figure 1-1 Team Organization

2 PURPOSE & SCOPE

This report documents the analyses performed by the AATS Team that provided substantiation for a most probable damage scenario for the Columbia accident. Damage conditions were analyzed to a level of fidelity that would provide the NASA OVEWG, NAIT, and CAIB sufficient insight to ensure that the appropriate corrective action steps would be taken prior to return to flight. In some cases, engineering level analysis was sufficient to understand the off-nominal conditions. This team was not chartered with the task of defining how the initial damage was incurred.

The AATS Team efforts were primarily focused on postulated damage conditions starting at entry interface (EI) and extending to approximately 615 seconds from EI. Evaluations of off-nominal indications during this time frame were expected to provide the best insight to identify the initial damage condition.

An evaluation of damage conditions consistent with aerodynamic increments just prior to loss of signal (LOS) was conducted for completeness.

It should be noted that analyses and tests conducted for the investigation were performed on representative geometries. The fact that these geometries were chosen for investigation purposes should not be misconstrued as exactly reproducing the damaged configuration encountered in flight. These

representative damage configurations, however, do provide insight into the nature and level of damage necessary to result in the loss of Columbia and her STS-107 crew.

3 METHODOLOGY

The completion of the scope of this team's charter required a significant amount of analyses to be completed in a short amount of time. To accomplish the largest amount of work in the shortest amount of time, many analysis efforts were performed parametrically in parallel with comparisons and integration completed at various points throughout the investigation. Some tasks were performed in sequence out of necessity. For example, most of the final thermal analyses could not be completed until internal aerothermodynamic environments were developed. Wherever possible, independent and/or redundant processes and tools were used to help ensure the validity of the analysis results and subsequent conclusions.

Overall, the approach used by the AATS Team was to postulate the approximate location and extent of damage experienced by Columbia during entry. The team would then formulate analyses or tests that would emulate the aerodynamic, thermal, and structural responses of the postulated hardware damage. The results of the analysis or test were compared to anomalous MADS and OI measured data and off-nominal aerodynamic increments associated with the STS-107 entry to determine if the postulated damage condition was feasible. Results were then integrated to ensure that the postulated damage condition could be supported by each technical discipline. Progression of damage was reviewed to make sure it made logical sense. Where appropriate, corresponding analysis of damage conditions were completed for the ascent phase of flight. Finally, postulated damage conditions were evaluated to ensure that they would not conflict with the condition of recovered hardware or other flight data.

Completion of these steps required the identification of key off nominal data that required the postulation of damage conditions. Figure 3-1 provides a high level summary of key data measurements and events that were identified to be evaluated.

GMT Time mm:ss	Time after EI sec	Key Data Measurements and Events
48:39	270	RCC panel 9 spar strain gauge shows off nominal response
48:59	290	Clevis fitting 9/10 sees first indication of temperature increase
49:49	340	OMS pod temperature experiences reduced heating
51:14	425	Panel 9 spar temperature starts off-nominal rise
52:16	487	First MADS measurement begins to fail behind wing spar
52:17	488	First temperature rise in wheel well (LMG brake line bit flip)
52:17	488	Xo 1040 spar strain gauge shows off-nominal response
52:19	490	Unusual response in chin panel outboard clevis temperature
52:30	501	Unusual water dump and vacuum vent nozzle temperature response
52:44	515	Start of delta yaw
52:50	521	Start of delta roll
54:09	600	Debris 5 (Flash "0")
54:10	601	Start of significant temperature rise in wheel well (LMG brake line b)
54:11	602	Reversal of delta roll trend
54:20	611	Start of Slow Aileron Trim Change
54:22	613	Mid Fuse and sidewall temperature rise
54:33	624	Flash 1

Figure 3-1 Key Data Measurements and Events

Several of the events occurred in nearly coincident time frames as shown in Figure 3-2. These corresponding events were reviewed to identify areas of commonality and to ensure consistency in damage progression.

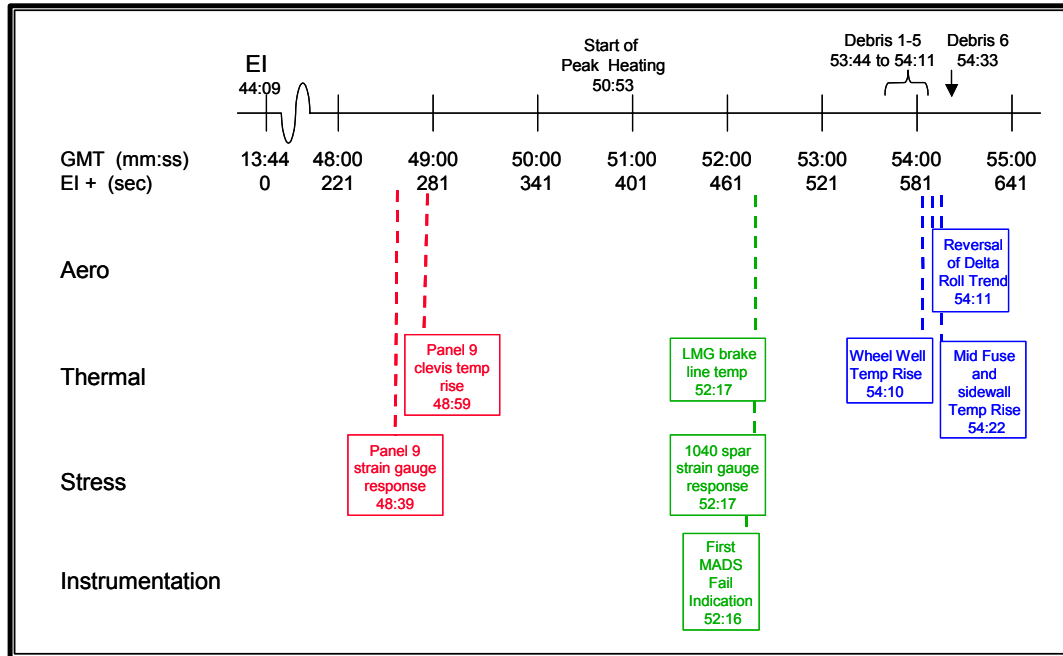


Figure 3-2 Corresponding Events

The AATS Team worked closely with the Scenario team. Analyses were used to formulate a most probable scenario of initial damage and damage progression within the scope of the team's charter. Coordination with the Scenario Team and the Technical Integration Team helped ensure that AATS analysis activities did not conflict with other investigation data/findings.

4 AERODYNAMICS

4.1 Introduction

4.1.1 Team Objectives

The STS-107 entry flight aerodynamic reconstruction effort had two primary objectives. The first was to define the aerodynamic forces and moments experienced by Columbia during atmospheric flight from entry interface (EI) up to the point of loss of signal (LOS) + 5 sec (the last reliable data set point). These extracted forces and moments were then compared to predictions obtained from the orbiter operational aerodynamic data base (OADB) with the resulting differences attributed to the effects of vehicle damage. This served as the basis for the second objective which focused on reproducing the observed off nominal force and moment aerodynamics through wind tunnel (WT) test and/or computational fluid dynamics (CFD) analysis of postulated damaged orbiter configurations. Developing a match between the extracted off nominal aerodynamics and the damage assessment test and analysis results was then used as one basis to substantiate or refute plausible damage scenarios. The ultimate goal was to correlate these results with a vehicle damage scenario that progressed from an initial stage at EI to a considerably more aerodynamically significant damaged configuration just prior to LOS, while maintaining consistency with results from the aerodynamic heating and other analyses. In the end, this leads to a damaged configuration that produced the overwhelming off nominal asymmetric aerodynamic moments resulting in Columbia's loss of control and vehicle breakup.

4.1.2 Nominal Orbiter Aerodynamic Entry Flight Overview

The Orbiter entry is initiated by the firing of the Orbiter Maneuvering System (OMS) jets, slowing the Orbiter and allowing the vehicle to descend to the atmospheric EI, nominally at an altitude of 400,000 feet. During the initial entry phase, which extends to a dynamic pressure of 20 psf. (approx. 250,000 ft), vehicle lateral/directional control and trim is provided by a combination of RCS jet firings, aileron deflections, and sideslip angle. This hypersonic entry flight phase, continuing down through a Mach number of less than five, is accomplished at a high angle of attack during which the blanketing effect of the wing and fuselage essentially precludes any use of the rudder for yaw control. With the rudder not activated until Mach 5, prior to this point in the entry the lateral axis is trimmed solely by aileron deflection with a resulting sideslip angle to balance the roll and yaw moments, augmented by occasional RCS yaw ret firings. Range control is achieved through a series of banking maneuvers while following a predetermined angle of attack schedule. STS-107 trajectory parameters from EI to LOS (approximately Mach 18 near 200,000 ft) are included in Figure 4.1-1 to Figure 4.1-3. Note that for the extent of the STS-107 entry, Columbia was in a high Mach Number, low dynamic pressure flight condition near the 40 deg nominal entry angle-of-attack.

Typically, a terminal phase would then begin as angle of attack is reduced below 18 degrees. As the vehicle continues its descent, air data probes are then extended (at approximately Mach 5) to provide air data relative to the Orbiter. Subsonic flight is attained at an altitude of approximately 40,000 ft. Range control during subsonic flight is obtained by angle of attack modulation with velocity control maintained by the rudder speed-brake. The approach and landing interface occurs at 10,000 ft and a pre-flare is initiated at the appropriate altitude, followed by a deceleration float and touchdown.

Aerodynamic coordinate systems, reference lengths and areas, etc. are included in Aerodynamic Appendices, Section 4.7.1

4.1.3 Chronology of Investigation – Test & Analysis

The STS-107 aerodynamic investigation began with a focus on the orbiter lower wing, primarily in the region of the main landing gear (MLG) door. This was based on the preliminary ascent foam debris impact assessment and operational instrumentation (OI) indications of off-nominal temperature and pressure sensor data in the left wing, particularly in the MLG wheel well. Testing was initiated in the Langley Research Center (LaRC) 20-Inch Mach 6 Air Tunnel, concentrating on lower surface tile damage scenarios, boundary layer transition effects and potential MLG door and/or wheel well cavity exposure.

Further analysis of the ascent debris trajectory suggested that foam may have impacted the WLE. Additionally, preliminary forensics of recovered Columbia hardware suggested WLE damage as an increasingly likely scenario. An LaRC inviscid (FELISA) CFD analysis of a damaged WLE reinforced carbon-carbon (RCC) panel, corroborated by preliminary LaRC WT test results, indicated side fuselage heating augmentation consistent with the OI data. Thus, the aerodynamic investigation priority was shifted to a WLE damage assessment with a concentrated effort to understand the aerodynamic and aerothermodynamic effects of damaged or missing WLE RCC panels. This combined aerodynamic/aerothermal approach was a fundamental part of the investigation process. The evaluations included WT testing in the LaRC Mach 6 air and carbon tetra-fluoride (CF₄) hypersonic facilities complemented with CFD analysis by various groups from across the agency. These results were focused even further by the recovery of the Orbiter Experiments (OEX) recorder and associated pressure, temperature and strain data as well as continuing forensic analysis of Columbia's recovered WLE components.

Subsequently the Technical Integration Team conducted a failure analysis technical interchange meeting (TIM) where, based on all the latest investigation information a decision was approved by the Orbiter Vehicle Engineering Working Group (OVEWG) board to concentrate on WLE RCC Panel 5-9 damage as the primary working scenario. Test and analysis of missing partial WLE RCC panels was initiated based on the recovery of portions of each of Columbia's left hand side WLE panels. These results extended the data set for missing full RCC panels to a range of WLE damage configurations. Additionally, leeside flow field effects became a focus of the investigation based on off-nominal readings from the mid fuselage and OMS pod surface thermocouples as well as the unique damage patterns on the left hand side OMS pod and vertical tail. The source of these leeside flow disturbances was evaluated by addressing increased venting as well as the development of various holes through the wing.

As a final investigation thrust, the potential for orbiter lower surface wing deformation was evaluated. This ultimately provided the best match as the source of the changing trends in the aerodynamic moments. Finally, the results of the test and analysis were combined into a potential damage progression path that can reproduce the extracted off-nominal aerodynamics from EI to just prior to LOS.

4.1.4 Approach / Processes – Methodology to Achieve Objectives

The STS-107 Aerodynamic Reconstruction process is illustrated by the flow chart depicted in Figure 4.1-4. The process consisted of two primary phases: Step 1) an Aerodynamic Extraction which then served as the basis for Step 2) Aerodynamic Damage Assessment.

4.1.4.1 Aerodynamic Extraction

Aerodynamic (aero) increments were extracted from flight data to establish the off-nominal aero moments due to damage using an iterative approach. Evaluation tools were developed to extract the un-modeled yawing, rolling and pitching moment increments as well as the normal, axial and side force increments using a three-step process. First, flight parameters including Mach number, angle-of-attack and sideslip, and control surface settings, were used to extract a predicted set of nominal forces and moments using the Orbiter OADB. Second, flight measured acceleration and rate data, estimated orbiter mass properties and estimated atmospheric data were used to extract flight aerodynamic forces and moments based on the standard aircraft equations of motion. Then, the difference between the two sets of data (flight extracted minus nominal Orbiter OADB) produced the un-modeled (off-nominal) delta aerodynamic forces and moments experienced in flight. Figure 4.1-5 provides an outline of this process.

These force and moment increments were then provided to the GN&C flight trajectory simulation for evaluation. Simulations of the STS-107 entry trajectory were performed with and without the off-nominal delta aerodynamic increments and provided trajectory data and flight control system responses. A comparison of the STS-107 flight sensor data against the simulated trajectory predictions with the off-nominal aero increments was used to assess the adequacy of the increments. While the technique employed essentially forces a match between flight and simulation, the distribution of the off-nominal flight response between aerodynamics, atmospheric conditions, model uncertainty, etc. was critical to establishing the final aero increment magnitudes to be attributed solely to damage. After multiple iterations of this process, a good match was produced by taking into account all of these aspects of the flight

reconstruction. The resulting aero increments were considered defined and ready to serve as a measure for the damage assessment evaluation.

4.1.4.2 Damage Assessment

Assessing the change in aerodynamics due to damage required a definition of modified configurations such as those shown in Figure 4.1-6 & Figure 4.1-7, for test and analysis, consistent with a postulated damage scenario. As previously mentioned in the chronology of the investigation, the range and specifics of the postulated damage varied as the investigation matured. For example, WLE damage was initially modeled by removal of entire RCC panels. As new data and findings emerged, the postulated damage configurations were modified (e.g. the follow on test of missing partial WLE RCC panels) to be more consistent with the latest available information and the rapid pace of the investigation. It should be noted that evaluation of the damaged configurations was approached as an integrated aerodynamic and aerothermodynamic effort. This combined aerodynamic/aerothermal approach was a fundamental part of the process throughout the investigation. The test and analysis results were balanced against both of these aspects in judging their merits in supporting any particular damage scenario. The aerothermal results are detailed in Section 5.2.

Also essential to the assessment were reliable hypersonic test facilities and analysis capabilities. All of the wind tunnel tests conducted in support of this investigation were completed in either of two LaRC hypersonic wind tunnel test facilities, the 20-Inch Mach 6 Air Tunnel or the 20-Inch Mach 6 CF4 Tunnel. The vast majority of the testing was ultimately conducted in the CF4 facility because of the established capability of this facility to reproduce high Mach number (13-18) orbiter aerodynamic characteristics by accurately simulating the relevant flow field gas dynamics (see Sections 4.3.1 and 5.2.3.1 for more details). Complementing the WT testing was the application of various CFD analysis codes. These ranged from basic Newtonian estimation routines (SNEWT-JSC & CBAERO-ARC) to inviscid Euler calculations (CART3D-JSC & FELISA-LaRC) as well as several high-fidelity viscous Navier-Stokes simulations (Overflow-JSC, LAURA-LaRC, GASP-ARC & USA-Boeing). CFD analyses results were provided for both wind tunnel and flight conditions (including high temperature gas chemistry effects). The CFD analysis tools were employed in various ways to support damage assessment and evaluation. First, Newtonian and inviscid methods were used as a rapid screening tool for postulated damage scenarios. The CFD flow fields generated for the various damaged configurations were reviewed to gain a more complete understanding of the resulting aerodynamic deltas. Additionally, the CFD analysis was used to evaluate Mach number and angle-of-attack sensitivities as well as WT-to-flight extrapolation. Finally, CFD analysis was employed heavily to interrogate the contribution of leeside flow interactions and any resulting contribution to the delta aerodynamic patterns. These test and analysis capabilities and results are covered in detail in Section 4.3.

For each damage scenario, wind tunnel test models and CFD analysis grids were modified to represent a damaged configuration. The method to establish the change in aerodynamics utilized a baseline run for comparison. First, the nominal or clean configuration aerodynamic baseline was established for each wind tunnel run or CFD analysis. Then the model/grid geometry was modified to represent the damaged configuration under consideration. The test or analysis was repeated with this modified model and the delta aerodynamic force (normal, axial & side) and moments (roll, pitch & yaw) were determined as the difference ($\Delta = \text{damaged} - \text{baseline}$). These assessment results were collected for the varied set of damaged configurations being considered, including lower surface wing gouges, raised MLG door forward edge, MLG door removed / open wheel well cavity, MLG and door deployed, missing WLE RCC panels (2-12 individually and in combination), partial RCC panels missing (lower half to apex), T-Seal slot, holes through wing with upper and/or lower carrier panel missing, wing deformation including lower surface depressions, as well as vertical tail and leeside interaction – see WT Test matrix (Aerodynamic Appendices, Section 4.7.3) and CFD Analysis case matrix (Table 4.3-6).

All the test and analysis results were then used in developing a match between the extracted off nominal aerodynamics and the damage assessment delta aerodynamics as well as the external aerodynamic heating patterns. The ultimate goal was to correlate these results with vehicle damage consistent with the final working scenario that progressed from an initial damage stage at EI to a considerably more aerodynamically significant damaged configuration just prior to LOS.

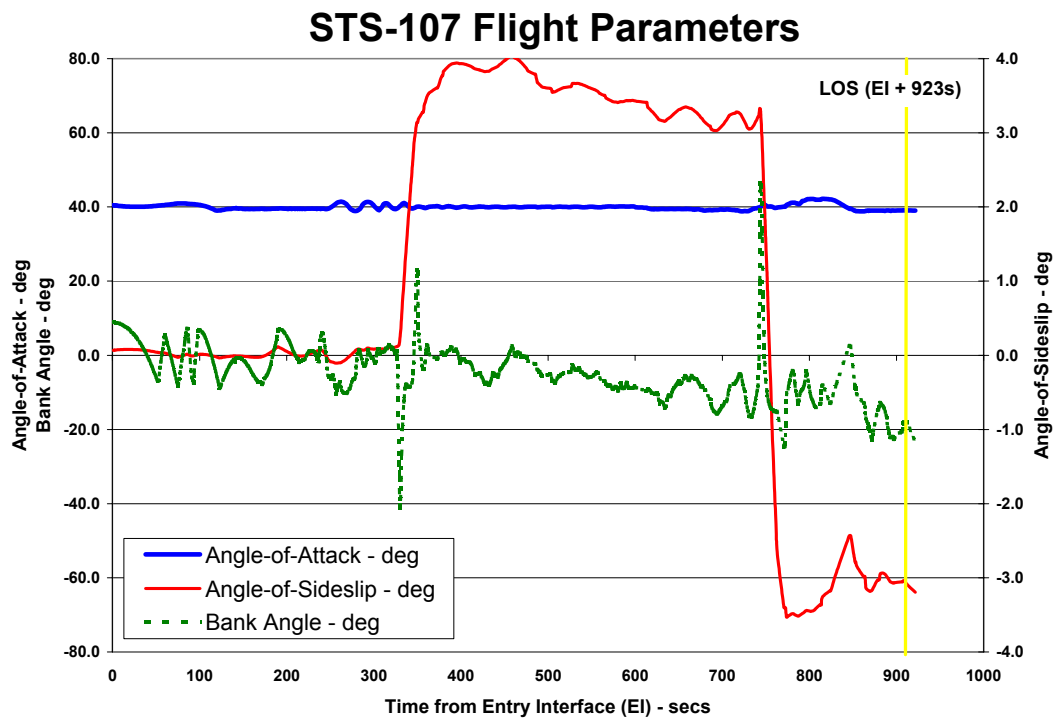


Figure 4.1-1 STS-107 Angle-of-Attack, Sideslip & Bank

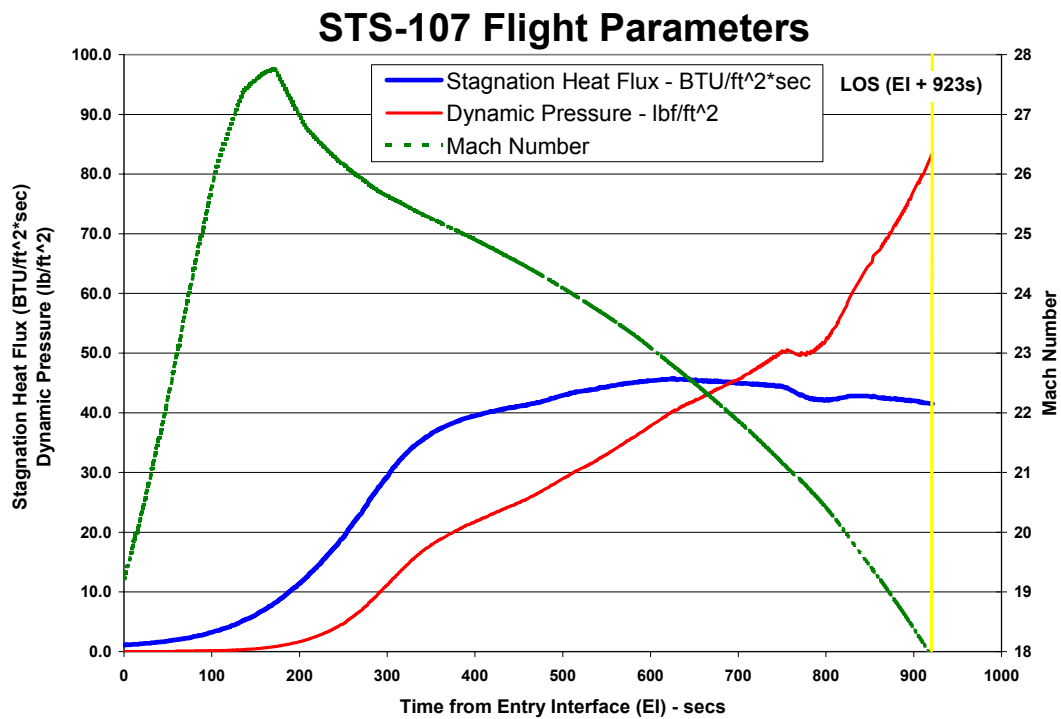


Figure 4.1-2 Mach No., Dynamic Pressure & Stagnation Heat Flux

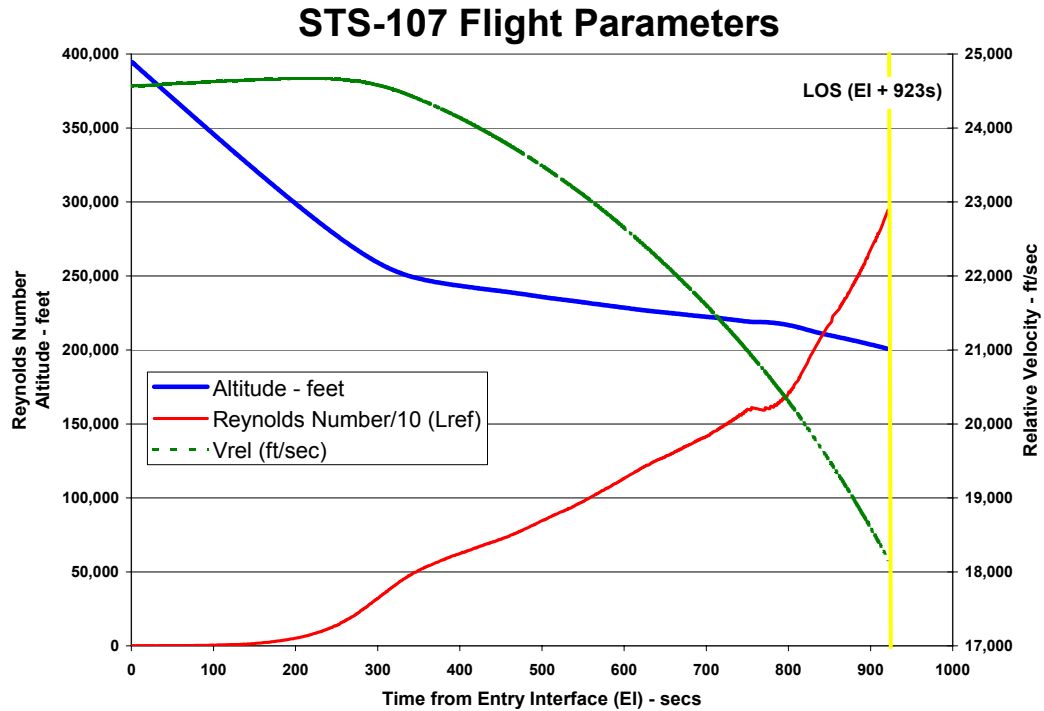


Figure 4.1-3 Altitude, Velocity & Reynolds No.

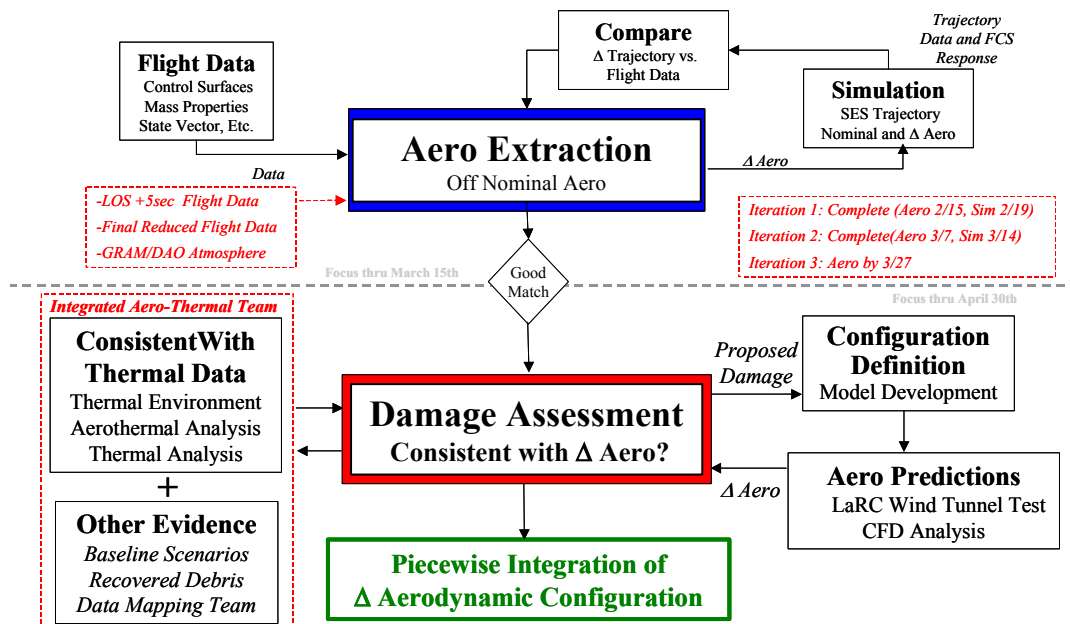
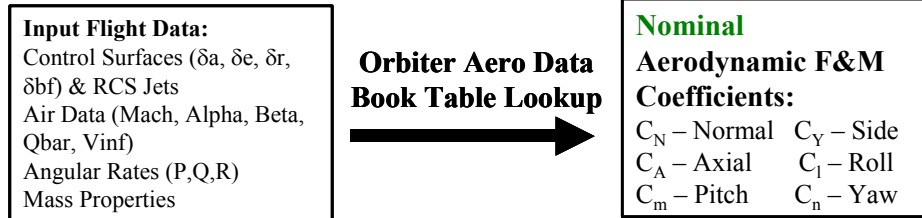
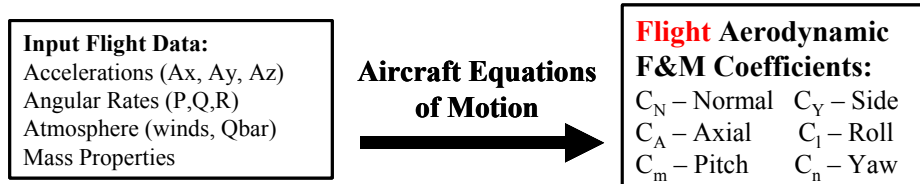


Figure 4.1-4 Aerodynamic Reconstruction Process

1) Orbiter aerodynamic database defines nominal aerodynamics



2) Aerodynamic coefficients extracted from flight data



3) Flight extracted - Nominal Database = Unmodeled (delta aero) F&Ms

$$\Delta C_{n \text{ Reconstructed}} = C_{n \text{ Flight Extracted}} - C_{n \text{ Aero Database}}$$

Figure 4.1-5 Aerodynamic Extraction Methodology



Figure 4.1-6 WT Model with WLE RCC panels (6 & 9) removed

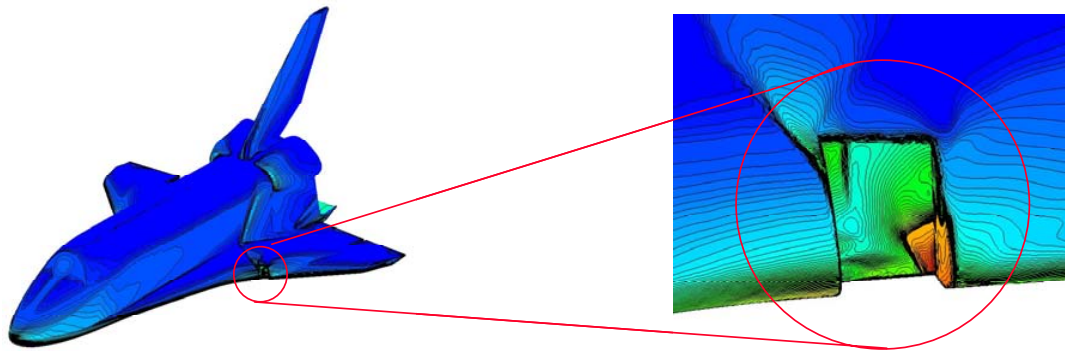


Figure 4.1-7 FELISA Grid with WLE RCC panel 9 removed

4.2 Aerodynamic Extraction

Aerodynamic (aero) increments were extracted from flight data to establish the off-nominal aero moments due to damage using an iterative approach. This section addresses the details of the atmospheric model, high altitude winds and the aerodynamic extraction process and results.

4.2.1 Atmospheric Model

An accurate simulation of the STS-107 entry depended in part on a reliable model of the environment through which the vehicle flew. By using the flight data from EI-5 to LOS and the wind information provided by experts from the Data Assimilation Office (DAO) and the Marshall Space Flight Center (MSFC), atmospheric parameters such as density, temperature, and pressure at a set of altitude reference points were derived with a process slightly modified from that used previously for post-flight analysis. Results compared favorably with the independent assessment of corresponding parameters from DAO/MSFC and contributed greatly to the fidelity of the resulting match between the integrated simulation output and the down listed flight data.

The original atmospheric reconstruction process used as its inputs a pre-defined set of 22 down listed measurements from the Orbiter Data Reduction Complex (ODRC), including such information as vehicle position and orientation, rates and accelerations, and control surface deflections, over the time period for which the atmospheric data was to be derived. This information along with data from the Orbiter OADB was used in an iterative process to generate an estimate of the atmospheric density, pressure, and temperature of the environment. This technique was then revised to make use of higher fidelity data compiled as a part of this investigation, as well as data that was not available when the code was originally developed.

Wind data from DAO/MSFC, for example, was incorporated into the determination of the values for angle of attack, sideslip, and true airspeed. As shown in Figure 4.2-1, the angle of attack (α) and sideslip (β), are defined by the angles the body-fixed frame must be rotated around the $-Y_b$ and Z_b axes, respectively, to align the X_b axis along the velocity vector. At high altitudes where there is no sensed air data available, a navigation-based angle of attack and sideslip are determined on-board relative to the Earth-fixed velocity provided by the inertial measurement unit (IMU). However, when the vehicle is flying through an atmosphere that is moving relative to the ground, the velocity of the vehicle relative to the Earth differs from that relative to the air. Thus, the true air speed (TAS) is comprised by the difference in the Earth-fixed velocity and the wind velocity, and it is this vector into which the body axis must be rotated to determine the environment angle of attack and sideslip.

Since the process resulted in rather noisy output at very high altitudes and there was no flight data available below 200,000 ft, the Global Reference Atmosphere Model (GRAM) data was used in those regions for the final data file delivery. In the lower altitude region, the GRAM data was used up to 190,000 ft, and a spline fit was used to smoothly connect the GRAM and reconstructed data in the intervening

10,000 ft region. At very high altitudes, the extremely low densities were not reliably reconstructed by the process, and the resulting temperature and pressure profiles were quite noisy. The GRAM data was identified as a reasonable approximation to this noisy data, and was substituted for reconstructed atmospheric data above 320,000 ft. Thus a smooth and continuous set of data representing the entire atmosphere was created for use in subsequent simulations. The final set of density, pressure, and temperature profiles appear as illustrated in Figure 4.2-2.

4.2.2 GSFC/DAO Upper Atmospheric Wind Model

In the course of the investigation, it became apparent that a more complete understanding of the atmosphere and in particular a more precise estimation of the high altitude winds and density encountered during entry was critical to the reconstruction of the flight and the associated aerodynamic increments. Since a direct and independent measurement of the density and winds is not available from the onboard data system an effort was initiated to use meteorological resources to generate an atmosphere along the orbiter trajectory for the time of entry.

Generation of a meteorologically derived atmosphere had not been done since very early in the space shuttle program and therefore there was a development effort involving many resources in the meteorological community. The DAO at the Goddard Space Flight Center (GSFC) was the principal organization tasked to provide the atmosphere. The DAO uses space and ground based resources on a regular basis to assimilate measured data for atmospheric research. In order to better support the requirement for high altitude (> 200,000 ft) meteorological data, the DAO additionally assimilated data from the Sounding of the Atmosphere using Broadband Emission Radiometry (SABER) instrument on the Thermosphere Ionosphere Mesosphere Energetics and Dynamics (TIMED) satellite. Through the assimilation process and several iterations, the DAO was eventually able to generate atmosphere data up to an altitude of approximately 250,000 ft., Figure 4.2-3 to Figure 4.2-5.

The DAO atmosphere was then faired with the GRAM February atmosphere by the MSFC. Details of the DAO assimilation and fairing methodology can be found in the STS-107 Natural Environments Document (Aerodynamic Reference 4.6.2).

4.2.3 Aerodynamic Increment Extraction Results

Three aerodynamic predictor tools were modified or developed to extract the STS-107 aerodynamic increments. These tools provided a source for rapid comparison between Orbiter OADB aero and flight predicted aero derived from the observed motion of the vehicle. Two existing tools had been developed as part of the experimental X-38 and X-40 flight test programs. Application of these tools to STS-107 was validated by processing flight data and simulator results from two previous Columbia flights (STS-109 & STS-73). A third tool was developed for the analysis using existing Orbiter OADB look-up routines to provide further substantiation. Also, hand calculations completed the analysis and served as a verification of results. Finally, an independent evaluation focused on the time frame from EI to EI+ 600 sec also confirmed these results.

As input flight data was analyzed and refined by the Integrated Entry Environment (IEE) team and as new atmospheric data became available, the aerodynamic increment model went through four revisions to improve accuracy by accounting for all relevant aspects of the flight reconstruction. Wind correction adjustments made to angle-of-attack and sideslip using the final DAO atmosphere greatly influenced the aerodynamic increment results in the fourth and final revision (Figure 4.2-6 thru Figure 4.2-10) (reducing the magnitude of the rolling and yawing moments by approximately 50%). Various uncertainties were also assessed to characterize the relative magnitude of the off-nominal aero forces and moments against other potential asymmetric aerodynamic contributions. These design level asymmetries are also depicted in the figures (note labels). The aerodynamic increment model reference table (Figure 4.2-14) was provided to the GN&C community for inclusion in flight simulations.

Evaluation of the resulting increments indicates that off-nominal aerodynamics were not apparent during the early portion of the STS-107 flight. The first clear indication of off-nominal yawing and rolling moments does not occur until EI + 515 and EI + 521 seconds, respectively. A corresponding small deviation in side

force can also be correlated to this time. The delta pitching moment is first observed in an off-nominal trend much later in the flight, around EI + 836 sec. Further review of data shows that substantial deviation in all three moments does not begin until around EI + 850 sec, which then continues through LOS. For clarity, an expanded section showing the substantial deviation in all three moments late in flight are provided in Figure 4.2-11 through Figure 4.2-13.

As discussed in the derived atmosphere model section, at high altitudes where there is no sensed air data available, the extraction technique must utilize the orbiter on board (normal) acceleration as an input to estimate the atmospheric density profile. As applied, this produces a normal force increment of zero. While necessary to accurately define the density, the zero normal force increment result is not considered accurate. Accounting for limitations presented by the data available, extracting accurate side and axial force increments were considered higher priority and the normal force extraction was thus sacrificed in the process.

Furthermore, it should be noted that the extracted force increments due to damage are a very small percentage (1-2%) of the expected total forces. This is consistent with the small off-nominal moments seen for the majority of the entry flight time. Considering the accuracy of the data available to extract these force increments, it was determined that the forces would not be considered a good measures of the damage induced aerodynamics. Therefore, the damage assessment did not attempt to match the aerodynamic force increments.

On the other hand, the extracted moments provide direct indication of off-nominal asymmetric aerodynamics. In flight the orbiter flight control system is continuously maintaining a trimmed (or zero moment) condition. Any small (non-zero) offset from this trimmed flight condition will manifest itself in the derived off-nominal moment increments. These delta aerodynamic moment increments are thus clear indicators of off-nominal aero and were the primary focus of the damage assessment efforts.

4.2.4 Correlation to Working Scenario

A thorough review of the final increments indicates that initially the damage to Columbia's left wing was too small to produce significant aero effects. The extracted moments early in entry (prior to EI + 500 sec) tend to correlate well with past OV-102 flight results from STS-109 and STS-73 (Figure 4.2-15 to Figure 4.2-17). Combined with the level of uncertainties accounted for in this flight regime, the near zero increments are consistent with no significant damage. As the flight progresses, a clear break in the previous flight trends becomes obvious in the rolling and yawing moment increments at a point after EI + 500 sec. The pitching moment increment, however trends well with previous flights (particularly STS-73) until even later in entry and can only be considered truly off-nominal sometime after EI + 800 sec.

To aid in the reconstruction effort and present correlation between vehicle reaction, debris sightings and onboard measurements, the increments were presented with these events labeled (Figure 4.4-20 to Figure 4.4-23). The correlation with this other available data provides the basis for defining the initial indication of off-nominal aerodynamics around EI+515 sec. While relatively small, the initial rolling and yawing moment increments are both negative. In this flight regime the only possible source of aerodynamic asymmetries are either due to a Yc.g. offset (i.e. other than on the centerline), a very small bent airframe term or the high altitude winds. Asymmetric boundary layer transition (ABLT) has been seen on a number of orbiter entry flights, but never this early in the entry profile, (in fact never prior to the end of STS-107 flight near Mach 18). Additionally, this (-roll/-yaw) pattern is inconsistent with previous asymmetric boundary layer transition observations which have always produced a +roll and -yaw for a left side ABLT. Since winds and c.g. offset have been accounted for and ABLT ruled out, the damage to Columbia's left wing is the only remaining source of the off-nominal aerodynamics.

A distinct change in the aerodynamic increment trend occurs at EI + 602 sec corresponding precisely with Debris Event No. 5 as well as the onset of the slow but steady aileron trim change response by Columbia's flight control system. At this point in flight, the rolling moment increment trend changes from increasing negative to increasing positive. It is postulated that this corresponds to an abrupt configuration change as the left wing damage progressed (this will be elaborated on in Section 4.5). After this point, both rolling (+) and yawing moment (-) trends increase in what is essentially a linear fashion until EI + 836 sec. It should be noted that up to this point in flight the aerodynamic increments are still relatively small (less than

the worst case asymmetric aerodynamic design levels). The orbiter flight control system has continued to easily account for this slight change in the vehicles aerodynamics and trimmed flight is maintained. At EI + 766 sec, the Orbiter completes the initial roll reversal with no apparent impact from the damaged left wing. However, around EI + 836 sec the aileron trim begins a sharp increase and the rate of rolling and yawing moment increment growth abruptly increases. These extracted moments eventually exceed asymmetric aerodynamic design levels as defined by the Orbiter OADB ABLT after EI + 877 sec.

Between EI + 920 and 928 sec (LOS + 5 sec) the off-nominal rolling and yawing moments dramatically increase in magnitude to levels exceeding 6 times the asymmetric aerodynamic design levels. Flight control responds by maximizing the aileron trim rate and eventually fires all 4 RCS yaw jets continuously to maintain trimmed flight. This rapid increase in the off nominal moments near the end of flight effectively saturates Columbia's flight control system trim capability and eventually led to loss of control and vehicle breakup. For further explanation of the vehicle response to the off nominal aerodynamics encountered see the STS-107 Integrated Entry Environment Team Final Report, Aerodynamic Reference 3.

Based on these observations, the final aero increments indicate that initial damage did not produce significant changes in the nominal aerodynamic properties of the vehicle early in flight (prior to EI + 515 sec). Therefore, the aerodynamic extraction cannot be used to conclude damage to Columbia's wing existed at EI. These increments should primarily be used for flight reconstruction and as a screening mechanism for wind tunnel and CFD damage progression assessments in correlation with the aerothermodynamic evaluations and the other available data.

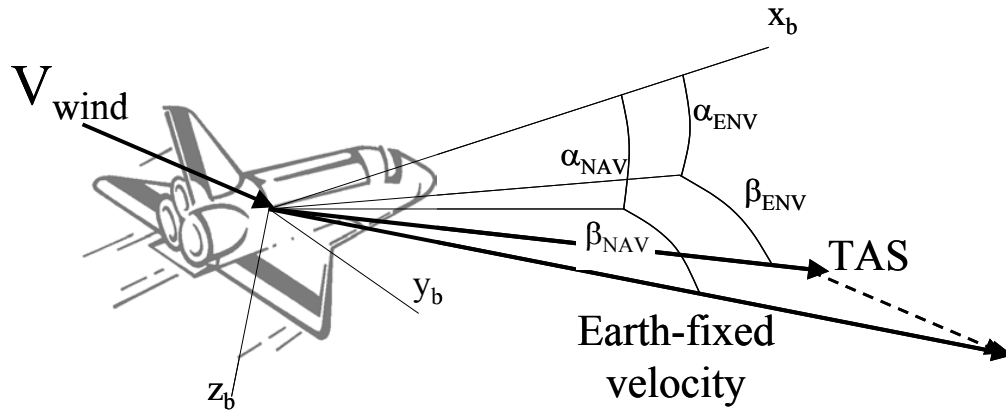


Figure 4.2-1 Determination of Angle-of-Attack & Sideslip

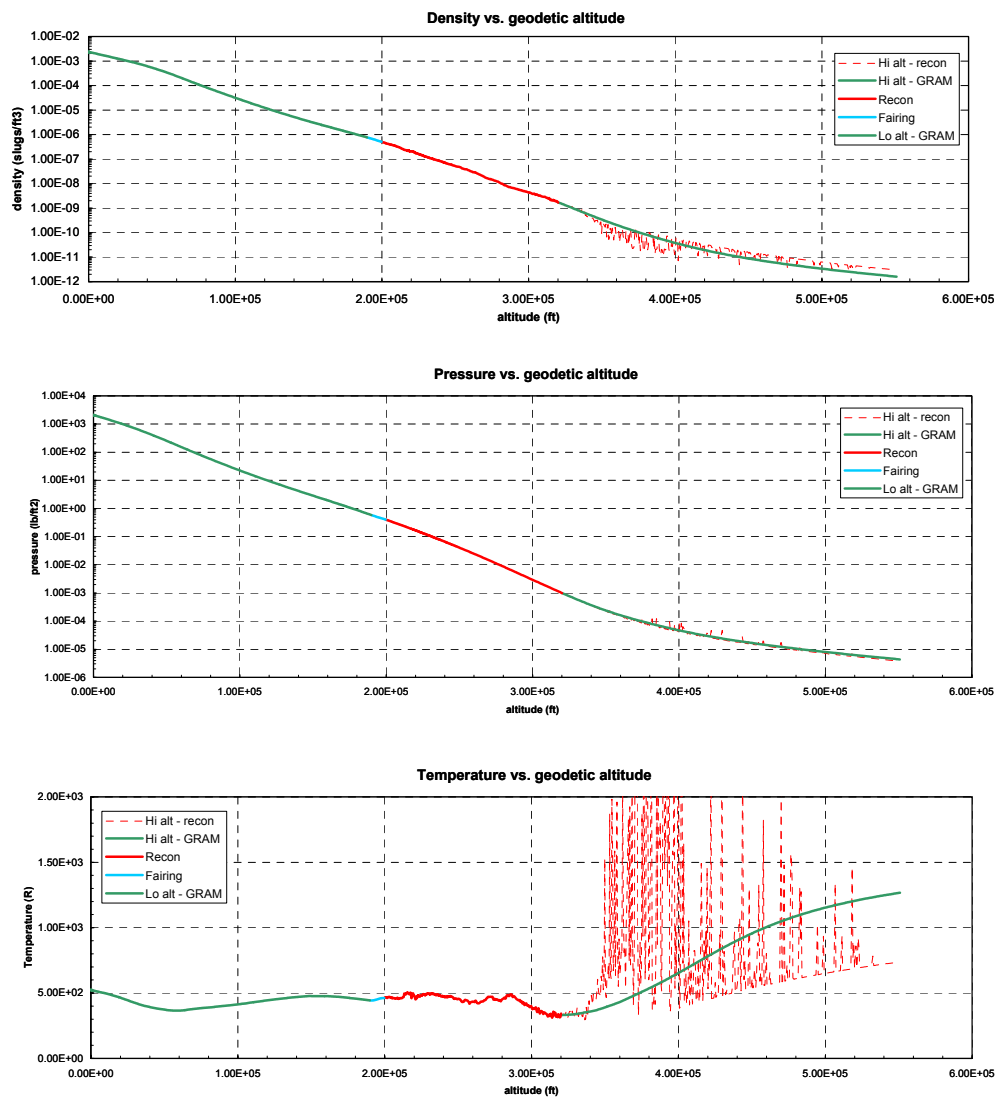


Figure 4.2-2 Reconstructed Atmospheric Density, Pressure & Temperature

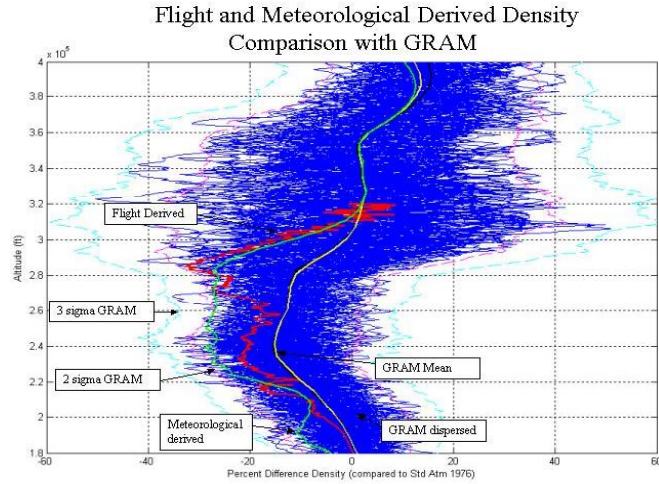


Figure 4.2-3 Flight & Meteorological Derived Density

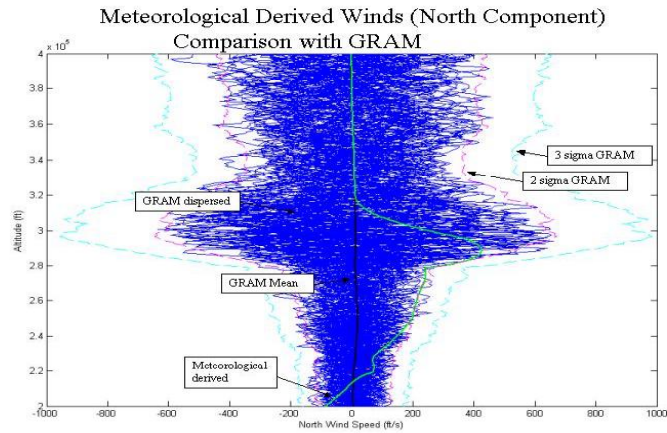


Figure 4.2-4 Meteorological Derived Winds (North Component)

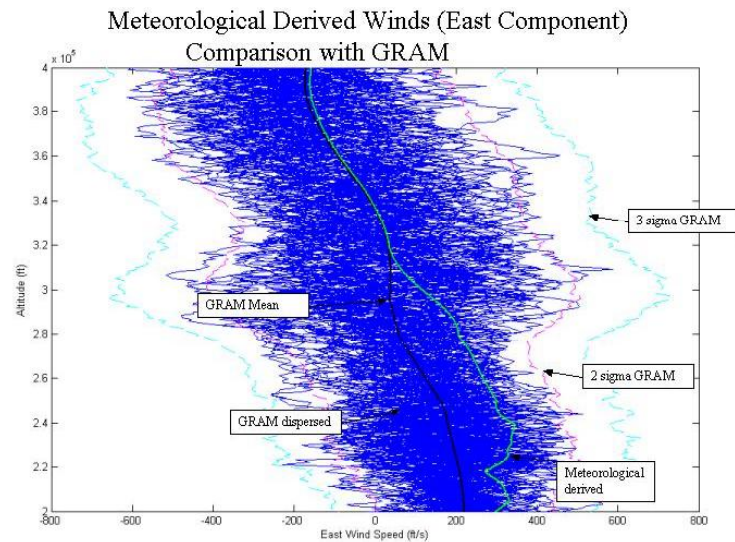


Figure 4.2-5 Meteorological Derived Winds (East Comp.)

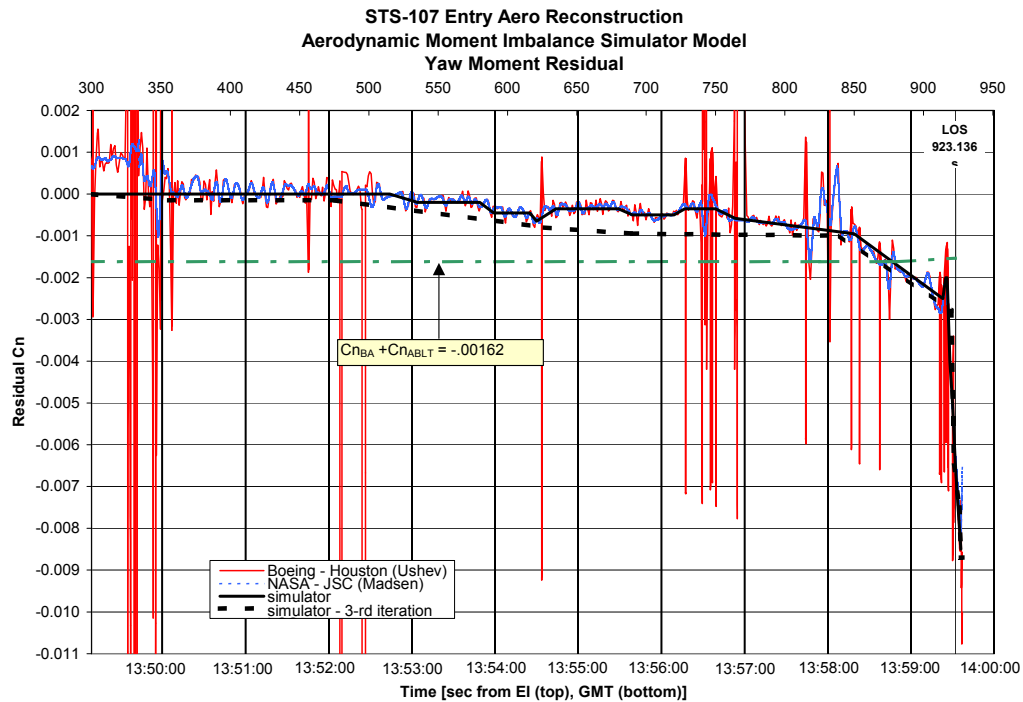


Figure 4.2-6 Delta Yawing Moment Coefficient

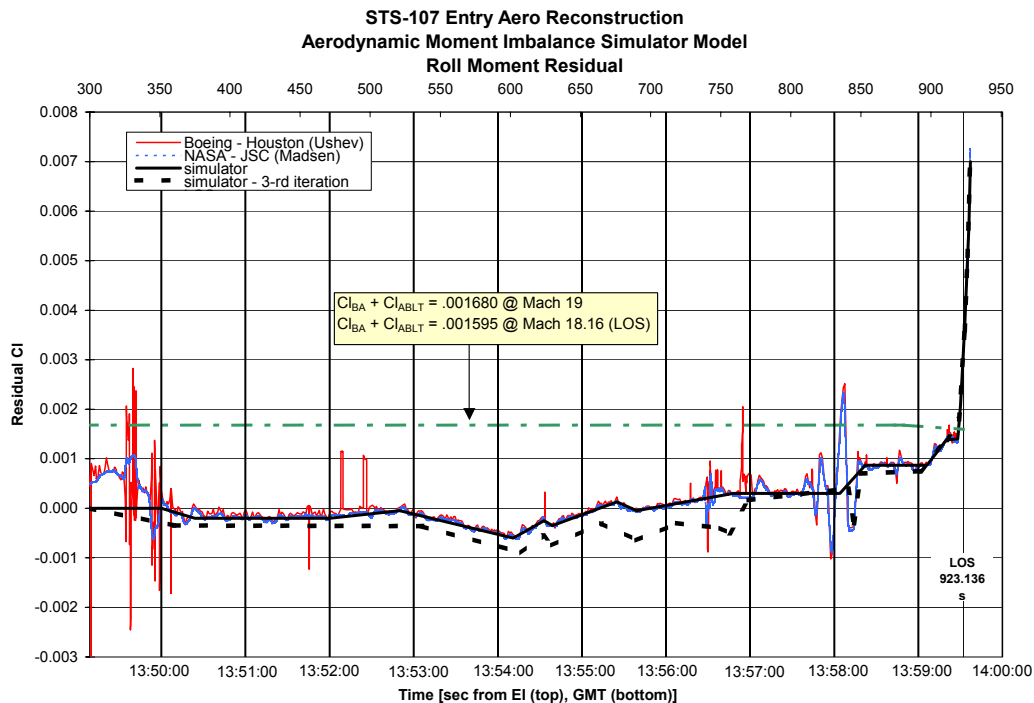


Figure 4.2-7 Delta Rolling Moment Coefficient

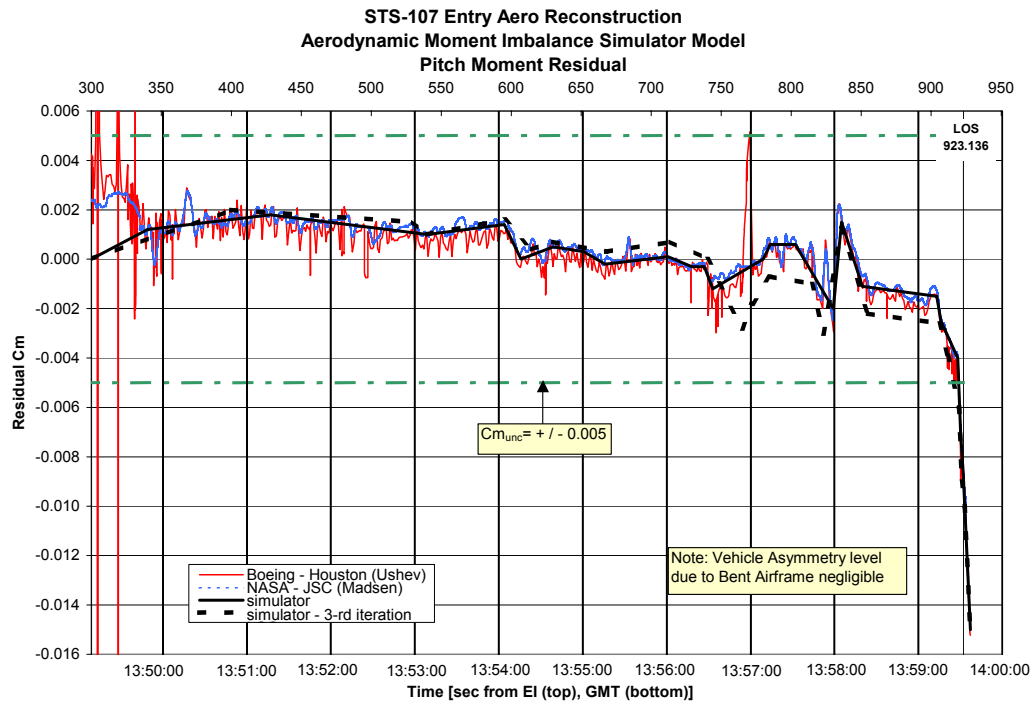


Figure 4.2-8 Delta Pitching Moment Coefficient

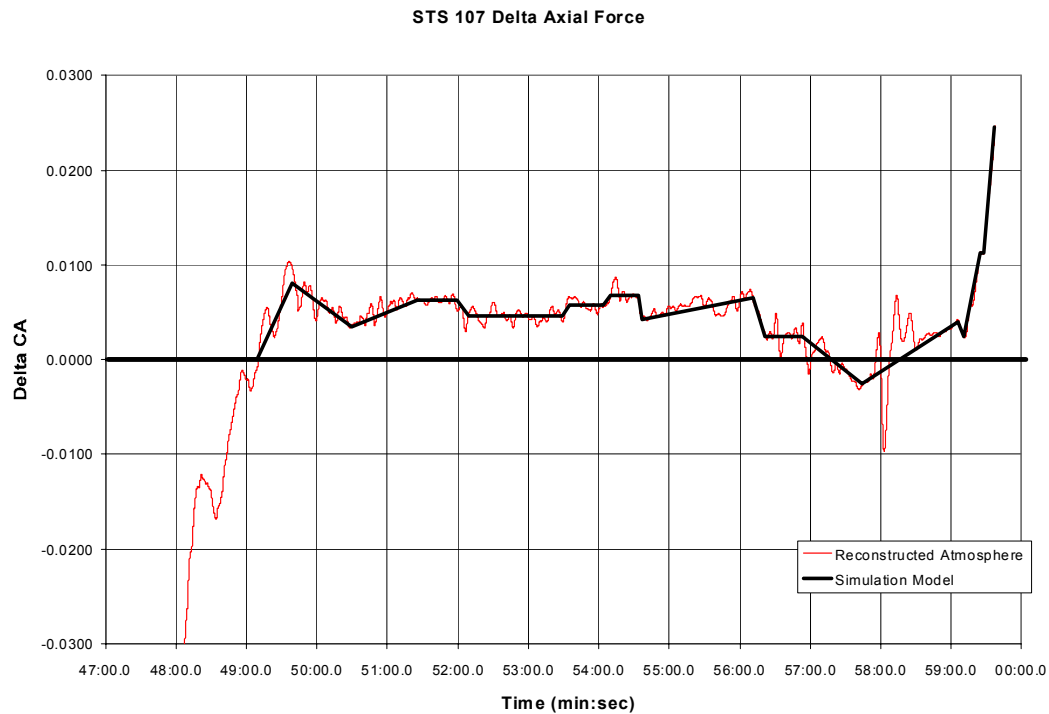


Figure 4.2-9 Delta Axial Force Coefficient

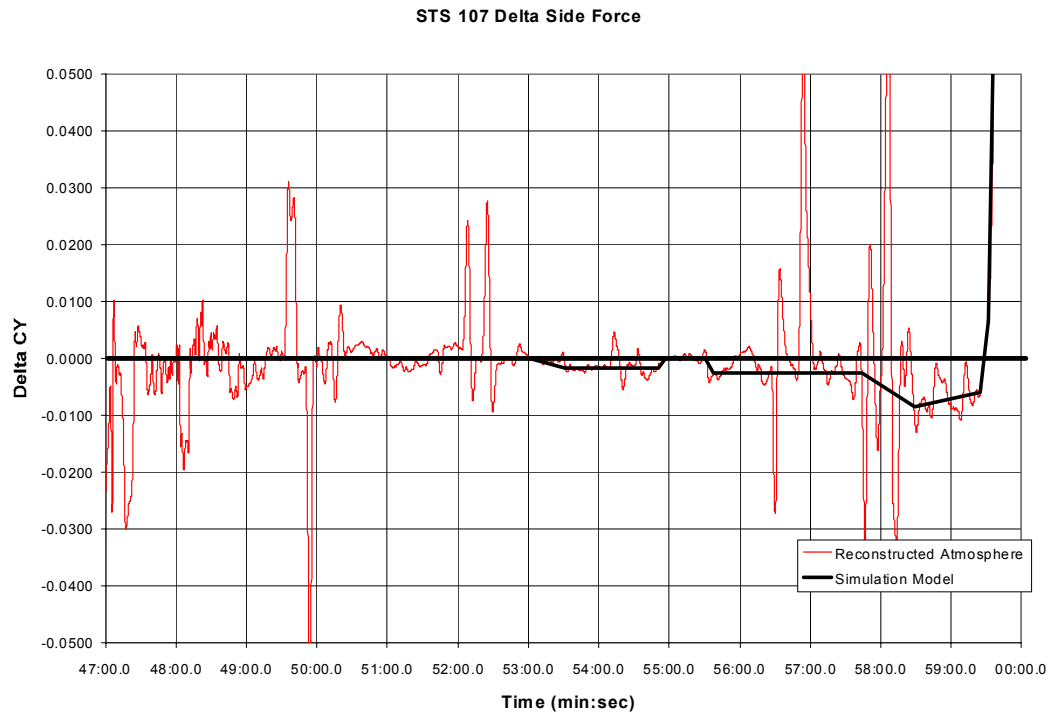


Figure 4.2-10 Delta Side Force Coefficient

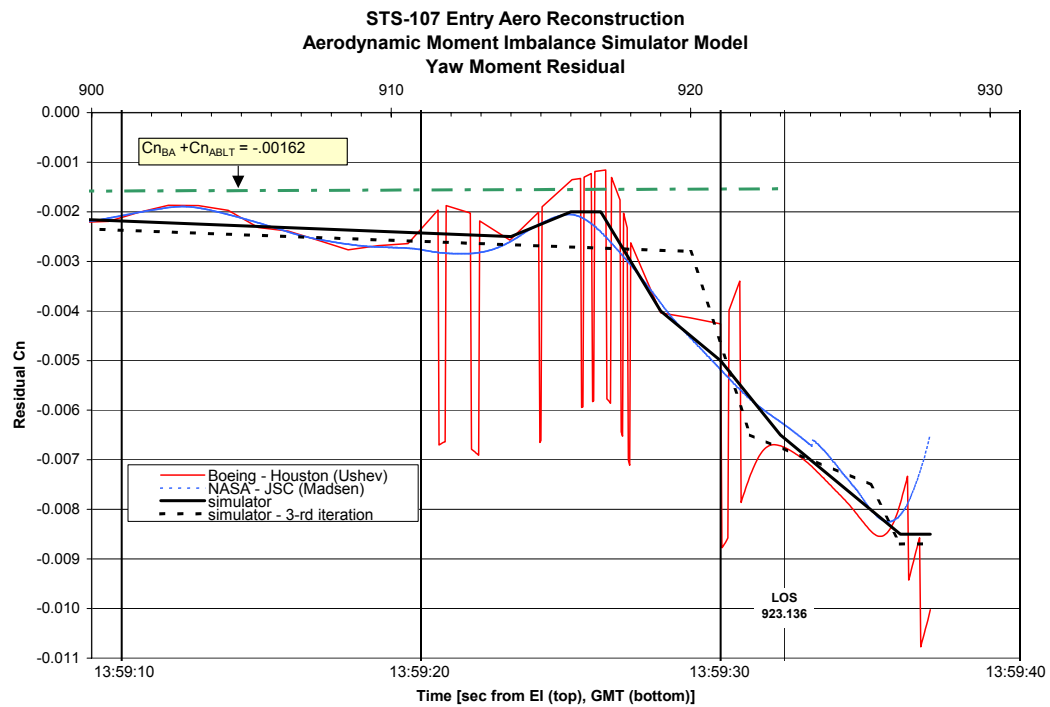


Figure 4.2-11 Delta Yawing Moment Coefficient (just prior to LOS)

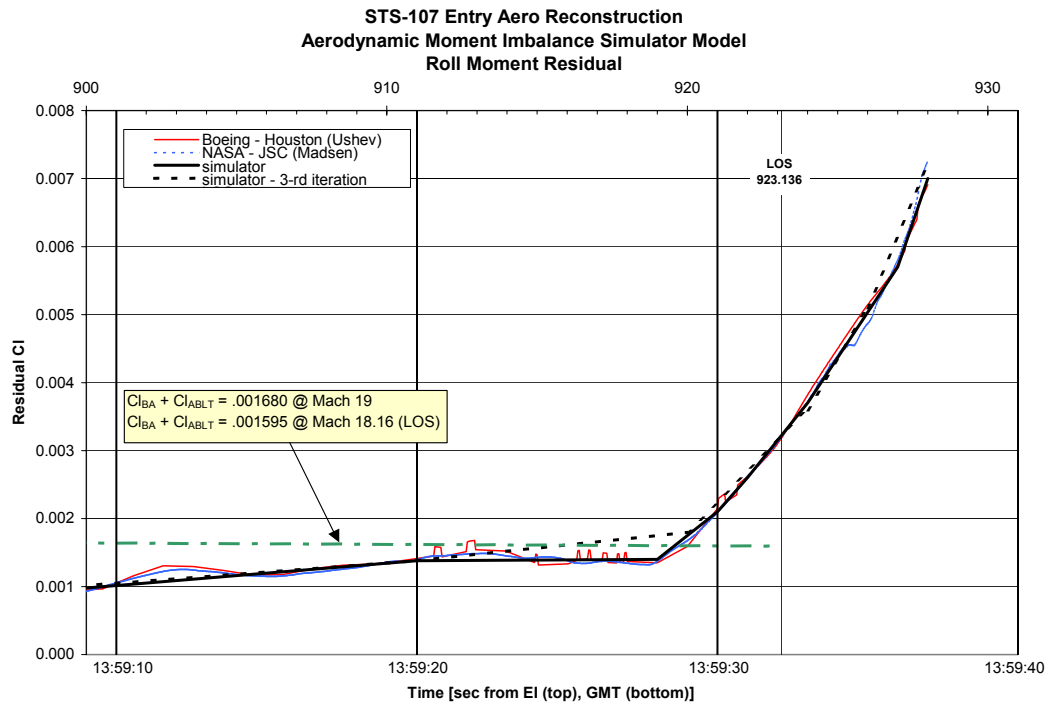


Figure 4.2-12 Delta Rolling Moment Coefficient (just prior to LOS)

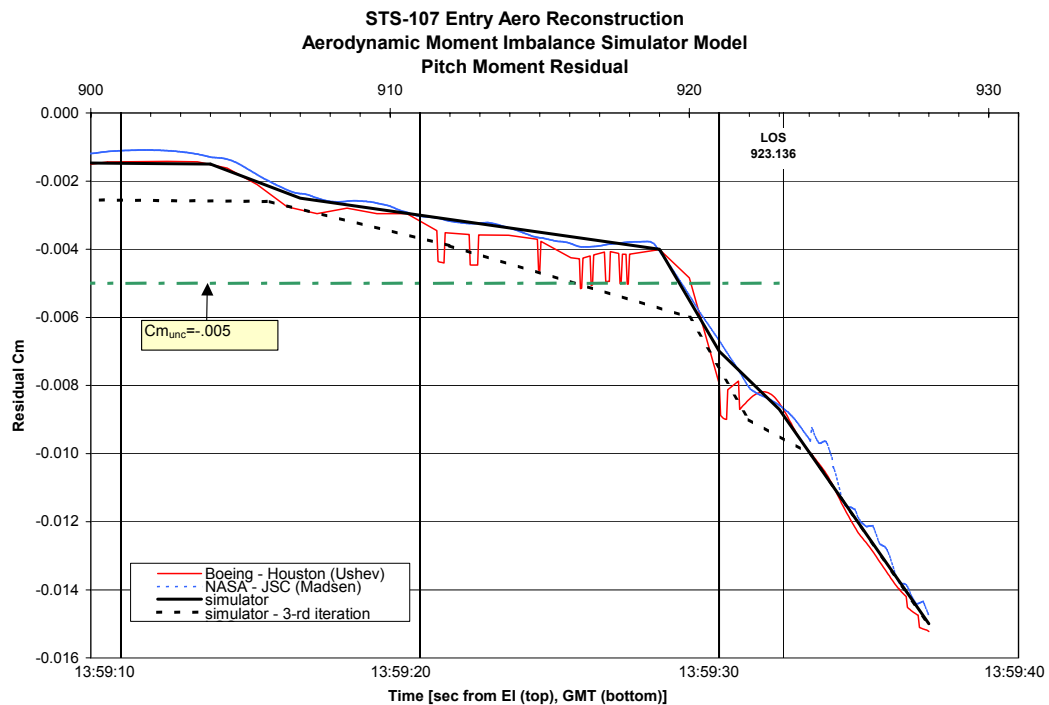


Figure 4.2-13 Delta Pitching Moment Coefficient (just prior to LOS)

STS-107 Simulator Moment Imbalance Model – Reference Table

(time is seconds from EI)

Pitch Moment (Cm)		Yaw Moment (Cn)		Roll Moment (Cl)		Axial Force (CA)		Side Force (CY)	
Time	Imbalance	Time	Imbalance	Time	Imbalance	Time	Imbalance	Time	Imbalance
0	0.00000	0	0.00000	0	0.00000	0	0.00000	0	0.00000
300	0.00000	300	0.00000	351	0.00000	360	0.00000	349	0.00000
340	0.00120	356	0.00000	375	-0.00020	368	0.00100	354	-0.00070
428	0.00180	515	0.00000	471	-0.00020	440	0.00100	695	-0.00160
540	0.00100	535	-0.00020	521	-0.00005	445	0.00050	719	-0.00190
595	0.00140	580	-0.00020	602	-0.00060	495	0.00050	730	-0.00050
607	0.00000	590	-0.00045	624	-0.00025	510	0.00120	740	-0.00050
630	0.00050	616	-0.00045	630	-0.00035	597	0.00300	745	-0.00120
652	0.00030	621	-0.00065	676	0.00013	606	0.00490	860	-0.00120
667	-0.00020	635	-0.00035	690	-0.00005	632	0.00200	862	0.00000
712	0.00010	680	-0.00035	759	0.00030	742	0.00200	875	0.00000
729	-0.00030	690	-0.00050	835	0.00030	764	0.00400	880	-0.00200
738	-0.00030	720	-0.00050	853	0.00087	769	0.00250	895	0.00000
744	-0.00120	728	-0.00035	897	0.00087	892	0.00480	924	-0.00400
780	0.00000	750	-0.00035	911	0.00138	897	0.00580	928	-0.02222
785	0.00060	764	-0.00058	919	0.00140	902	0.00450		
803	0.00060	850	-0.00095	921	0.00210	916	0.01250		
830	-0.00200	914	-0.00250	922	0.00260	919	0.01250		
836	0.00150	916	-0.00200	924	0.00370	928	0.02450		
851	-0.00110	917	-0.00200	927	0.00570				
904	-0.00150	919	-0.00400	928	0.00700				
907	-0.00250	921	-0.00500						
919	-0.00400	923	-0.00650						
921	-0.00700	927	-0.00850						
923	-0.00870	928	-0.00850						
928	-0.01500								

Figure 4.2-14 STS-107 Delta Aero Increment Model

Delta Yawing Moment (using downlisted Qbar NAV)

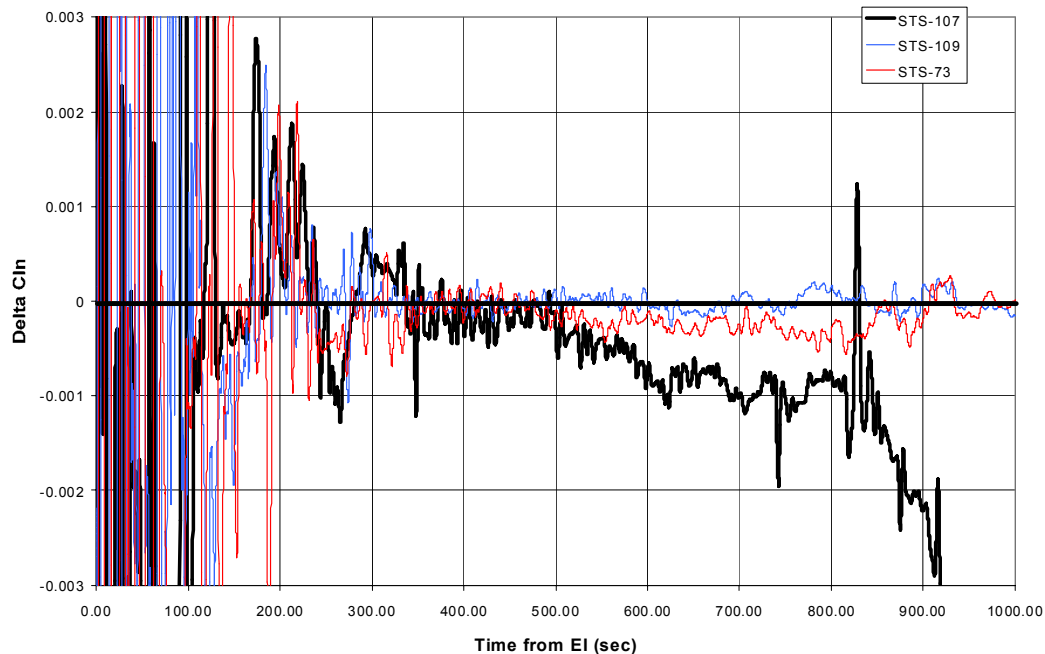


Figure 4.2-15 Delta Yawing Moment (STS-107, 109 & 73)

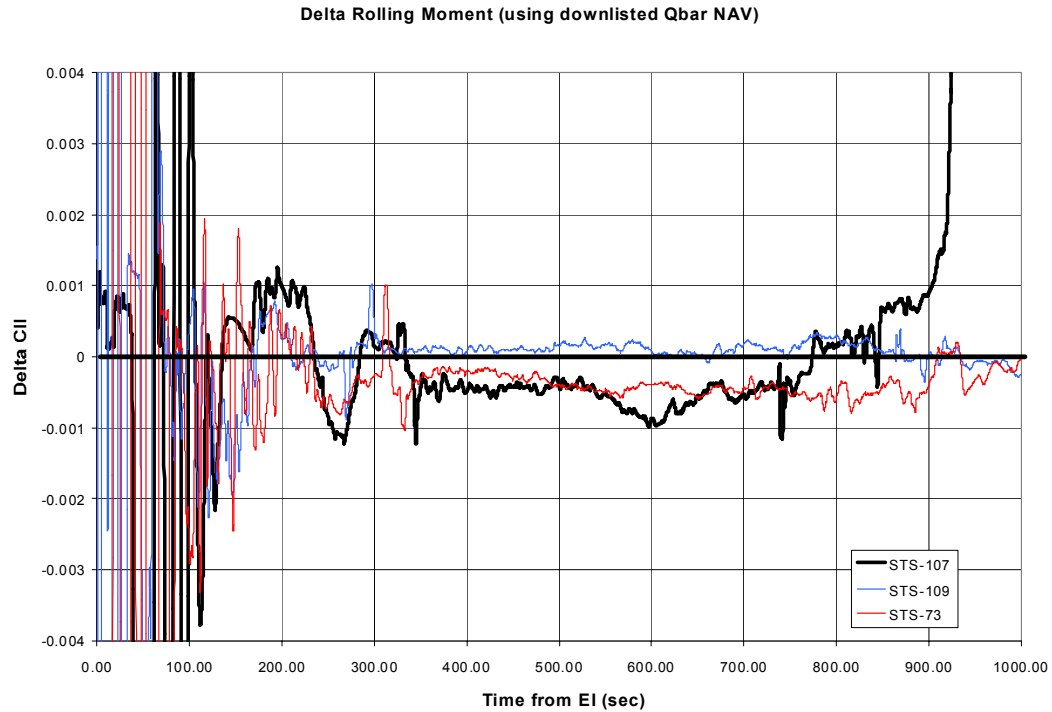


Figure 4.2-16 Delta Rolling Moment (STS-107, 109 & 73)

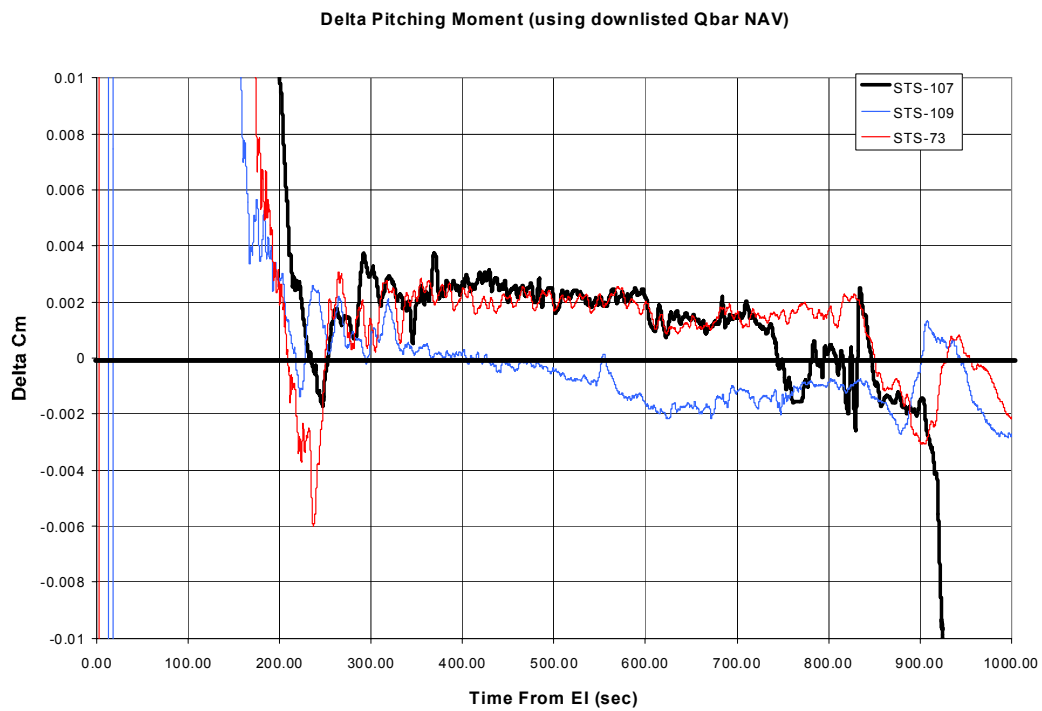


Figure 4.2-17 Delta Pitching Moment (STS-107, 109 & 73)

4.3 Damage Assessment Aero

4.3.1 Wind Tunnel Testing

Aerodynamic tests in support of the Columbia accident investigation were conducted in two hypersonic wind tunnels at the NASA Langley Research Center. The primary purpose of these tests was to measure the forces and moments generated by a variety of outer mold line alterations (damage scenarios). Simultaneously acquired global heat transfer mappings were obtained for a majority of the configurations tested. Schlieren photography visualizing the shock structures in the flow was utilized when possible. The damage scenarios evaluated included asymmetric boundary layer transition, gouges in the windward surface acreage thermal protection system tiles, wing leading edge damage (partially and fully missing RCC panels), holes through the wing from the windward surface to the leeside, deformation of the wing windward surface, and main landing gear door and/or gear deployment. The aerodynamic data were compared to the magnitudes and directions observed in flight, and the heating images were evaluated in terms of the location of the generated disturbances and how these disturbance might relate to the response of discrete gages on the Columbia Orbiter vehicle during entry.

4.3.1.1 Wind Tunnel Facilities

The two facilities used in this investigation were the 20-Inch Mach 6 Air Tunnel and the 20-Inch Mach 6 CF4 Tunnel. These facilities are conventional (as compared to impulse), low-enthalpy, blow-down type hypersonic tunnels. The Mach 6 air tunnel uses heated, dried, and filtered air as the test gas. Typical operating conditions for the tunnel are: stagnation pressures from 30 to 500 psia; stagnation temperatures from 760 to 1000 °R, free stream Mach number from 5.8 to 6.1; free stream unit Reynolds numbers from 0.5 to 8 million per foot; a free stream and post-normal shock ratio of specific heats (γ) of 1.4; and a normal shock density ratio of 5.3. The facility has a two-dimensional contoured nozzle leading to a closed, solid-wall test section with dimensions of 20.5 by 20 inches. The test core varies from 12 to 14 inches depending on the operating condition. Nominal run time is approximately 60 to 120 seconds, although longer runs times are possible.

The CF4 Tunnel uses heated, dried, and filtered carbon tetrafluoride (Freon 14; molecular weight of 88 which is three times heavier than air) as the test gas. Typical operating conditions for the tunnel are: stagnation pressures from 85 to 2000 psia; stagnation temperatures up to 1300 °R, free stream Mach number from 5.9 to 6.0; free stream unit Reynolds numbers from 0.02 to 0.55 million per foot; a free stream γ of 1.21 and a post-normal shock γ of 1.10; and a normal shock density ratio of 11.7. The facility has a contoured axisymmetric nozzle with a nozzle exit diameter of 20 inches, leading to an open-jet test section. The test core varies from 12 to 14 inches depending on the operating condition. Nominal run time is approximately 20 seconds.

The test conditions in the two facilities for the tests performed for this investigation are summarized below. The majority of the runs in the Mach 6 air tunnel were made at a length Reynolds number of 2.4 million (based on a reference body length of 1290.3 inches full scale), which corresponds roughly to flight at Mach 19 and 207,00 feet, near loss of signal. The majority of the runs in the CF4 tunnel were made at a length Reynolds number of 0.36 million (based on a reference body length of 1290.3 inches full scale), which corresponds roughly to flight at Mach 25 and 256,00 feet.

Nominal Flow Conditions in NASA LaRC Aerothermodynamics Laboratory

Facility (x10 ⁶)	M_∞	q_∞ (psi)	$P_{t,1}$ (psi)	$T_{t,1}$ (°R)	ρ_2/ρ_∞	Re_∞ /ft
20-Inch Mach 6 Air	5.90	1.04	60	890	5.2	1.0
	5.94	2.10	125	910	5.3	2.1
	5.96	3.05	180	910	5.3	3.0
20-Inch Mach 6 CF4	5.94	0.65	750	1180	11.7	0.27
	5.94	1.27	1330	1210	11.7	0.45

4.3.1.2 Applicability of Wind Tunnels to STS-107 Flight Conditions

The loss of STS-107 occurred during entry at high Mach number and enthalpy levels, and relatively low Reynolds numbers. At these flight conditions high-temperature effects (i.e. flow chemistry) are significant due to the dissociation-recombination and ionization of the gas as it passes through the vehicle bow and wing shocks. These high-temperature effects increase the shock density ratio and lower the specific heat ratio (γ) of the gas within the shock layer, causing shocks to lie closer to the vehicle surface and altering their interaction locations; these high-temperature effects cause the gas to expand to lower pressures than would occur for a non-reacting gas. The CF4 tunnel provides a simulation of these high-temperature effects via its low value of γ , which is near the value in the Orbiter windward flow field at hypervelocity flight conditions. For example, lower pressure levels than expected on the rear windward portion of the Shuttle were identified as the root cause of the so-called Orbiter pitch-up anomaly that occurred during the first flight of Columbia, STS-1, wherein the Orbiter experienced a nose-up pitch increment relative to pre-flight predictions. The CF4 tunnel has been used to successfully demonstrate the magnitude and direction of this pitch-up increment. While the ability of the CF4 tunnel to accurately simulate the leeside flow has not been validated to the extent of the windward flow, the damage scenarios investigated have their initiation on the wing leading edge and the windward surface, and thus the CF4 tunnel is expected to provide credible simulation of their effects.

The Mach 6 air tunnel uses a perfect gas, but all the flow physics phenomena such as flow separation-reattachment, boundary layer transition, and shock-shock interactions, will be present. The high-temperature effects may alter the level and location of these phenomena, but should not add or delete from them. Thus the Mach 6 air tunnel may be used as a preliminary or screening facility, with the CF4 tunnel used to refine the results. A more detailed discussion of the use of these facilities and their relation to the flight environment can be found in section 5.2.3.1.

4.3.1.3 Wind Tunnel Models

Two types of force-and-moment models were used in this investigation, one made from stainless steel and several from cast silica ceramic. The steel model was an existing 0.0075-scale model that was modified to allow testing of gear and door deployment. A wheel well with a maximum depth of 0.35 inches was machined into the wing, a door was fabricated with a tab to allow installation on the model, and a simplified gear was constructed consisting of a single rod ending in a wheel assembly. The ceramic models were built from a mold that used the steel model as a pattern. Individual models were slip cast, and then a steel sleeve was bonded to the inside to accept the strain-gage force balance. The ceramic models then had the locations of the RCC and carrier panels marked using a coordinate measurement system by the LaRC surface verification laboratory. Individual missing panels were removed using the location marks as a guide. Several photographs of the models with the different damage scenarios are shown in Figure 4.3-1. All models had 0° control surface deflections of the elevons and body flap. The gap between the inboard and outboard elevons was present for the ceramic models, but was filled in for the steel model.

4.3.1.4 Test Techniques

Force and moment measurements were obtained using a six-component water-cooled balance. The balance was selected to maximize accuracy of the lateral-directional data. One balance was used for the steel model and another for the lighter-weight ceramic models. Usual corrections for balance interactions, weight tares, and sting bending were made. A baseline (no damage, 0° control surface deflections) set of aerodynamic coefficients was established for each model over an angle-of-attack range from 38° to 42°. This baseline was then subtracted from subsequent runs of the different damage scenarios to provide the residual aerodynamic increments.

The global heat-transfer mappings obtained in the Mach 6 air tunnel were obtained using an infrared (IR) imaging system with an un-cooled micro-bolometer-based focal plane array detector. The measured infrared radiation was converted to surface temperatures using the emittance of the target, which for the phosphor-coated fused silica model was determined to be 0.906. The global heat-transfer mappings obtained in the CF4 tunnel were generated with the two-color relative-intensity phosphor thermography

technique. IR techniques are not applicable to the CF4 tunnel as the freon gas absorbs the infrared radiation. The ceramic models were coated with phosphors that fluoresce in two regions of the visible spectrum when illuminated with ultraviolet light. The fluorescence intensity is dependent upon the amount of incident ultraviolet light and the local surface temperature of the phosphors. A temperature calibration of the system conducted prior to the study provides tables used to convert the ratio of green and red intensity images to global temperature mappings. For both the infrared and phosphor techniques, the global heat-transfer images are computed assuming one-dimensional semi-infinite heat conduction. The advantage of these techniques is their non-intrusive and global resolution of the quantitative heat-transfer data. These thermography techniques were used to identify the heating footprints associated with complex, three-dimensional flow phenomena such as boundary layer transition locations, flow separation and reattachment locations, etc. that would be extremely difficult to resolve using discrete measurement techniques.

4.3.1.5 Results from 20-Inch Mach 6 Air Tunnel

4.3.1.5.1 Raised boundary layer trips and gouge

At the beginning of the investigation the primary area of interest was early asymmetric boundary layer transition (ABLT), and in damage to the acreage tiles on the windward surface. Damage scenarios tested in the Mach 6 tunnel therefore included a single boundary layer trip at RCC panel 6 (0.6 inch high full scale), a gouge in the center of the main landing gear door (approximately 7 by 32 by 4 (WxLxD) inches, full scale), a raised main landing gear door (raised 0.9 inch full scale), and 7 trips (0.6 inch high full scale) arrayed span-wise across the leading edge of the door (to further simulate a raised door panel). In addition a "full" asymmetric transition configuration was tested which had 10 trips along the wing leading edge as well as 2 trips well forward near where surface protuberances were observed to cause early transition during flight of STS-28 ($x/l = 0.26$). The extent of the turbulent flow generated by these disturbances is shown in Figure 4.3-2. The turbulent wedge from the single trip at RCC panel 6 is swept outboard and affects only the outermost portion of the left wing, as compared to the trips along the forward edge of the main landing gear door, which affect the flow more inboard. These individual trips were more effective than the raised door (not shown) as the door acted more like a two-dimensional trip or step, which is not as effective in promoting turbulent flow. The gouge did not produce turbulent flow, although a small increase in heating was generated. The "full" asymmetric transition case is seen to provide turbulent flow over the aft 2/3 of the left side of the model windward surface. The aerodynamic increments generated by these OML changes are shown in Figure 4.3-3(rolling moment) and Figure 4.3-4 (yawing moment). The gouge in the door and the raised door had minimal effect on the model aerodynamics. The single trip at RCC panel 6 and the 7 trips at the door leading edge had similar effects to each other, causing a positive rolling moment (right wing down) and a small negative yawing moment (nose left). All increments were less than the "full" ABLT condition.

4.3.1.5.2 Main Landing Gear/Door Deployment

Possible deployment of the main landing gear was examined by testing various combinations of the gear, door, and an open wheel well. In general the results were similar to those determined in the CF4 tunnel and will be discussed in the next section.

4.3.1.6 Results from 20-Inch CF4 Tunnel

4.3.1.6.1 Main Landing Gear/Door Deployment

Deployment of the main landing gear and door was tested in the CF4 tunnel, as well as the Mach 6 air tunnel. Although not a leading initial damage scenario, this scenario was examined due to the large aerodynamic moments observed towards the end of flight, which to this point had not been observed in any of the tunnel tests. An open wheel well (no door), door alone, gear alone, and door and gear deployed were tested. Filler plates were used to create three different depths of the open wheel well in order to simulate the presence of the gear (it was thought that the presence of the gear would tend to fill in the cavity, making the wheel well effectively shallower). A sketch of these configurations is shown in Figure 4.3-5. The aerodynamic results in terms of delta rolling, yawing, and pitching moments for these configurations are shown in Figure 4.3-6. Large rolling and yawing moments were generated for the door

and/or gear combinations (lines D and E) consistent with flight, but pitching moments were in the opposite direction than those inferred from flight measurements. However, for the open wheel well configurations (lines A and B), as the cavity was made shallower, all three moments increased, and in the same direction as flight. This trend is consistent with “open” and “closed” type cavity flows. For the deeper cavity, some flow re-circulates within the cavity, but the main flow essentially passes over the cavity; as the depth is decreased, the flow impinges on and attaches to the cavity floor, a shock is formed as the flow reaches the aft wall, and the pressure on the cavity floor is significantly increased. This increased pressure generates the rolling, yawing, and pitching moments observed.

4.3.1.6.2 Missing Full RCC Panels

As the investigation progressed it was known that two temperature instruments on the left side of the fuselage (V34T1106A, V09T1724A) had experienced large increases in heating rates. Investigators at Langley had modified the wing leading edge with a “notch”, both experimentally and computationally, and side fuselage disturbances near these gages were produced by both techniques. Given this knowledge, an extensive survey of wing leading edge damage in terms of missing RCC panels was undertaken. Five ceramic models were fabricated with one or more missing RCC panels. The missing panel area was filled and a baseline data set was again generated. The filled area was then removed and incremental aerodynamic data obtained. Simultaneous heat transfer images were obtained, but their discussion is left to section 5.2.3.4, where results from dedicated heat transfer models are presented. The aerodynamic results for single missing panels as a function of panel location are shown in Figure 4.3-7 through Figure 4.3-9. The solid line represents a least-square linear fit to all the single-panel-missing data. The results show a nearly constant negative value of delta roll for a given missing panel location (Figure 4.3-7). This left-wing-down roll is believed to be due to loss of lift on the left wing due to the loss of area. Delta yawing moment (Figure 4.3-8) exhibited a relatively strong dependence on missing panel location, with a more nose-left yawing moment generated for the more outboard locations. The solid forward facing rear wall and side walls of the notch generate a shock system causing a local high-pressure area, and combined with the larger moment arm for more outboard locations, leads to the observed trend. Delta pitching moment (Figure 4.3-9) showed a dependence on missing panel location also, as nose-down pitch increased for more outboard panel locations. Multiple missing RCC panels were also tested; for instance, one series of tests started with panel 6 out, then 5 and 6, then 5 through 7. A sample of these results is given in Figure 4.3-10 through Figure 4.3-12, where delta roll, yaw, and pitch are plotted as a constant against time from entry interface. The dominant trend is that the delta roll, delta yaw, and delta pitch increments all become progressively more negative (left wing down, nose left, nose down) as the number of missing panels is increased. Superposition of single missing RCC panels was somewhat successful in predicting two-panel out increments, but less so for three or more panels missing.

A brief series of tests examined Reynolds number effects. Missing RCC panel 9, and missing RCC panels 6 and 9 together, were tested at two Reynolds numbers, 0.27 and 0.46 per foot. No significant Reynolds number effect was observed for this factor of two variation in Reynolds number.

4.3.1.6.3 Missing Partial RCC Panels

As more of the debris was recovered and analyzed, a scenario emerged that a partially damaged RCC panel or panels may more appropriately model the actual damage, as opposed to a full panel missing. Thus a series of tests was undertaken to look at the effect of missing lower RCC panels. The wing leading edge was modified by removing the lower portion of the panel from the wing apex to the start of the lower carrier panel. The aerodynamic results for individually removed lower panels 4 through 9 are shown in Figure 4.3-13 through Figure 4.3-15. The solid line again represents a least-square linear fit to the data. For comparison, the linear fit to the full panel out data presented in the previous section is shown by the dashed line. Overall, the magnitudes of the rolling, yawing, and pitching moment increments for missing partial panels were smaller than those for a full missing panel. The rolling moment increment was slightly more positive (right wing down) for a more outboard missing panel location. This trend is believed due to the locally increased pressure acting on the underside of the RCC panel cutout, and thus as the moment arm increases with increasing outboard location, the roll becomes more positive. The yawing moment was nearly constant for any particular missing panel location, which was different than for the full panel out data where a strong dependence on panel location was observed. The pitching moment was again more nose-down for more outboard panel locations.

A recurring question was what wing leading edge or windward surface damage scenario would provide aerodynamic characteristics observed in flight and simultaneously generate leeside disturbances (side fuselage heating) also observed in flight. This had been shown to be possible for a full missing panel. Phosphor thermography images taken for the series of missing lower RCC panels (Figure 4.3-16) show that for panel 4, and to a lesser extent panel 5, a disturbance is generated that moves to the leeside of the model. This disturbance is not observed for missing partial panels 6 or 9. The relative location of the partially missing panel to the local attachment line largely determines if the disturbance is swept to the leeside.

4.3.1.6.4 Holes and Slots through the Wing

Another mechanism examined for flow reaching the leeside was through holes or slots in the upper surface. For one series of tests, small holes (0.030-inch diameter model scale, 4 inch diameter full scale) were drilled through the wing, from windward surface to the leeside, at the carrier panel locations behind RCC panels 6, 9, and 12 (separate runs). No effect of these holes through the wing was seen in either the aerodynamic increments or the side fuselage images. For another series of tests, a 0.030-inch hole was drilled from the windward surface (center, aft end of the partially missing panel 8) to the leeside side through upper carrier panel 8. Afterwards this hole was widened to a 0.030-inch slot, in effect removing most of the upper carrier panel. Phosphor thermography images of the fuselage side are shown in Figure 4.3-17. A slight effect on heating to the OMS pod can be seen for the single hole. The slot creates a larger disturbance in the leeside flow field, resulting in increased heating on the side of the fuselage and the OMS pod, similar to that observed for a full missing panel, though the heating rate is lower. The aerodynamic increments in rolling and pitching moments associated with the hole and slot are very small, but there is a measurable increase in the nose-left yawing moment increment when the hole is widened to a slot, as shown in Figure 4.3-18.

4.3.1.6.5 Effect of Vertical Tail

Another aspect that was investigated was whether flow to the leeside was impinging on or in some way affecting the flow on the vertical tail. A piece of the vertical tail had been found that showed damage to the left side, but not the right. In addition, the tail was seen as a possible contributor to the large roll and yaw increments seen late in flight, and especially for the change in rolling moment behavior after EI + 600 sec. A model was tested with the tail on and off, with and without panel 9 missing. As observed from the table in Figure 4.3-19 for missing RCC panel 9, the increments with and without the vertical tail are very close in value, leading to the conclusion that the tail was not affected nor a contributor to the moments in question.

4.3.1.6.6 Windward Surface Depression

A final series of aerodynamic tests were performed to determine if a damage scenario related to deformation of the left wing would cause the change in direction of the rolling moment seen to occur 602 seconds after entry interface. Influenced by the results from the open wheel well, a shallow depression was created in the left wing windward surface to simulate what might occur as the wing internal structure was degraded and the lower skin was pressed inward by the greater external surface pressure. A single groove was milled into the lower surface of the model, starting just behind RCC panel 8. The length of this groove was varied in three increments with the longest groove extending slightly past the aft end of the wheel well. This groove was then widened to simulate progressive damage. Measured aerodynamic moments show (Figure 4.3-20 through Figure 4.3-22) that a minimum length of the groove is needed to provide a measurable increase in rolling moment, similar to the critical depth of the open wheel well. The required aspect ratio (L/h) of the groove is greater than for the open wheel well; this effect may be related to the angle of the local streamlines, in that they will cross the groove as opposed to running parallel to it, thus in effect shortening the groove and reducing the aspect ratio. However, the depression does indeed cause a positive (right wing down) rolling moment as observed in flight, and the magnitude of the rolling moment increases as the width of the depression is increased. Furthermore, the yawing moment and pitching moment generated by the depression are similar in magnitude and in the same direction as observed for flight.

4.3.1.7 Observations:

4.3.1.7.1 Asymmetric Boundary Layer Transition

The preliminary work done in the Mach 6 air tunnel focused primarily on ABLT. For the damage scenarios examined, the rolling and yawing moments generated were consistent in terms of direction with the Shuttle ABLT model, which is a positive rolling moment (right wing down) combined with a negative (nose left) yawing moment. These results are inconsistent with the extracted STS-107 flight data for the early portion of the flight, which have a left-wing down rolling moment combined with a nose-left yawing moment, indicating that asymmetric transition was not an initiating cause of the accident. Boundary layer transition may have been a contributor later in the flight, when the rolling moment trend became positive.

4.3.1.7.2 Progressive Damage Scenario

As a final summation to the aerodynamic work, a progressive build-up of individual damage scenarios was developed and compared to the flight moment increments. The results are shown in figures Figure 4.3-23 through Figure 4.3-25. The time from entry interface is subjective, as are the damage scenarios themselves. Nonetheless, a plausible scenario can be developed, which has the same trends as the flight data, although an exact correlation of flight magnitudes and time is not achieved. The initial damage is loss of the lower portion of RCC panel 8. The magnitudes of the moment increments are small, as they were for the first 500 seconds of flight. This initial damage is followed by the addition of the slot through the upper portion of carrier panel 8, and then the complete removal of panel 9 at 615 seconds from entry interface (EI). It was at this time (615 seconds) that significant heating to the side fuselage was seen, and both the slot in carrier panel 8 and the complete removal of panel 9 allow flow to impinge on the leeside of the vehicle. The reversal in direction of the rolling moment is attributed to the windward surface depression, with the magnitude increasing as the size of the depression is increased (as more of the internal wing structure is degraded). The yawing and pitching moments continue their increasing negative trend as the depression is enlarged.



Figure 4.3-1 Wind Tunnel Test Model Configurations

28

Effect of raised trips and MLGD gouge

20-inch Mach 6 Air $\alpha=40^\circ$ $Re_L = 2.4 \times 10^6$

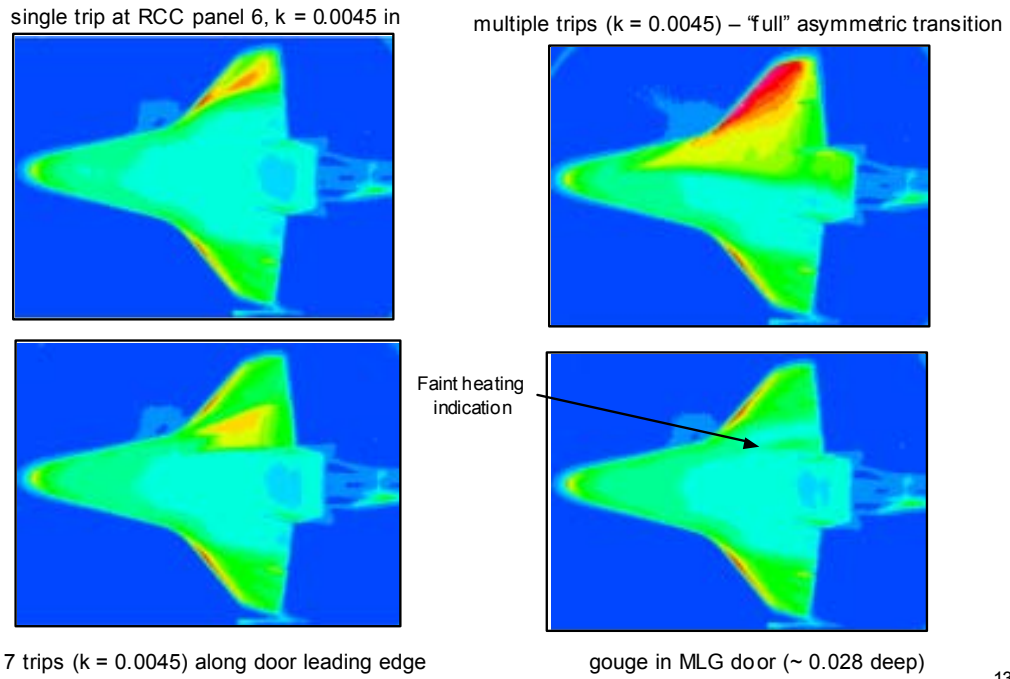


Figure 4.3-2 Infra-red Thermography Images Showing Extent of BL Transition

13

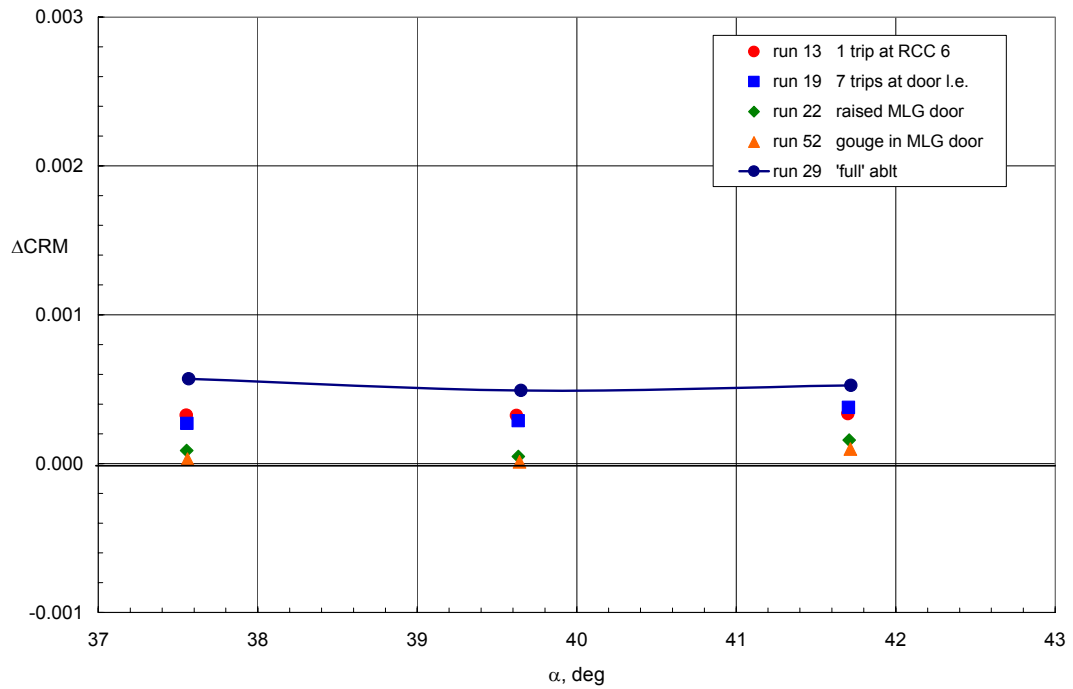


Figure 4.3-3 Boundary Layer Transition Aerodynamic Increments (Delta Roll)

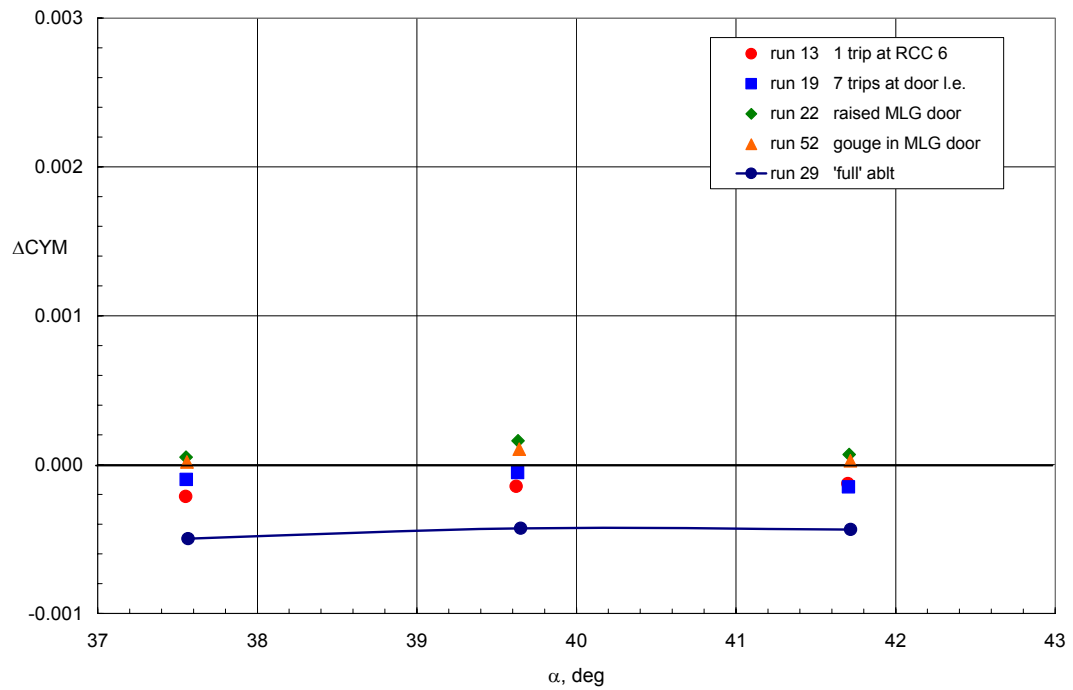


Figure 4.3-4 Boundary Layer Transition Aerodynamic Increments (Delta Yaw)

Test Configurations – Steel Model

Large OML Changes

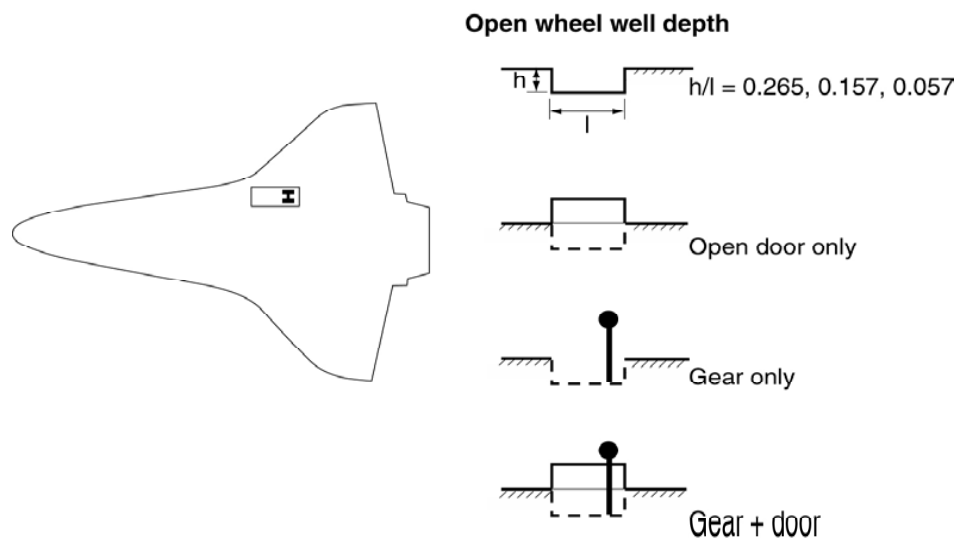


Figure 4.3-5 Stainless Steel Model Configurations Tested

MLG Door / Gear Scenarios in 20-Inch CF4 Tunnel

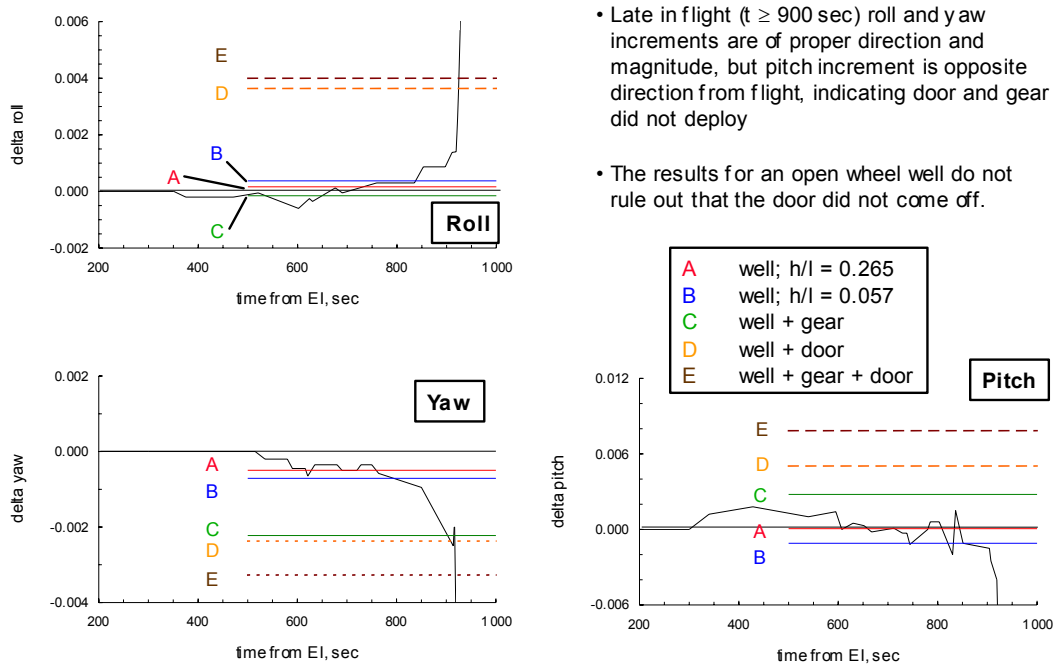
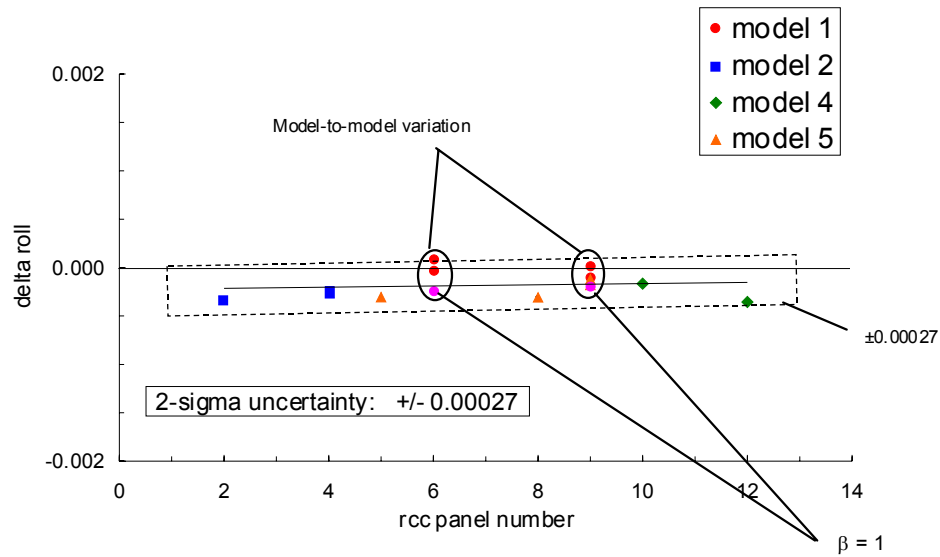


Figure 4.3-6 Aerodynamic Increments (Roll, Pitch, Yaw) for MLG Door Scenarios

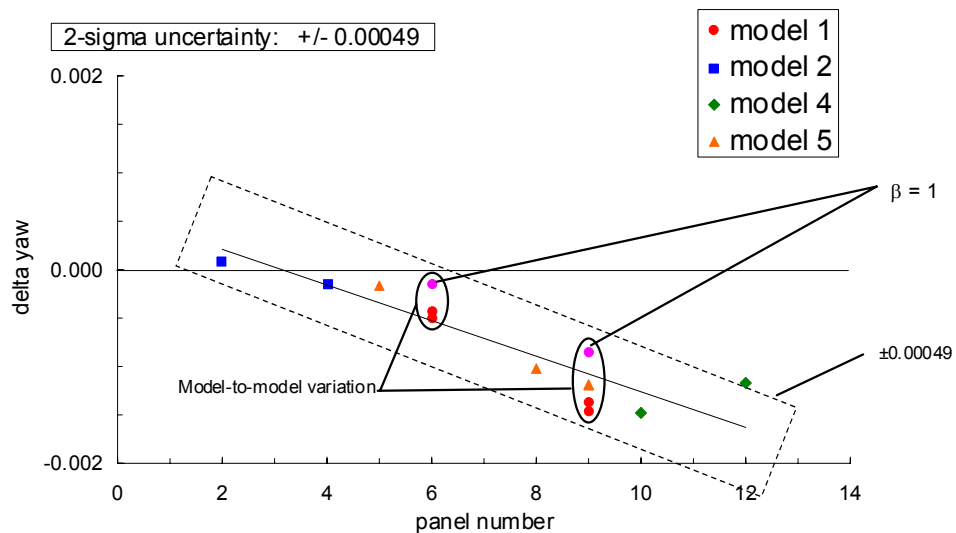
Rolling Moment Trends, Single missing panel 20-Inch CF4 Tunnel, $\alpha = 40^\circ$



- Roll increment is relatively constant for a given missing panel

Figure 4.3-7 Aerodynamic Increment (delta Roll) – Missing Full RCC Panel by Location

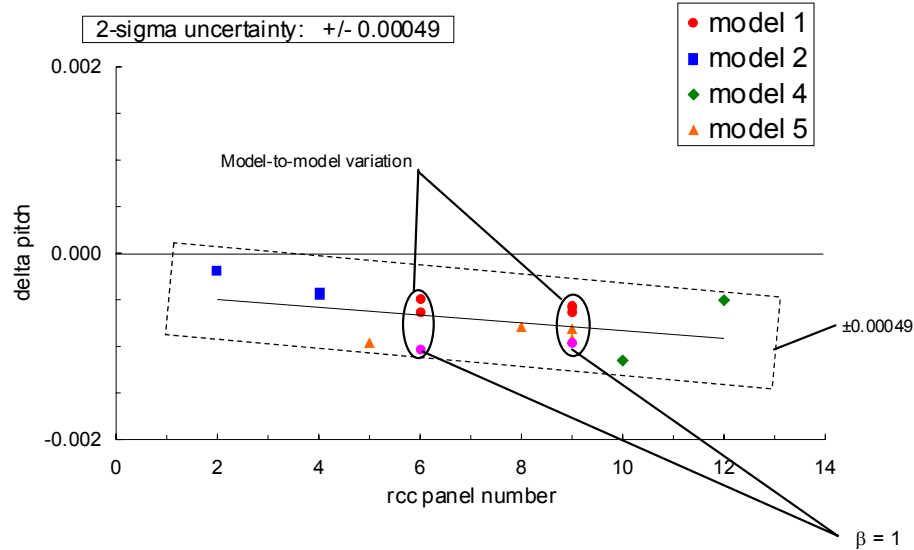
Yawing Moment Trends, Single missing panel 20-Inch CF4 Tunnel, $\alpha = 40^\circ$



- Yaw increment is highly dependent on panel outboard location

Figure 4.3-8 Aerodynamic Increment (delta Yaw) – Missing Full RCC Panel by Location

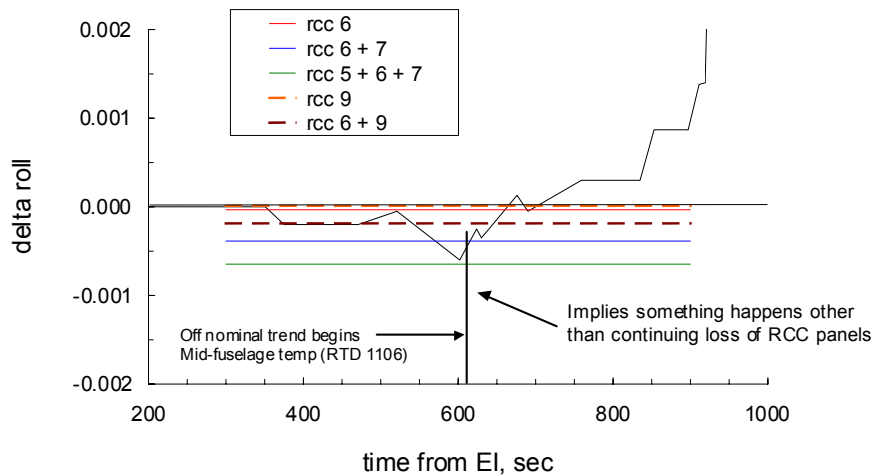
Pitching Moment Trends, Single missing panel 20-Inch CF4 Tunnel, $\alpha = 40^\circ$



- Pitch increment is moderately dependent on panel location

Figure 4.3-9 Aerodynamic Increment (delta Pitch) – Missing Full RCC Panel by Location

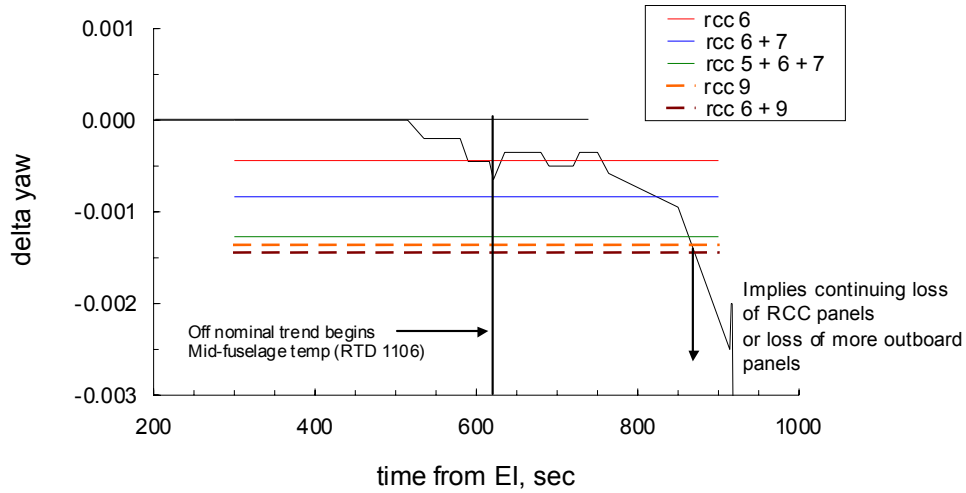
Rolling Moment Trends, Missing RCC Panels 5 – 9 20-Inch CF4 Tunnel, $\alpha = 40^\circ$



- Roll increment increases with increasing number of panels missing
- Two adjacent panels have larger increment than two separated panels
- Roll trend reverses at 615 sec; opposite effect from losing more leading edge panels

Figure 4.3-10 Rolling Moment Increment Trends - Missing RCC Panels 5-9

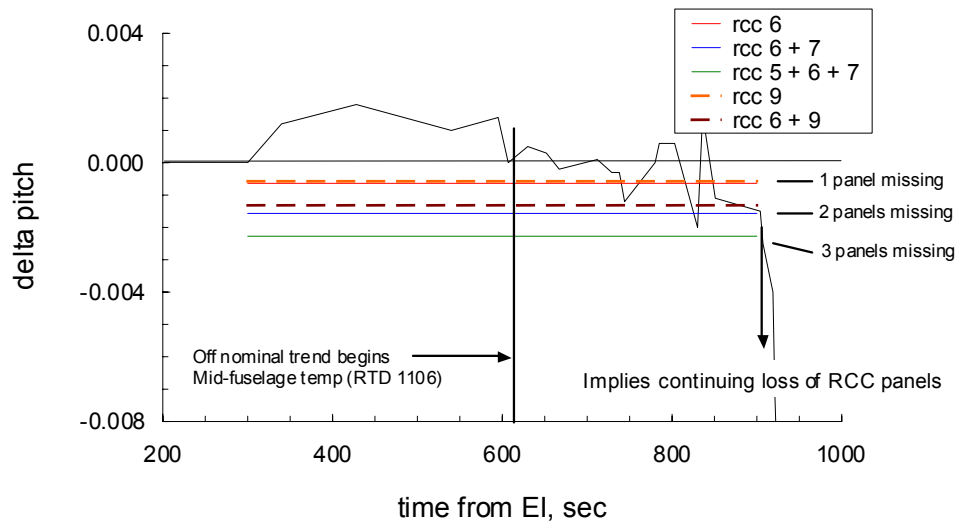
Yawing Moment Trends, Missing RCC Panels 5 – 9 20-Inch CF4 Tunnel, $\alpha = 40^\circ$



- Yaw increment increases for more outboard panels
- Yaw increment increases with increasing number of panels missing

Figure 4.3-11 Yawing Moment Increment Trends - Missing RCC Panels 5-9

Pitching Moment Trends, Missing RCC Panels 5 – 9 20-Inch CF4 Tunnel, $\alpha = 40^\circ$



- Pitch increment nearly independent of panel outboard position
- Pitch increment increases nose-down with increasing number of panels missing

Figure 4.3-12 Pitching Moment Increment Trends - Missing RCC Panels 5-9

34

Results for missing lower RCC panel – residual roll

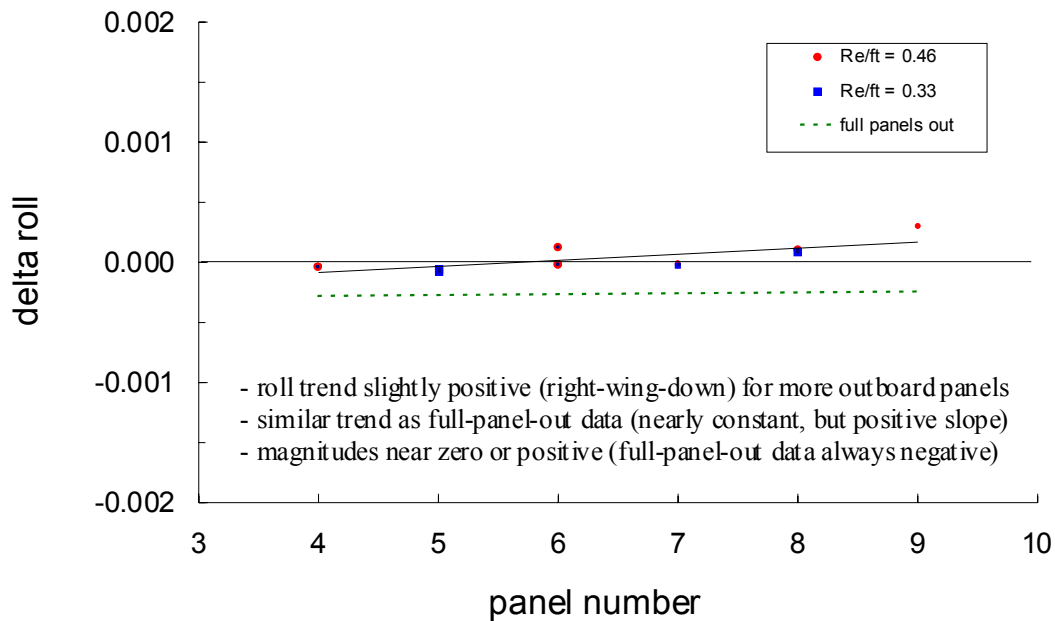


Figure 4.3-13 Aerodynamic Increment (delta Roll) – Missing Partial RCC Panel by Location

Results for missing lower RCC panel – residual yaw

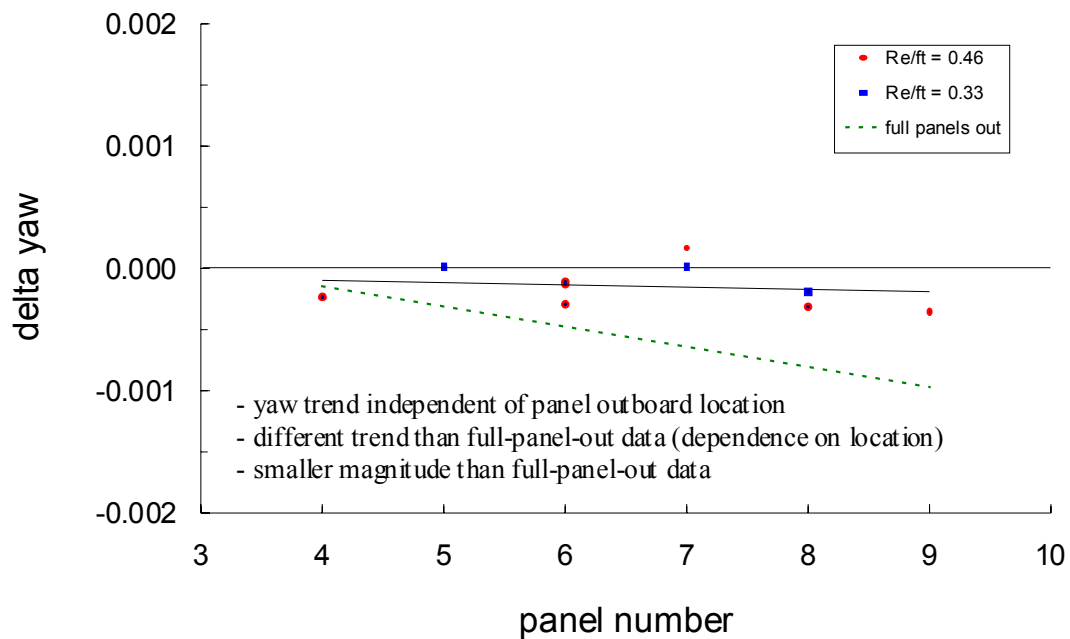


Figure 4.3-14 Aerodynamic Increment (delta Yaw) – Missing Partial RCC Panel by Location

35

Results for missing lower RCC panel – residual pitch

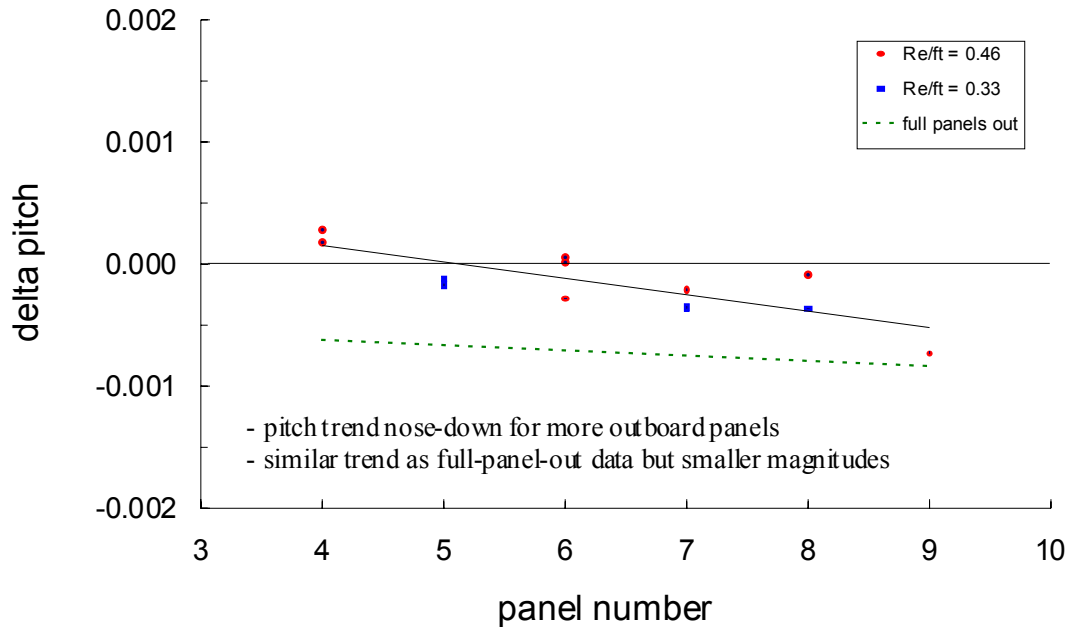


Figure 4.3-15 Aerodynamic Increment (delta Pitch) – Missing Partial RCC Panel by Location

Side impingement as function of panel location – lower half panel removed

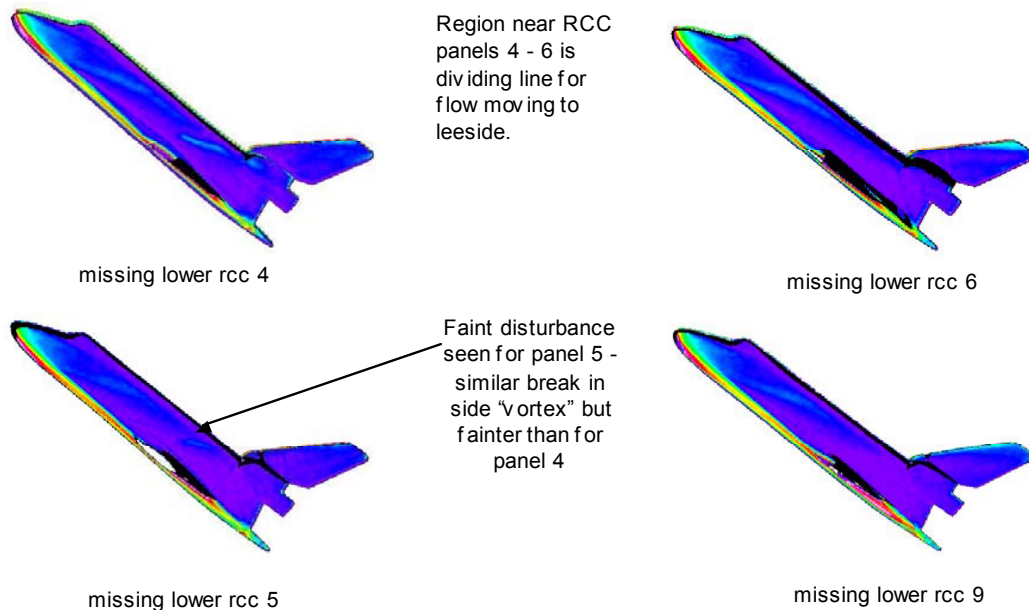


Figure 4.3-16 Side Fuselage Heating Augmentation – Missing Partial RCC Panel

Effect of hole or slot through upper carrier panel – missing lower RCC panel 8

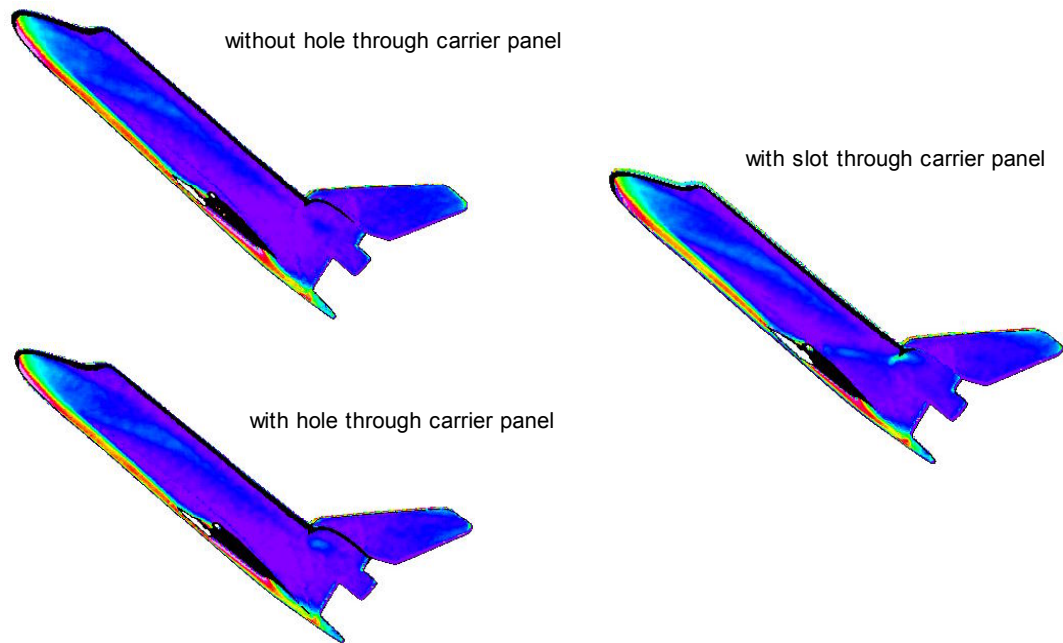


Figure 4.3-17 Side Fuselage Heating Augmentation – Missing Partial RCC Panel + Hole/Slot

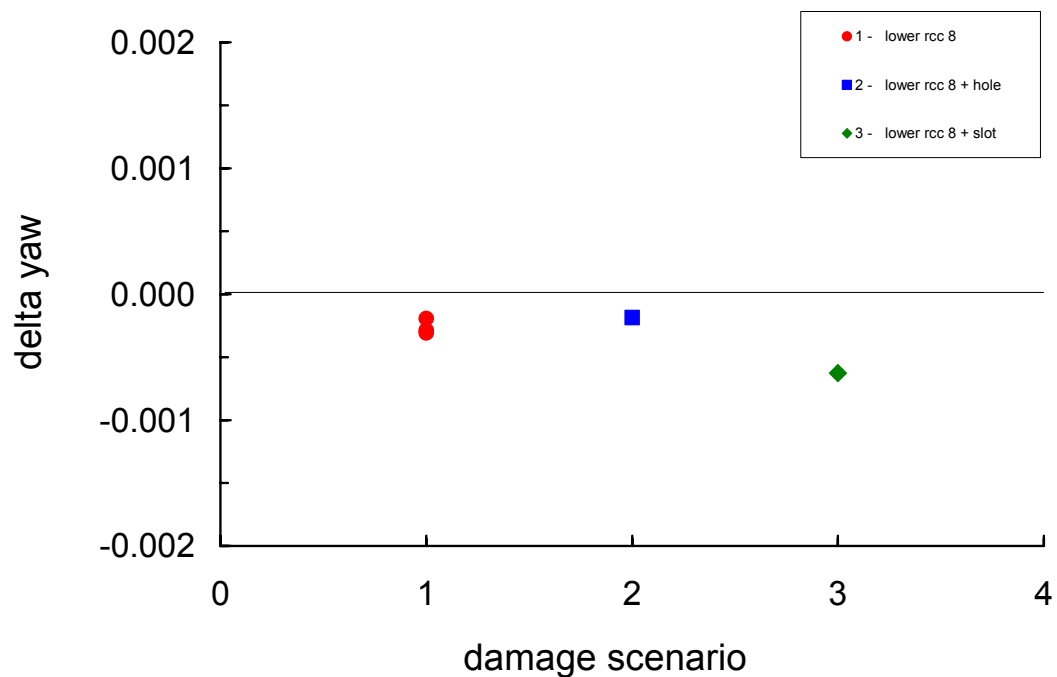


Figure 4.3-18 Aerodynamic Increment (delta Yaw) – Missing Partial RCC Panel + Hole/Slot

37

Vertical Tail on / off, missing Panel 9

Run	Tail	Alpha	Re/ft	ΔC_{m}	ΔC_{y_m}	ΔC_m	ΔC_Y	Model
30	on	40.2	0.45	-0.00006	-0.00115	-0.00105	0.00013	A
44	on	40.5	0.46	0.00007	-0.00131	-0.00128	-0.00037	5
45	on	40.5	0.45	0.00008	-0.00132	-0.00128	0.00022	5
63	off	40.5	0.46	-0.00007	-0.00122	-0.00125	-0.00006	5
64	off	40.5	0.44	-0.00013	-0.00122	-0.00117	0.00006	5
Avg	on	40.4	0.45	0.00003	-0.00126	-0.00120	-0.00001	
Avg	off	40.5	0.45	-0.00010	-0.00122	-0.00121	0.00000	
Delta		-0.1	0.00	0.00013	-0.00004	0.00001	-0.00001	

Effect of vertical tail is negligible, for missing RCC panel 9

Figure 4.3-19 Aerodynamic Increments -- Missing Full RCC Panel 9 with & w/o Vertical Tail

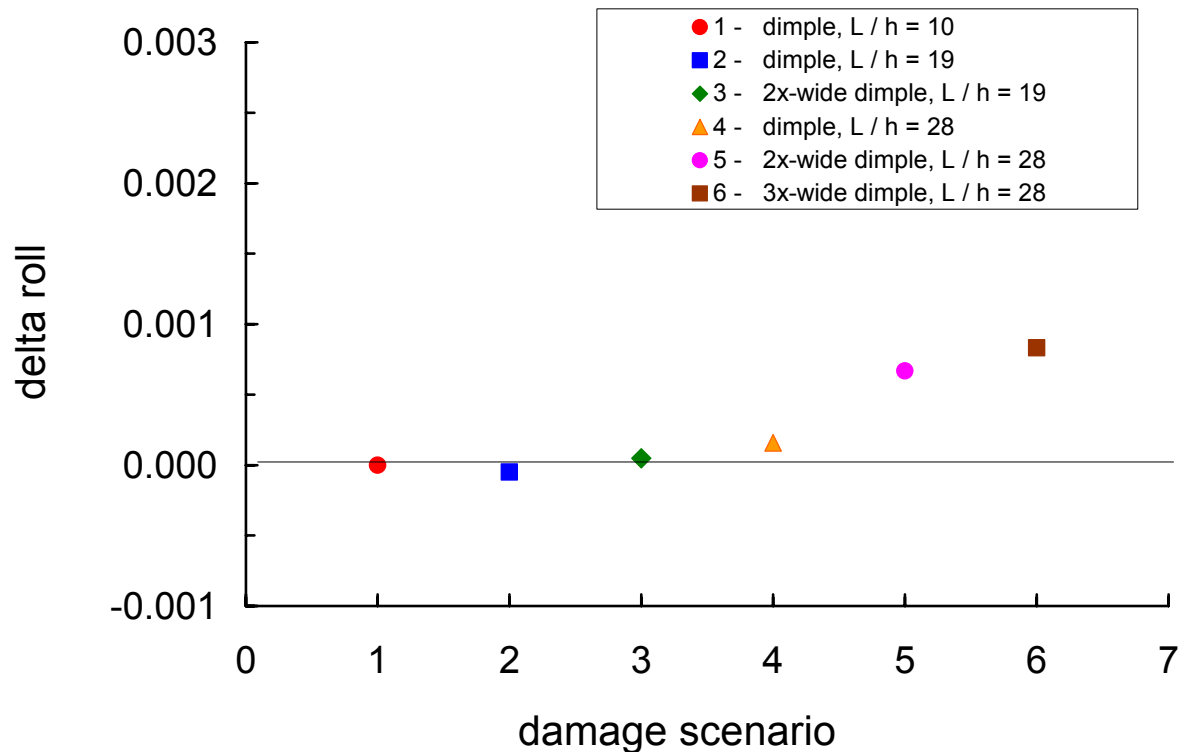


Figure 4.3-20 Aerodynamic Increment (delta Roll) – Lower Wing Surface Deformation / Dimple

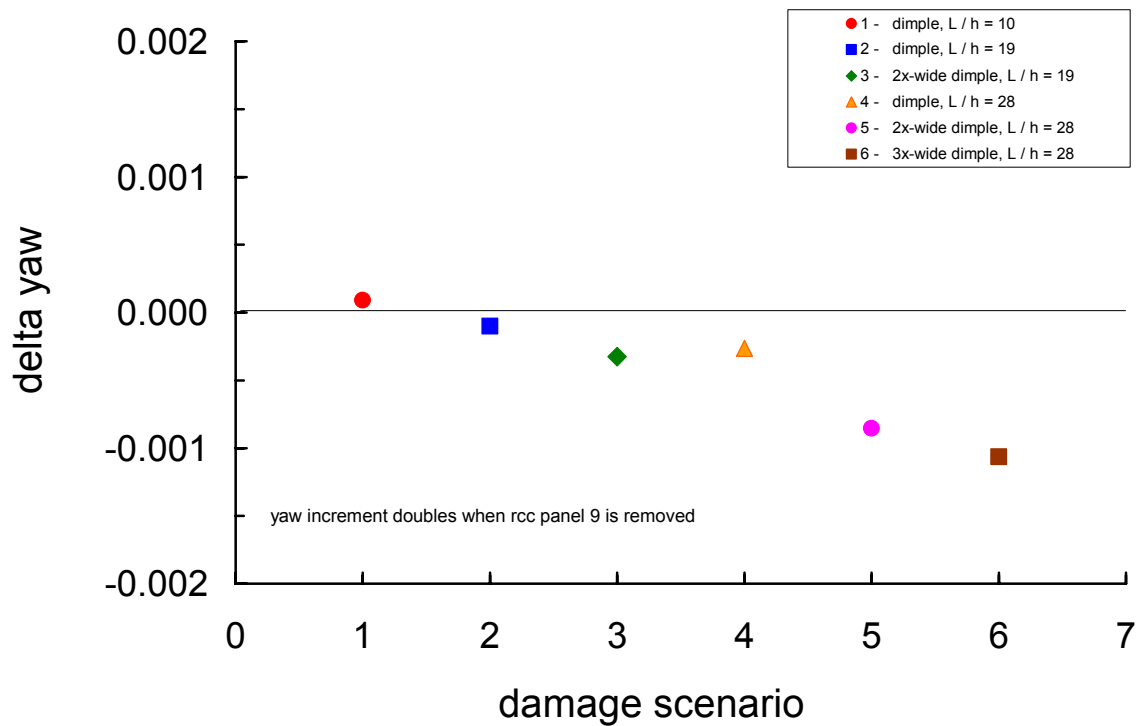


Figure 4.3-21 Aerodynamic Increment (delta Yaw) – Lower Wing Surface Deformation / Dimple

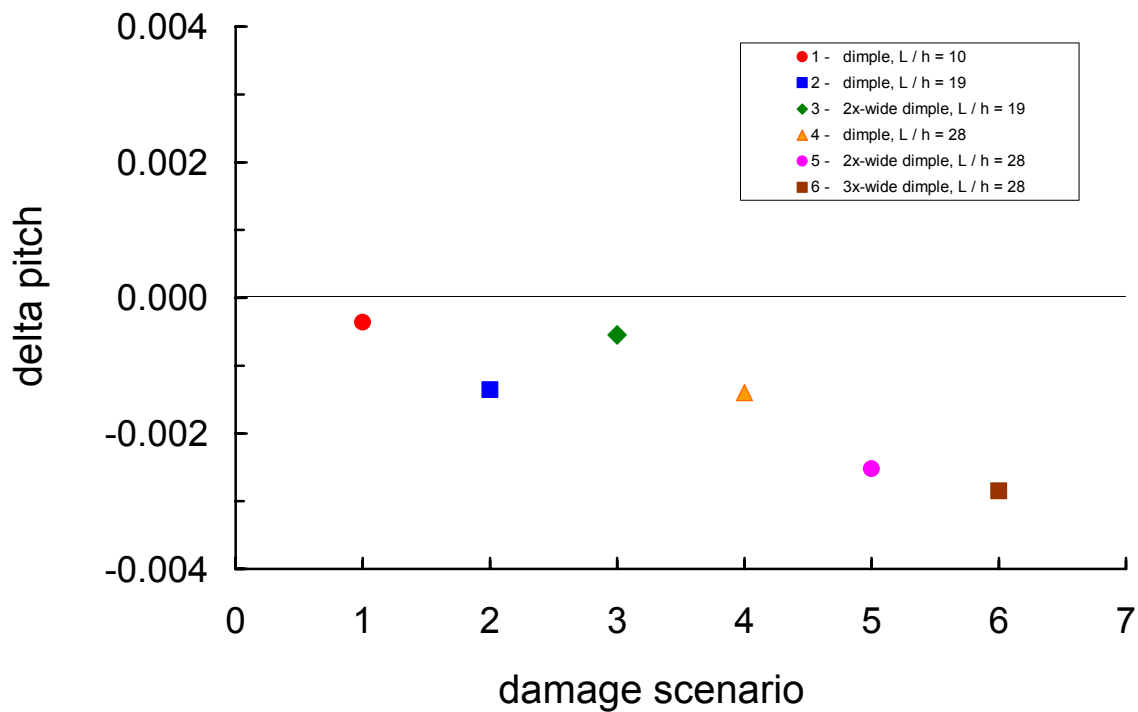


Figure 4.3-22 Aerodynamic Increment (delta Pitch) – Lower Wing Surface Deformation / Dimple

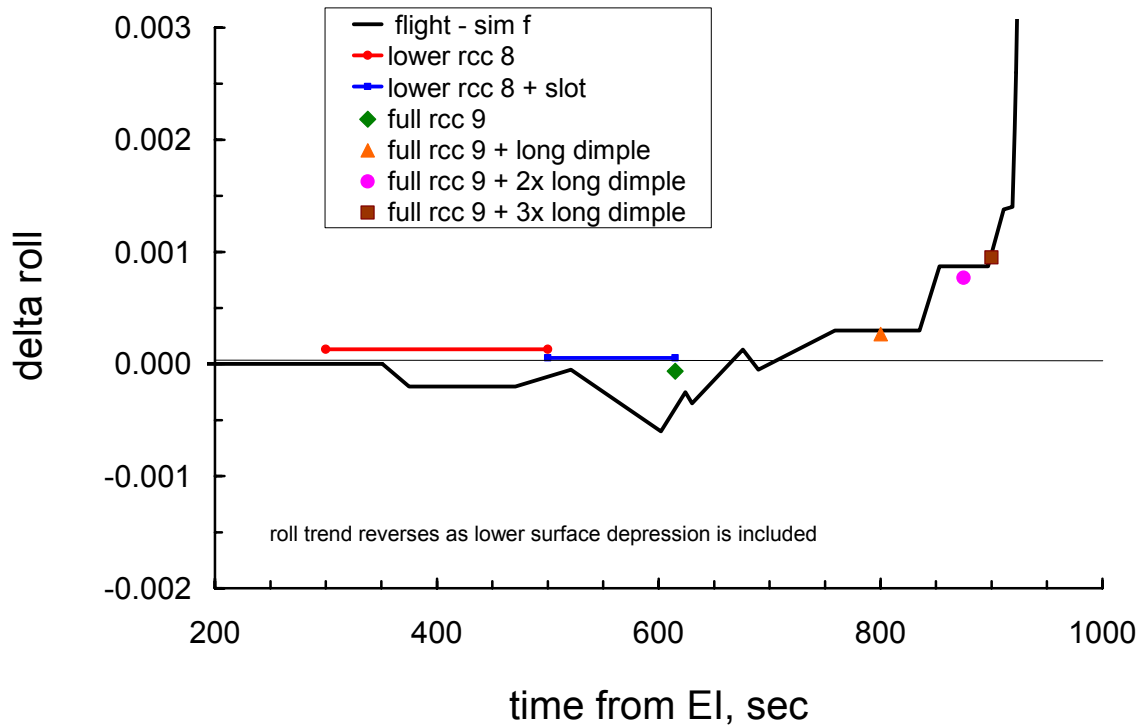


Figure 4.3-23 Aerodynamic Increment (delta Roll) – Damage Progression

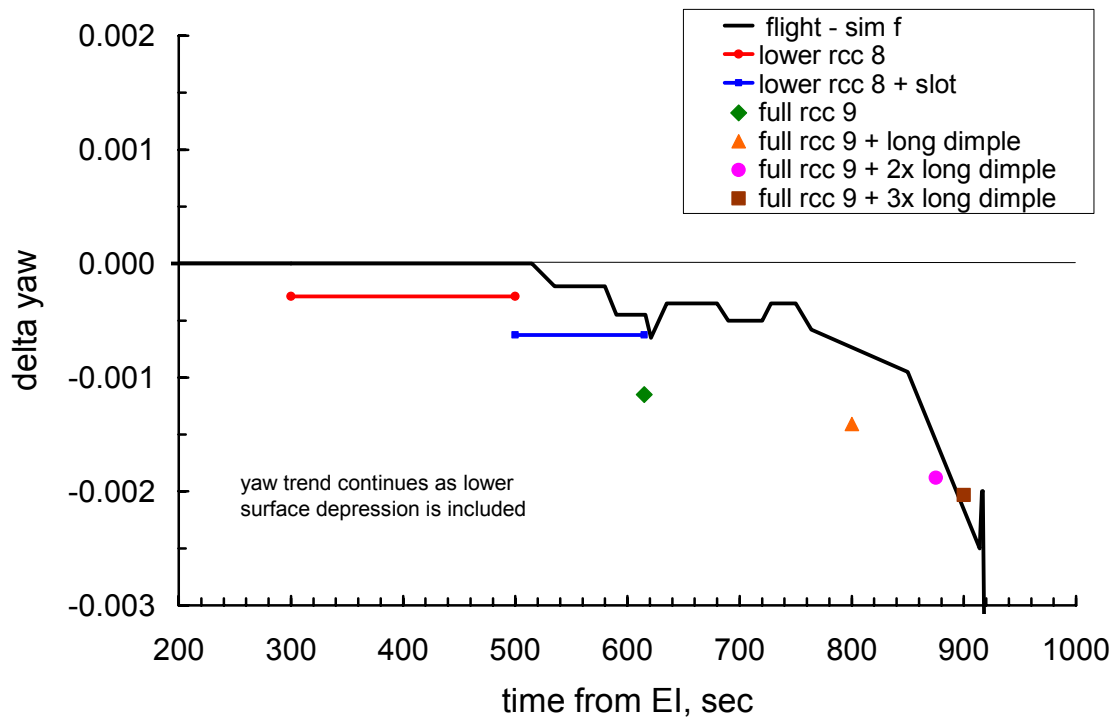


Figure 4.3-24 Aerodynamic Increment (delta Yaw) – Damage Progression

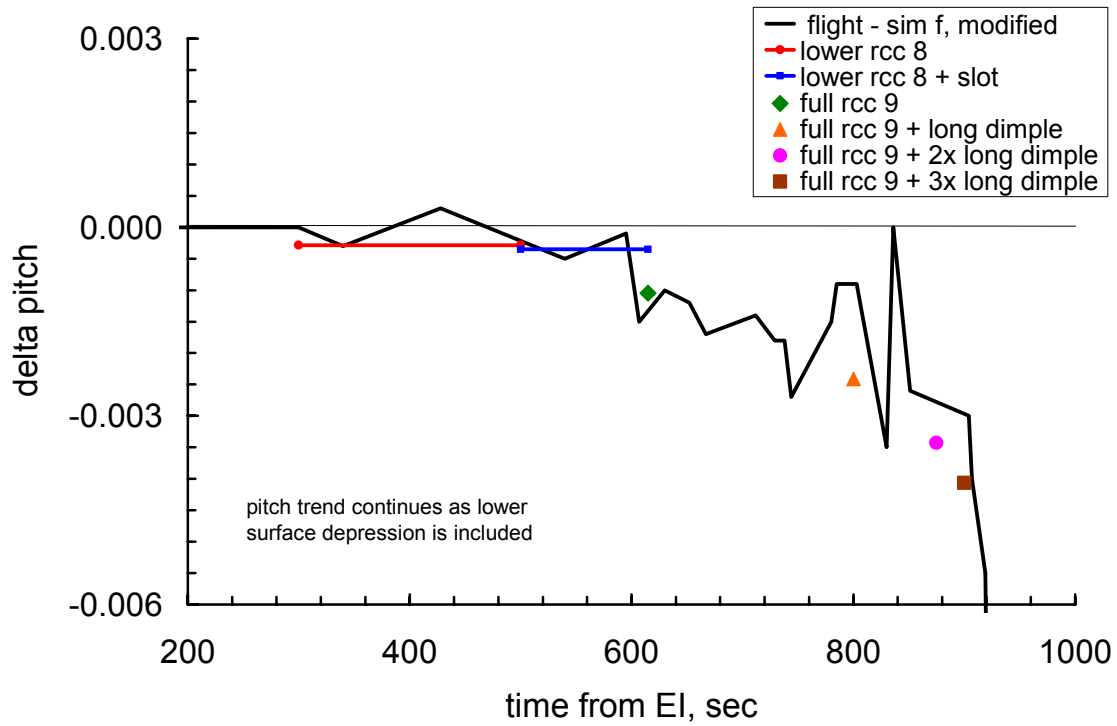


Figure 4.3-25 Aerodynamic Increment (delta Pitch) – Damage Progression

4.3.2 Damage Assessment Using Computational Fluid Dynamics

Computational tools were used to complement the wind tunnel testing of Columbia damage scenarios. The ability to simulate flight and wind tunnel conditions provided a bridge between the extensive wind tunnel test program and the STS-107 flight. The flow solutions provided a detailed view of the flow field characteristics and the contribution of orbiter components (vertical tail, wing, etc.) to aerodynamic forces and moments. In some cases, rapid, inviscid, unstructured CFD methods were able to guide the wind tunnel efforts. The inviscid methods are limited by the inability to accurately simulate viscous dominated flows such as occur in the highly separated flow region on the leeward side of the orbiter, but still proved very useful in a screening capacity. The structured mesh viscous methods are limited by the time it takes to develop a mesh for a complex geometry and in solution time. Having a limited number of the more accurate viscous solutions available provided a valuable check on the lower fidelity inviscid methods and served as an additional bridge between wind tunnel and flight conditions.

The sections below present the background for and data from computations that contributed to the understanding of the final damage scenario. Additional work performed by the analysts to verify assumptions of the computations, and on early analysis that led to the final working scenario is presented in the Aerodynamic Section Appendices.

4.3.2.1 CFD Analysis Introduction / Application Description

Several computational tools of varying levels of fidelity were used to predict aerodynamic forces and moments in support of the investigation. The inviscid methods provided a rapid meshing capability and a highly parallelized solution algorithm that allowed them to be used to screen a large number of damage scenarios over the course of the investigation. Development of the computational meshes for the viscous solver took much longer (weeks instead of a day), and the flow solutions were more computationally intensive (days/weeks instead of hours); thus the viscous solvers were used primarily as a check on the more abundant (from an aerodynamic perspective) inviscid work. The application of the various flow solvers utilized is briefly described and summarized in Table 4.3-1. Each is described in more detail in Aerodynamic Appendices Section 4.7.8.

The inviscid, unstructured mesh tool FELISA was the computational 'workhorse' of the aerodynamic investigation. It provides the capability to turn around complex geometries (mesh + solution) in under 2 days. Additionally its unique (among inviscid solvers) capability to model the flight environment with equilibrium air chemistry as well as the perfect gas environment of the Mach 6 air facility and the environment of the CF₄ tunnel provided ground test to flight condition trending. The inviscid, Cartesian mesh code CART3D was used to provide a set of rapid solutions at the Mach 6 air wind tunnel conditions. The viscous overset mesh solver OVERFLOW provided several Mach 6 laminar air solutions and was used to specifically address leeside flow interactions including the effects of the SILTS pod on the vertical tail. The viscous solvers GASP, USA and LAURA provided a set of solutions for the undamaged orbiter at hypervelocity flight conditions with full non-equilibrium chemistry, matched against a several solutions corresponding to wing leading edge damage scenarios, and a few coupled external/internal solutions.

4.3.2.2 STS-107 CFD Analysis Case Definition

Several sets of flow conditions were used in the analysis process. In the initial phase of the investigation, flow conditions and corresponding solutions for the STS-2 trajectory that have been widely reported in the open literature, and are listed in Table 4.3-2, were used as investigators geared up to support the investigation. Once the flight data from STS-107 became available, a joint effort undertaken by the aerodynamic and the aerothermodynamic teams, established a common set of flight conditions for use in all computational analyses. Table 4.3-4 lists the CFD points that were chosen along the STS-107 trajectory. Together, the 10 points span the range of STS-107 atmospheric flight conditions from entry interface (EI) to loss of signal (LOS). Points labeled condition AA and condition A were chosen for DSMC analysis at rarefied gas dynamic conditions, while the points, B and 1 - 6 were chosen for continuum flow (Navier-Stokes and Euler) methods. The conditions labeled 1-6 were chosen along the trajectory to correspond to key events that were noted in the initial evaluation of the OI data, and are described in Table 4.3-4. The CFD points were established well before the OEX data recorder was recovered and the MADS data became available. A final point, condition VN, was added near the end of the investigation to capture

42

the point at which the vacuum vent and water supply nozzle thermocouples indicate a brief off-nominal increase in temperature rise rate.

The challenge associated with the selection of the points was the lack of detailed atmospheric information during STS-107 entry flight combined with the need to quickly establish common CFD conditions to support the rapid pace of the investigation. In order to establish the complete set of conditions for these data points, several sources of information were combined. The most crucial data came from the GPS tracking that accompanied the OI telemetry data set. The GPS data provided the most accurate information on position (altitude, longitude, latitude) and relative velocity (speed, flight path angle, azimuth angle). The aerodynamic/ aerothermodynamic teams next assessed the OI data, which provided inertial navigation data information. While these data sets were less accurate in providing velocity and position compared to the GPS data, they did provide reasonably accurate information on vehicle attitude (alpha, beta and bank) as well as the actual control surface deflections (body flap, inboard and outboard elevons). To complete the needed data set, the February GRAM atmosphere model was utilized. An important note regarding the GPS velocity and OI derived vehicle attitude information is that neither accounts for the presence of any winds. When the CFD points were defined, the DAO/MSFC atmospheric reconstruction had not yet been developed. Furthermore, no attempt was made to re-compute the atmospherically derived parameters or account for the effect of wind on vehicle velocity and attitude parameters. By the time the DAO/MSFC atmospheric model became available, the computationally expensive CFD calculations were well under way. It is important to note that the delta aerodynamic analyses show little sensitivity to Mach number and angle of attack. Table 4.3-3 gives an accounting of how all the parameters were calculated. Figure 4.3-26 through Figure 4.3-29 depict various key trajectory parameters and labels the chosen CFD analysis conditions.

Additionally, CFD cases were run at wind tunnel conditions for both the Langley Mach 6 air and CF₄ facilities. The wind tunnel flow conditions used for the various flow solvers are shown in Table 4.3-5.

4.3.2.3 Configuration Summary and Analysis

All of the baseline and damaged configurations that were analyzed and the flow solver(s) and conditions used for analysis are summarized in Table 4.3-6. The scenarios are grouped by type/progression of damage, with baseline geometries listed first. The damaged configurations are grouped into three categories. The first group is for single and multiple missing RCC panels (full or partial), and includes the initial panel 6 damage simulation. The second grouping is a series of cases for progressive damage, increasing in severity, in the region of RCC panel 9. The third group of computations was for windward surface deformations, including an open wheel well and windward surface depressions/dimples (these simulate possible structural deformation of the wing skin due to the internal heating damage to the intermediate wing structure). The following subsections discuss the geometries, flow conditions, and analysis tools and present flow field images as well as the delta aerodynamic moment increments. The delta aerodynamic forces are not discussed here, as the extraction of these quantities from the flight data was considered unreliable.

4.3.2.3.1 Baseline Geometry and Analysis

While it would have been ideal for every computational and wind tunnel model to be generated from the same solid CAD model, time constraints and the availability of existing models already tailored to each particular application led to the decision to 'go with what we have' and to assess the impact of this decision when a common geometry became available. An 1997 CAD geometry was the basis for all of the computational meshes that existed prior to the Columbia accident. The 2003 CAD geometry was made available to all of the investigators shortly after the accident, and served as the geometry for the common baseline mesh (detailed in Aerothermodynamics Section 5.2.4.2) used for all of the structured mesh viscous computations. Table 4.3-7 lists the geometries that various computational meshes were generated from, and their relationship to the two 'official' CAD definitions. An effort was made to ensure that all investigators were modeling the damage consistently. The common geometries that were used to model the damaged orbiter are listed in Table 4.3-8.

An important assumption was made in all of the analysis, both wind tunnel and computational. Even if the model did not exactly capture the absolute aerodynamics of the orbiter at flight conditions, the delta

aerodynamic coefficients (calculated as $\Delta = \text{damaged} - \text{baseline}$) yield a reasonable approximation (when the damaged and baseline models are as close as possible with the exception of the damage area). For the computations great care was taken to have comparable mesh spacing in areas not affected by the damage. This eliminated any potential for deltas due to mesh differences corrupting the results.

Several geometric modeling simplifications were made for the various computations on an individual code and scenario basis. Early in the investigation, many computations were made excluding the vertical tail. The vertical tail is typically not important for hypersonic aerodynamics at high angle of attack conditions, and its presence in a simulation adds a significant number of mesh points while hindering solution convergence. As it became apparent via Columbia's recovered debris forensics that there was significant off-nominal flow to the OMS pod and vertical tail, the tail was added into most computational models. Additionally, except for one set of OVERFLOW calculations, none of the computational models included the SILTS pod located on the tip of Columbia's vertical tail. For most cases, only half-body (i.e., 180°) simulations were computed, assuming no flow across the centerline of the vehicle. This modeling decision is the norm for CFD simulations as it facilitates more rapid simulations. While the assumption of no flow across the centerline was not strictly valid for the simulations where the leeside flow of the vehicle was interacting with flow through WLE damage, both FELISA and OVERFLOW results indicated that this assumption had little effect on predicted aerodynamic forces and moments (See Aerodynamic Appendices, section 4.7.5 for details of the OVERFLOW evaluation.) Also, the base of the orbiter was not modeled, another typical simplification for hypersonic simulations when the primary interest is heating or aerodynamic screening. The complex separated base flow typically requires a large mesh, and further slows convergence. It was apparent early in the investigation that damage was centered near the WLE or the wheel well, and that any effect to the base flow was likely insignificant. For many of the viscous simulations, the body flap was not included and neither were the gaps between the inboard and outboard elevons and the fuselage. Since the investigation was primarily concerned with the delta aerodynamics, no attempt was made to model the body flap and elevons at STS-107 flight deflections; all control surfaces were set at the zero degrees or trail position. Unless otherwise noted, all computations presented here assume a half-body, and do not compute the base flow. Additionally, a notation is made when the tail or body flap is not present in the computation.

Flow solutions on the baseline (undamaged) geometry were used by the Aerodynamics Team to compute the differences in aerodynamic forces and moments between the baseline and the damaged configurations, and for flow field comparisons. The External Aerothermodynamics Team also made extensive use of the baseline solutions to determine environments for engineering heating methods. To understand how well the inviscid and viscous computational methodologies reproduced the Orbiter OADB, a comparison was made between the OADB data and CFD results. Solutions computed on the baseline geometry as well as a missing panel 6 geometry with FELISA, and on the baseline geometry (without the body flap) with LAURA were utilized for this evaluation

The total normal and axial forces, and pitching moments for the solutions at CFD conditions 1 through 6 are plotted against time from EI of the STS-107 trajectory in Figure 4.3-30 (Note: side force, rolling and yawing moments are all zero for the symmetric baseline). The force and moments for the FELISA solutions are computed with and without the body flap, to serve as a bridge between the Orbiter OADB data and the LAURA computations. For pitching moment, the FELISA data is in better agreement with both the Orbiter OADB data and LAURA computations later in the flight, suggesting that the inviscid equilibrium chemistry model is not as appropriate for the higher Mach number range ($M > 21$). The trend in the LAURA predictions against FELISA without the body flap is similar to the trend of the Orbiter OADB data against the full FELISA solution, suggesting that the LAURA data is in good agreement with the flight database. The FELISA missing panel 6 result is also included in Figure 4.3-30 to illustrate how relatively small the delta aerodynamics due to damage are with respect to the absolute aerodynamics. A detailed discussion of this topic is included in the Aerodynamic Appendices Section 4.7.4.2.

4.3.2.3.2 Full RCC Panel missing

A damage scenario considered early in the investigation was that an entire RCC panel or perhaps several panels had been lost. This scenario was reinforced by an early FELISA computation (and subsequent wind tunnel testing) that showed windward flow passing through a notch in the WLE created by a simulated missing RCC panel. The notch was modeled with solid side surfaces and the open channel

44

behind the RCC panels was not represented. The flow was compressed as it passed through the notch, sending a jet over the leeward surface of the wing where it impinged on the side of the fuselage. This was this first evidence of a source for the augmented heating recorded by Columbia's fuselage and OMS pod surface temperature measurements. Consequently, a large portion of the computational effort in the investigation was spent looking at missing RCC panel configurations to gain an understanding of the effect of location and size of WLE damage on the aerodynamics and aerodynamic heating characteristics of the vehicle. The bulk of the computations were performed utilizing FELISA at both CF4 tunnel and flight conditions to establish a link between the wind tunnel results and the STS-107 flight data. A limited number of CART3D and OVERFLOW solutions were exercised at Mach 6 air and at flight Mach numbers with perfect gas (see Aerodynamic Appendices sections 4.7.5 (OVERFLOW) and 4.7.6 (CART3D) for more details), to provide additional insight into the trends shown with the wind tunnel and with FELISA. Additionally fully reacting Navier-Stokes calculations, primarily in support of the aerothermodynamic evaluation, were completed using LAURA, GASP and USA codes for several specific WLE damage cases. (see Aerodynamic Appendices Section 4.7.7 (USA) and Aerothermodynamics Section 5.2.4.5 (LAURA & GASP) for more details). Even though the debris recovery and subsequent analysis led to a more complex picture of the damage progression, the insight into the delta aerodynamics and the corresponding flow field characteristics gained by systematically looking at missing RCC damage proved invaluable to the investigation.

Numerous codes and both wind tunnels were utilized to study the effect of missing panel 6. While this damage was later ruled out for the STS-107 flight by recovered debris and while it had a very small impact on the aerodynamics, it offers an opportunity to explore the flow physics that are associated with wing leading edge damage. The initial panel 6 missing configuration was defined in the days after the accident without the benefit of a CAD definition, and, as shown in Figure 4.3-31, does not encompass the full RCC panel. This geometry roughly corresponds to the panel 6 'notch' geometry that was also evaluated in the wind tunnel.

Streamlines for both the baseline (blue) and missing RCC panel 6 (red) configurations are shown in Figure 4.3-32, for a FELISA computation at an STS-2, Mach 24 condition. With the orbiter at a 40° angle-of-attack, there is a strong expansion around the WLE, and the leeside flow field pressure and density are very low. When a section of material (such as an RCC panel) is removed from the orbiter WLE, the resulting gap has the effect of channeling the higher energy flow from the windward to the leeside, forming a jet-like flow structure. This 'jet' of high enthalpy flow carries substantially higher momentum than the surrounding leeside flow, and therefore is not significantly influenced by it. Pressure contours shown in Figure 4.3-33 (STS-107 Mach 24.2 condition) show the footprint of a shock on the leeside surface, and flow impingement on the side fuselage. This impingement would have the effect of increasing the heating rate on the side fuselage, a trend that was identified by the OI flight data early in the investigation. The effect of the missing panel on the windward surface is localized. The windward view of streamlines in Figure 4.3-32 show that the flow pattern is not affected just inboard of the missing panel, and the C_p (pressure coefficient) contours in Figure 4.3-33 indicate that the pressure distribution on the windward acreage of the damaged wing is essentially unchanged by the damage.

The full list of missing RCC panel cases analyzed computationally is given in Table 4.3-10, with the configuration details (tail/no tail, etc) and the flow conditions for each computation. Figure 4.3-34(a-e) shows the missing panel configurations as run with FELISA, except for the cases with all panels 1-7 removed. The surface pressure (C_p) contours on the side fuselage are shown in Figure 4.3-35 for each configuration at the STS-107 CFD condition 2 (Mach 24.2, $\alpha=40^\circ$). The disturbance on the fuselage moved further down the body and produced a higher C_p as the location of the missing RCC panel moved outboard (Figure 4.3-35a). For multiple missing panels, the trends are not as clear. There is a significant increase ($> 2x$) in the peak pressure on the side fuselage for missing panels 6+7 as compared to 6 only (Figure 4.3-35b). Removing more panels (5+6+7 or 1-7) spreads the region of influence, and the peak pressure drops. Figure 4.3-36 shows the leeside view for missing panels 6, 6+7, and 9. The influence of the size and orientation of the missing panel(s) is evident in the footprint of the expansion out of the channel and the shock due to the resulting 'jet' directed towards the fuselage. The missing panel 9 and missing panels 6+7 results show significantly stronger interaction on the wing leeside than the panel 6 removed case. For missing panels 6+7, the disturbance actually expands upstream of the damage area, indicating the strength of the jet relative to the leeside flow.

All computational methodologies consistently produced negative delta yawing (ΔC_n) and pitching moments (ΔC_m), and near zero to negative delta rolling moments (ΔC_l) for a full missing RCC panel. Magnitudes of the predicted aerodynamic moments varied with the geometry, and to a lesser degree with flow condition (Mach 6 air, CF4, flight). The trends observed are very similar to those measured in the wind tunnel.

The delta aerodynamic moments computed with FELISA for several panel out configurations at flight (CFD condition 2, Mach 24.2) and CF4 are compared to the CF4 wind tunnel results in Figure 4.3-37. The x-axis of the plot is simply the configuration (labeled individually). The lines connecting the points for each configuration are included only to illustrate the trends; there is no expectation that interim damages can be predicted. Overall, the trend agreement between the computations and the wind tunnel is excellent. As additional RCC panels are removed, the moment increments become more negative. Delta pitching and rolling moments are relatively constant as the missing panel location moves outboard, while the yawing moment increment shows a more negative trend as the missing panel moves outboard. A single FELISA solution at flight (CFD condition 2, Mach 24.2) was computed for the full missing RCC panel 6 (RCC + carrier panel) to compare to the initial, or notched panel 6 results. Removing more material at the same location has a noticeable impact on the pitch and roll increments, but little effect on the yawing moment increment.

While the trends shown by the FELISA computations are consistent with the CF4 wind tunnel results, there is definite variation in magnitudes. Comparing the computed CF4 data to the WT measured values, FELISA over-predicts the roll, under-predicts the pitch increment, with close agreement for the yawing increment. When comparing flight condition to CF4 predictions, the flight computations produce consistently lower (larger value, more negative) pitch and yaw increments, while predicting higher (smaller value, more positive) rolling moment increments. While these differences appear large on the scales plotted in Figure 4.3-37, the magnitude of all of the delta moments for the missing panel configurations are represent very small aerodynamic values. The level of correlation between the flight and CF4 computations and the wind tunnel data shown in Figure 4.3-37 strongly suggest that the trends shown in the wind tunnel results are valid for STS-107 flight conditions.

The delta aerodynamic moments from missing panel computations using OVERFLOW, CART3D, LAURA, GASP, are shown in Figure 4.3-38, with the data in Figure 4.3-37 repeated. There is some variation in the geometries for the missing panel 6 and missing panel 9 cases, making exact comparisons impracticable. The CART3D computations did not include a vertical tail, the viscous GASP and LAURA computations terminated the grid systems at the body flap, and both GASP and OVERFLOW results were completed with and without the vertical tail (OVERFLOW with the SILTS pod – Aerodynamic Appendices section 4.7.5). Despite this range of geometry, the agreement for missing panel 6 is reasonable, with near zero increments. There is more of a spread for the missing panel 9 computations with larger increments indicated. Only CART3D and FELISA were used for the multiple missing panels. The CART3D Mach 6 computations indicate the same trends as FELISA and the wind tunnel, but with less variation for the multiple missing panels. For wing leading edge damage the results from all the various tools all indicate relatively small, negative moment increments with similar trends as the damage varies. While the variation suggest the exact magnitudes are uncertain, the body of data suggests the trends are legitimate and can be used to understand how this type of damage of relates to the STS-107 reconstruction.

With computational simulations, the contributions to the vehicle aerodynamics of each vehicle component (vertical tail, wing, etc.) can be isolated. Figure 4.3-39 shows the definition of the vertical tail, wing, OMS pod, and fuselage regions of the orbiter for which component contributions of the delta aerodynamics were calculated. Figure 4.3-40 shows the contributions of each of these regions to the total delta aerodynamic moments for missing panel configurations at flight conditions (CFD condition 2, Mach 24.2). Also shown are the total aerodynamic moments for the CF4 tunnel results. As in Figure 4.3-37, the missing panel configuration is plotted along the x-axis. Each component is color coded according to the colors in Figure 4.3-39, and labeled on the plot, with the solid symbols representing flight computations. Figure 4.3-41 repeats the format of Figure 4.3-40, with hollow symbols for predictions at CF4 WT conditions.

Figure 4.3-40(a) and Figure 4.3-41(a) clearly show that the pressure loads to the wing dominate the delta pitching moment for both flight and CF4 conditions. For the multiple missing panel cases (6+7, 5+6+7) at flight conditions, Figure 4.3-40(b) and (c) show that the delta rolling and yawing moments are also dominated by the wing. For the single missing panels, however, the influences of the vertical tail and wing

balance each other in roll, essentially yielding a zero total increment. The vertical tail, the fuselage and the wing all produce negative increments for yawing moment, thereby providing a relatively large, negative delta yawing moment. The vertical tail contributions are more pronounced in flight for missing panel 9 than for missing panel 6. The CF4 (Figure 4.3-40) conditions show more influence of the vertical tail on the delta rolling and yawing moments for all configurations, with only missing panel 9 giving a positive contribution to the total delta rolling moment. Overall the component breakdown results indicate that there is not a large enough delta rolling moment contribution from the vertical tail to cause a substantial positive (right wing down) total delta rolling moment as seen late in flight.

Several of the missing panel configurations were run at multiple flight conditions to establish trends in the delta aerodynamics due to variations in the flight conditions. Figure 4.3-42 shows the computed delta aerodynamic moments and the extracted flight increments plotted against time from EI. The angle of attack varies between 38° and 42° (See Table 4.3-4 for the flow conditions at each point). The CF4 computational and wind tunnel results are also shown to the right of the trajectory data. The delta pitching moment shows little variation, for each missing panel configuration, over the trajectory. The delta rolling moment shows somewhat of a negative trend toward the end of the trajectory, but the variation is small. Only the delta yawing moment shows a definite (more positive, smaller value) trend across the trajectory. A more systematic study where angle of attack and flow condition were varied independently confirmed that only the delta yawing moment was strongly influenced by the Mach number; these results are contained in Aerodynamic Appendices Section 4.7.4.4..

Overall, the computational results (both for flight and CF4 conditions) for missing panel damage scenarios were consistent with the wind tunnel results. The flow field analysis from these computations clearly indicates that when the windward flow is diverted by WLE damage, the flow field on the leeside of the vehicle is disturbed in a way that is consistent with the increased heating patterns observed during the STS-107 flight. The aerodynamic test and analysis results demonstrate that as more material is removed from the WLE all of the delta moments trend to more negative values. This is counter to the trend toward a more positive rolling moment seen later (after EI + 600 sec) in the STS-107 flight. These two observations taken together suggest the initial STS-107 aerodynamic increments are consistent with WLE damage. However, an additional damage progression scenario, other than simply continuing loss of RCC panel(s), is required to explain the aerodynamic trends later in flight.

4.3.2.3.3 Progressive Damage in Region of RCC Panel 9

As the investigation progressed, the primary damage location was focused towards RCC panels 8-9. The recovered WLE hardware also suggested that, at least initially, the damage was not as extensive as a full missing RCC panel. The second grouping of damaged configurations is a series of damaged configurations, increasing in severity, in the region of RCC panel 9. The damage scenarios and complete set of flow conditions for FELISA cases are shown in Table 4.3-11. Representative cross-sections of the wing in the region of panel 9 are shown for each damage scenario in Figure 4.3-43. For ease of discussion, these damages will be referred to as (a) – (g), as ordered in Figure 4.3-43. Damages (a) – (d) are partial damages to RCC panel 9, and (e) – (g) correspond to full RCC panel 9 missing configurations. Damage (a) is the lower half of RCC panel 9 missing, with solid walls, and is the same configuration as tested in the CF4 wind tunnel. Damage (b) is a 1.0 inch slot from windward to leeside, at the front edge of the upper and lower carrier panels. Damage (c) is the lower half panel 9 with an internal cavity ‘carved’ out, and the upper carrier panel removed to create a flow path from windward to leeside. This geometry is repeated in damage (d), with an additional 810 in² of leeside material removed aft and inboard of the upper carrier panel, for a total leeside exit area of ~1000 in². The full panel missing geometries include an RCC panel 9 missing, damage (e) and the full RCC and both (upper and lower) carrier panels missing damage (f), (this data is repeated from the section on missing full RCC panels). Damage (g) has the same damage as in (d), but with the full RCC panel removed. Both damages (d) and (g) were created in an effort to direct as much mass flow as possible towards the OMS pod and vertical tail, to establish if it was possible to generate the positive delta rolling moment observed in flight by directing flow from the windward to leeside through a hole in the upper wing surface aft of the leading edge. Additional evaluation of progressive wing damage using CART3D is discussed in Aerodynamic Appendices Section 4.7.6.

The leeside flow fields for several of these damages at flight conditions (CFD condition 4, M=20.2) are shown in Figure 4.3-44. The flow patterns on the leeside wing and the side fuselage appear very similar,

despite the fact that the flow is coming through very different size damage geometries. The strength of the impingement (maximum C_p) on the side fuselage increases as the size of the hole increases beyond the upper carrier panel area, but is relatively constant for cases (d) – (g). The similarities in the flow patterns and pressure levels suggest that it is very difficult to isolate the damage size and location from correlations with the side fuselage MADS data. A wide range of damage scenarios, that enable windward to leeward flow, appear equally valid.

The delta aerodynamic moments for FELISA cases with progressive damage in the RCC panel 9 region, at flight (CFD condition 4, $M=20.2$) and CF4 conditions, are shown in Figure 4.3-45. The half panel 9 geometry (a) gives a very small increment in rolling (positive) and yawing (negative) moments, as no windward flow is diverted to the leeside. The delta aerodynamics for the one inch wide slot at RCC panel 9 are essentially zero. Establishing a larger flow path by removing the whole upper carrier panel 9 (c) continues the small positive increment to the rolling moment, and significantly shifts the yawing moment to a more negative value. When the size of the hole on the leeside is increased (d) from 188 in² (size of the upper carrier panel) to 998 in², there is little change in the delta rolling moment, and a small increase in the delta yawing moment. For the full panel out cases, the delta rolling moment becomes more negative as more WLE material is removed, from (e) to (f), while the delta yaw stays constant. When the additional leeside material is removed in (g), the delta yawing moment becomes less negative, and the delta rolling moment remains unchanged.

The component breakdown of the contributions to the delta aerodynamic moments is shown in Figure 4.3-46 and Figure 4.3-47 (See Figure 4.3-39 for the component definition). For delta rolling moment, the vertical tail gives a consistently positive contribution, which is offset to some degree by the wing. The half panel cases ((c) and (d), primarily) result in a small contribution from the wing, and thus a positive rolling moment. The full panel cases ((e) – (g)) have more contribution from the wing, resulting in a slightly negative rolling moment. The delta yawing moment is consistently negative, with fuselage and tail contributing more for the flight cases than the CF4. This analysis of component contributions to the total delta aerodynamics further underscores the observation that a large positive roll does not come from the flow over the vertical tail.

The leeside flow fields suggest that any of the damage progression configurations enabling flow to the leeside ((c) – (g)) can produce a significant disturbance on the side fuselage and OMS pod. The aerodynamic data, however, indicate that the damage that produces the more positive delta rolling moment (albeit near zero) is one with only partial damage to the RCC panel with flow to the leeside through an area behind the RCC, rather than a complete RCC panel missing. This set of damage scenarios did not produce a large positive rolling moment increment as observed late flight (EI + 800 sec). Indeed, it is clear that progressively damaging a particular RCC panel does not produce the steadily increasing trend in rolling moment increment seen in flight. This suggests that there must be another type of damage in addition to the WLE damage scenarios examined.

4.3.2.3.4 Windward Surface Deformation (Depressions and WLE Deformation)

One of the clearest trends in the reconstructed flight data was a change in the trend of the delta rolling moment that occurred around 600 seconds after EI. This change in rolling moment trend, and particularly the relatively large positive rolling moment late in flight (> EI + 800 sec), was not explained by any of the full or partial RCC panel damage configurations. Early wind tunnel tests with shallow wheel well cavities exposed had indicated that windward surface cavities could produce the positive roll and negative yaw observed late in flight.

A third group of computations conducted to investigate windward surface depressions/dimples in an attempt to model the structural deformation of the wing due to the heating damage to the intermediate wing internal structure. The depressions are assumed to result from the wing skin “dimpling” due to failure of the ribs and delamination of the wing honeycomb skin panels. Figure 4.3-48(a) shows an intermediate length ($L=98$ ”) depression that extends to the end of the wheel well, and has a depth that is approximately half ($d=2.8$ ”) of the depth modeled in the wind tunnel. Figure 4.3-48(b) shows the damage configuration that corresponds to full length, “single wide” (1w) depression with RCC panel 9 removed that was also tested in the CF4 tunnel. The depression created in the ceramic wind tunnel model was milled such that the interior corners were rounded, as opposed to sharp edges in the FELISA model. Aerodynamic

increments for the intermediate length dimple at 2 depths and a full length depression with and without RCC panel 9 removed were computed with FELISA for flight and CF4 conditions. The structural analysis group at JSC performed a FEM simulation of the global deformation of the wing, assuming failure and degraded strength of the structure in the intermediate wing box area. Additional engineering calculations were made on the damaged structure to simulate the localized deformation of the wing skin. Figure 4.3-48(c) shows the resulting geometry, as modeled with FELISA. The structural analysis efforts to understand the wing deformation late in flight are covered in Section 7.5. An additional geometry, which was an attempt to deform the WLE by rotating several of the RCC panels, around RCC panel 9, is included in this group. Figure 4.3-49 shows the deformed geometry overlay on the original. In the region of RCC panel 9, the WLE is rotated up. The amount of rotation tapers off away from RCC panel 9. Table 4.3-12 summarizes the damaged geometries and flow conditions that were run with FELISA for the windward surface deformation cases.

Windward surface pressure contours and surface streamlines are shown in Figure 4.3-50 for CF4 conditions and in Figure 4.3-51 for flight (CFD Condition 4, $M=20.2$) conditions, for several of the windward surface damage configurations. The depression configurations that simulate the 'single wide' wind tunnel geometries show a very strong compression along the aft face of the damaged area. The shorter length depression shows the same flow pattern in the expansion area at the front of the depression as the longer length. Thus, the longer depression has more area that is at a higher pressure than the baseline. Additionally, the shallower depression shows a smaller and weaker compression at the aft face of the depression. The character of the flow patterns for the damage resulting from the structural analysis is quite different than for the 'single wide' geometries. Since there are no sharp slope changes, a gentle expansion then recompression of the flow occurs within the dimpled area, and therefore a smoother and smaller variation in the surface pressure. This results in smaller delta aerodynamic moments than for the wind tunnel cases configurations.

The delta aerodynamics for the windward damage cases and corresponding CF4 tunnel data are shown in Figure 4.3-52. The WLE deformation case showed zero delta rolling and pitching moments, and a relatively small increment in yawing moment. The zero increment in rolling moment is due to canceling contributions of an increase in normal force (giving positive rolling moment) and a positive side force (which gives a negative rolling moment). It is possible that a WLE deformation that rotates more RCC panels at a smaller angle so less side force is produced would show a positive delta rolling moment. The agreement between the computations and wind tunnel for the single wide depressions is comparable for the delta yawing and pitching moments, but is not as good quantitatively for rolling moment as has been shown for other damaged configurations evaluated (See Figure 4.3-37 and Figure 4.3-45). The computations show the largest positive rolling moment for any of the damage configurations assessed, and is positive for all of the depressions considered. The wind tunnel only showed positive delta rolling moment for the longer depressions. This discrepancy is likely due to a combination of geometry differences (particularly the contoured back wall of the depression for the wind tunnel model) and a strong viscous component to this cavity-like flow. The damage from the structural analysis dimple configuration shows a smaller, though still positive rolling moment increment, and very small pitch and yawing moment increments. This is expected, in part because the strong compression at the back of the single width depression will produce larger delta moments when compared to the more gentle sloping of the structural analysis depression.

In addition to showing computed and measured delta aerodynamics, Figure 4.3-52 also shows an estimate, using simple superposition, of the delta aerodynamics for the cases where the windward surface damage was combined with a missing RCC panel. The superposition values compare well with the computed values for the longer, single width depression combined with missing RCC panel 9, and indicate that the postulated structural damage would produce the positive roll and negative yaw that was seen in flight.

Overall, the delta aerodynamics computed with FELISA for windward surface damage configurations corroborate the trends produced in the wind tunnel. The data trends support the hypothesis of progressive internal structural damage occurring late in the flight that produces a gradual windward surface deformation. This gradual deformation produces the steady increase in rolling moment and yawing moment increments seen late in flight.

Tables

Computational Tools Used in STS-107 Investigation - Aerodynamic Analysis					
Code / Tool	Physics Model	Mesh type	Available Gas Models	Mach number range	Analysts
FELISA	Inviscid	unstructured	perfect gas air, CF4 gas, equilibrium air	restricted by continuum flow boundaries	LaRC (Bibb, Prabhu)
CART3D	Inviscid	cartesian unstructured	perfect gas air	<10 (applied @ Mach 6)	JSC (Dries, Greathouse)
OVERFLOW	Viscous	structured, overset	perfect gas air	<18 (applied @ Mach 6)	JSC (Lillard)
LAURA	Viscous	structured	perfect gas, equilibrium, non-equilibrium, CF4	restricted by continuum flow boundaries	LaRC (Gnoffo, Bobskill, Thompson)
GASP	Viscous	structured	perfect gas, equilibrium, non-equilibrium	restricted by continuum flow boundaries	ARC (Reuther, Jones)
USA	Viscous	structured	perfect gas, equilibrium, non-equilibrium	restricted by continuum flow boundaries	Boeing-HB (Rajagopal)

Table 4.3-1 CFD Flow Solvers used in Aerodynamic Analysis for STS-107 Investigation

OEX / STS-2 Conditions							
Case	Mach	Angle-of-Attack (Alpha) deg	Angle-of-Sideslip (Beta) deg	Velocity ft/sec	Density slug/ft^3	Temperature °R	Reynolds Number / ft
STS-2a	18.07	40°	0°	18429.4	3.1673E-07	433.1	9070
STS-2b	24.3	40°	0°	22704.5	1.1200E-07	363.6	17950

Table 4.3-2 STS-2 Conditions Utilized in Initial Phase of Investigation

Parameter	Derivation	Comment
altitude	GPS data	
longitude	GPS data	
latitude	GPS data	
Velocity	GPS data	should be wind corrected to get true airspeed
flight path angle	GPS data	should be wind corrected
azimuthal angle	GPS data	should be wind corrected
density	GPS altitude + GRAM February model	should be updated with DOA/MSFC atmosphere
temperature	GPS altitude + GRAM February model	should be updated with DOA/MSFC atmosphere
dynamic pressure	GPS velocity + density	should be updated with DOA/MSFC atmosphere
viscosity	Sutherland Law + Temperature	should be updated with DOA/MSFC atmosphere
Mach number	GPS velocity + Temperature	should be updated with DOA/MSFC atmosphere
Reynolds number	GPS velocity + Temperature	should be updated with DOA/MSFC atmosphere
Stagnation radiative equilibrium Heat Flux	Fey-Ridell + GPS data + GRAM data	should be updated with DOA/MSFC atmosphere
Stagnation radiative equilibrium Temperature	Fey-Ridell + GPS data + GRAM data	should be updated with DOA/MSFC atmosphere
Alpha	OI inertial navigation data	should be wind corrected
Beta	OI inertial navigation data	should be wind corrected
Bank	OI inertial navigation data	should be wind corrected
Body Flap	OI data	
Left Inboard Elevon	OI data	
Left Outboard Elevon	OI data	
Right Inboard Elevon	OI data	
Right Outboard Elevon	OI data	

Table 4.3-3 Parameter Calculation Method for STS-107 Investigation Conditions

Point Name	Comments	GMT (mm:ss.ss)	Time past e.i. (sec)	Altitude (ft)	VREL (ft/sec)	Mach Num.	Reynolds # per foot (Re/ft)	Alpha (deg)	Beta (deg)
Condition AA	350,000 ft DSMC point	45:40.0	91.04	350,274	24,622	25.10	26	40.78	-0.29
Condition A	300,000 ft DSMC vs NS comparison point	47:26.6	197.60	300,004	24,666	27.04	456	39.55	0.30
Condition B	Early Entry Navier-Stokes solution point	49:00.7	291.68	261,730	24,603	25.70	2,679	41.35	-0.07
Condition 1	Start Peak Heat	50:53.0	404.00	243,048	24,116	24.87	5,872	40.17	-0.06
Condition 2	First Off Nominal Event	52:20.4	491.36	236,527	23,554	24.17	7,644	39.99	-0.25
Condition VN	Off nominal vent nozzle temp. rise rate	52:45.3	516.32	234,623	23,368	23.94	8,274	40.04	-0.50
Condition 3	Mid Fuselage Bond Line Temperatures @ x=1215 and 1410 start off nominal trend	54:24.2	615.20	227,423	22,505	22.91	10,997	39.59	-0.47
Condition 4	Start of elevon roll trim corrections	57:35.2	806.24	216,064	20,210	20.30	16,244	42.01	-0.69
Condition 5	Near start of sharp aileron trim	58:23.2	854.24	209,368	19,428	19.35	20,729	38.87	-0.52
Condition 6	Last Good GPS point	59:30.4	921.44	200,767	18,164	17.88	27,409	39.02	-1.16

Point Name	Comments	GMT (mm:ss.ss)	Time past e.i. (sec)	Density (slugs/ft^3)	Temp (deg R)	Dynamic Pressure (lbf/ft^2)	Viscosity (slugs/(ft*sec))	Stag. heat flux (BTU/ft^2*sec)	Stag. rad. eq. Temp. (deg R)
Condition AA	350,000 ft DSMC point	45:40.0	91.04	3.345E-10	400.4	0.1014	3.169E-07	2.620	1,627
Condition A	300,000 ft DSMC vs NS comparison point	47:26.6	197.60	5.181E-09	346.2	1.5762	2.802E-07	11.102	2,289
Condition B	Early Entry Navier-Stokes solution point	49:00.7	291.68	3.314E-08	381.5	10.0292	3.043E-07	27.844	2,881
Condition 1	Start Peak Heat	50:53.0	404.00	7.568E-08	391.2	22.0077	3.108E-07	39.651	3,147
Condition 2	First Off Nominal Event	52:20.4	491.36	1.017E-07	395.2	28.2189	3.135E-07	42.559	3,203
Condition VN	Off nominal vent nozzle temp. rise rate	52:45.3	516.32	1.113E-07	396.4	30.3782	3.142E-07	43.528	3,221
Condition 3	Mid Fuselage Bond Line Temperatures @ x=1215 and 1410 start off nominal trend	54:24.2	615.20	1.552E-07	401.4	39.2967	3.176E-07	45.643	3,258
Condition 4	Start of elevon roll trim corrections	57:35.2	806.24	2.610E-07	412.5	53.3117	3.248E-07	42.119	3,195
Condition 5	Near start of sharp aileron trim	58:23.2	854.24	3.515E-07	419.6	66.3299	3.294E-07	42.824	3,208
Condition 6	Last Good GPS point	59:30.4	921.44	5.064E-07	429.3	83.5424	3.356E-07	41.502	3,182

Point Name	Comments	GMT (mm:ss.ss)	Time past e.i. (sec)	Bank (deg)	Body Flap (deg)	Lf. Inbrd. El. (deg)	Lf. Outbrd. Elv. (deg)	Rt. Inbrd. Elv. (deg)	Rt. Outbrd. Elv. (deg)
Condition AA	350,000 ft DSMC point	45:40.0	91.04	-0.19	-4.32	1.97	1.88	1.97	1.96
Condition A	300,000 ft DSMC vs NS comparison point	47:26.6	197.60	1.36	-4.28	1.97	1.91	1.97	1.96
Condition B	Early Entry Navier-Stokes solution point	49:00.7	291.68	1.79	-4.46	-1.03	-1.06	-1.27	-1.25
Condition 1	Start Peak Heat	50:53.0	404.00	78.55	1.18	-2.30	-2.32	-3.54	-3.55
Condition 2	First Off Nominal Event	52:20.4	491.36	72.77	1.19	-2.71	-2.67	-3.53	-3.51
Condition VN	Off nominal vent nozzle temp. rise rate	52:45.3	516.32	72.05	1.19	-2.74	-2.74	-3.50	-3.45
Condition 3	Mid Fuselage Bond Line Temperatures @ x=1215 and 1410 start off nominal trend	54:24.2	615.20	66.75	1.23	-2.17	-2.21	-3.18	-3.19
Condition 4	Start of elevon roll trim corrections	57:35.2	806.24	-68.57	-1.81	-4.58	-4.58	-3.51	-3.50
Condition 5	Near start of sharp aileron trim	58:23.2	854.24	-56.75	-0.26	-3.27	-3.14	-1.37	-1.38
Condition 6	Last Good GPS point	59:30.4	921.44	-63.85	0.09	-6.07	-6.03	-1.63	-1.64

Table 4.3-4 STS-107 Investigation CFD Case Flight Conditions

Mach 6 Air Conditions (LaRC Tunnel)							
Case	Mach	alpha,	beta,de	velocity, ft/sec	density, slug/ft ³	T, °R	Reynolds Number / ft
LAURA Wind Tunnel	5.94	40°	0°	3092.9	6.3517E-05	113.0	2.08 Million/ft
OVERFLOW Wind Tunnel	5.96	40°	0°	3096.0	2.5556E-05	112.3	2.98 Million/ft
Perfect Gas, FELISA, CART3D	6	40°	0°	---	---	---	---

Mach 6 CF4 Conditions (LaRC Tunnel)							
Case	Mach	alpha,	beta,de	velocity, ft/sec	density, slug/ft ³	T, °R	Reynolds Number / ft
LAURA, low Re	5.894	40°	0°	2917.5	1.4805E-05	357.7	0.17 Million/ft
LAURA, high Re	5.902	40°	0°	2934.1	4.7026E-05	361.2	0.55 Million/ft
LAURA, final	5.913	40°	0°	2910.9	3.8915E-05	353.0	0.46 Million/ft
FELISA	5.85	40°	0°	2994.0	2.9393E-05	387.4	---

Table 4.3-5: Wind Tunnel Conditions Utilized in STS-107 Investigation

Scenario		Flow Solver	Mach 6	CF4	Flight
WLE Damage - Full / Partial Missing RCC					
Panel 6 removed	includes LaRC initial panel 6, RCC 6, and RCC+carrier panel 6	FELISA	X	X	X
		CART3D	X		
		OVERFLOW	X		
		LAURA			X
		GASP			X
		USA			X
Panels 6-7 removed	includes RCC 6+7, and RCC+carrier panel 6+7	FELISA		X	X
		CART3D	X		
Panels 5-7 removed	includes RCC 5+6+7, and RCC+carrier panel 5+6+7	FELISA		X	X
		CART3D	X		
Panel 9 removed	includes RCC 9, and RCC+carrier panel 9, LAURA/GASP also with open RCC channel	FELISA		X	X
		CART3D	X		
		OVERFLOW	X		
		GASP			X
		LAURA			X
Panels 1-7 removed		FELISA		X	X
		CART3D	X		
Half Panels Removed	CART3D (7, 8, 9), FELISA (9), GASP (6, 9)	FELISA		X	
		GASP			X
		CART3D	X		
Missing T-Seal 9		CART3D	X		
Progressive Damage near RCC Panel 9					
Half Panel 9	solid walls	FELISA		X	
		CART3D	X		
		GASP			X
Half Panel 9 with RCC cavity, upper carrier panel missing	GASP has vented walls, no upper cavity	FELISA		X	X
		GASP			X
Half Panel 9 with cavity, upper carrier panel missing, additional leeside material removed		FELISA		X	X
RCC Panel 9 removed		FELISA		X	X
RCC + carrier panels at 9 removed		FELISA		X	X
RCC 9, upper carrier 9, and additional leeside material removed		FELISA		X	X
Lower Carrier Panel 8 w/large upper wing hole		CART3D	X		
Half 8 (w/Full Panel 9 removed or small upper wing hole or large upper wing hole)		CART3D	X		
Windward Surface Damage					
WLE deformation	GEOLAB modification	FELISA		X	
B. Scallion dimple (depression created between the 163 and 192 ribs)	2 lengths, 2 depths, with and without RCC 9 removed	FELISA		X	X
Depression from structural analysis	Depth = 5.09"	FELISA		X	X

Table 4.3-6 Master Configuration Matrix for STS-107 Aerodynamic Analysis

Geometry Model / Mesh	Original Geometry Source	Comments
LaRC legacy structured mesh	1997 CAD definition	
gridTool model		All FELISA meshes were built from a gridTool watertight surface model, which was built from the LaRC legacy structured mesh.
FELISA unstructured surface mesh		CART3D meshes were built using the FELISA baseline mesh for the surface geometry
ARC legacy structured mesh		
Boeing legacy structured mesh		
Common Baseline Grid	2003 CAD definition	.igs and .stp exported geometry (R. Gomez-JSC)

Table 4.3-7 Geometry Pedigree for Baseline Geometries

Auxiliary Geometry for Damage Analysis	Short Name	Source	Comments
SILTS Pod	SILTS Pod	JSC Engineering	Simplified representation estimated from SILTS Pod drawings
LaRC initial panel 6	LaRC initial panel 6	OEX Aerothermodynamics Symposium, NASA CP 3248, Part2, page 759	Estimated RCC panel 6 location from drawing in report -- <i>referred to as initial panel 6 definition or panel 6 "notch"</i>
Initial RCC Panel Definition	Greathouse RCC	Orbiter Drawings	RCC panel corner points were digitized from orbiter drawings. Leading edge was cut into individual pieces to approximate RCC panels 1-22
Dries/GEOLAB RCC and Carrier Panel Definition	Dries/GEOLAB	Drawing 221-50000 Rev. A, General Arrangement; Drawing MD-V70-10-002, Wing Reference System Diagram; LESS/RCC Recovery and Reconstruction Data	Panel locations provided by JSC/K. Dries and integrated into CAD definition by LaRC/GEOLAB

Table 4.3-8 Damage Geometry Pedigree

Scenario	Configuration Details	geometry pedigree	Flow Solver	STS-2	STS-107						CF4 Air Tunnel	Mach 6 Air Tunnel
					1	2	3	4	5	6		
Baseline, half body	with vertical tail, bodyflap	1997 FELISA	a, b	X	X	X	X	X	X	X	X	X
		1997 CART3D										X
		1997 USA										
	full body with vertical tail, bodyflap	1997 FELISA									$\beta = -1^\circ, +1^\circ$	
		2003 OVERFLOW										X
	vertical tail with SILTS pod	1997 LAURA	a, b	X	X	X				X		
		2003 LAURA	a, b	X	X	X				X	X	X
		2003 GASP	a, b	X	X	X				X	X	X
	without bodyflap	1997 FELISA			X							
		1997 CART3D										X
		2003 OVERFLOW										X
	without vertical tail, bodyflap	1997 GASP										

Table 4.3-9 Baseline Orbiter Cases

Scenario	Configuration Details	geometry pedigree	Flow Solver	STS-2	STS-107						CF4 Air Tunnel	Mach 6 Air Tunnel
					1	2	3	4	5	6		
Full missing RCC panels												
Panel 6 removed	LaRC panel 6, vertical tail, bodyflap	1997	FELISA	a, b	X	X	X	X	X	X	X	X
	LaRC panel 6, no vertical tail	1997	CART3D									X
	LaRC panel 6, no vertical tail	2003	OVERFLOW									X
	LaRC panel 6, without bodyflap	1997	LAURA		X							
	RCC only, without bodyflap	2003	GASP		X							
	RCC + carrier panel 6, vertical tail, bodyflap	1997	FELISA			X						
	??	1997	USA						X???			
panels 6-7 removed	RCC + carrier panel, vertical tail, bodyflap	1997	FELISA		X	X	X	$\alpha = 38^\circ, 40^\circ, 42^\circ$	X	X	X, $\alpha = 40^\circ$	
	RCC only, no vertical tail	1997	CART3D									X
panels 5-7 removed	RCC + carrier panel, vertical tail, bodyflap	1997	FELISA			X					X	
	RCC only, no vertical tail	1997	CART3D									X
panel 9 removed	RCC + carrier panel, vertical tail, bodyflap	1997	FELISA		X	X	X	X			X	
	RCC only, no vertical tail	1997	CART3D									X
	RCC only, vertical tail, bodyflap	1997	FELISA		X	X		X			X	
	RCC + carrier panel, vertical tail, bodyflap, full (360°)	1997	FELISA								$\beta = -1^\circ, 0^\circ, +1^\circ$	
	RCC only, with vertical tail and SILTS pod, full (360°)	2003	OVERFLOW									X
	RCC only, without vertical tail	2003	OVERFLOW									X
	RCC only, without tail, without bodyflap	2003	GASP		X							
	RCC only, without tail, without bodyflap. Vented RCC channel	2003	GASP		X							
	RCC only, vented RCC channel	2003	LAURA		X							
panels 1-7 removed	RCC only, no vertical tail	1997	FELISA			X					X	
			CART3D									X

Table 4.3-10 Missing RCC cases, FELISA

Scenario	Configuration Details	geometry pedigree	Flow Solver	STS-2	STS-107						CF4 Air Tunnel	Mach 6 Air Tunnel
					1	2	3	4	5	6		
Progressive Damage near RCC Panel 9												
half panel 9	solid walls, with vertical tail, bodyflap	1997	FELISA								X	
		1997	CART3D									X
	solid walls, without vertical tail, no bodyflap	2003	GASP		X							
	vented RCC channel, without vertical tail, no bodyflap	2003	GASP		X							
slot behind RCC panel 9	width ~ .5"	1997	FELISA								X	
	width ~ 1"	1997	FELISA								X	
half panel 9 with RCC cavity, upper carrier panel missing		1997	FELISA					X			X	
	vented RCC channel, without vertical tail, no bodyflap	2003	GASP		X							
half panel 9 with cavity, upper carrier panel missing, additional leeside material removed		1997	FELISA					X			X	
RCC 9 removed	RCC 9 only	1997	FELISA		X	X		X			X	
RCC + carrier panels at 9 removed		1997	FELISA			X	X	X			X	
RCC 9, upper carrier 9, and additional leeside material removed		1997	FELISA			X		X			X	

Table 4.3-11 Progressive Damage at RCC Panel 9, FELISA Cases

Scenario	Configuration Details	geometry pedigree	Flow Solver	STS-2	STS-107						CF4 Air Tunnel	Mach 6 Air Tunnel
					1	2	3	4	5	6		
Windward Surface Damage												
wheel well cavity open	d = 6", 15", 30"		FELISA								X	
WLE deformation	GEOLAB modification		FELISA								X	
scallion dimple (depression created between the 163 and 192 ribs)	L=98", d=2.8"	1997	FELISA								X	
	L=98", d=5.4"	1997	FELISA								X	
	L=150", d=5.3"	1997	FELISA			X	X	X			X	
	L=150", d=5.3", RCC 9 removed	1997	FELISA			X	X	X			X	
depression from structural analysis	d = 5.09"	1997	FELISA			X	X	X			X	

Table 4.3-12 Windward Surface Damage, FELISA Cases

Figures

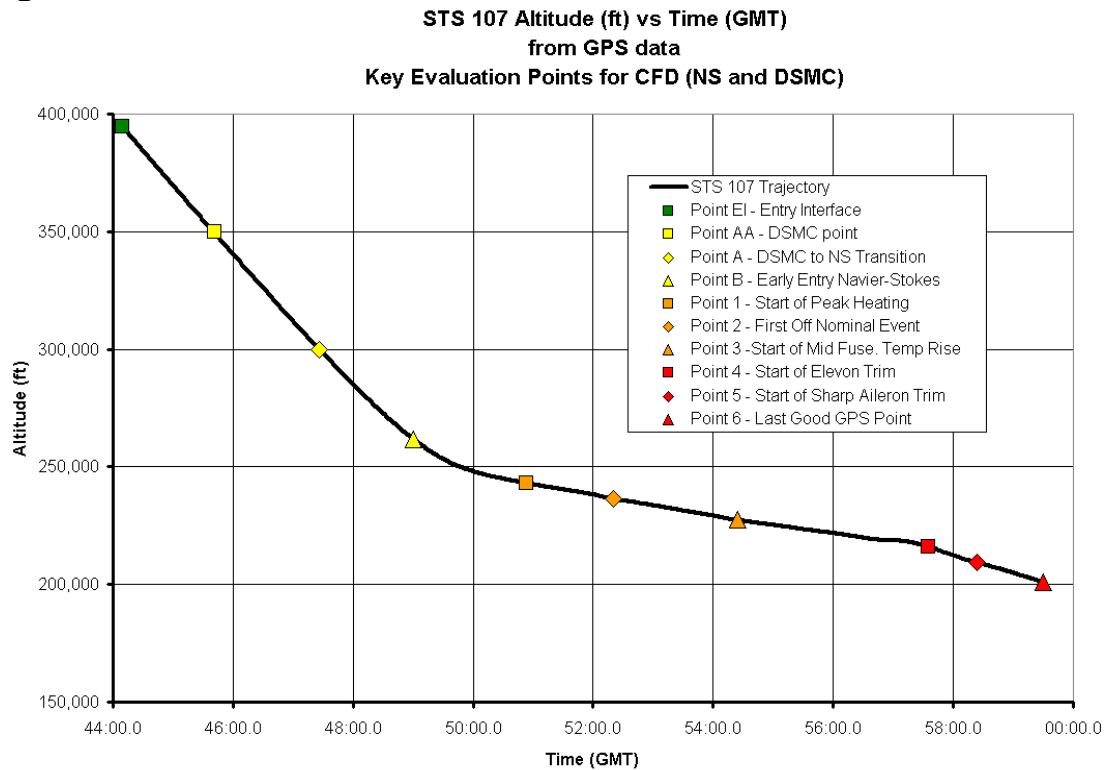


Figure 4.3-26 STS-107 Trajectory (Altitude vs. Time)

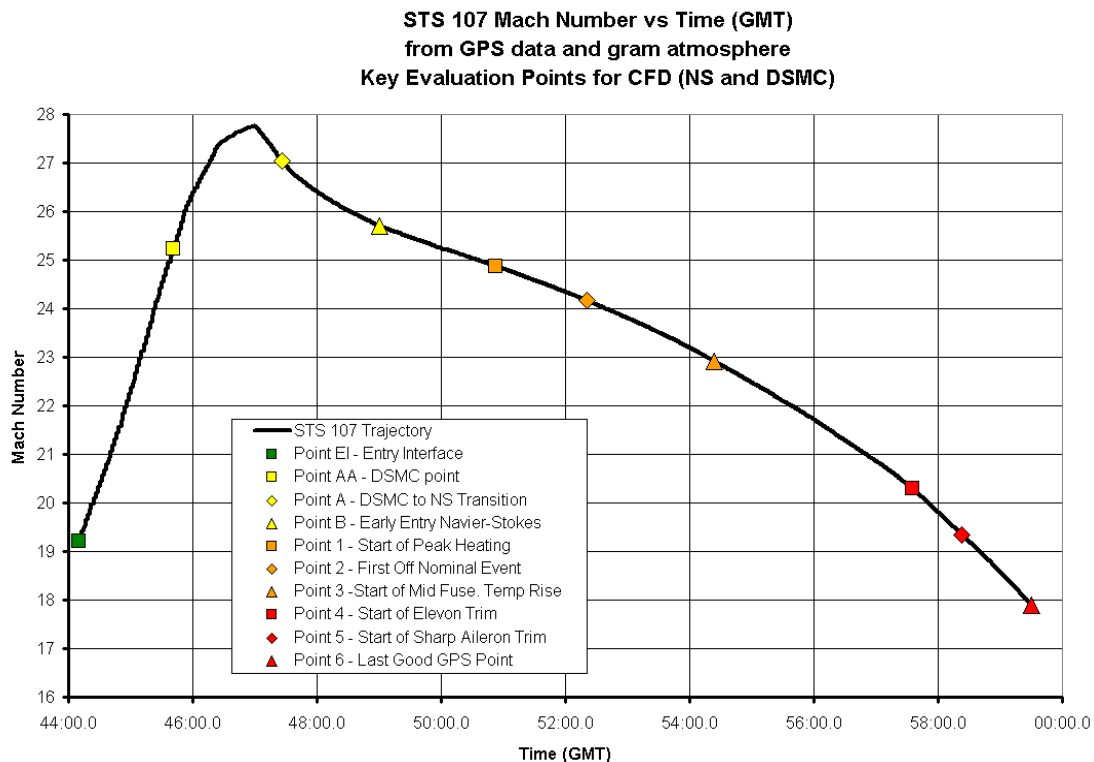


Figure 4.3-27 STS-107 Trajectory (Mach No. vs. Time)

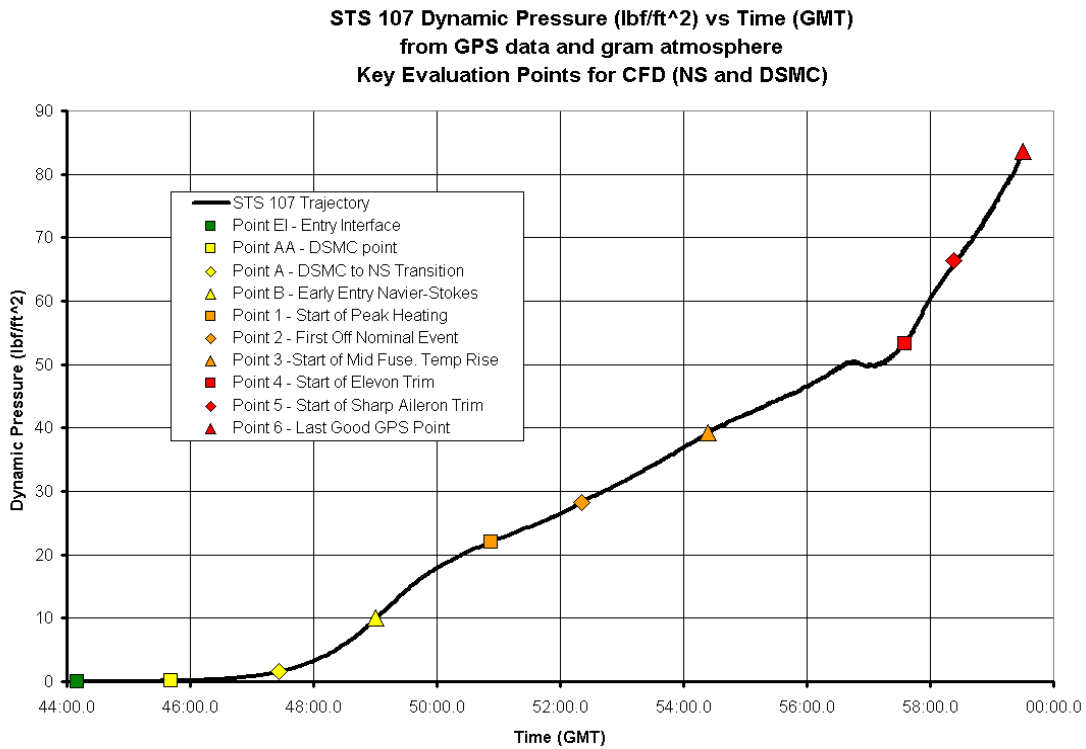


Figure 4.3-28 STS-107 Trajectory (Dynamic Pressure vs. Time)

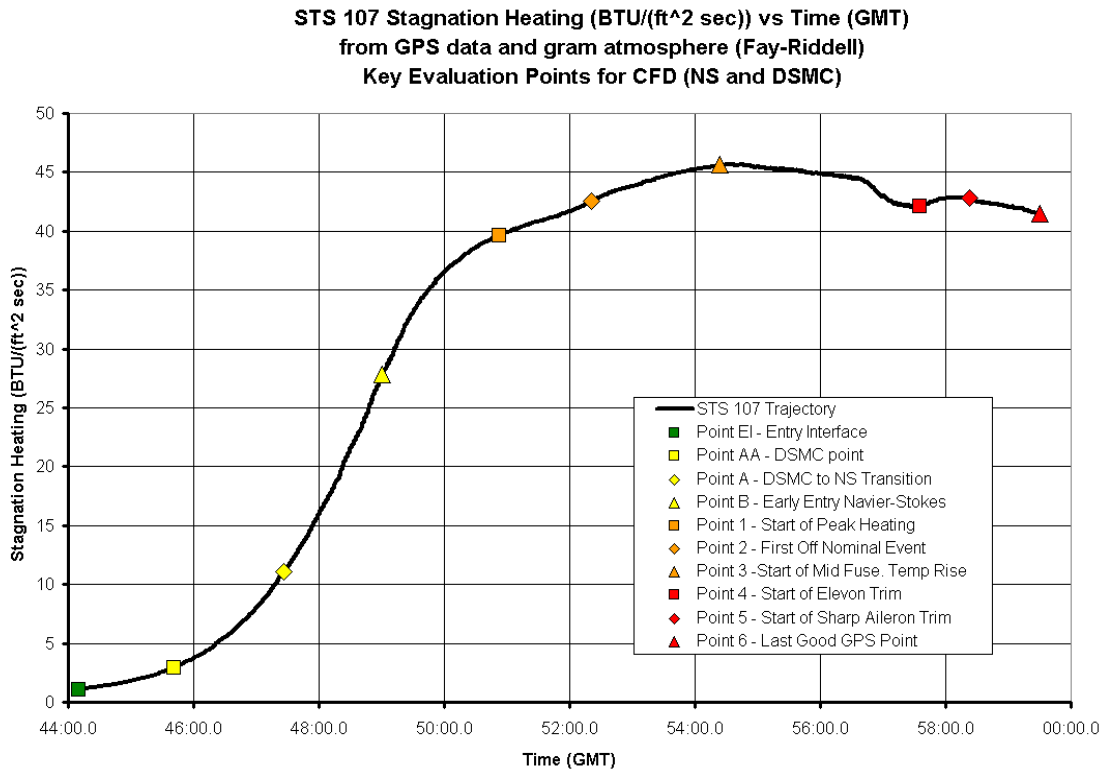


Figure 4.3-29: STS-107 Trajectory (Stagnation Point Heating vs. Time)

58

Comparison of Inviscid FELISA to Viscous LAURA Solutions and Flight Database

- Aerodynamic Coefficients vs. Time from Entry Interface
 - FELISA - Equilibrium Air
 - LAURA - Finite Rate Chemistry, Thermal Equilibrium
 - Angle of attack varies over flight
- LAURA geometry doesn't include bodyflap, FELISA loads reduced with and without bodyflap.
- FELISA has elevon gaps, LAURA does not

FELISA vs. LAURA
(no bodyflap)

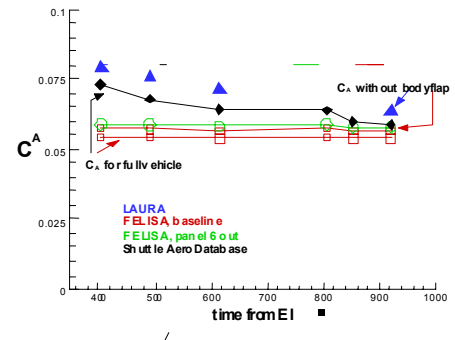
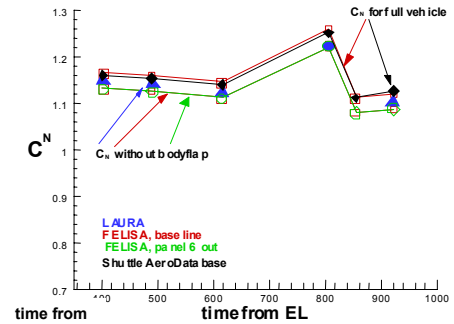
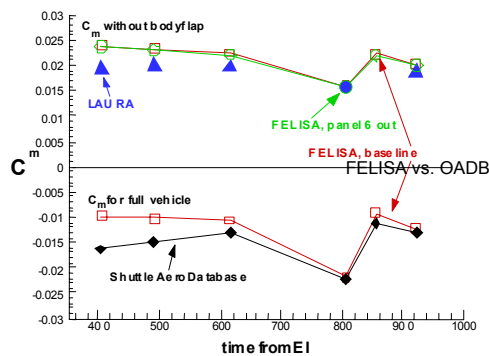


Figure 4.3-30 Baseline Aerodynamic Comparisons (Orbiter OADB vs. CFD Prediction)

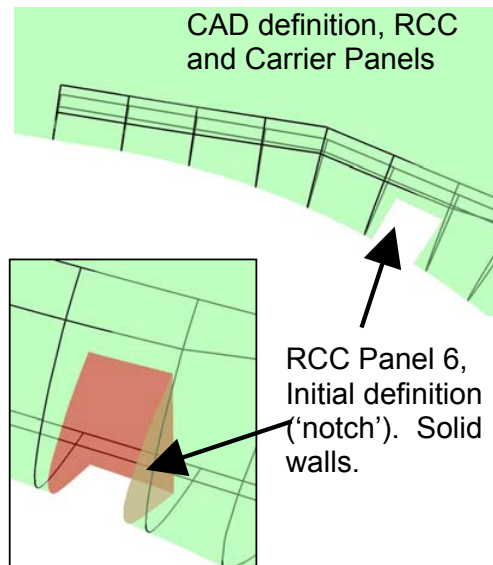


Figure 4.3-31 RCC Panel 6, Initial Definition

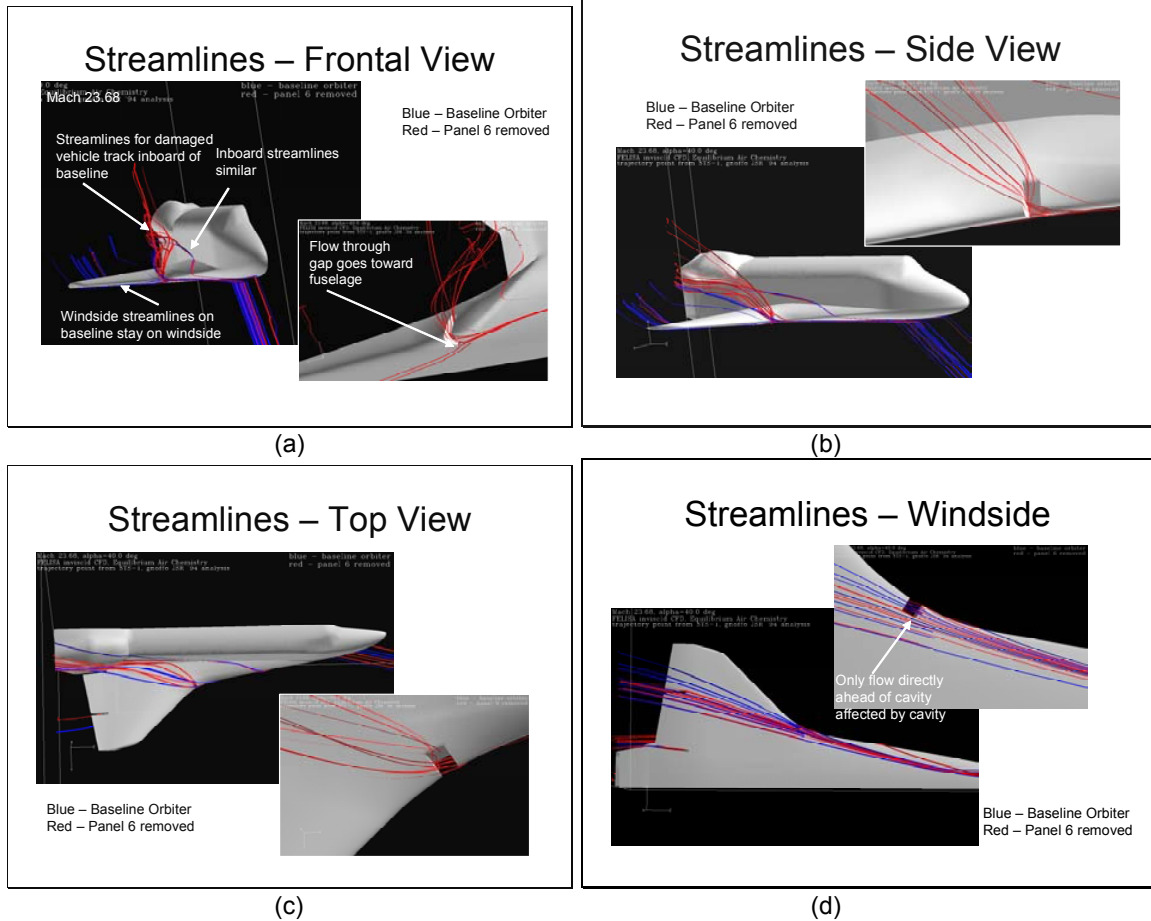


Figure 4.3-32 Nominal & Missing RCC Panel 6, Streamlines

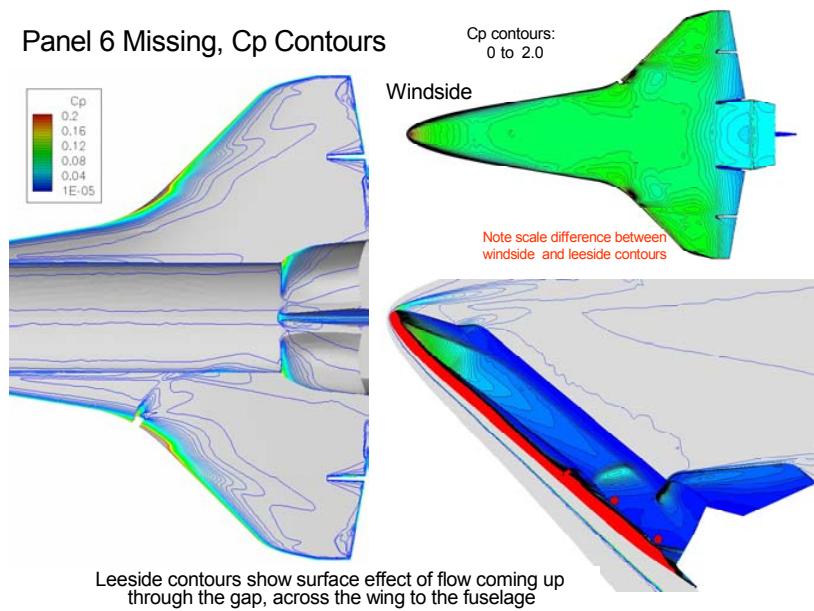


Figure 4.3-33 Panel 6 Missing – Surface Pressure Distribution

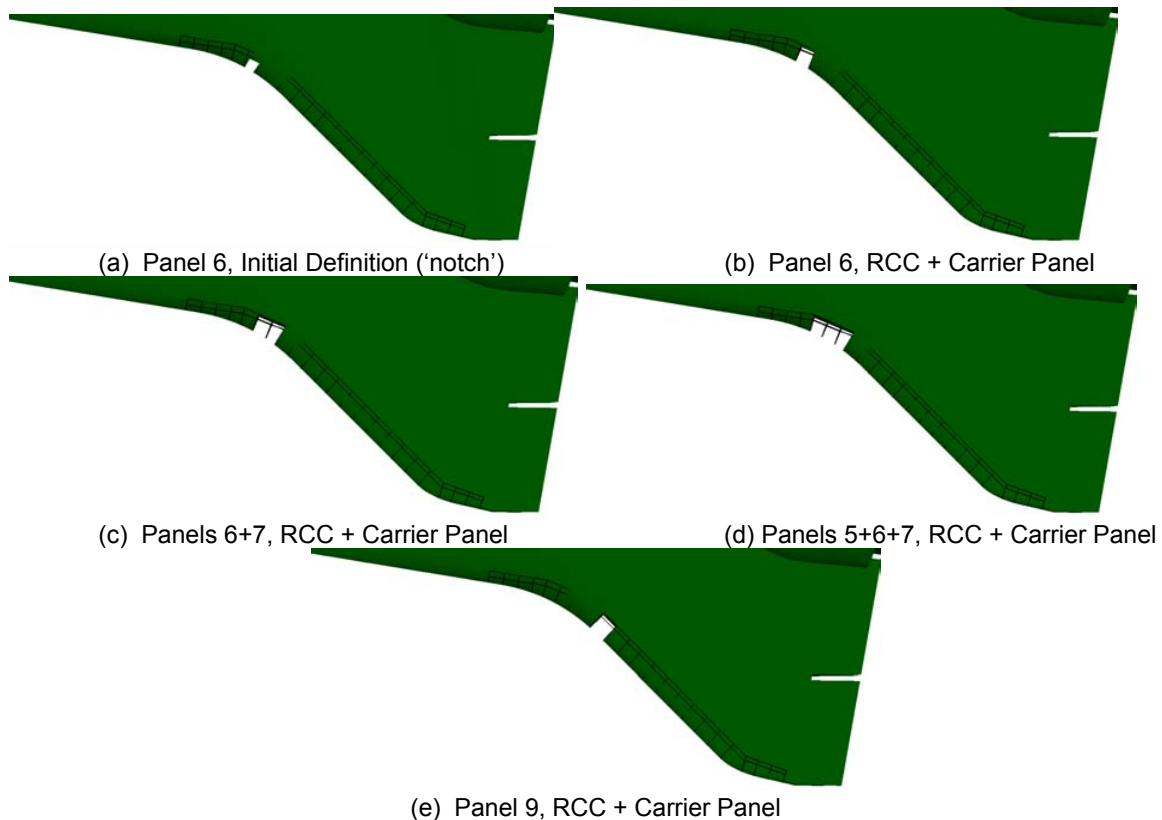
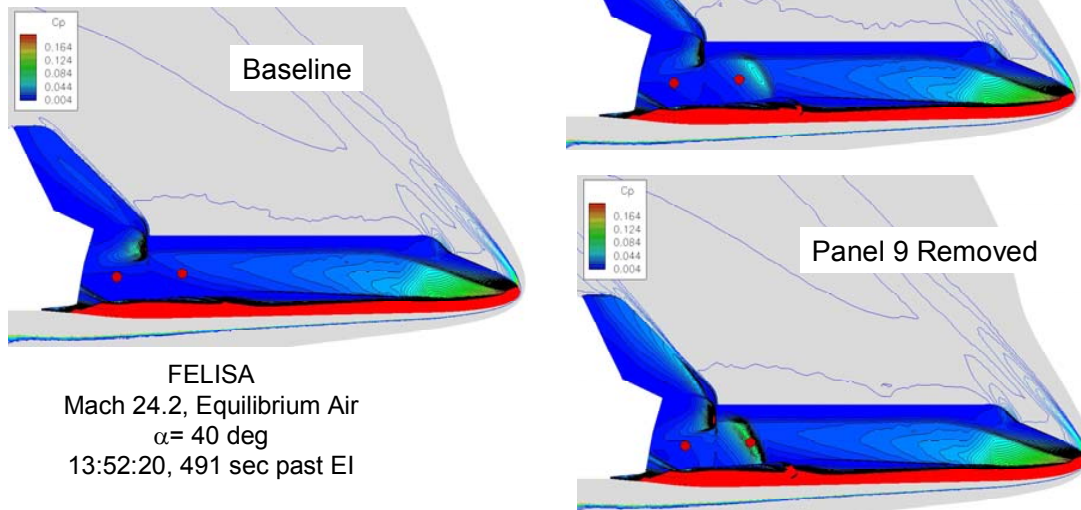


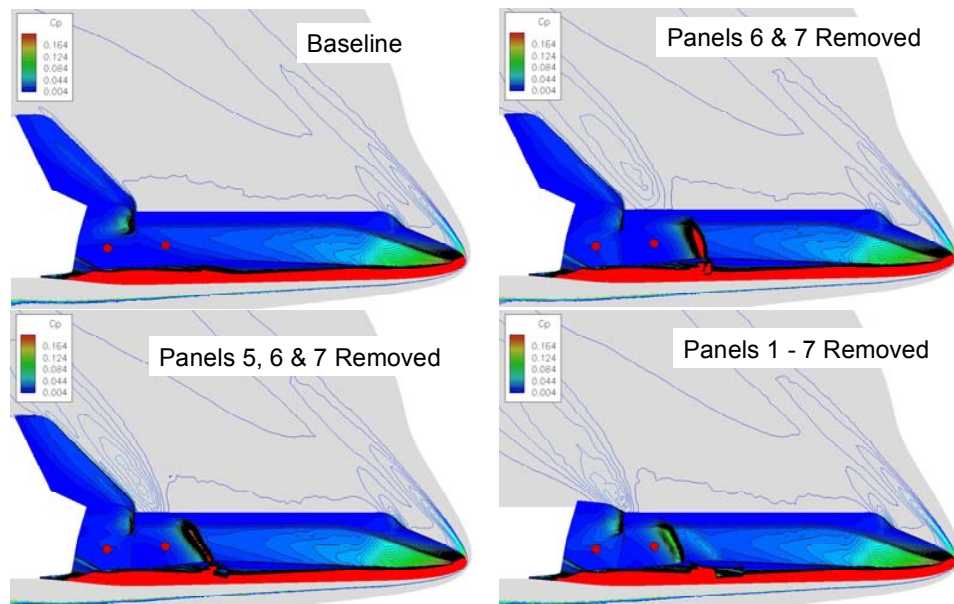
Figure 4.3-34 Missing RCC Panel Geometries, FELISA

Side Fuselage Cp for Single Panel Missing Scenarios



(a) Single RCC Panel Missing

Side Fuselage Cp for Multiple Panels Missing Scenarios



(b) Multiple RCC Panels Missing

Figure 4.3-35 Missing Panels, FELISA Cp Contours, side view

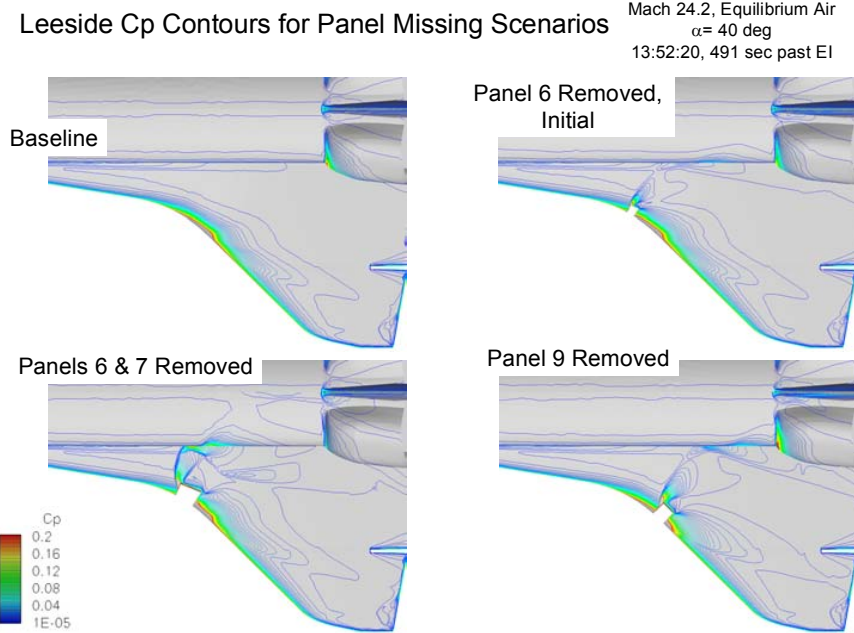
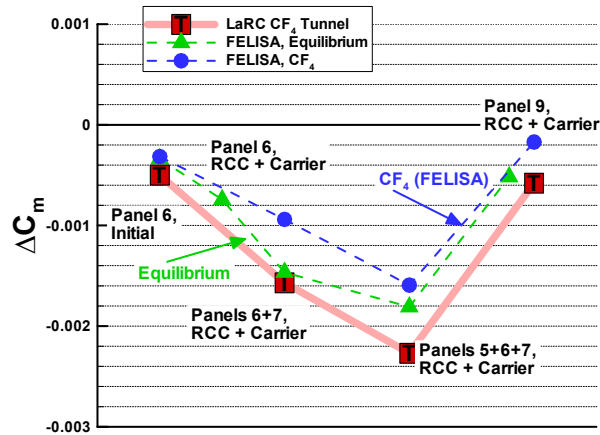
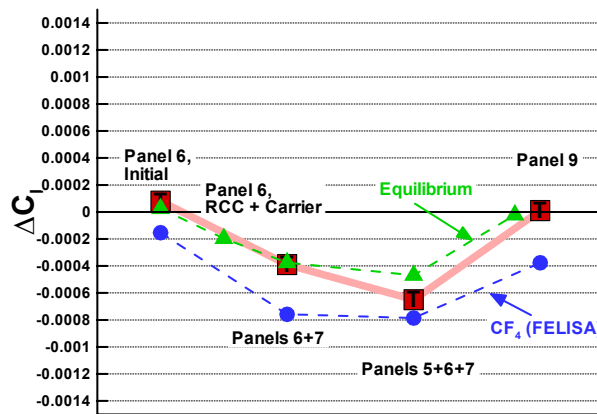


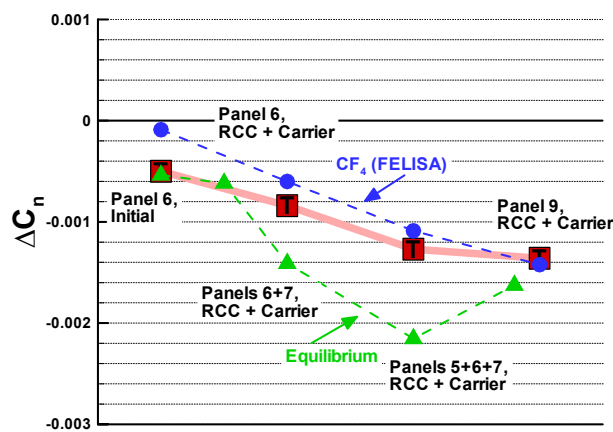
Figure 4.3-36 Missing Panels, FELISA Cp Contours, Leeside View



(a) Delta Pitching Moment

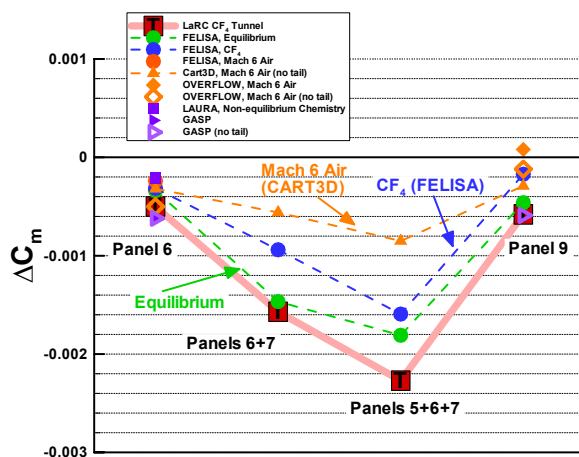


(b) Delta Rolling Moment

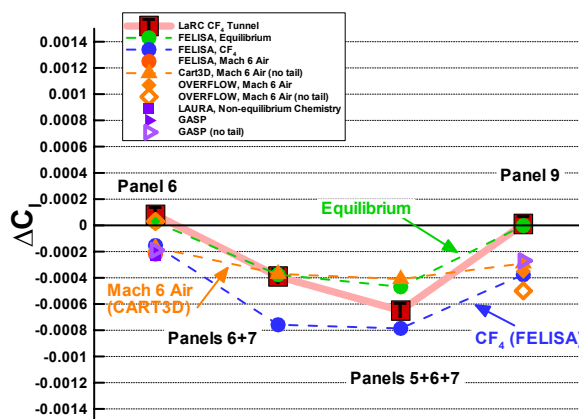


(c) Delta Yawing Moment

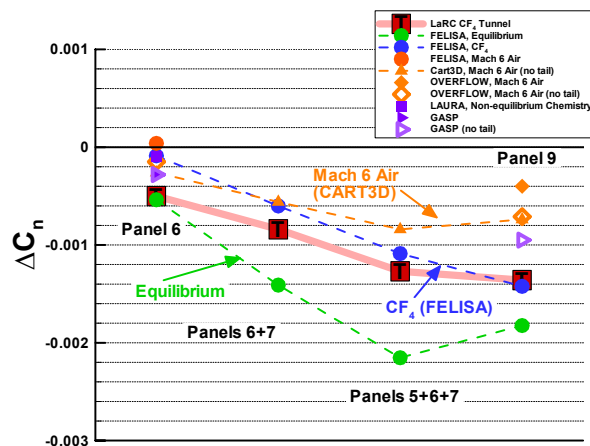
Figure 4.3-37 Missing Panel Delta Aero, FELISA and CF4 Tunnel



(a) Delta Pitching Moment



(b) Delta Rolling Moment



(c) Delta Yawing Moment

Figure 4.3-38 Missing Panel Delta Aero, All Computations and CF4 Tunnel

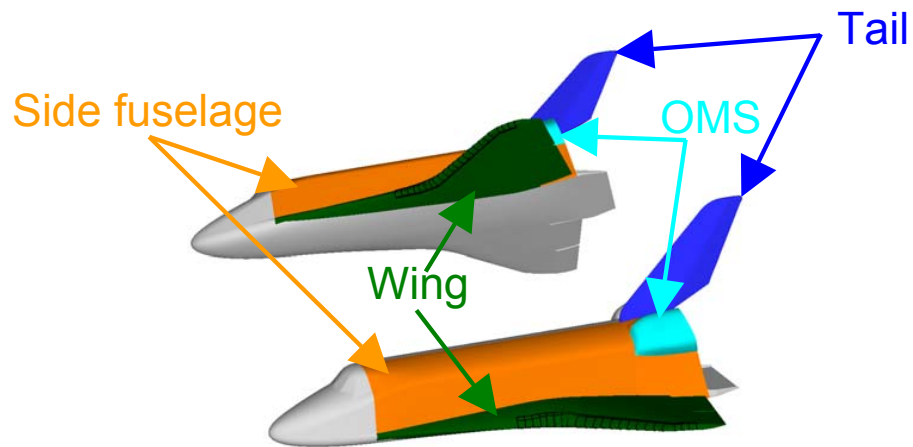
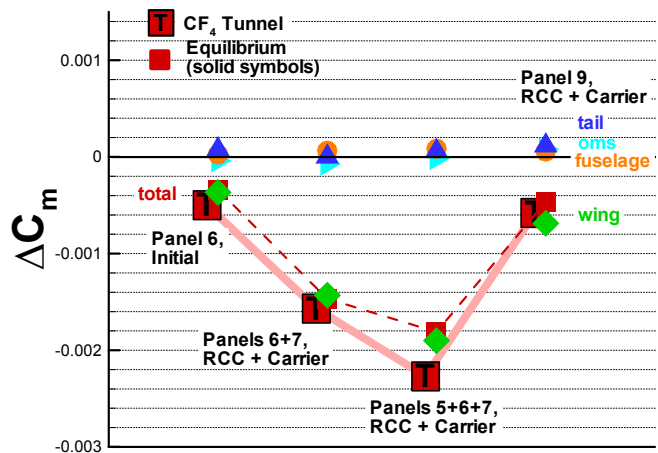
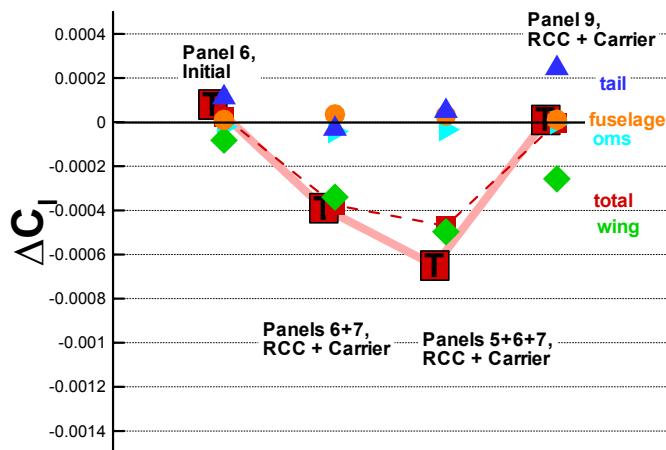


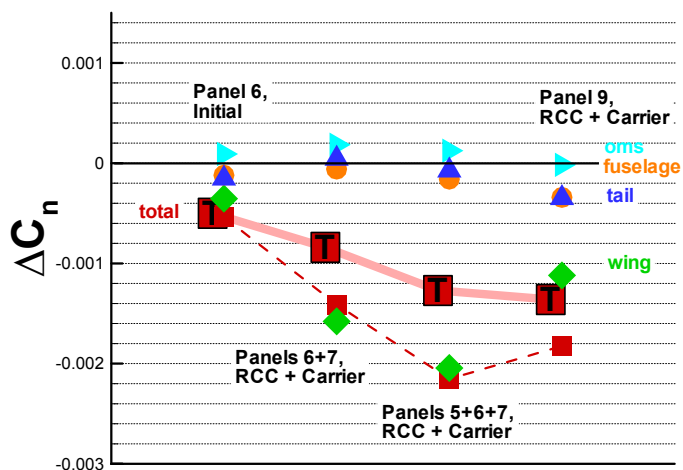
Figure 4.3-39 Orbiter Delta Aerodynamic Component Definition



(a) Delta Pitching Moment

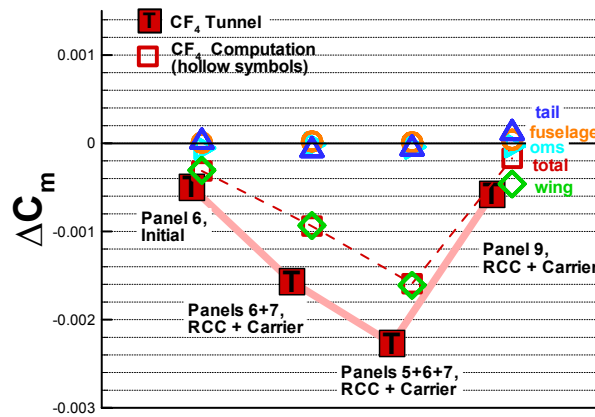


(b) Delta Rolling Moment

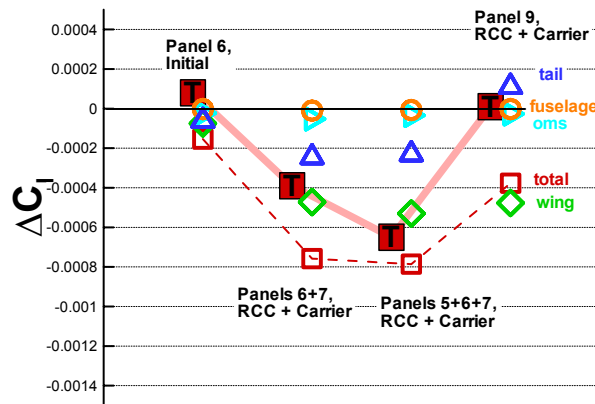


(c) Delta Yawing Moment

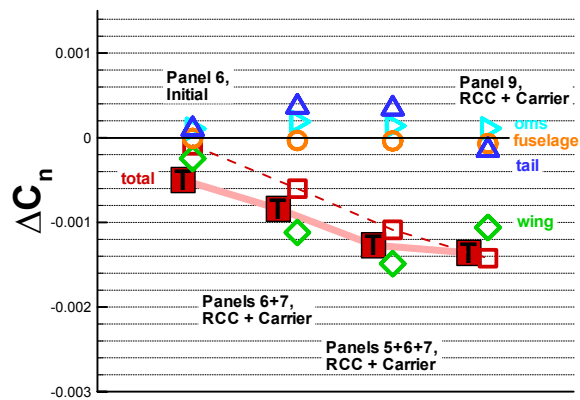
Figure 4.3-40 Missing Panel Delta Aero Component Breakdown(Flight Condition 2)



(a) Delta Pitching Moment

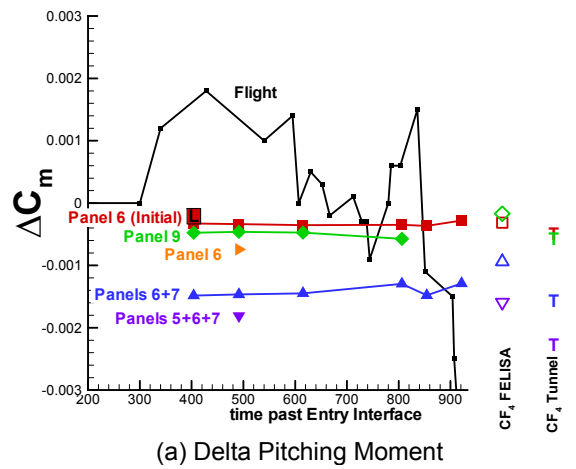


(b) Delta Rolling Moment

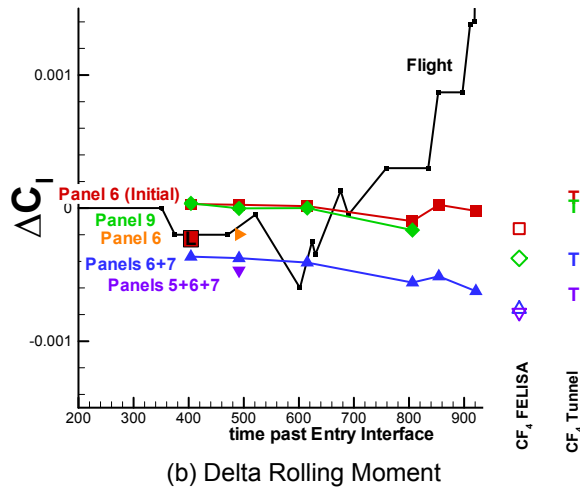


(c) Delta Yawing Moment

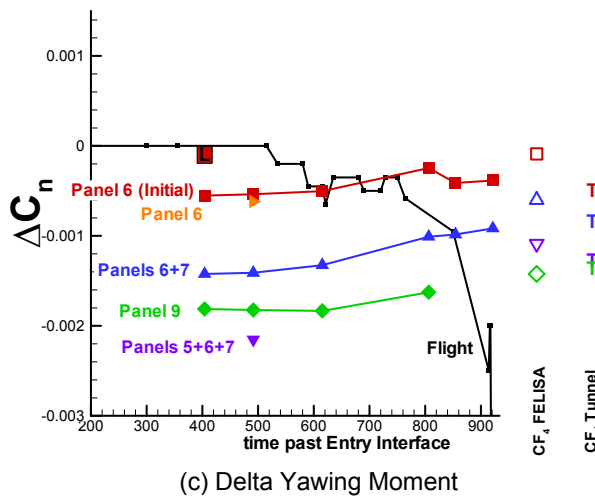
Figure 4.3-41 Missing Panel Delta Aero Component Breakdown (CF4 WT Condition)



(a) Delta Pitching Moment

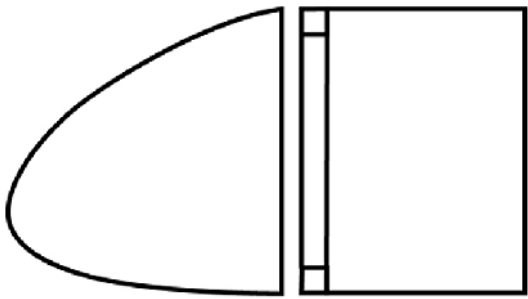


(b) Delta Rolling Moment

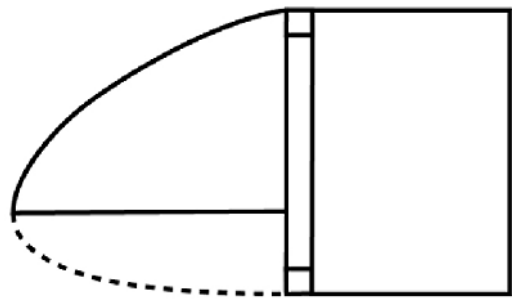


(c) Delta Yawing Moment

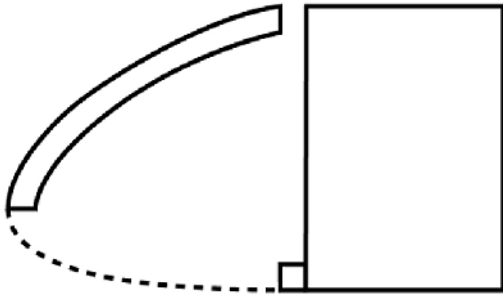
Figure 4.3-42 Missing Panel Delta Aero, Across Trajectory



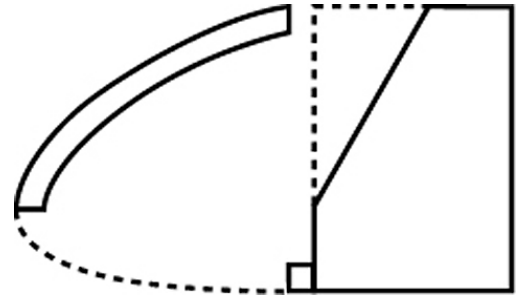
(a) Partial Panel 9 Damage, Slot



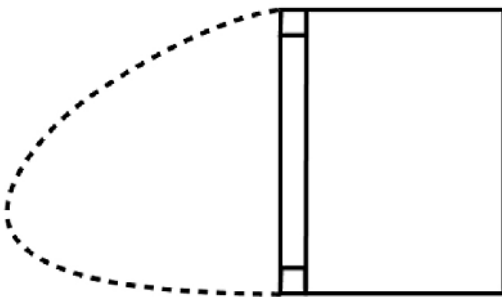
(b) Partial Panel 9 Damage, Half-Panel 9



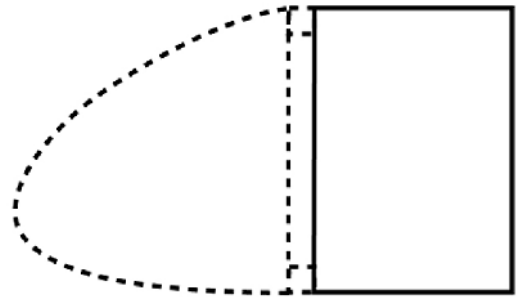
(c) Half Panel 9 with Cavity and
Upper Carrier Panel 9 Removed



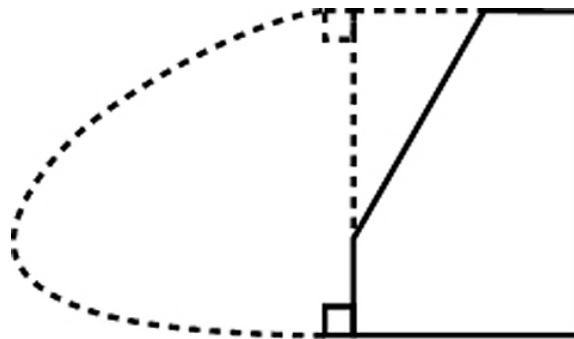
(d) Half Panel 9 with Cavity,
Upper Carrier Panel 9, and Leeward Material removed



(e) RCC 9 Removed



(f) Panel 9 Removed, RCC + Carrier Panel



(g) RCC Panel 9, Upper Carrier Panel 9, and Leeward Material Removed

Figure 4.3-43 RCC Panel 9 Progressive Damage Configurations

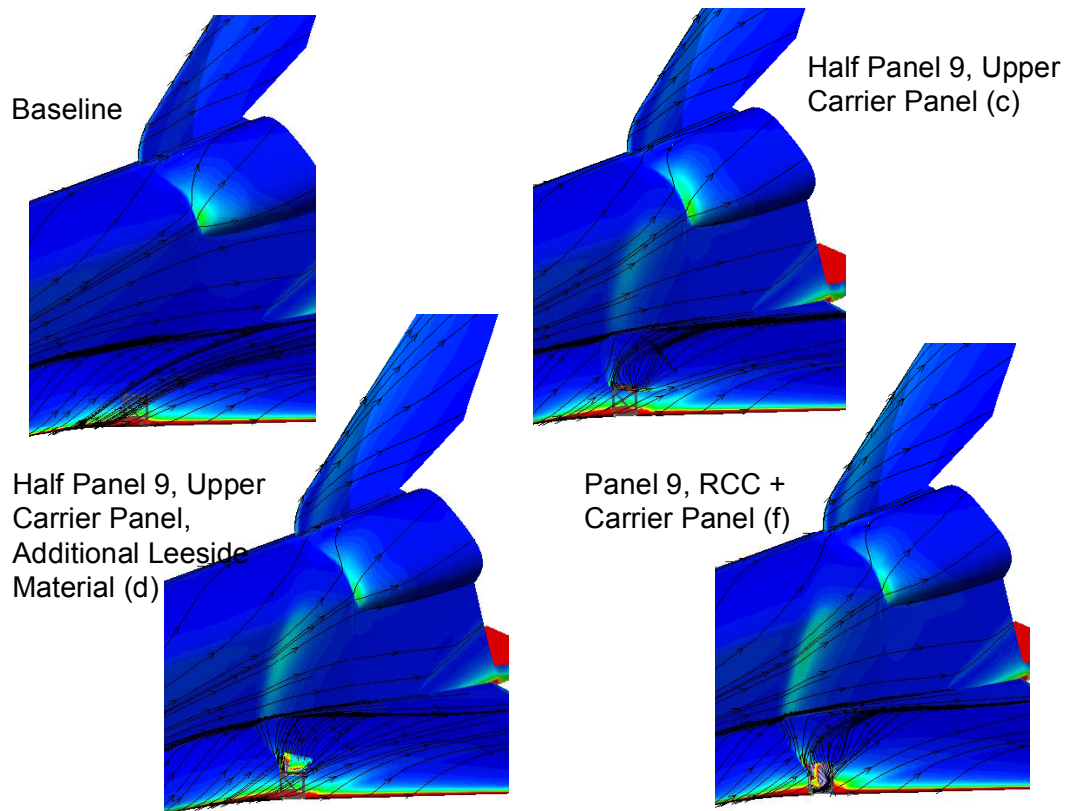
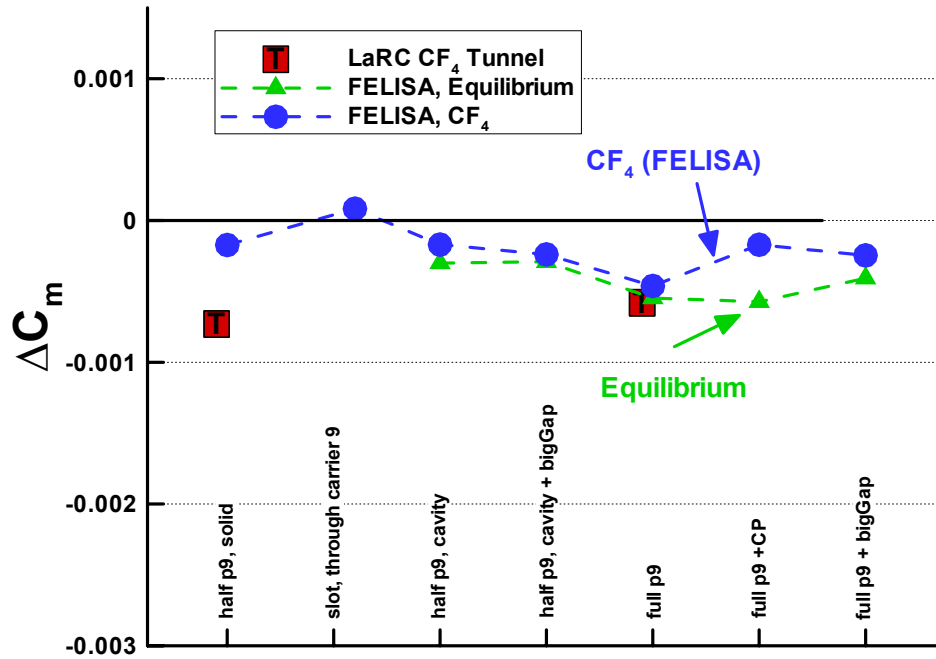
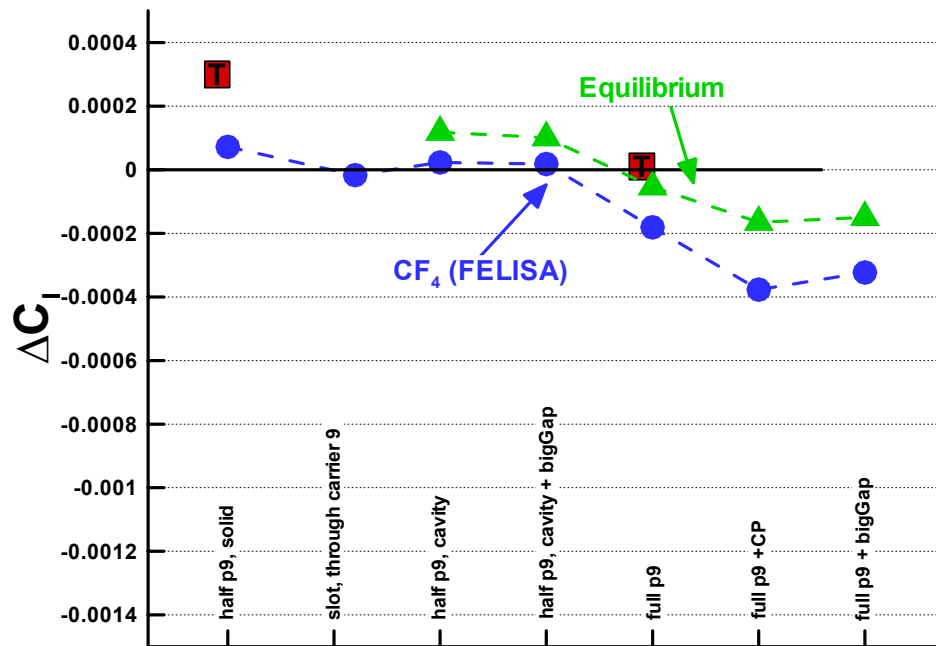


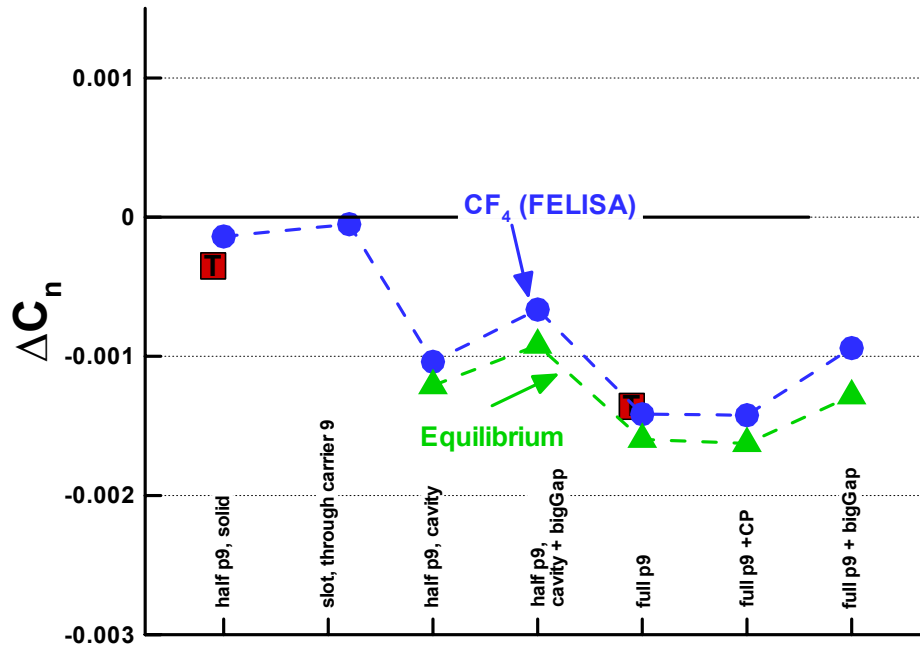
Figure 4.3-44: Leeward Flow field for Selected Panel 9 Progressive Damage Configurations



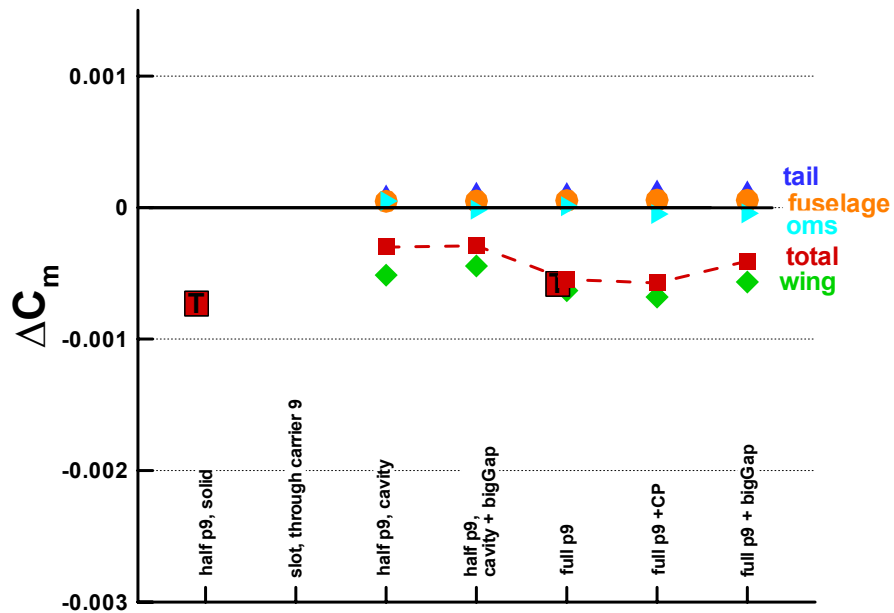
(a) Delta Pitching Moment



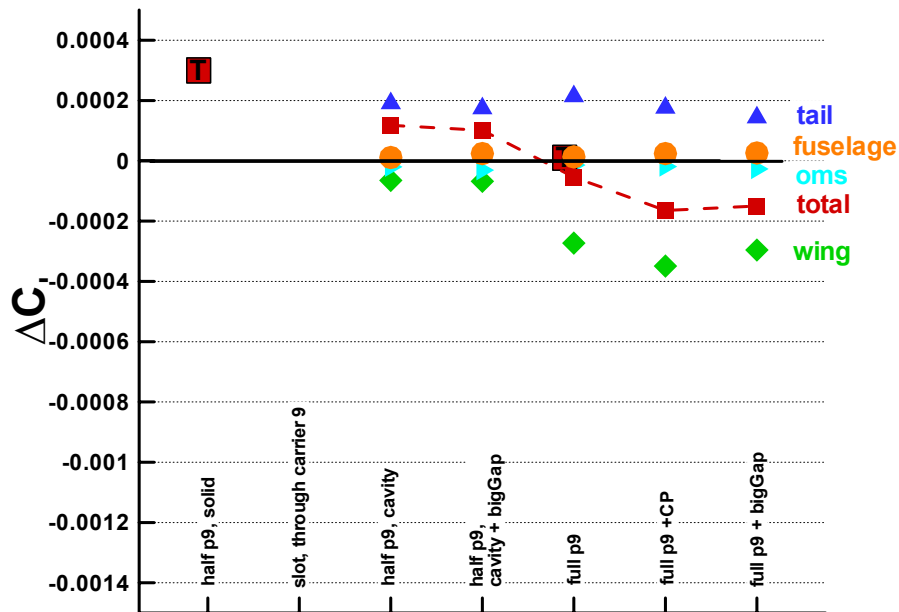
(b) Delta Rolling Moment



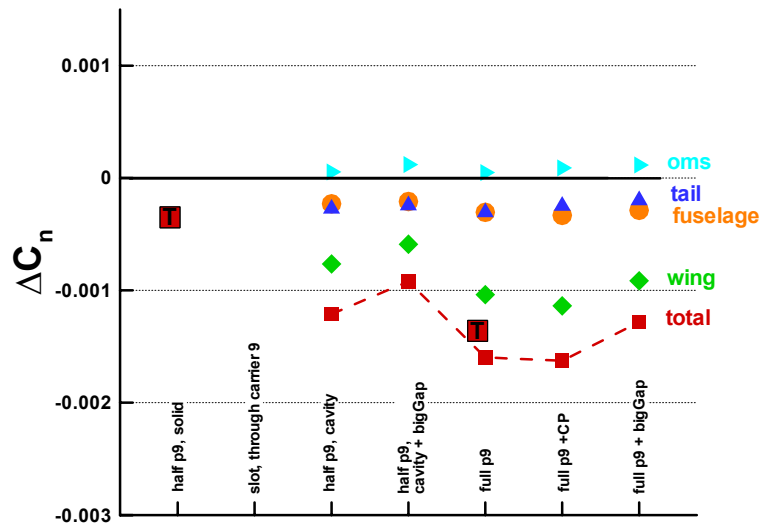
(c) Delta Yawing Moment
Figure 4.3-45 Partial Panel 9 Damage Progression, Delta Aero



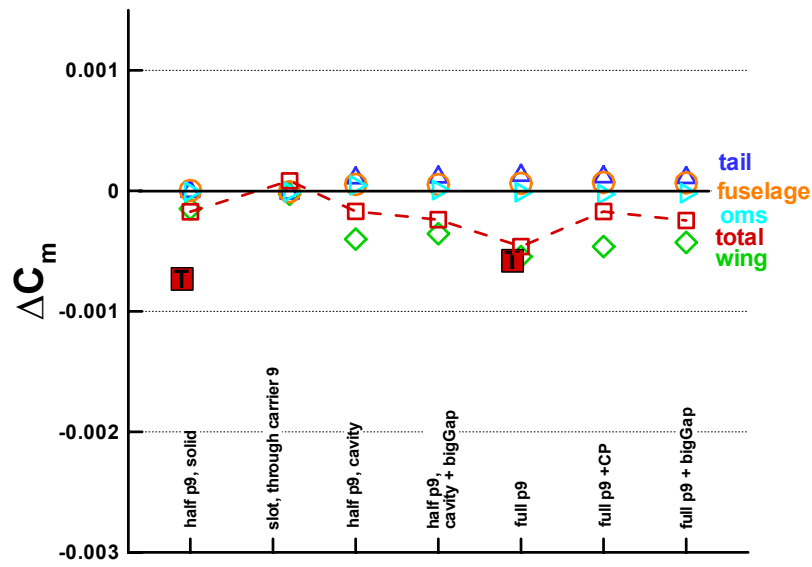
(a) Delta Pitching Moment



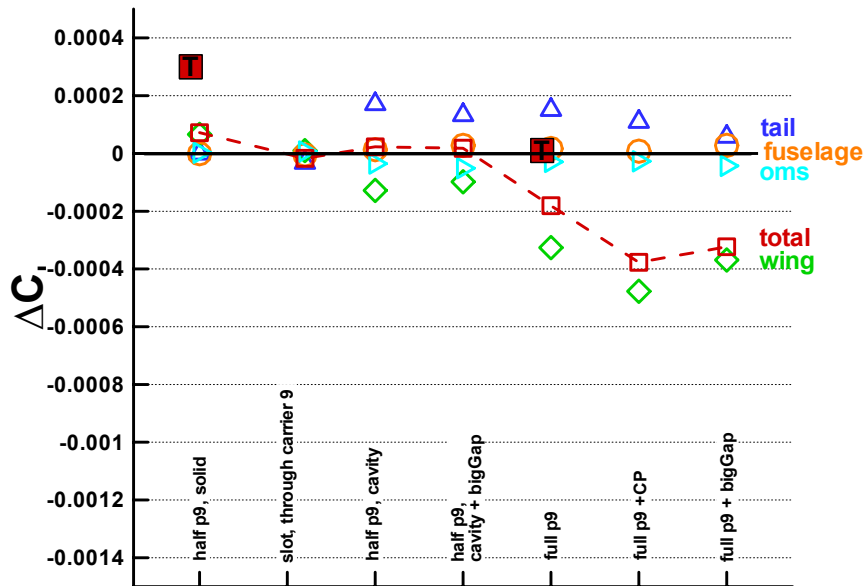
(b) Delta Rolling Moment



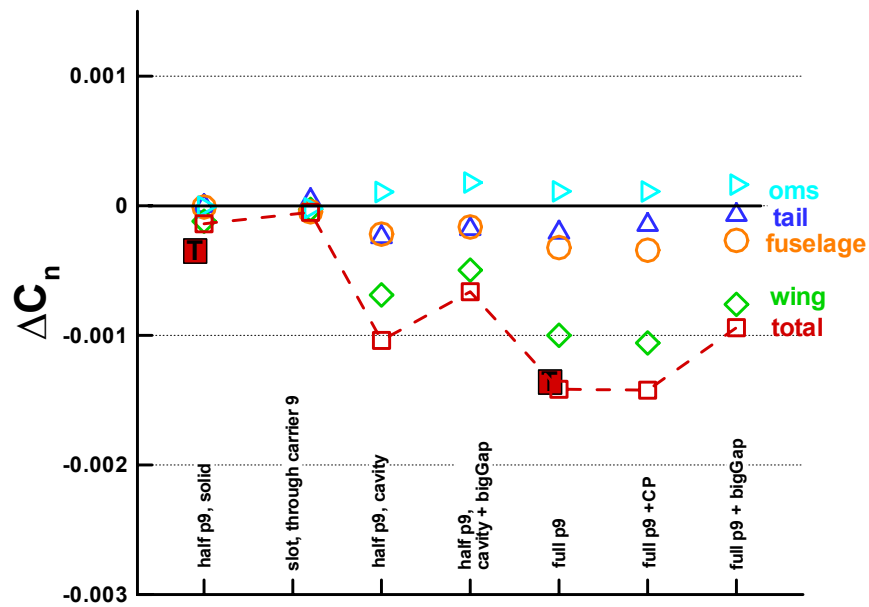
(c) Delta Yawing Moment
Figure 4.3-46 Partial Missing Panel 9 Delta Aero Component Breakdown(Flight Condition 2)



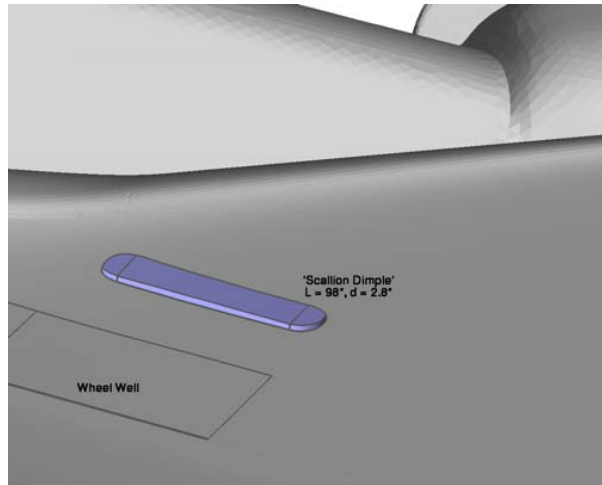
(a) Delta Pitching Moment



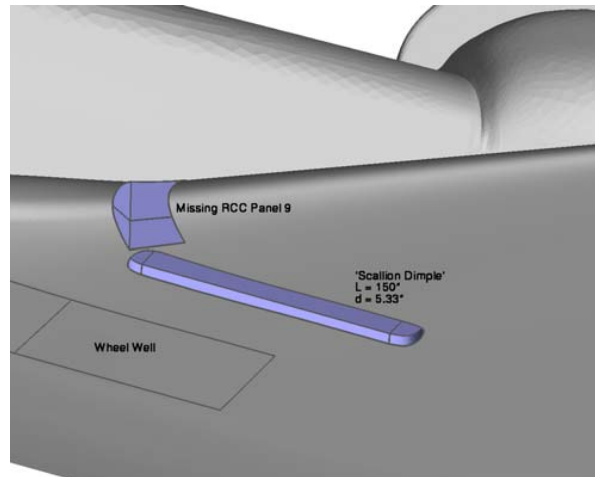
(b) Delta Rolling Moment



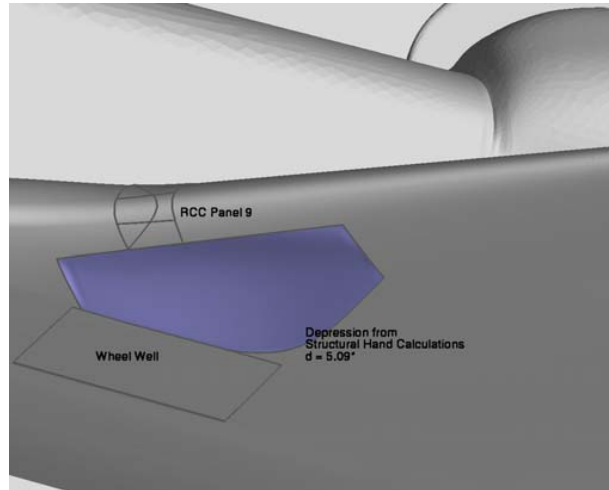
(c) Delta Yawing Moment
Figure 4.3-47 Partial Missing Panel 9 Delta Aero Component Breakdown(CF4 WT Condition)



(a) Intermediate Length Windward Surface Depression



(b) Long Windward Surface Depression with RCC Panel 9 Removed

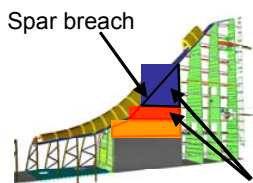


(c) Depression from Structural Calculations, $d = 5.03''$

Figure 4.3-48: Windward Surface Damage Configurations

Wing Leading Edge Deformation

- Geometry Assumptions:
 - spar compromised at panel 8-9
 - RCC will twist upwards and toward back
 - Deformation allowed in red and black regions
- Aero Effect:
 - Increased angle of attack in panel 7-10 region



Deformation
allowed

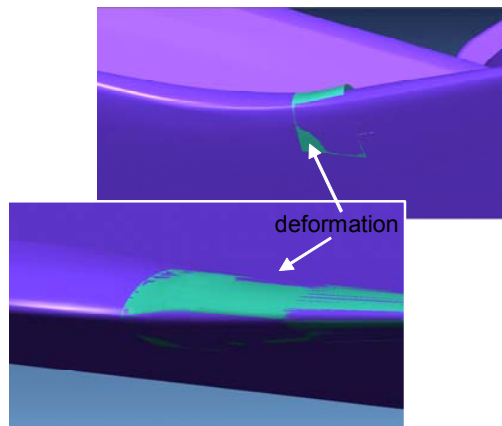


Figure 4.3-49 Geometry for Wing Leading Edge Deformation

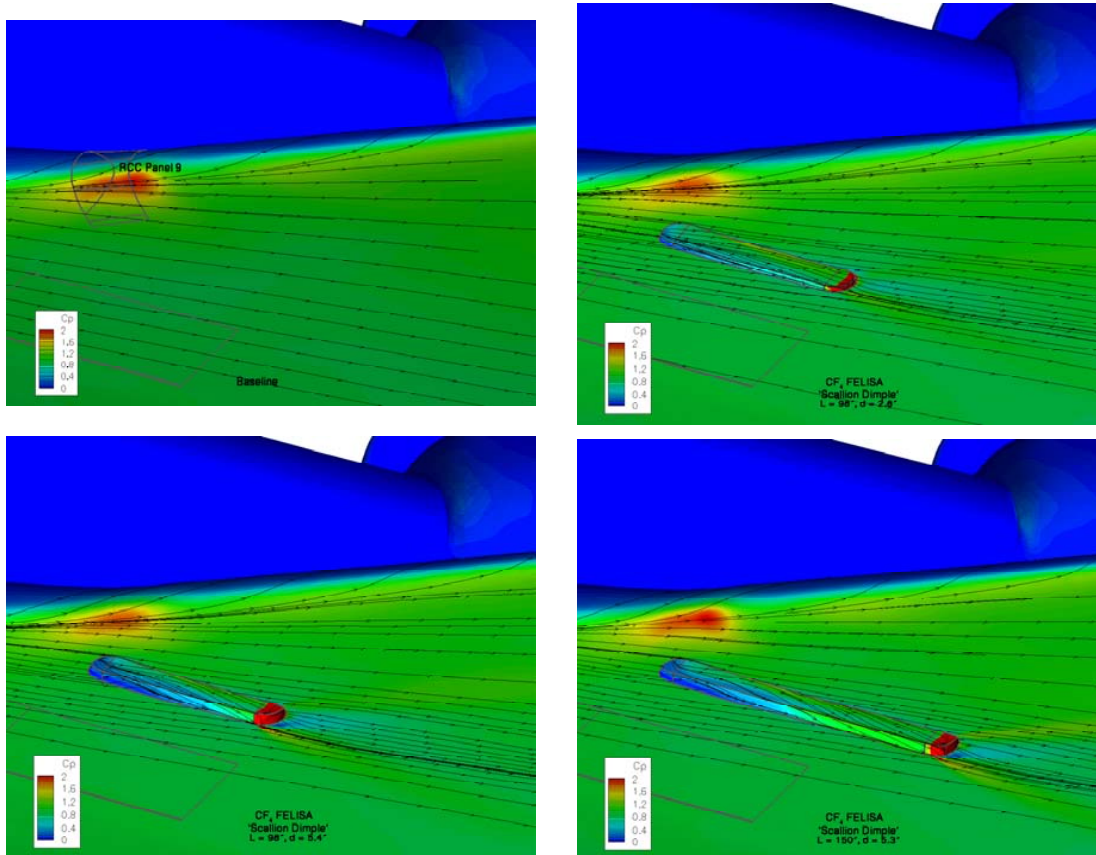


Figure 4.3-50: Pressure Contours and Streamlines - Windward Surface Depressions (CF4 WT Condition)

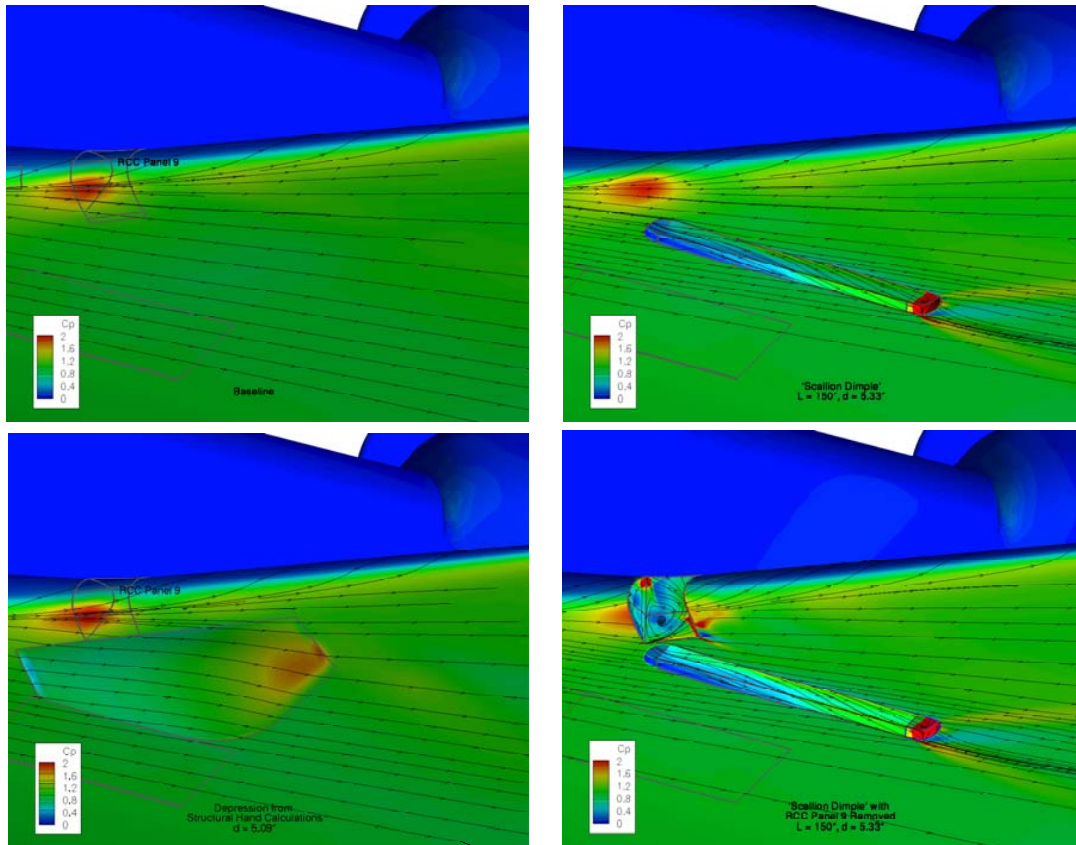
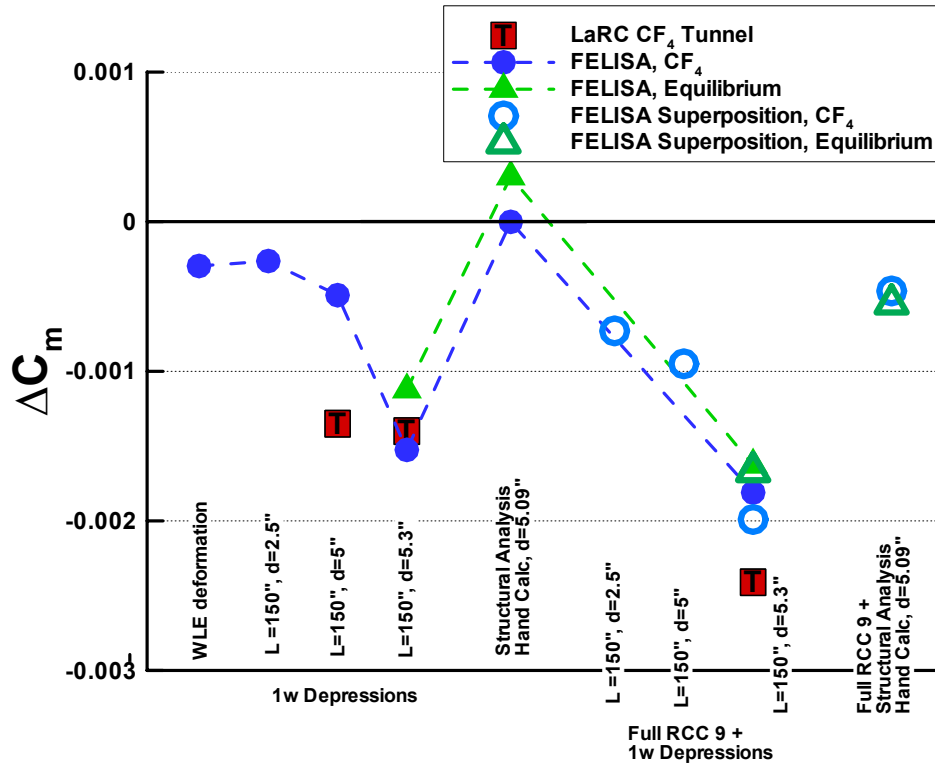
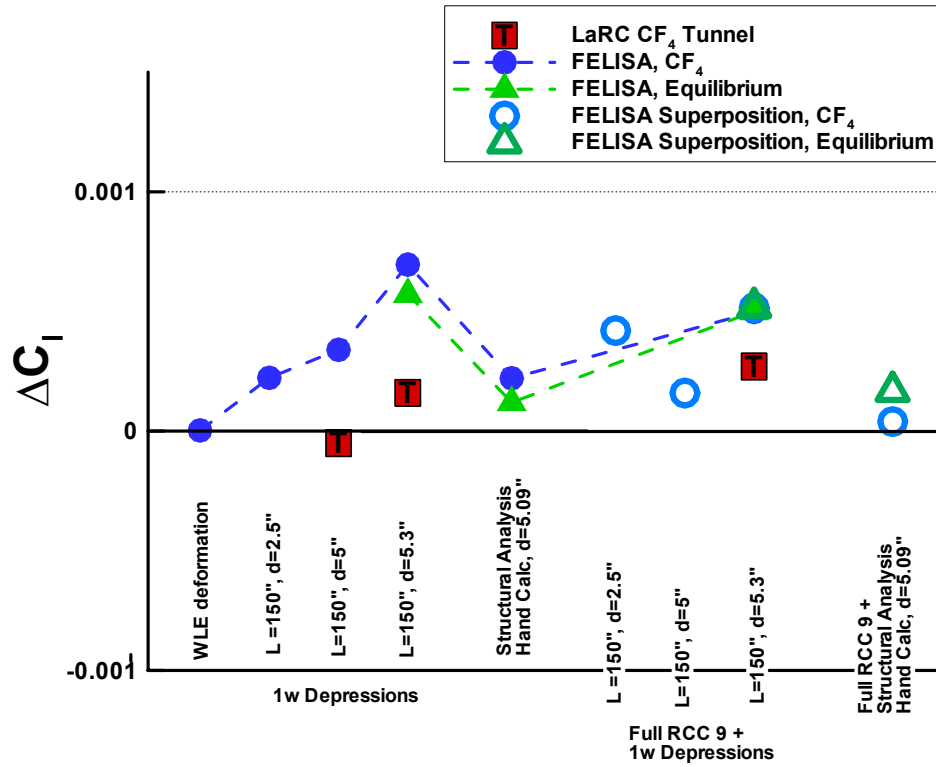


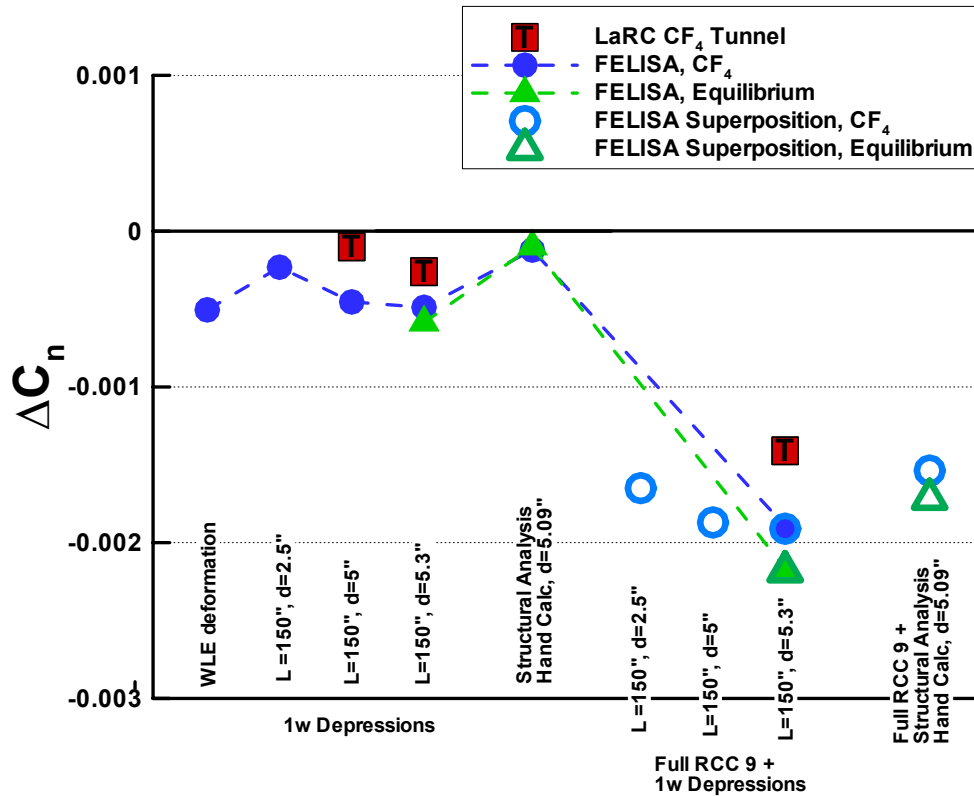
Figure 4.3-51: Pressure Contours and Streamlines - Windward Damage Configurations (Flight CFD Condition 4)



(a) Delta Pitching Moment



(b) Delta Rolling Moment



(c) Delta Yawing Moment
Figure 4.3-52 Windward Structural Damage, Delta Aerodynamic Moments

4.4 Application of Data to the Working Scenario

4.4.1 Correlation of CFD & WTT – Results by Timeline Section

The ultimate goal of the STS-107 aerodynamic reconstruction was to correlate the CFD analysis and WT test damage assessment results to the extracted flight delta aerodynamics from an initial damage stage at EI through a damage propagation that is consistent with the final working scenario. To develop a postulated damage progression the timeline was divided into four periods. Each timeline period represents a particular damaged configuration stage along the progression. The test and analysis results of a representative damaged configuration are then compared with the extracted aero increments for each timeline period. When providing a match, these comparisons lead to a postulated damage progression. Consistency with the working scenario is achieved by correlating to other available sources of data, timeline events, aerothermal, thermal, stress test and analysis results, OEX data signatures, recovered hardware forensics, etc. The resulting damage progression and data correlations are explained in this section.

4.4.1.1 Initial Timeline Section – No Observable Aerodynamic Increments

As stated in Section 4.3, off-nominal aerodynamics were not apparent during the initial portion of Columbia's STS-107 entry flight profile. This initial timeline period starts at EI (GMT 13:44:09) and extends to EI + 515 sec (GMT 13:52:44) corresponding to flight conditions which range from Mach 28 down to 24.4, with dynamic pressure increasing from 0 to 25 psf while descending through altitudes from 400,000 to 235,000 ft. The official timeline (and working scenario) identifies several major events during this period of flight (see Figure 4.4-20).

The initial portion of this time frame EI to EI + 330 sec / GMT 13:44:09 -13:49:39 suggests a breach or hole in a WLE RCC panel (5-9) existing at EI. This conclusion is supported by instrumentation near RCC Panel 9 responding to an apparent WLE internal flow thermal event. No identifiable aerodynamic increments are observed during this time frame. This is followed by a period from EI + 330 to 460 sec / GMT 13:49:39 -13:51:49 in which the initial indication of a leeside flow disturbance becomes apparent. This leeside disturbance is identified via left hand side OMS pod and fuselage surface temperature measurements indicating substantially reduced heating levels (below those seen on previous Columbia flights). Again no identifiable aerodynamic increments are observed in this time frame. Based on analysis and internal wing measurements the wing leading edge spar is breached sometime in the period covering EI + 460 to 515 sec / GMT 13:51:49 -13:52:44. This corresponds to the timeframe where all measurements along WLE Spar along with numerous others within left wing fail. Still, no identifiable aerodynamic increment is observed.

It is apparent from the data that during this initial (515 sec) atmospheric flight period the orbiters left wing is damaged to the extent that internal and external thermal events are occurring, without any clear indication of off-nominal aerodynamics. Several results from the investigation's test and analysis of probable initial damage support this observation.

An analysis, to define internal heating to the WLE spar, was completed for a circular hole in RCC panel 6 using the LaRC Navier-Stokes LAURA code. Hole sizes of 2, 4 and 6 inch diameter were analyzed at STS-107 flight condition 1 (Mach 24.7, AOA =40.2, h=243,000 ft). As shown in Figure 4.4-1, there is little if any change (even locally) to the computed external surface temperature distribution. As expected the aerodynamic normal and axial force increments extracted for this case are negligible (less than 0.3% of the total). In the wind tunnel this level of damage and its potential disruption of the flow field was evaluated by placing boundary layer trips along the wing leading edge. In Figure 4.4-2, the measured surface heating distribution shows that a relatively small area of the lower wing surface is affected for a single trip located at RCC panel 6. It should be noted that on STS-107 starting around EI + 370 sec, an external surface thermocouple, (V07T9666A) downstream of RCC panel 9 indicates a small increase in heating, similar to what this type of lower

surface heating augmentation could produce (see Aerothermodynamics Section 5.2.1.2). However, the associated aerodynamic moment increments measured for this test run are very small (essentially zero) and are listed in Table 4.4-1.

The reduced levels of heating on the fuselage and OMS Pod require some interaction of the higher energy windward flow with the relatively low energy leeside flow. While this interaction produces the change in heating during this time period, there is no associated change in aerodynamics. The source of the reduced heating has been attributed to flow exiting the WLE cavity through design vent locations along the wing upper surface at the RCC / carrier panel interface (see Aerothermodynamics Section 5.2.3.5). Several wind tunnel runs with either a single or multiple holes through (windward to leeward) the wing at these venting locations were conducted early in the investigation to identify any potential aerodynamic effects. In Figure 4.4-3, the measured surface heating distribution shows a fairly widespread disturbance over the lower wing surface due to the presence of these holes. However, the associated aerodynamic moment increments measured in these runs are also very small (essentially zero) and are listed in Table 4.4-1. (Note subsequent testing to better characterize the venting as the source of the reduced heating has been successful – however these dedicated aerothermal tests did not include simultaneous aerodynamic force and moment measurements – see Aerothermodynamics Section 5.2.3.4.). Given the suspected initial breach in the lower surface of an RCC panel, progression to a missing partial panel damaged configuration is plausible. Wind tunnel testing (section 4.3.1.6.3) and CFD analysis (section 4.3.2.3.3) results indicate little or no aerodynamic increments for this type of damage. Additionally the observed orbiter data (loss of measurements) suggests the onset of internal wing damage occurring during this time period. This is consistent with growing upper surface damage and increased venting or flow through an upper carrier panel, via the WLE breach yielding the observed aerothermodynamic response but still producing little or no aerodynamic change.

4.4.1.2 Timeline Section Two – Initial Onset of Aerodynamic Increments

The first clear indication of off-nominal aerodynamics has been identified at EI + 515 sec (GMT 13:52:44). This second timeline period extends from that point to EI + 602 sec (GMT 13:54:11) and corresponds to flight conditions ranging from Mach 24.4 down to 23.2, with dynamic pressure continuing to increase from 25 to 37 psf as Columbia descended from an altitude of 235,000 to 229,000 ft. The official timeline identifies several major events during this period of flight (see Figure 4.4-21) including a significant change in the leeside flow disturbance. The fuselage and OMS Pod measurements that were indicating reduced heating levels begin registering increased heating levels (above those seen on previous Columbia flights). Nearly all (99%) of the left wing instrumentation in the 4 major wire bundles which run along the MLG wheel well have failed by the end of this period. Additionally, the first four instances (captured by ground observers) of debris leaving the orbiter are recorded. During this time period the delta yawing and rolling moment increments show a slow steady negative growth trend. By EI + 602 sec, the off nominal delta yawing moment has increased to -0.00045 with delta rolling moment increasing to -0.0006.

Based on the WT test and CFD analysis results, WLE RCC panel damage provides the best match to the aerodynamic and aerothermodynamic events observed during this time period. Extensive test and analysis of missing full WLE RCC panels was conducted to provide a comprehensive evaluation of this particular damage scenario. As mentioned, a follow on partial missing WLE RCC panel test and analysis was conducted in order to maintain consistency with the latest recovered hardware forensics, which included significant portions of every left wing RCC panel except for panel 9. (The details are covered in Section 4.3.1.6 – WT test and Section 4.3.2.3 – CFD analysis).

In testing and analysis the clearest way to affect the leeside flow field was to provide a path for the higher energy windward flow to pass through the wing. A missing RCC panel produces this flow path. Additionally, depending on panel location, it produced augmented heating to the side of the fuselage and OMS pod, consistent with the onboard measurements. In Figure 4.4-4 WT test aerodynamic heating measurements and

Figure 4.4-5 CFD analysis surface pressures the side fuselage effects due to the flow field interaction are clearly indicated. The aerodynamics for missing RCC panels are summarized in Figure 4.4-6 and presented along with the flight extracted aerodynamic increments for rolling and yawing moment. The shaded area represents the range of CF4 wind tunnel test data for all of the single panel testing. Several specific WT test and CFD analysis points are also included. The data shows that a missing RCC panel will produce the negative roll and yaw increments consistent with this time period (Yawing moment test data being slightly larger in magnitude than the flight data, rolling moment slightly lower). At the EI + 602 sec time point the data for a missing RCC Panel 9 is possibly the best match to the aerodynamic increments (as well as the side fuselage/OMS Pod heating augmentation pattern, see Aerothermodynamics Figure 5.2.3-16).

The recovered debris is more consistent with a partial WLE damage scenario. As mentioned previously, the WT test and CFD analysis of these configurations produced little if any rolling moment increment (actually positive for partial panels 8 & 9, see Figure 4.3-13) and a reduced (relative to a full panel) yawing moment increment (see Figure 4.3-14). Given that WLE damage most likely started as a breach in the lower half of the RCC, an expected progression would be growth to a partial panel type damage configuration. However, the side fuselage impingement is not evident from WT test results of missing partial RCC panels 6 through 9, see Figure 4.3-16. All test and analysis results show that to produce the augmented heating on the fuselage, flow through the wing (or WLE) is required. Combining a missing half panel 9 with a missing upper carrier panel did produce OMS Pod and possibly side fuselage heating augmentation without any significant aerodynamic increments. Based on these results, a partial panel damage configuration is more consistent with the initial timeline period (EI to EI + 515 sec where no clear indication of aerodynamic increments is consistent with the partial panel missing data) than with this second time period.

Another suggested damage progression involved multiple missing RCC panels. Test and analysis were conducted for this damage scenario in an attempt to match the flight extracted aerodynamics time history. Results, shown for yawing moment in Figure 4.4-7 and rolling moment in Figure 4.4-8, cover single then multiple missing panel combinations ranging over RCC panels 5 through 9. For rolling moment the continuing loss of WLE panels produces the maximum negative rolling moment observed at EI + 602 sec, while the yawing moment grows well beyond the levels observed during this time period. While this yawing moment trend is consistent with the time history beyond EI + 602 sec, the rolling moment trend is not. This implies that the damage progression must have involved something other than a continuing loss of RCC panels.

4.4.1.3 Timeline Section Three – Rolling Moment Increment Trend Reversal

At EI + 602 sec (GMT 13:54:11) the delta rolling moment trend abruptly reverses sign from increasing negative to a gradual increasing positive trend which continues for nearly all of the remainder of flight. The third timeline period focuses on this distinct event and extends to EI + 710 sec (GMT 13:55:59). Flight conditions range from Mach 23.2 to 21.7, dynamic pressure from 37 to 47 psf over altitudes from 229,000 to 222,000 ft. The official timeline identifies continuing major events during this period of flight (see Figure 4.4-21). Several of these occur within approximately 10 seconds of the abrupt rolling moment trend reversal. These include observed Debris event 5 (@ EI + 602 sec), as well as the start of the slow aileron trim change, mid-fuselage bondline off-nominal temperature trends indicating increased sidewall heating levels and off scale low temperatures in the left hand elevon hydraulic system (all @ EI + 611 sec). These are followed by several observed flash events, Debris event 6 considered particularly large as well as Debris events 7 through 13 through the end of this period. During this timeline period while the delta rolling moment is gradually increasing in a positive trend, the delta yawing moment remains relatively constant. At the EI + 710 sec point, the delta rolling moment has become positive at +0.0001 and the delta yawing moment is essentially unchanged at -0.005.

The combination of a negative yawing and rolling moment increment prior to EI + 602 sec has been attributed to the increased drag and decreased lift on the left wing produced by wing leading edge

damage. The abrupt change in rolling moment trend requires an increasing wing lift condition and/or a side force increment developing on the leeside (above the c.g.). Numerous potential contributing sources were evaluated in order to develop the most probable explanation for this significant event.

The onset of ABLT was first considered as a possible explanation for the observed trend. While no orbiter entry has previously experienced boundary layer transition prior to Mach 19, given the suggested extent of damage to the wing leading edge, the possibility of an early ABLT seemed plausible. While the change in rolling moment trend is consistent with a left wing ABLT, the fact that the delta yawing moment remains constant is not. To illustrate this, Figure 4.4-9, shows the flight extracted delta rolling and yawing moment with wind tunnel predicted ABLT increments applied at EI + 602 sec. The increments were established from a wind tunnel run forcing full ABLT over the left hand side of the orbiter (full ABLT as shown in Figure 4.3-2 through Figure 4.3-4). These results clearly illustrates that early ABLT is not consistent with the yawing moment and therefore cannot be the source of the delta rolling moment trend reversal.

Another plausible explanation considered involved the potential for disturbed flow over the inboard elevon surface thereby altering the control surface effectiveness yielding the change in the rolling moment increment trend. This theory was bolstered by the recovered left hand inboard (LHIB) elevon actuator (debris item 7327) which incurred significant damage including a casing burn through suggesting the possibility of high energy flow through the wing and onto the actuator. However, the wing box primary vent is through the mid-fuselage and there is no design vent through the aft spar, (however there is some leakage). Also, the flipper door vents are intended to vent the elevon cove area only and not the wing. Therefore, no clear design flow path exists. Also the inboard elevon hinge moment data, Figure 4.4-10, shows no indication of off-nominal behavior during this time period and particularly nothing is evident at EI + 602 sec. Additionally, LHIB Elevon temperature sensors remained operational with nominal data throughout the time period. Based on the data available and these observations, there is no indication of flow exiting from aft spar and disturbing elevon flow field during this time period so as to contribute to the change in the rolling moment increment trend

From the point of wing leading edge spar breach (approx. EI + 460 sec) the internal wing cavity was ingesting the high energy air and being pressurized. In this time period, based on the MLG measurements, it is suspected that the outboard wall of the wheel well cavity is breached and allowing this cavity to pressurize. Recovered left hand MLG door and adjacent structure and TPS indicate patterns suggesting potential outflow from the wheel well at some point during the flight. It was postulated that this jet flow exiting the MLG door area could interact with the external flow field and produce the observed rolling moment increment trends.

A baseline solution for CFD Point 1 (Table 4.3-4 - Mach 24.7, AOA =40.2, h=243,000 ft) in the STS-107 accident investigation was modified to include effects of a scarfed, conical nozzle directed toward the centerline of the vehicle from the forward, inboard corner of the landing gear door. The intent of the simulation was to approximately model effects of a relatively large internal wing pressure, fueled by combusting aluminum, which deforms the corner of the landing gear door and directs a jet across the windward surface. This simulation did not include details of aluminum combustion but does consider extremes of internal conditions ($p_{\text{internal}} = 2 \rho_{\infty} V_{\infty}^2$ and $T_{\text{internal}} = 4000 \text{ K}$) that are expected to provide an upper limit on this potential effect. *(An associated analysis of flow through a breach in the leading edge of Panel 6 into a vented cavity indicates internal pressures of $(1/8) \rho_{\infty} V_{\infty}^2$ fed by an external pressure of $(1/2) \rho_{\infty} V_{\infty}^2$).* The analysis includes interaction of the shock layer flow with the jet. The scarfed nozzle has a 3-inch diameter throat and a 1.3 ft² elliptical footprint on the windward surface. Perturbations to baseline aerodynamic coefficients are expected to scale with throat area for the specified internal conditions because the interaction disturbs only a small region (roughly double the exit area) in the vicinity of the exit plane. Aerodynamic coefficient perturbations are of order 10^{-3} to 10^{-5} of right-half-body values. These values account for both interaction and any potential thrust generated by the exiting jet. The exiting jet is substantially entrained in the windward boundary layer with relatively weak perturbations to the external flow as

shown in Figure 4.4-11. These results indicate that external flow interaction with an exiting jet is an unlikely source for the delta rolling moment trend reversal.

The recovered hardware included a portion of the left hand OMS pod and several portions of the vertical tail (VT). All showed a consistent pattern of heavy damage with Aluminum deposits on the left hand side, while the right hand side remained relatively clean. This forensic evidence combined with the increased heating indications on the left hand fuselage sidewall plus the relatively large moment arm available via the VT suggest disturbed flow on the left hand side of the vehicle as an explanation for the rolling moment increment trends. Flow through wing leading edge damage and/or a hole through the upper wing surface with a resulting leeside (Fuselage, OMS, VT) flow interaction could produce the relatively small delta pressure on the VT required to reproduce delta rolling and yawing moment trends seen during this time period.

It has already been noted that flow through the WLE via a missing RCC panel produces an interaction with the leeside flow field and that this interaction increases the heating rate on both the fuselage side and the OMS pod. As part of the investigation into this leeside interaction being correlated to the aerodynamic increment pattern, other flow paths through the wing were investigated. Debris event 5 is better characterized to be more like a flash event and is closely followed by Flash event 1 and then immediately followed by Debris event 6 (see Figure 4.4-21) which is considered by evaluation as the largest debris shed by the orbiter. Together, these have been hypothesized to be the onset of an upper wing surface breach (flashes representing venting of ingested gas/burned internal wing components) and then Debris event 6 is the release of a large section of the upper wing skin. Therefore the additional flow paths through the wing investigated included flow in through lower WLE damage and out via missing upper carrier panels or missing upper surface acreage as well as holes directly through the wing from windward to leeward side.

An extensive evaluation to characterize the leeside interaction effects was undertaken through WT test, CFD analysis and hand calculations to determine the plausibility of this contribution and evaluate the various potential sources for windward surface flow to interact with the leeward side flow. It should be noted that the leeside flow field with strake vortex along with OMS pod and VT interaction is extremely complicated, even without the added complexity of interaction due to wing damage. This complexity is illustrated in Figure 4.4-12, showing the details of the flow patterns and the local interactions over this region of the orbiter at hypersonic flight conditions.

As stated, some of Columbia's recovered hardware came from the VT. Figure 4.4-13 shows recovered Columbia hardware, VT Spar, debris item No. 52092. The difference in damage to the left and right sides is evident. Additionally the left hand side pattern suggests an aft-to-fore / base-to-tip flow direction. CFD analysis was conducted to investigate the possibility of this flow pattern and the changes to this interaction as a function of wing damage. In Figure 4.4-14 the flow patterns from inviscid calculations are shown for both a baseline and a missing RCC panel 9 case. These are compared against the direction inferred from the damage pattern. The missing panel has a small effect on the flow pattern over the VT. The patterns seen on the recovered hardware are not consistent with the CFD results. These inviscid calculations and analysis for various Panel 9 damage scenarios (including holes through the wing) are detailed in section 4.3.2.3.3. This includes a breakdown of the contributions from different orbiter components (Wing, Fuselage, Tail, OMS). In Figure 4.3-39 through Figure 4.3-41 this breakdown is detailed. These results suggest that while the VT can contribute partially to the positive delta roll trend, change to the wing flow field remains the principle contributor to the aerodynamic moment increments.

Because of the complexity and concerns that an inviscid solver may not adequately capture these leeside interactions, Navier-Stokes CFD analysis was also completed for a RCC Panel 9 missing case to further assess these interactions. In Figure 4.4-15 the change in pressure on the vertical tail is shown along with the delta aerodynamic increments. This analysis of the tail flow field and the delta pressures clearly demonstrate differences in the flow field for the Panel 9 missing case. However, the delta pressure change is very small, likewise the delta aero increment from the vertical tail is very small. For this case an order of magnitude less than the increments from the wing (see

Table 4.7-6). The details of this analysis are reported in the Aerodynamics Appendices, Section 4.7.4.

As a final check to ensure that the nature of this highly separated flow field was not being misinterpreted, several wind tunnel test runs were made with and without the VT. The details of these test runs are covered in 4.3.1.6.5 with the actual test data listed in Figure 4.3-19. The aerodynamic increments with and without the vertical tail are very close in value, supporting the conclusion that the vertical tail was not the major contributor to the delta aerodynamic increments for a missing panel 9 configuration.

One other point to put forth concerns consistency with the flight data extraction. If interaction with the vertical tail was the primary contributor to the change in delta rolling moment trends via increased pressure on the left hand side of the vertical tail, this would manifest itself in a positive (being out the right wing) side force increment. Flight data extraction of the side force increment shows a small but negative (out the left wing) side force increment (Figure 4.2-10) during this time period. This inconsistency between extracted force and moments implies the primary contributor must be a change in lift, likely produced by the wing, to yield the rolling moment increment trend.

While clear evidence of leeside flow field interaction exists for the fuselage and VT (i.e. recovered debris, temperature measurements, etc.), the reproduction of required delta pressure pattern has not materialized in either test or analysis. Leeside interaction is not the primary contributing source to the delta rolling moment trend reversal in this time period.

Lower surface damage configurations were initially centered around the MLG/wheel well area and were assessed via WT testing of the stainless steel model in the LaRC Mach 6 air facility. Various damaged configurations were evaluated including MLG and door deployed as well as three open wheel well cavities of various depths. The results of the testing produced several important observations.

The MLG and door deployed configuration produced both large positive rolling moment and large negative yawing moment increments similar to extracted aerodynamic trends seen just prior to LOS. However the configuration also produced a large positive pitching moment increment (see lines D & E in Figure 4.3-6). This wind tunnel measured pitching moment increment is not consistent with the large negative pitching moment extracted from flight just prior to LOS. Based on these results it is clear that the MLG did not deploy prematurely.

Another extension of these results was to utilize the MLG (only) down, with no door, test configuration as representative of lower wing surface damage that results in a forward facing step. Test results for this configuration produce both large -yawing and -rolling increments as shown in (Figure 4.4-16) This is not consistent with the (-yaw/+roll) flight extracted trends seen late in flight and suggest that whatever damage Columbia's left wing was enduring did not result in a lower surface forward facing step.

An open wheel well of various depths was investigated as part of this series of testing. These results provided the first indication that an open cavity on lower wing produces (+) rolling and (-) yawing moment increments, consistent with changing trend for roll moment and constant yaw moment seen after EI + 602 sec. (see Figure 4.4-16). As can be seen in the data the shallower cavity yields larger increments (both yaw and roll).

The lower surface cavity wind tunnel results combined with forensic evidence, the extracted aerodynamic flight data patterns and wing structural design/loading suggest a lower surface deformation as the damaged configuration that best reproduces the observed change in rolling and yawing moments. The gradual aerodynamic moment increment growth is consistent with leeward debris and not loss of windward surface material. A lower surface deformation or recession could yield the necessary gradual change to windward surface by slowly growing in area and/or depth. To

assess this scenario in more detail a combined aerodynamic, internal heating and structural analysis was completed.

The orbiter intermediate wing structure was not designed to carry large loads and essentially supports the lower and upper skin and the associated distributed loads. The WLE spar, the outboard wheel well wall and the 1191 spar provide the primary strength and serve to outline the intermediate wing area (Figure 4.4-17). Structural analysis was used to define possible wing deformation considering the aerodynamic loads and potential internal wing damage. Finite element model analysis provided global wing deformation. Associated stress calculations were then used to provide localized skin deformation. The hot gas entering the intermediate wing does so as a high energy plume, therefore damage to much of the internal structure is likely to have occurred. The predicted wing deformation (global and local) was heavily influenced by the hypothesized damage which included reduced structural modulus to represent missing or severe damage to the WLE spar behind one RCC panel, reduced strength of the spar caps, missing wing truss tubes, and loss of wing skin inner face sheet. For structural analysis details see Section 7.5.

Structural and surface deflections from the analysis were provided to the aerodynamics group for assessment. The global structural deformation is relatively small. Even considering the damage, the overall delta between an undamaged wing and a damaged wing yielded a deflection change of less than 0.8 inches. The wing deflection (z-component) is shown in Figure 4.4-18. Newtonian aerodynamic analysis of this deformation produced a small -yawing and +rolling moment increments.

Similarly the local surface skin deflections as generated through stress analysis were also evaluated. These provided relatively large (maximum of 5+ inches) surface deflections Figure 4.4-19. Newtonian as well as inviscid (FELISA - Section 4.3.2.3.4 and CART3D) calculations were completed on this localized damaged configuration. These calculations also produced small -yawing and +rolling moment increments. Note that the global and local wing deformations were not combined and these cases were independently assessed. While the CFD analysis yields the correct signs (-yaw/+roll) the values are relatively low.

Wind tunnel testing of lower surface recession was completed in the LaRC CF4 tunnel. Test configurations considered a range of width and length for a 5 inch deep recession behind RCC panels 8 and 9. Three lengths were considered ranging from $X_o=1146$ to 1243. Single, double and triple wide recessions were tested (single being 23 inches wide). Testing was done with and without RCC panel 9 missing. These results are summarized in Section 4.3.1.6.6 and the configurations and results are shown in Figure 4.3-20 through Figure 4.3-22. These lower surface depressions do result in a positive (right wing down) rolling moment as observed in flight, and the magnitude of the rolling moment increases as the width of the depression is increased. Furthermore, the yawing moment and pitching moment generated by the depression are similar in magnitude and in the same direction as observed for flight.

The test and analysis concentrated on this timeline period in an attempt to identify the cause of the distinct pattern in the flight extracted aerodynamics. Several possible contributors to the change in rolling moment trend were identified and include leeside flow field effects, potential (very) early ABLT and flow through the wing. However, none of these serve as the primary contributor. Of all of the plausible explanations evaluated, only a lower wing surface deformation appears consistent with the data and therefore the rolling moment delta trend change is attributed to wing deformation.

4.4.1.4 Timeline Section Four – Progressive Damage Aerodynamics

The fourth timeline period covers what is essentially the remainder of flight from EI + 710 sec through EI + 918 sec (GMT13:55:59 – 13:59:27), just prior to LOS. Flight conditions range from Mach 21.7 to 17.8, dynamic pressure from 47 to 83 psf over altitudes from 222,000 down to 200,000 ft. The official timeline identifies continuing major events during this period of flight (see Figure 4.4-22 and Figure 4.4-23). These include debris events 14-17, loss of instrumentation within the

wheel well cavity, the sharp increase aileron trim rate, loss of upper and lower wing skin (OI) temperature measurements each suggesting a continuing degradation of the left wing. However Columbia does complete a planned roll reversal around EI + 765 sec with nominal performance indicating major vehicle and wing integrity still exists.

While the exact state of Columbia's damaged left hand wing is unknown, despite the extensive internal wing damage, the hypersonic aerodynamic asymmetries remain manageable, with the orbiter windward surface still basically intact. Based on the continuing observations of debris loss, the expected continual damage to the wing internal structure, the gradual increase in +rolling moment increment and - yawing moment increment as well as the onset of a -pitching moment increment, that the lower surface wing deformation remains the most plausible explanation for the aerodynamics observed during this time period.

The results for progressive growth in the lower wing surface deformation are summarized in section 4.3.1.6.6 (wind tunnel testing) and section 4.3.2.3.4 (CFD analysis). The wind tunnel test configurations and results are shown in Figure 4.3-20 through Figure 4.3-22. The data indicates that as the lower surface depression width increases from a single to triple wide configuration, the rolling moment (+), yawing moment (-) and pitching moment (-) increments each gradually increase in magnitude as observed in flight during this time period.

CFD analysis of the single wide lower surface depressions provided similar trends as the wind tunnel for rolling, yawing and pitching moment Figure 4.3-52. When combined (by superposition) with RCC panel 9 missing the resulting rolling moment (+), yawing moment (-) and pitching moment (-) increments each reach magnitudes consistent with those observed in flight during this period. Also included in these plots are the data for the localized lower wing skin deformation as predicted by stress analysis for a substantially damaged intermediate wing structure. While the CFD analysis yields the correct signs (-yaw/+roll) the values are relatively low for this case.

Overall, the delta aerodynamics computed and measured for windward surface damage configurations correlate well with the increments observed late in flight. The data trends support the hypothesis of progressive internal structural damage that produces a gradual windward surface deformation. This gradual deformation produces the steady increase in rolling moment and yawing moment as well as the pitching moment increments seen during this late period in flight.

4.4.2 Damage Progression Theory and Supporting Aero

Based on the damage assessment and timeline period correlations covered in Section 4.4.1, the following is a postulated damage progression theory based on the results of the aerodynamic investigation. This damage progression, approached from an aerodynamic perspective, is consistent with the working scenario and attempts to maintain consistency with other data from the investigation. References are made to figures which include a combination of aerodynamic extraction results and the major timeline events noted.

An initial WLE breach (small hole or slot) in an RCC panel exists at entry interface. By EI + 300 sec thermal events are occurring internal to the WLE cavity, however no identifiable aerodynamic increments are observed. The breach continues to grow into a larger hole and between EI + 300 to 450 sec has resulted in the loss of most of a lower RCC (7,8 or 9?) panel. The partial missing RCC panel configuration produces little if any delta aerodynamic effect, nothing observable (see Figure 4.4-20). Breach of the WLE spar follows somewhere between EI + 450 to 500 sec and internal wing pressurization and heating damage begin. Still no external aerodynamic effect is observed. As the WLE damage progresses it results in the onset of high energy windward flow passing through the WLE and interacting with the leeside flow field between EI + 500 to 600 sec (see Figure 4.4-21). The OMS pod and side fuselage surface temperature measurements indicate increased heating as a result of this interaction. This is most likely the result of loss of a considerable portion of RCC Panel 9 and/or an upper carrier panel (9,10 or 11?) and produces the first clear indication of off nominal aerodynamic increments (-yaw & -roll). Both continue to slowly increase with negative growth trends

for approximately 90 seconds. By EI + 600 sec internal wing damage has become significant. The four major OI/MADS wire bundles have burned through and the MLG wheel well wall is likely breached, much of the intermediate wing structure has been significantly damaged. Soon after, breaches through the left hand wing upper surface begin to develop as marked by a series of flash events, Debris 5 (or Flash "0") at EI +602 sec and Flash 1 (EI +624 sec) indicating a forced external venting of the gas and damaged material built up in the intermediate wing. At EI + 627 sec, Debris 6 (the largest observed debris event) most likely represents a large portion of the upper wing surface departing the orbiter. This release of the internal pressure buildup relieves the offset to the external lower surface pressure and combined with the extensive internal wing damage results in the onset of a lower wing surface deformation or dimple. Initiated at the EI + 602 sec mark, this corresponds to the Debris 5 flash event, the onset of the slow aileron trim change and the change in the delta rolling moment increment trend, which abruptly changes sign and begins positive growth. Beyond EI + 630 sec (see Figure 4.4-22), the WLE damage becomes extensive, perhaps to the point of loss of lower RCC Panel 8 and most or all of RCC Panel 9. The combination of WLE damage and lower surface wing deformation produces the slow growth in the delta rolling (+) and yawing (-) moment increments. The continuing observed debris events are postulated as primarily upper surface structure and TPS, so despite the extensive wing damage, the hypersonic aerodynamic asymmetries remain manageable, with the orbiter windward surface still basically intact. As the lower surface deformation continues to grow, between EI + 700 to 850 sec, it produces gradually larger delta rolling (+) and delta yawing (-) moment increments. Even with the developing damage to the left wing, Columbia completes a planned roll reversal with nominal performance at approximately EI + 765 sec. Shortly after this maneuver, at EI + 835 sec (see Figure 4.4-23) the aileron trim rate increases sharply in response to a corresponding sharp increase in the growth of both the rolling and yawing moment increments. The initial delta pitching (-) moment increment is now also observed. As large scale wing deformation continues to grow beyond EI + 870 sec the asymmetric aerodynamics exceed design levels. Columbia manages trimmed flight for approximately another 60 sec, eventually requiring the use of all 4 RCS aft yaw jets and maximum rate of aileron to maintain trim. However, the asymmetric yaw and roll moment growth increases drastically exceeding 6 times the design levels just prior to LOS + 5 sec. Under this extreme asymmetric condition, the flight control system can no longer maintain trimmed flight. Columbia soon departs from controlled flight leading to the loss of vehicle and crew.

The damage assessment results summarized in section 4.4.1 can be mapped to this progressive damage scenario. Since the exact damaged configuration can never truly be known, a subjective placement of the measured aerodynamic increments along the timeline of the extracted increments is reasonable. In Figure 4.4-24 through Figure 4.4-26 the rolling, yawing and pitching moment increments from the LaRC CF4 wind tunnel test results of configurations in line with the damage progression outlined above are presented. The time history trends of the yawing, rolling and pitching moment increments can be matched remarkably well. Although an exact correlation of flight magnitudes and time is not achieved, since the exact damaged configuration is unknown, a plausible damage progression scenario has been developed which has the same aerodynamic trends as the extracted flight data.

As a final comment on the damaged configuration test and analysis results, it must be pointed out again that the nature of this analysis and the conclusions to be drawn from them should be limited to a proper engineering perspective. The test and analysis conducted for the aerodynamic (and aerothermodynamic) portion of the investigation were performed on representative geometries. The representative geometries that have been assessed were chosen in a very dynamic investigation environment as engineers interpreted the latest results from wind tunnel testing, CFD analysis, flight measurement evaluation, recovered hardware forensics, etc. The fact that these geometries were chosen for investigation purposes should not be misconstrued as exactly reproducing the damaged configuration encountered in flight. These representative damaged configurations, however, do provide an insight into the nature and level of damage necessary to result in the loss of Columbia and her STS-107 crew.

TABLES

CASE	Damage Location	ΔC_m	ΔC_n	ΔC_l
Boundary Layer Trip	RCC Panel 6	-0.00062	-0.00015	0.00032
Boundary Layer Trip	RCC Panel 6 (fwd)	-0.00019	-0.00004	0.00019
Holes Through Wing	4 holes (Mach 6)	0.00012	-0.00008	0.00017
Hole Through Wing	Carrier Panel 6 (CF4)	0.00040	0.00006	-0.00005
Hole Through Wing	Carrier Panel 9 (CF4)	0.00010	-0.00004	0.00000
Hole Through Wing	Carrier Panel 12 (CF4)	0.00014	-0.00003	-0.00004
Flight Extracted	EI to EI + 515 sec	0.0000	0.0000	0.0000

Table 4.4-1 Aerodynamic Increments – WT Results for BL Trips & Hole(s) Through Wing

	Full-vehicle baseline	Δ interaction (new-baseline)	Δ thrust	Δ net
axial	.0781751	$1.23 \cdot 10^{-7}$	$3.07 \cdot 10^{-7}$	$4.30 \cdot 10^{-7}$
side	0	$3.66 \cdot 10^{-5}$	$-8.12 \cdot 10^{-5}$	$-4.46 \cdot 10^{-5}$
normal	1.1322635	$-3.03 \cdot 10^{-5}$	$4.08 \cdot 10^{-5}$	$1.05 \cdot 10^{-5}$
roll	0	$-2.79 \cdot 10^{-5}$	$2.76 \cdot 10^{-5}$	$-0.03 \cdot 10^{-5}$
pitch	.0279899	$3.98 \cdot 10^{-5}$	$2.67 \cdot 10^{-6}$	$4.25 \cdot 10^{-5}$
yaw	0	$8.50 \cdot 10^{-6}$	$-5.53 \cdot 10^{-6}$	$2.97 \cdot 10^{-6}$

Table 4.4-2 Aerodynamic Increments – LAURA CFD – Jet exiting MLG door w/External Flow Interaction

FIGURES

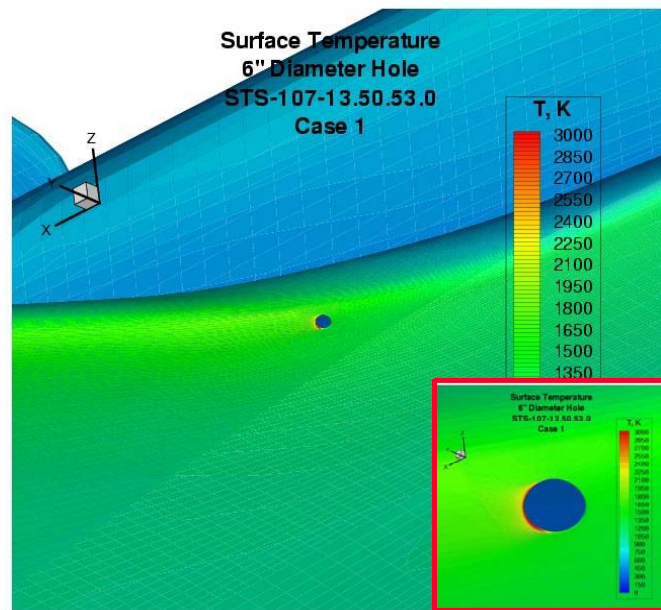


Figure 4.4-1 Surface Temperature - LAURA CFD Analysis – 6” Hole in WLE RCC Panel 6

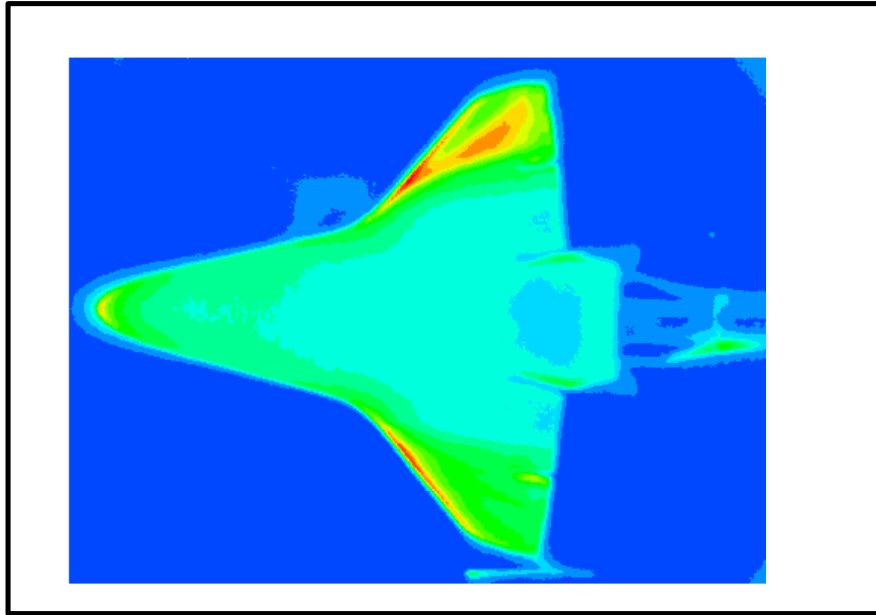


Figure 4.4-2 Infra-red Thermography Surface Heating Distribution – BL Trip at RCC Panel 6

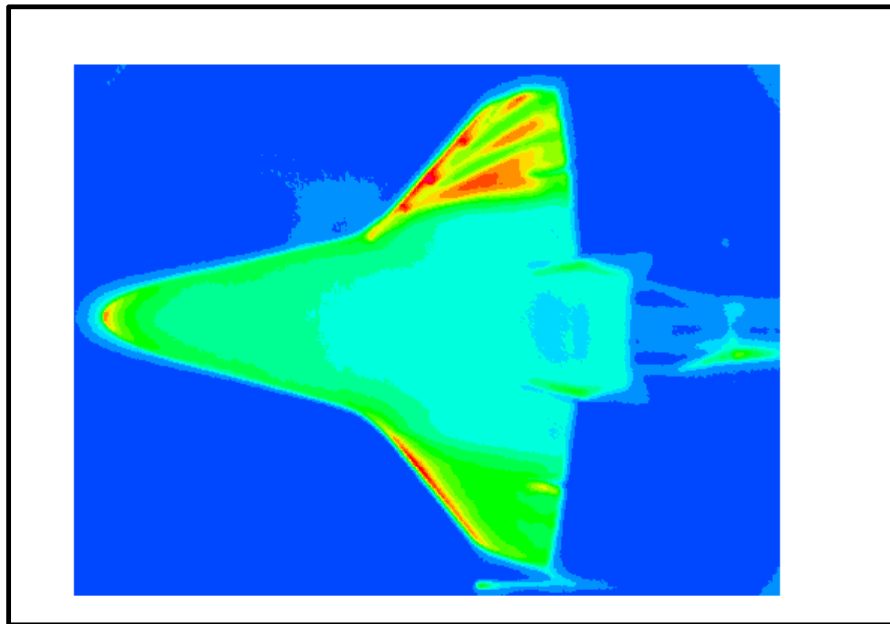


Figure 4.4-3 Infra-red Thermography Surface Heating Distribution – Holes (4) at RCC Vent Locations

Experimental **Aeroheating** -- 20-inch CF4 tunnel, $\alpha = 40^\circ$

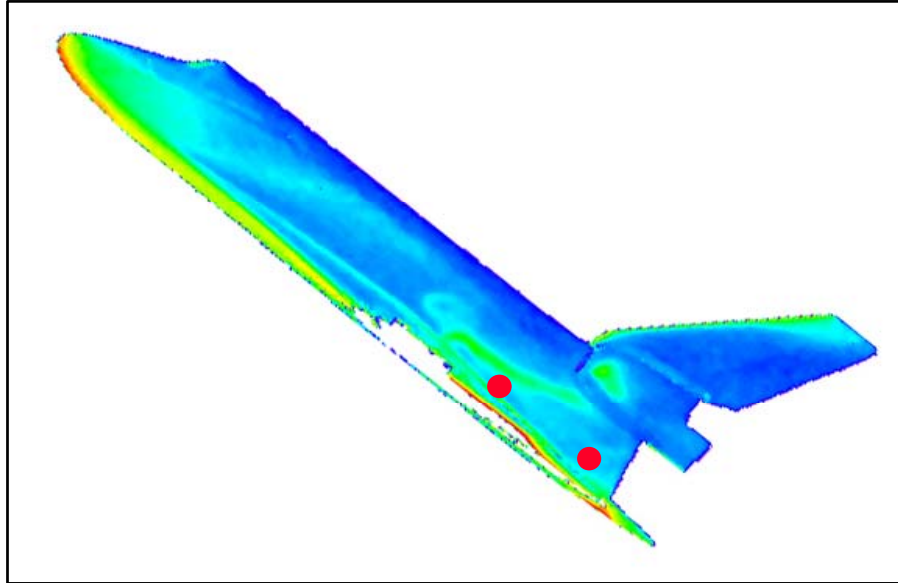


Figure 4.4-4 Phosphor Thermography WT Test Surface Heating Distribution – RCC Panel 9 Missing

FELISA Prediction of **Surface Pressure**

M = 24.2, Equilibrium air, $\alpha = 40^\circ$

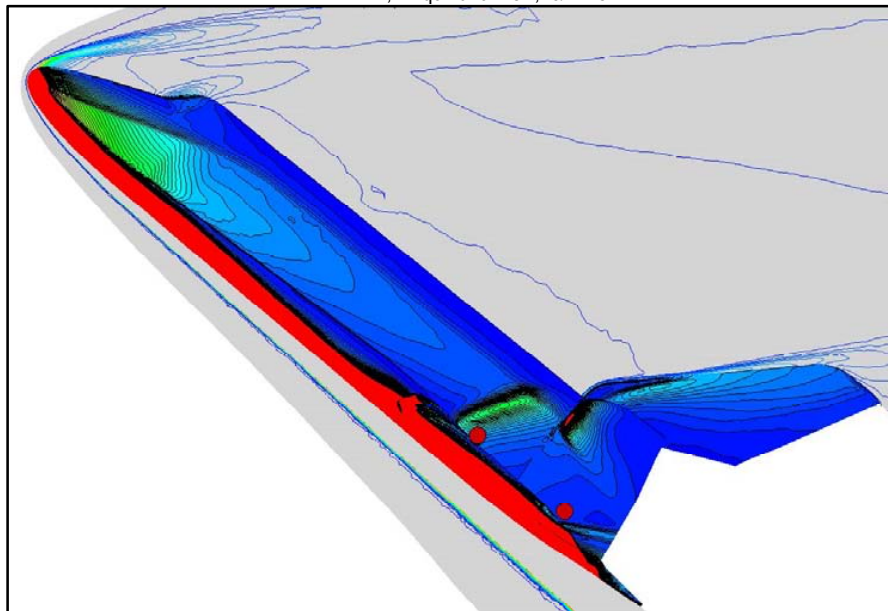
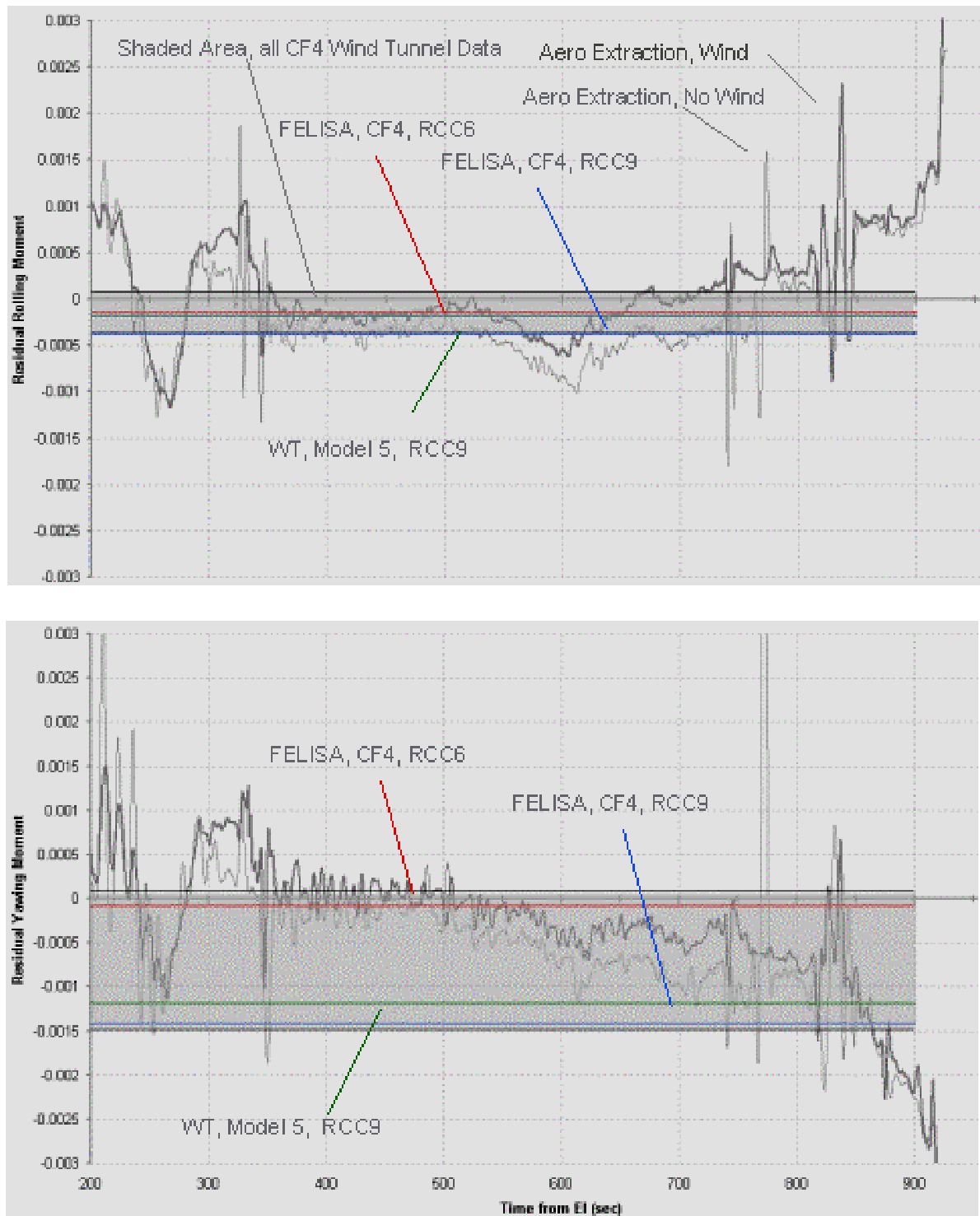


Figure 4.4-5 Surface Pressure Distribution – CFD Analysis - RCC Panel 9 Missing



**Figure 4.4-6 LaRC CF4 WT Test & FELISA (Inviscid) CFD Results – Single Panel Damage
Predicted Delta Aerodynamics vs. Flight Extracted Increments**

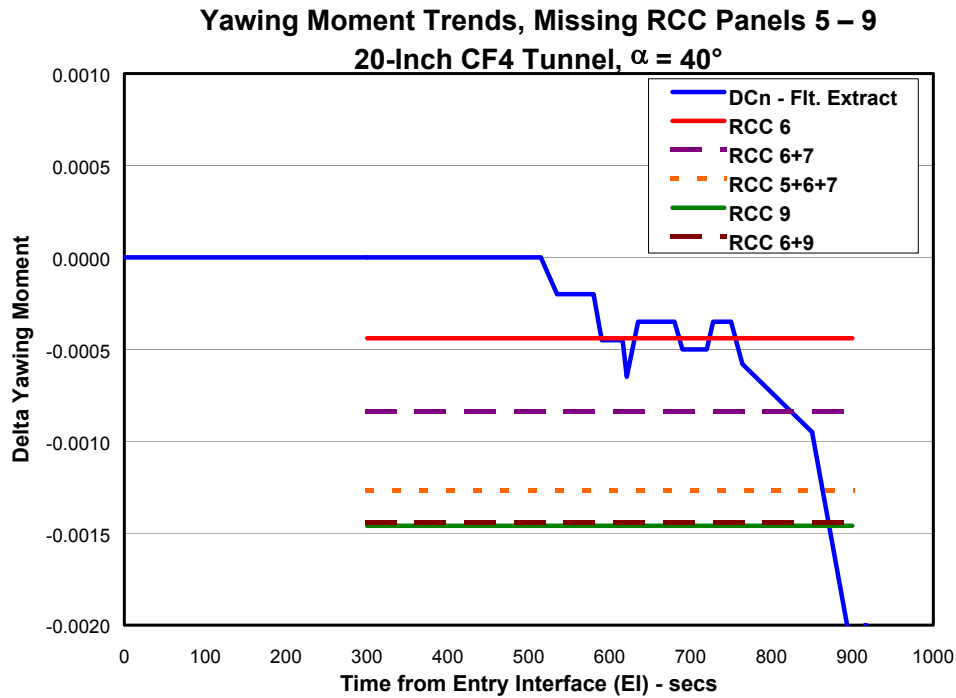


Figure 4.4-7 Aerodynamic Increment (delta Yaw) - Multiple RCC Panels Missing

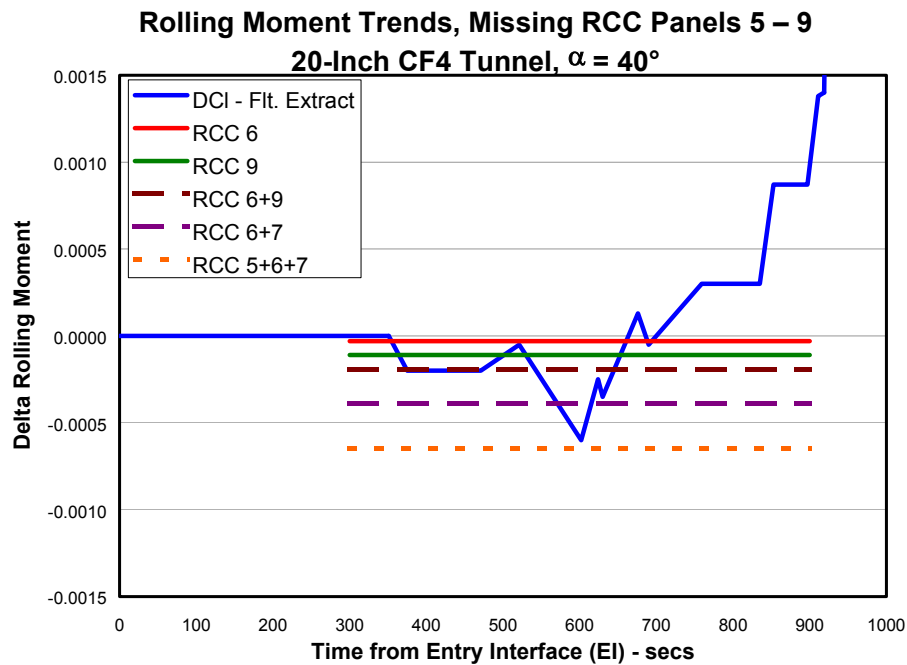


Figure 4.4-8 Aerodynamic Increment (delta Roll) - Multiple RCC Panels Missing

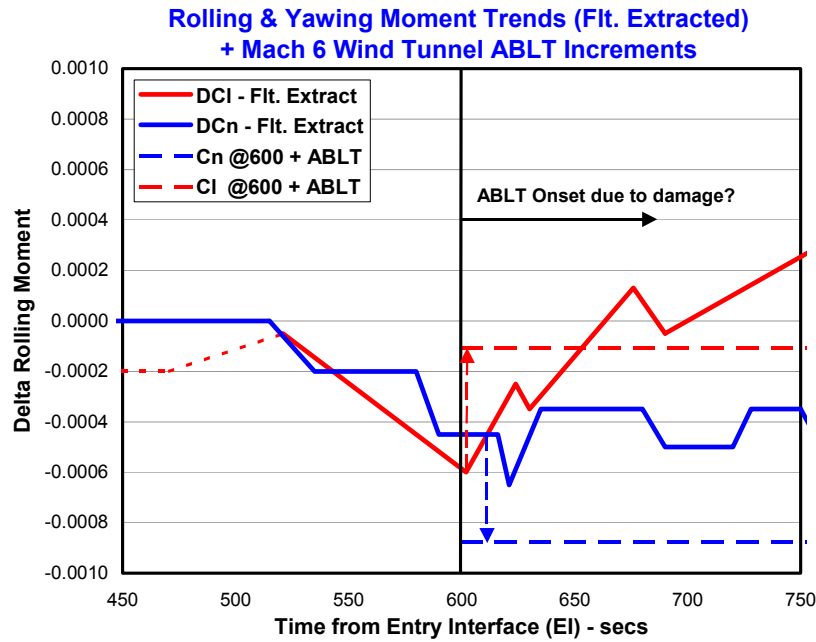


Figure 4.4-9 Delta Rolling Moment Trend Change - Early ABLT Onset?

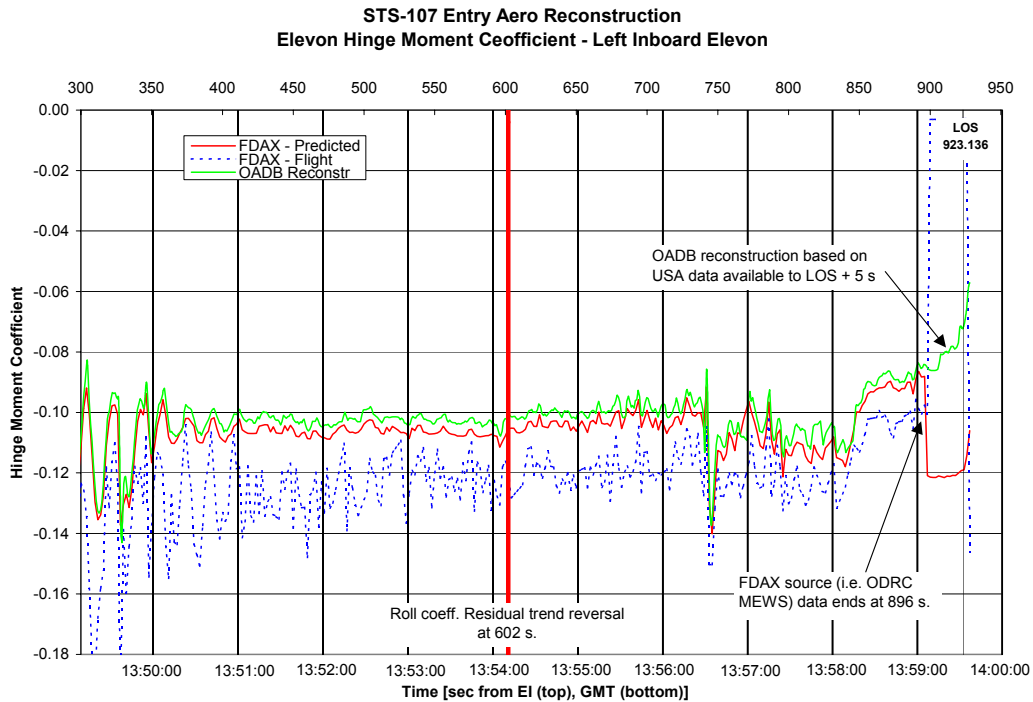


Figure 4.4-10 Delta Rolling Moment Trend Change – Disturbed flow over LHIB Elevon?

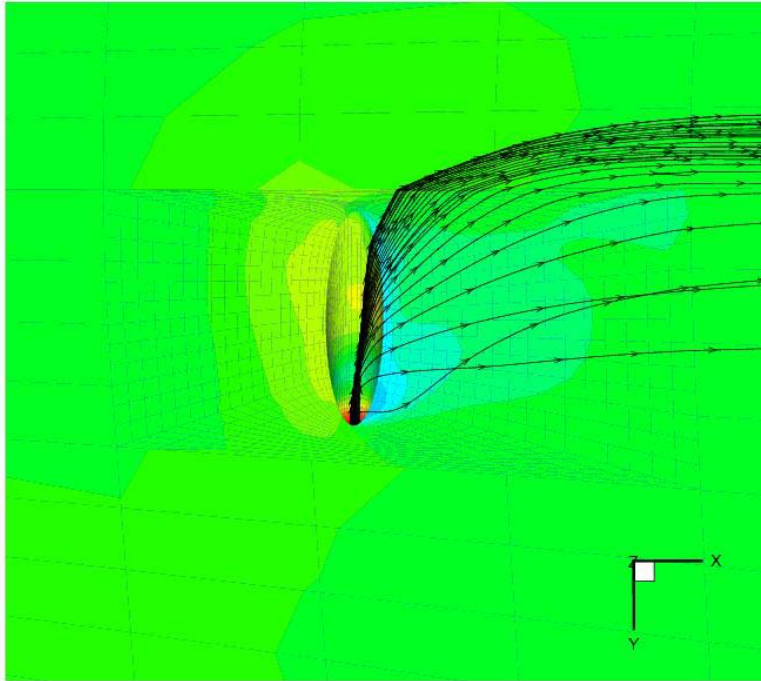


Figure 4.4-11 Delta Rolling Moment Trend Change – Flow Interaction w/Exiting Jet?

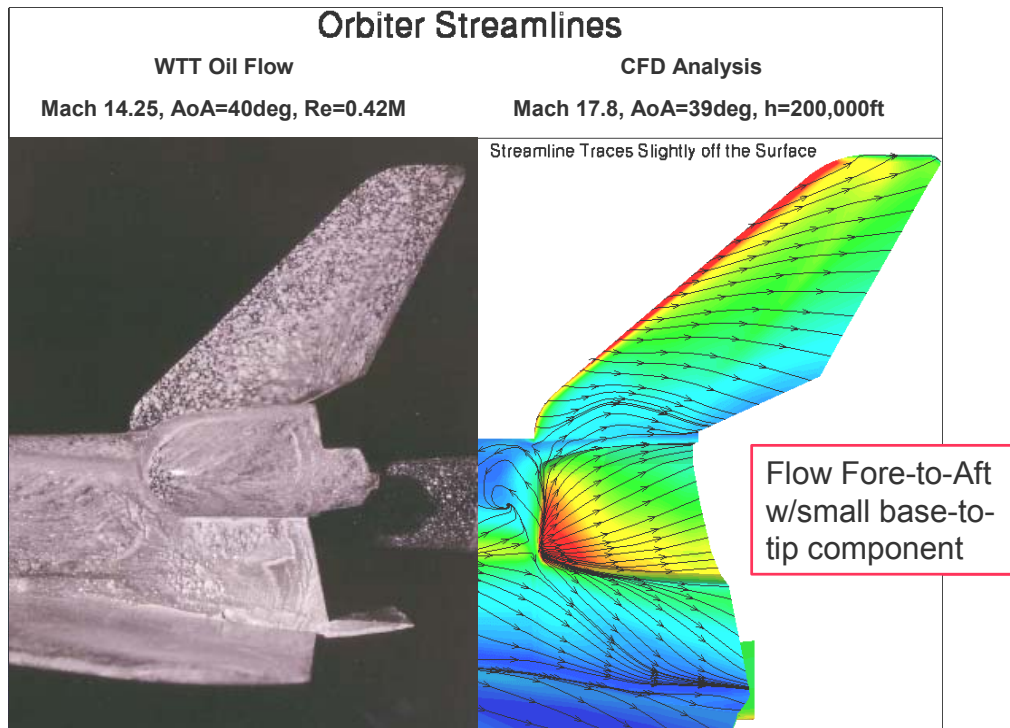


Figure 4.4-12 Orbiter Leeside (Fuselage, VT, OMS) Flow Field Visualization

FELISA --Inviscid Solver
Mach 24.2, Equilibrium Air, $q = 28.2$ psf, $\alpha = 40$ deg (13:52:20, El+491 sec)

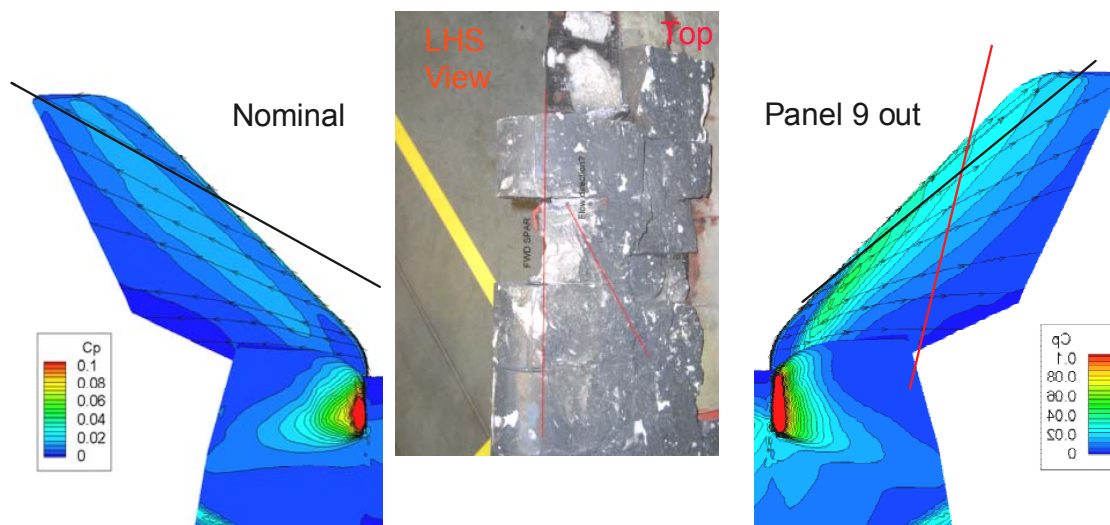


Figure 4.4-14 VT Flow Patterns - FELISA CFD Results - Baseline & w/Panel 9 Missing

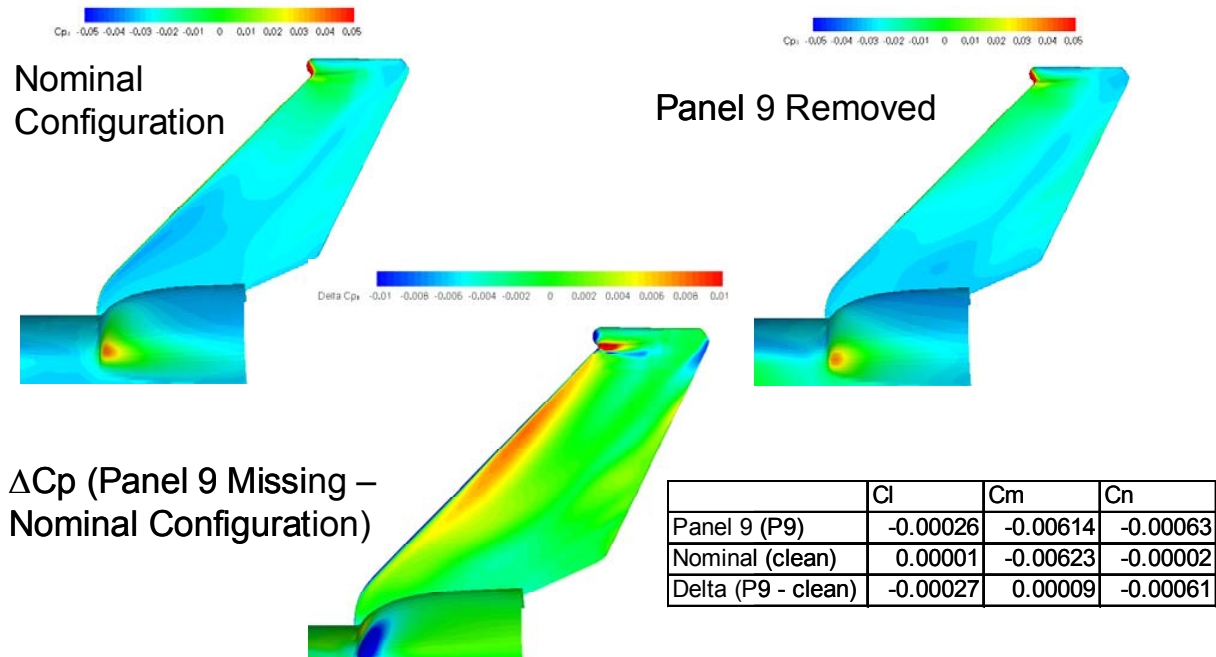


Figure 4.4-15 Leeside Flow Interaction - Overflow CFD analysis - Delta CP on Vertical Tail

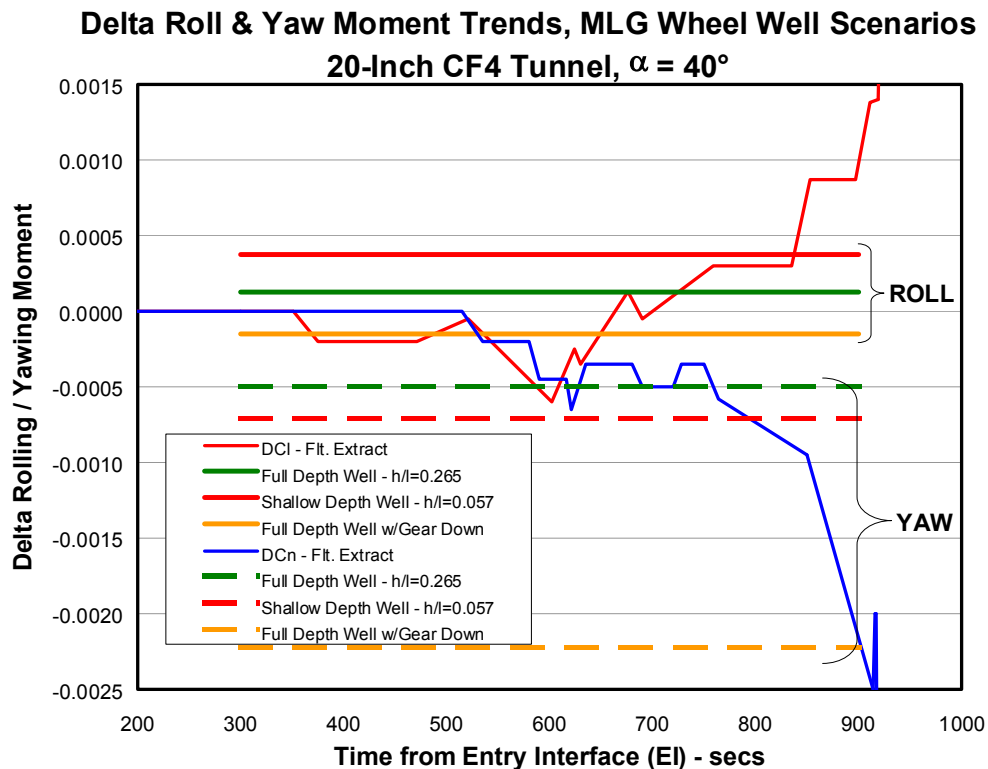


Figure 4.4-16 Delta Aero Increments - Roll & Yaw (MLG Wheel Well Scenarios)

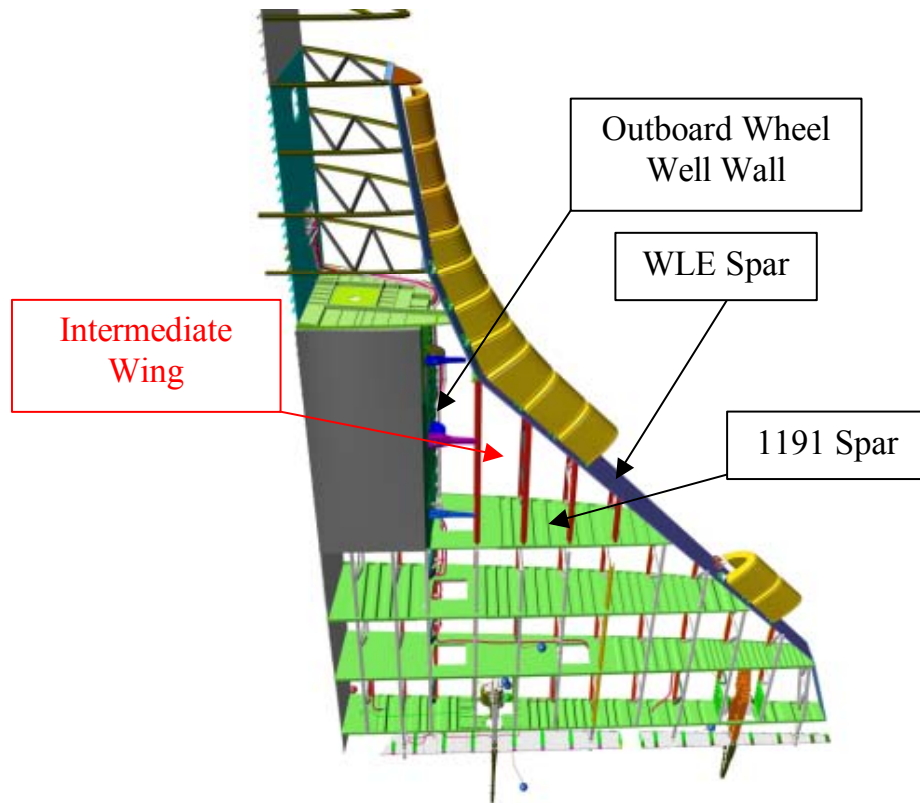


Figure 4.4-17 Orbiter Wing Structure Layout - Intermediate Wing Area

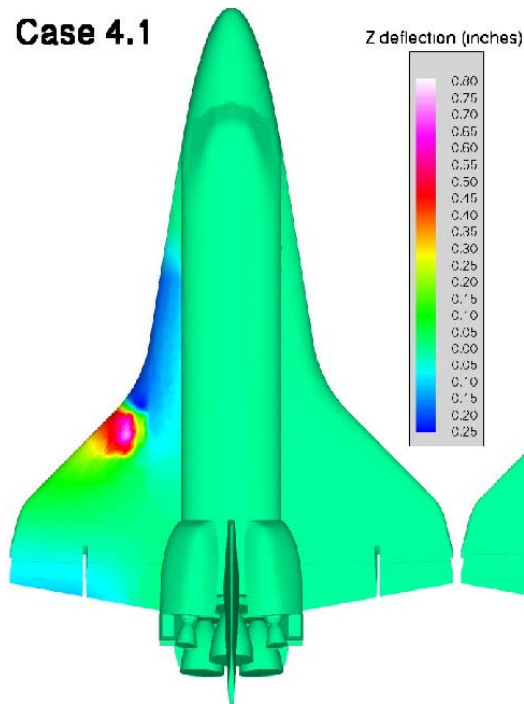


Figure 4.4-18 Orbiter Wing Structure Delta Deflection – Surface (z) Change With Damage

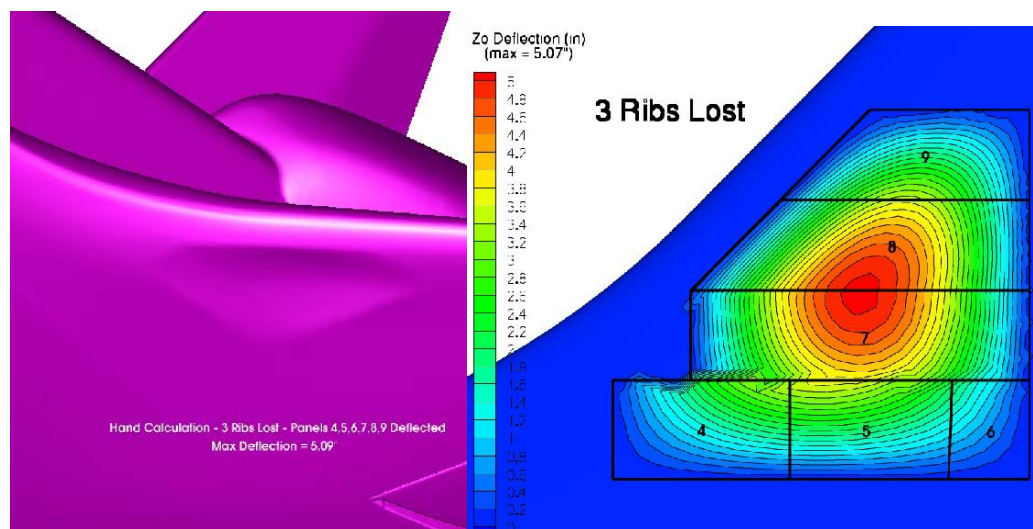


Figure 4.4-19 Orbiter Wing Surface (Skin) Deflection (z) – With Damage – 3 Ribs lost

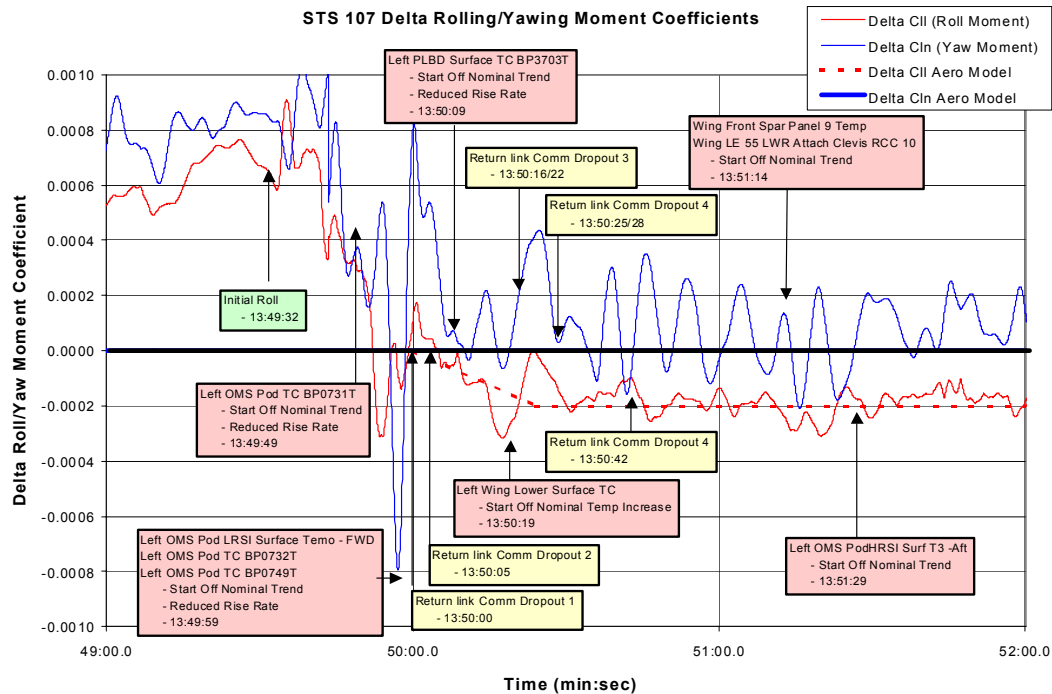


Figure 4.4-20 Aero Increments GMT 13:49:00 to 13:52:00

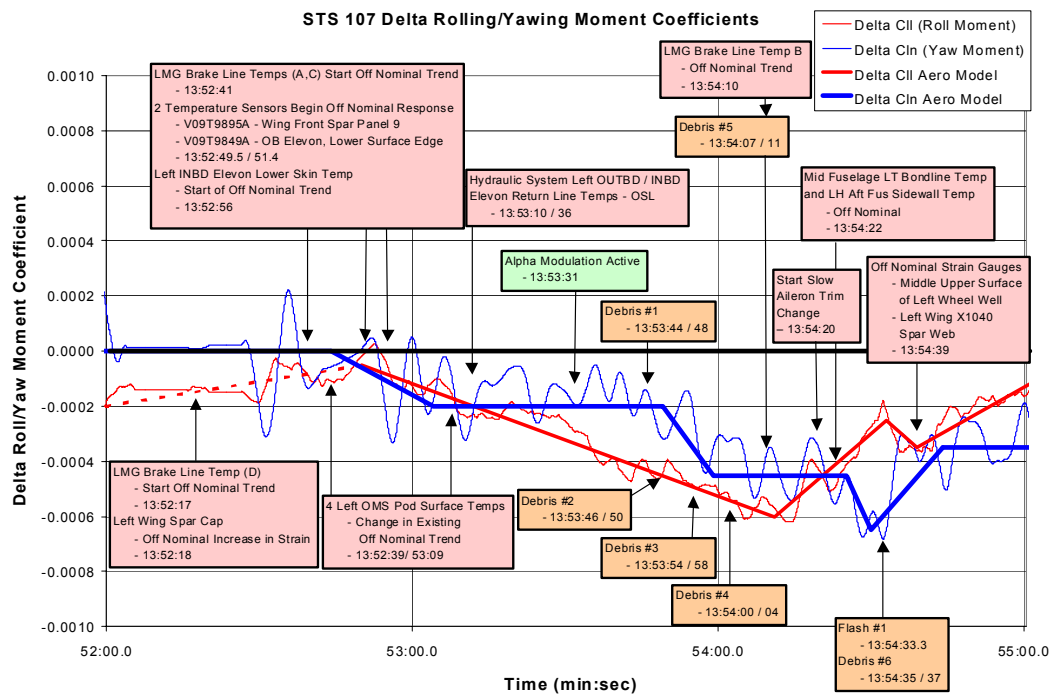


Figure 4.4-21 Aero Increments GMT 13:52:00 to 13:55:00

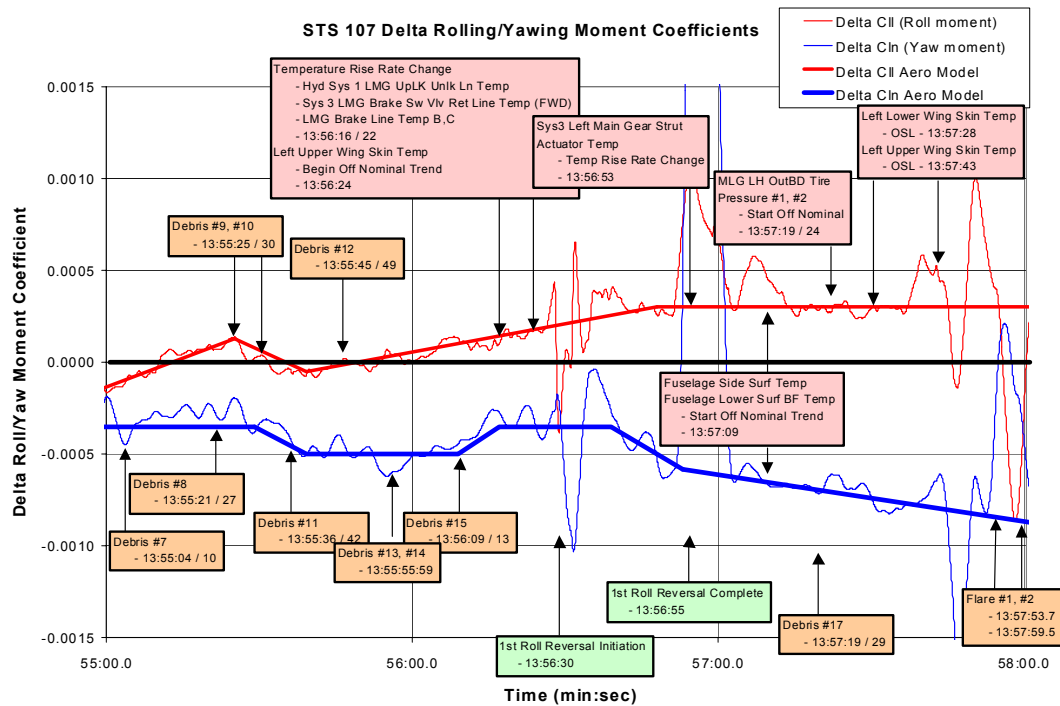


Figure 4.4-22 Aero Increments GMT 13:55:00 to 13:58:00

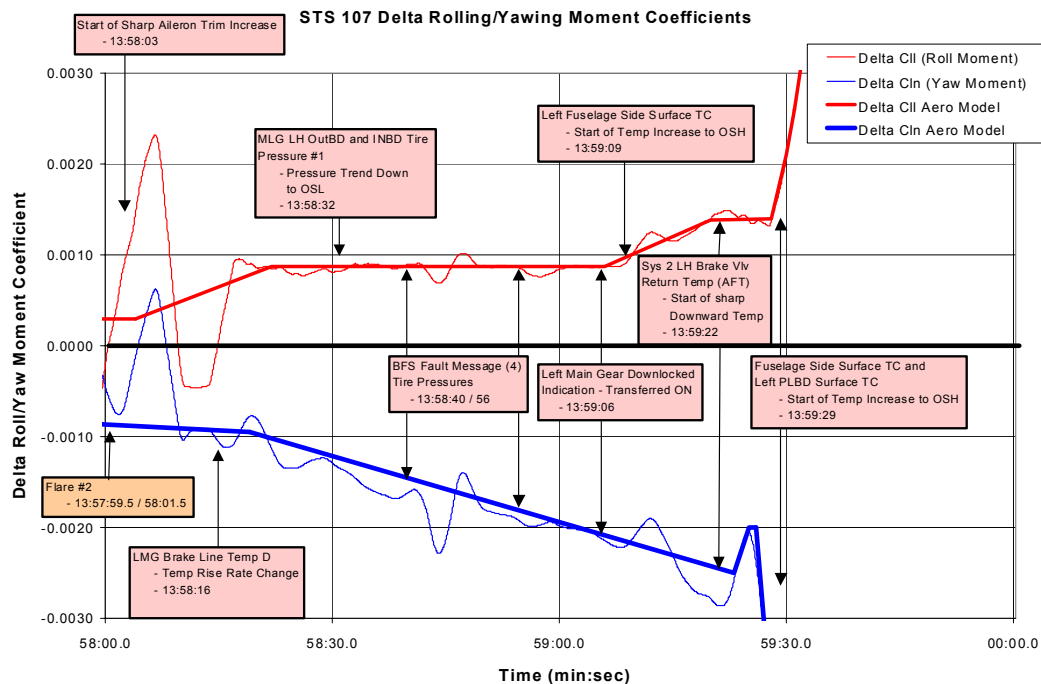


Figure 4.4-23 Aero Increments GMT 13:58:00 to 13:59:30

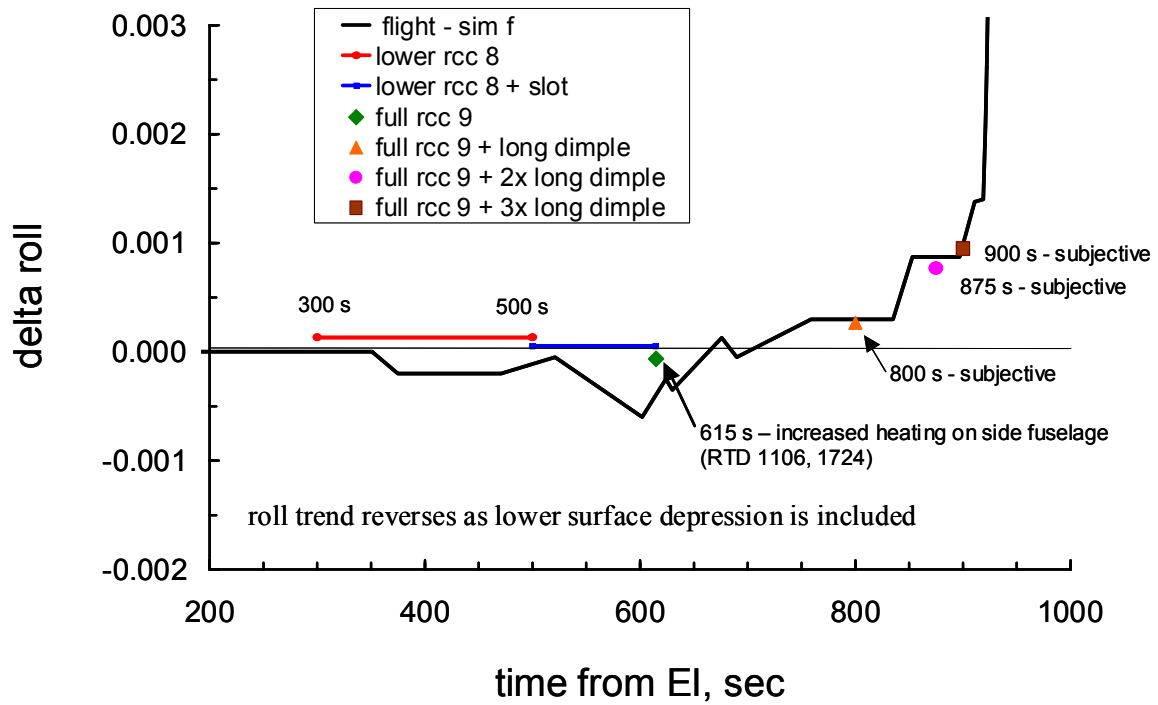


Figure 4.4-24 Aerodynamic Damage Progression Scenario – Delta Rolling Moment

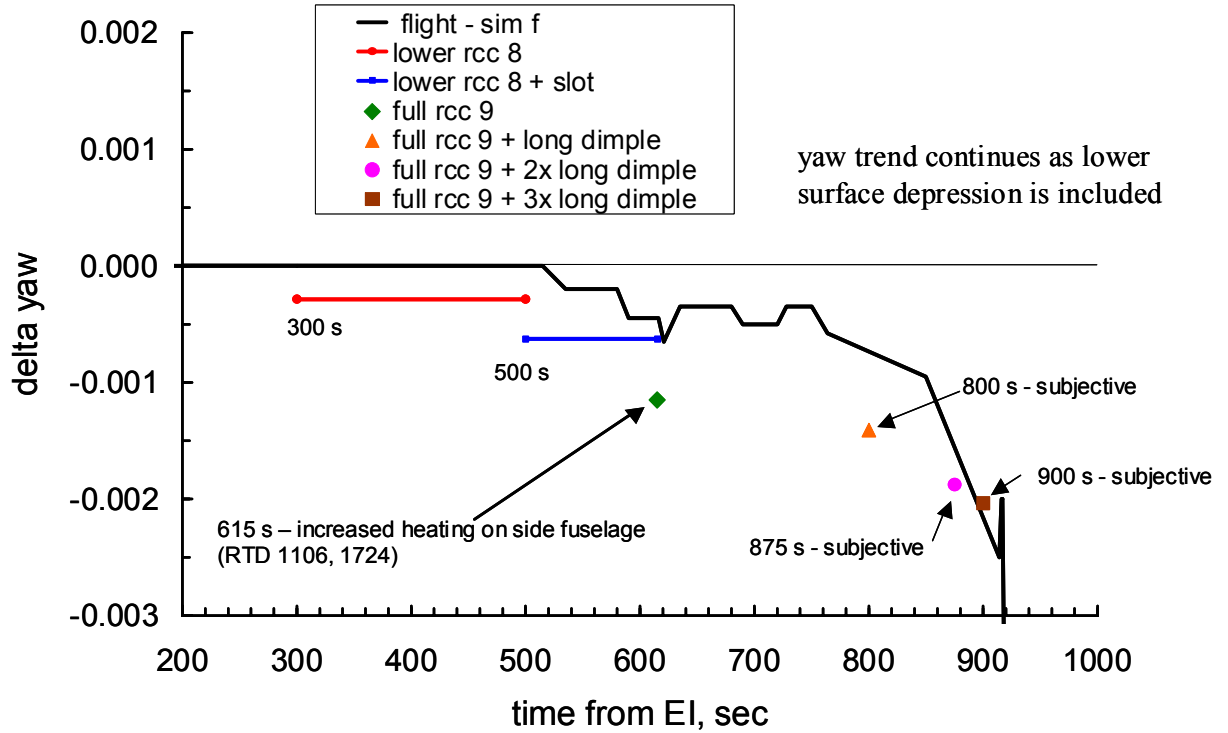


Figure 4.4-25 Aerodynamic Damage Progression Scenario – Delta Yawing Moment

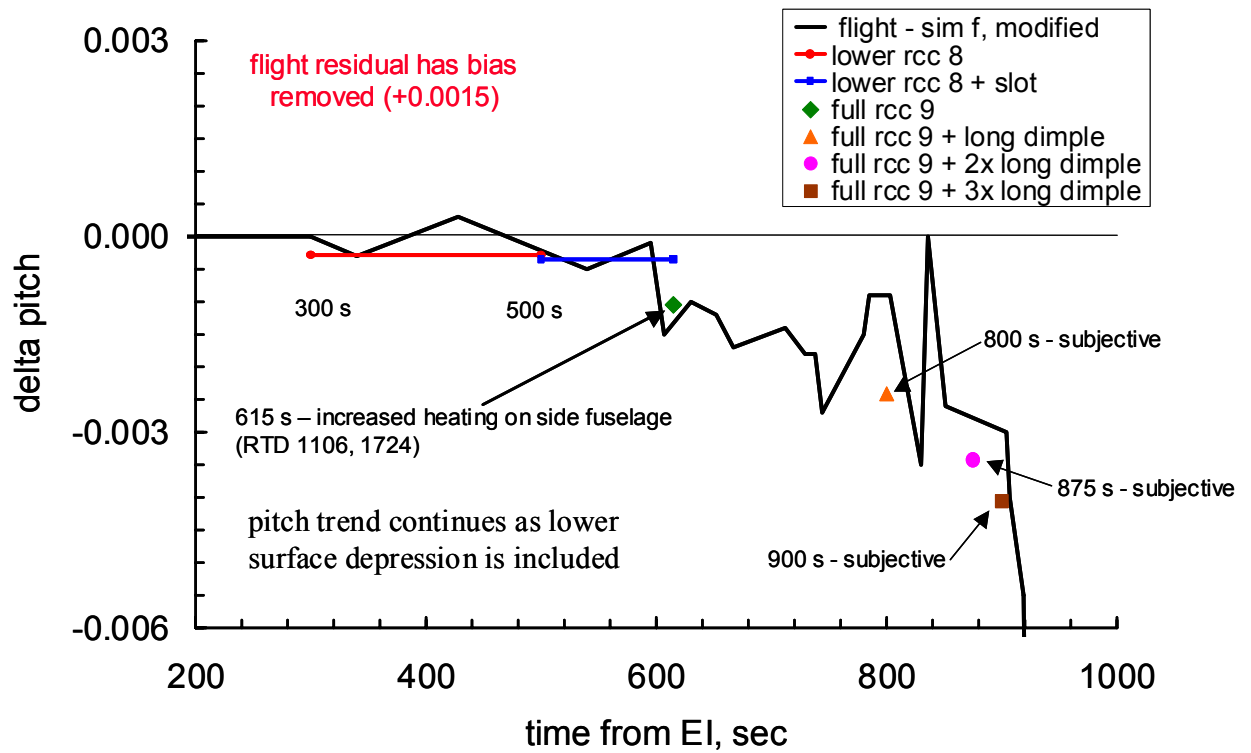


Figure 4.4-26 Aerodynamic Damage Progression Scenario – Delta Pitching Moment

4.5 *Summary – conclusions & observations*

- 1) Flight measured Orbiter rates, accelerations, trajectory parameters, control surface deflections, etc. can be used to define the off-nominal aerodynamics experienced by Columbia during STS-107 entry flight. The off-nominal aero is characterized by delta aerodynamic force and moment increments (Delta defined as Actual - Nominal).
- 2) High altitude winds have a pronounced effect on the magnitude of the off-nominal delta aerodynamic forces and moments, as much as 50%, but do not effect the trends vs. time.
- 3) Off nominal aerodynamic increments are not clearly evident until after EI + 515 sec.
- 4) At EI + 602 sec, the rolling moment increment trend abruptly reverses from increasing negative to increasing positive, corresponding to several other timeline events. These include the first evidence of flight control system compensation for asymmetric aero due to damage as well as debris event No. 5 (or Flash event "0").
- 5) The extracted moments do not exceed asymmetric aerodynamic design levels as defined by the Asymmetric Boundary Layer Transition (ABLT) model until very late in the flight timeline (after the EI + 877 sec point).
- 6) The flight control system manages the growing asymmetry as designed throughout the flight up to Loss of Signal (LOS).
- 7) The off nominal aerodynamics increase rapidly in the last 60 sec of flight producing overwhelming asymmetric moments (after EI + 920 sec) resulting in Columbia's loss of control leading to vehicle breakup.
- 8) Wind tunnel test and CFD analysis of proposed damaged configurations has been successful in producing aerodynamic increments consistent with a progressive damage scenario.
- 9) Initial delta aerodynamic yawing (-) and rolling (-) increments are not consistent with early ABLT which has always produced opposite signs for these moments.
- 10) Wing leading edge (RCC panel) damage produces the (-) roll and (-) yaw increments early in flight (plus the augmented heating observed on the side fuselage and OMS pod).
- 11) The primary source of the rolling moment trend change (@EI + 602 sec) cannot be attributed to leeside (VT, OMS, fuselage) interaction
- 12) Lower wing surface deformation (i.e. cavity or depression) produces the (-) yawing and (+) rolling moment increment trends seen later in the flight. These deformations are consistent with anticipated internal wing damage due to ingestion of hot gas through a Wing Leading Edge breach.
- 13) Increments measured for Main Landing Gear / Door deployment while matching the roll and yaw increments later in flight do not match the pitching moment. Based on this data the Main Landing Gear did not prematurely deploy.
- 14) Based on WT test and CFD analysis results a progressive damage scenario can be matched to the extracted aerodynamic increments that is consistent with other observed data trends, analysis and recovered hardware forensics.
- 15) The test and analysis conducted for the aerodynamic (and aerothermodynamic) portion of the investigation were performed on representative geometries. The fact that these geometries were chosen for investigation purposes should not be misconstrued as exactly reproducing the damaged configuration encountered in flight. These representative damaged configurations, however, do provide an insight into the nature and level of damage necessary to result in the loss of Columbia and her STS-107 crew.

4.6 *References – Aerodynamics*

- 1) Operational Aerodynamic Design Data Book, STS85-0118-1 CHG 8, August, 1996
- 2) STS-107 Natural Environments Report, MSFC ED44 (03-012), May 16, 2003
- 3) STS-107 Integrated Entry Environment (IEE) Team Final Report, NSTS-37382, May 30, 2003
- 4) OV-102 Investigation Vehicle Data Mapping (VDM) Team Quantitative Report, Preliminary - Rev. 6, May 02, 2003.

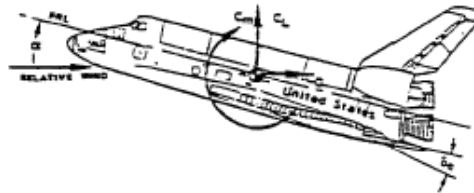
4.7 Appendices – Aerodynamics

4.7.1 Aerodynamic Definitions, Coordinate Systems and References

The following figures (pages from the Orbiter OADB) summarize the Orbiter aerodynamic coordinate system, aerodynamic definitions, moment reference center and the reference areas and lengths.

The aerodynamic force and moment sign convention is illustrated in Figure 3.1.5-4 which also includes the longitudinal equations for conversion from stability to body axis system.

STABILITY AXIS



Conversion to body axis system:
 $C_N = C_L \cos \alpha + C_D \sin \alpha$
 $C_A = C_D \cos \alpha - C_L \sin \alpha$

BODY AXIS

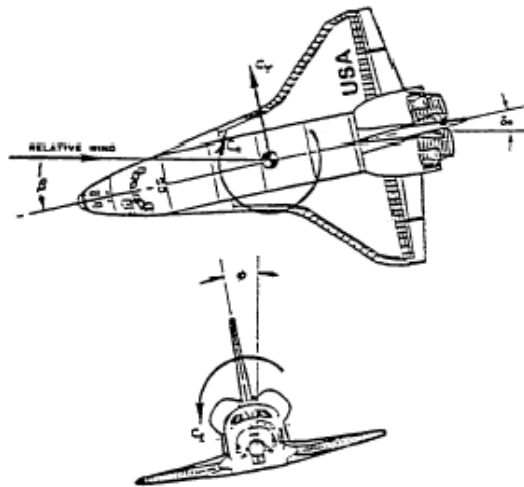


Figure 3.1.5-4
ORBITER SIGN CONVENTION

4.2.1.1 LONGITUDINAL AERODYNAMICS. The basic aerodynamic characteristics for the longitudinal degrees-of-freedom are presented as full-scale, rigid and elastic, forces and moment in both the stability and body axis systems (cf. Section 3.1.5). These forces and moments are defined for three phases or categories:

- 1.) ON-ORBIT (PAYLOAD BAY DOORS OPEN)
- 2.) ON-ORBIT (PAYLOAD BAY DOORS CLOSED)
- 3.) ENTRY



The total longitudinal forces and moment for the Orbiter Vehicle are defined as:

$$\begin{aligned}
 \text{LIFT FORCE, } L_{\text{TOTAL}} &= \bar{q} S_w C_{L_{\text{TOTAL}}} + L_{\text{RCS}} \quad (\text{lb}) \\
 \text{NORMAL FORCE, } N_{\text{TOTAL}} &= \bar{q} S_w C_{N_{\text{TOTAL}}} + N_{\text{RCS}} \quad (\text{lb}) \\
 \text{DRAG FORCE, } D_{\text{TOTAL}} &= \bar{q} S_w C_{D_{\text{TOTAL}}} + D_{\text{RCS}} \quad (\text{lb}) \\
 \text{AXIAL FORCE, } A_{\text{TOTAL}} &= \bar{q} S_w C_{A_{\text{TOTAL}}} + A_{\text{RCS}} \quad (\text{lb}) \\
 \text{PITCHING MOMENT, } M_{\text{TOTAL}} &= \bar{q} S_w \bar{c}_w C_{M_{\text{TOTAL}}} + M_{\text{RCS}} \quad (\text{ft-lb})
 \end{aligned}$$

$$\begin{aligned}
 \text{where, } \bar{q} &= \text{dynamic pressure} \quad (\text{lb/ft}^2) \\
 S_w &= \text{Wing Reference Area} \quad (2690.00 \text{ ft}^2) \\
 \bar{c}_w &= \text{Wing Mean Aerodynamic Chord} \quad (39.56 \text{ feet}) \\
 &\quad (\text{see Figure 3.1.5-2b})
 \end{aligned}$$

RCS flow field interactions are defined as contributions to the total forces or moment rather than coefficients since the terms due to jet thrust and impingement are independent of dynamic pressure and cannot, therefore, be normalized in the conventional manner.

4.2.1.1-1

RSS99D0001

4.2.1.2 LATERAL-DIRECTIONAL AERODYNAMICS. The basic aerodynamic characteristics for the lateral-directional degrees-of-freedom are presented as full-scale, rigid and elastic, force and moments in the body-axis system (cf. Section 3.1.5). The lateral-directional characteristics are defined under the same three categories listed in Section 4.2.1.1.

The total lateral-directional force and moments for the Orbiter Vehicle are defined as:

$$\begin{aligned}\text{SIDE FORCE, } Y_{\text{TOTAL}} &= \bar{q} S_w C_{Y_{\text{TOTAL}}} + Y_{\text{RCS}} & (\text{lb}) \\ \text{YAWING MOMENT, } \dot{\alpha} K_{\text{TOTAL}} &= \bar{q} S_w b_w C_{n_{\text{TOTAL}}} + \dot{\alpha} K_{\text{RCS}} & (\text{ft-lb}) \\ \text{ROLLING MOMENT, } \dot{\phi} L_{\text{TOTAL}} &= \bar{q} S_w b_w C_{l_{\text{TOTAL}}} + \dot{\phi} L_{\text{RCS}} & (\text{ft-lb})\end{aligned}$$

where, \bar{q} = dynamic pressure (lb/ft²)

S_w = Wing Reference Area (2690.00 ft²)

b_w = Wing Span (78.057 ft)
(see Figure 3.1.5-2b)

RCS flow field interactions are defined as contributions to the total force or moments rather than coefficients since the terms due to jet thrust and impingement are independent of dynamic pressure and cannot, therefore, be normalized in the conventional manner.

3.1.5 ORBITER VEHICLE. The aerodynamic design of the Orbiter Vehicle configuration is the result of a selection which would achieve high cross-range aerodynamically and which would be capable of trimmed flight over a wide range of angles of attack. The double-delta wing planform, combined with a moderately low fineness ratio (approximately 5) body, minimizes interference heating effects, provides the required L/D ratio to meet cross-range requirements, and possesses an acceptable trim range over the flight Mach regime. Figure 3.1.5-1 presents a general arrangement drawing of the Orbiter Vehicle.

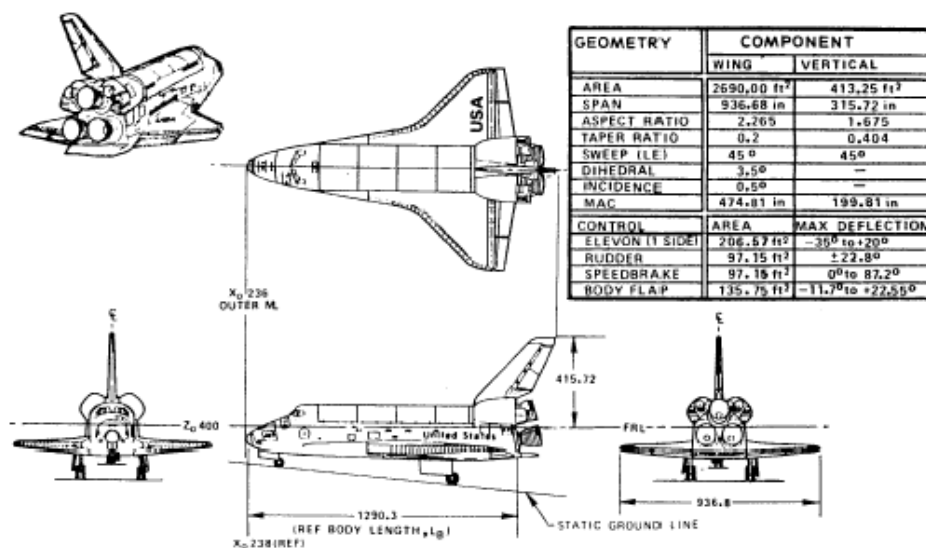
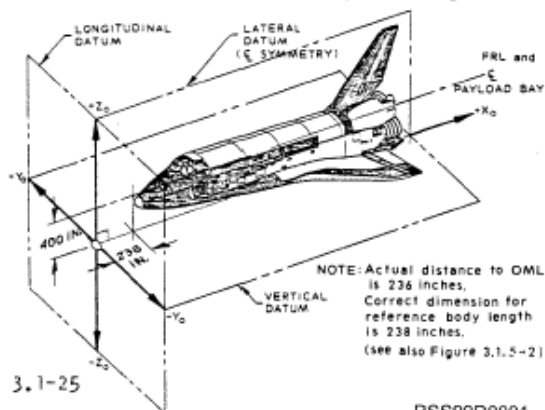


Figure 3.1.5-1
ORBITER GEOMETRY

Orbiter Vehicle design geometry is presented in Figure(s) 3.1.5-2 (a through f). The Orbiter Vehicle axis system for design drawing and mass properties statements is illustrated in the sketch. This axis system is defined in the Space Shuttle Master Dimensions Specification (Reference 3-7) and on Figure 3.1.5-2. All vehicle and design drawing axes systems are in accordance with NASA Phase B Technical Directives 2519 and 2519A.



4.7.2 Surface Pressure Entry Data Evaluation

Orbiter Experiments (OEX) pressure data was installed on Columbia in support of the Ascent Wing Loads Verification Program. The pressure transducers were therefore sized (typically 0 to 16 psia) for ascent load environments and analysis of these flight results were incorporated into the Performance Enhancement Design Airloads database. These specific requirements limited the use of data for the entry phase. Entry data review was typically performed for the Mach 3.5 to 0.6 region which covers the Operational Entry Airloads Database. Since culmination of the Airloads Verification Program, the typical extent of the entry review was for instrument functionality and signature comparisons with past flights.

Analysis of the OEX recorder pressure data for STS-107 was made possible with the finding, identification and processing of the OEX data recorder. This data included 181 wing pressure measurement gages on two of the three Pulse Code Modulation (PCM) units of the recorder. PCM1 had 91 gages while PCM2 had 90 gages with no measurements recorded on PCM3. A previous instrument survey performed for STS-109 (Columbia's previous flight) had identified that only 116 gages were producing useable data. These 116 gages break down as 68 for left wing (41 upper, 27 lower) and 48 for the right wing (34 lower and 14 upper). The only active pressure gages on Columbia during STS-107 were those on the wings.

Analysis of the STS-107 OEX entry pressure data was of very limited use for aerodynamic evaluation. Even though data was recorded to EI + 970 seconds, the useful recorded pressures typically do not start until around 1420 seconds after EI near Mach 3.5, Figure 4.7-1. Since the extent of STS-107 entry was above this condition and at such high altitude, low density conditions, no useful aerodynamic data was recorded. Most pressure gages exhibited pressure "spikes" in the EI + 480-660 sec and 930-970 sec regions, with these trends identified on both wings Figure 4.7-2. OEX pressure data utilization was limited to identification of these off-nominal signatures. The first gages to exhibit this behavior and the failure patterns were provided to the Time Line Group for inclusion of OEX pressure data into the master time line in support of the working scenario.

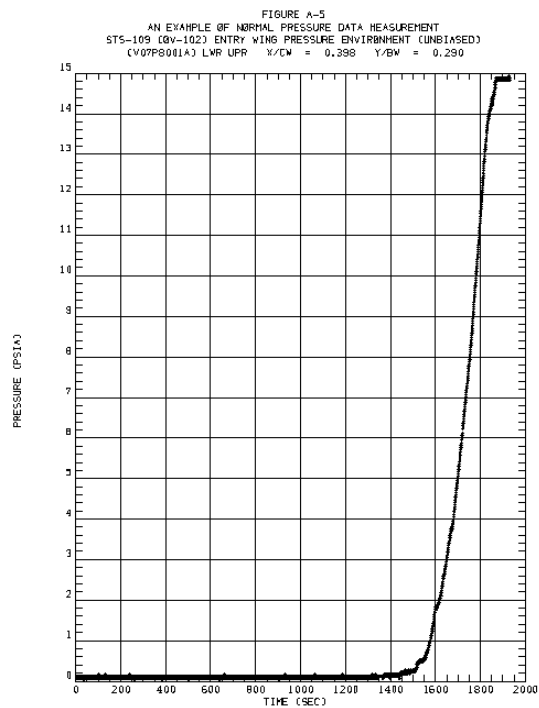


Figure 4.7-1 Typical OEX Entry Pressure Gage Signature (STS-109)

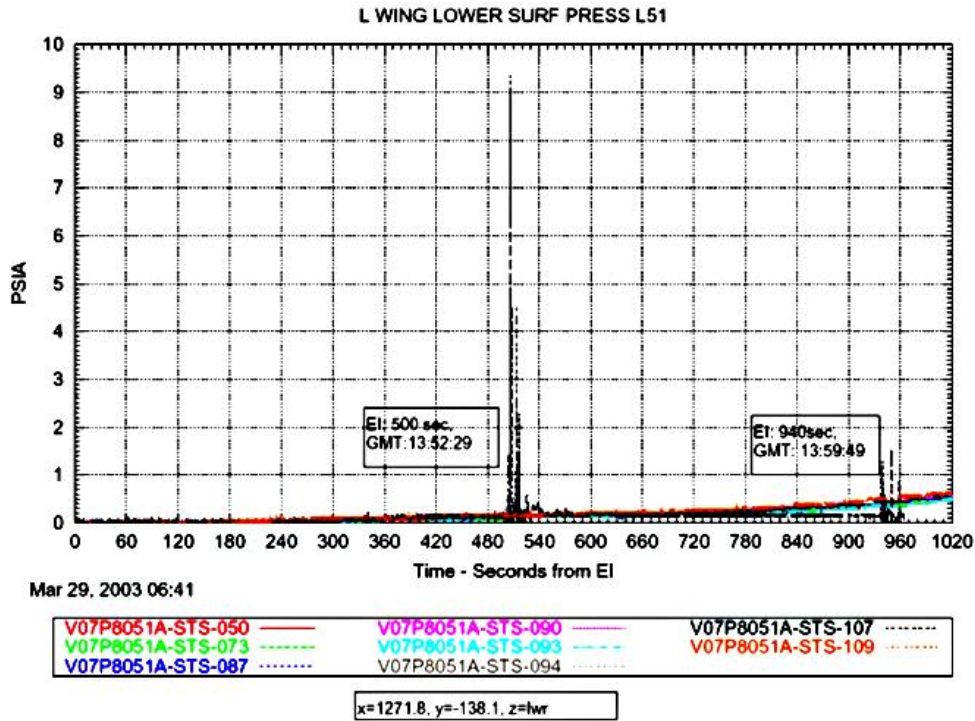


Figure 4.7-2 Typical OEX Entry Pressure Gage Signature (STS-107)

4.7.3 Wind Tunnel Test Matrix – Comprehensive Listing

Test	Run	Re/ft	Alpha	Beta	Mach	Gamma	Model	Configuration
6853	9	3.0	37.5	0.0	6.00	1.40	ceramic 1	baseline - ceramic 1; Re/ft = 3.0e6
6853	10	2.9	37.6	0.0	6.00	1.40	ceramic 1	baseline - ceramic 1, repeat; Re/ft = 3.0e6
6853	11	2.9	37.5	0.0	6.00	1.40	ceramic 1	baseline - ceramic 1, repeat; Re/ft = 3.0e6
6853	12	3.0	37.6	0.0	6.00	1.40	ceramic 1	trip at rcc panel 6 (1 trip, 0.0035 in)
6853	13	2.9	37.6	0.0	6.00	1.40	ceramic 1	trip at rcc panel 6 (1 trip, 0.0045 in)
6853	14	2.9	37.6	0.0	6.00	1.40	ceramic 1	trip at rcc panel 9 (1 trip, 0.0045 in)
6853	15	3.0	37.6	0.0	6.00	1.40	ceramic 1	trip at rcc panel 9 (1 trip, 0.0045 in)
6853	16	3.0	37.6	0.0	6.00	1.40	ceramic 1	trip at rcc panel 6 (1 trip, 0.0050 in)
6853	17	3.0	37.5	0.0	5.99	1.40	ceramic 1	trip at rcc panel 6 (1 trip, 0.0045 in)
6853	18	3.0	37.6	0.0	5.99	1.40	ceramic 1	trip at MLG door le, outboard corner (1 trip, 0.0045 in)
6853	19	3.0	37.6	0.0	5.99	1.40	ceramic 1	trips along MLG door le (7 trips, 0.0045 in)
6853	20	3.0	37.6	0.0	5.99	1.40	ceramic 1	trips along MLG door le (7 trips, 0.0045 in)
6853	21	3.0	37.6	0.0	5.99	1.40	ceramic 1	trips along MLG door le, down side (12 trips, 0.0045 in)
6853	22	3.0	37.6	0.0	5.99	1.40	ceramic 1	raised MLG door (1 "trip", 0.0065 in)
6853	23	3.0	37.5	0.0	5.98	1.40	ceramic 1	raised MLG door w/ slash (1 "trip", 0.0065 in)
6853	24	3.0	37.6	0.0	5.98	1.40	ceramic 1	trip at rcc panel 6; match test 6852 (1 trip, 0.0035 in)
6853	25	3.0	37.6	0.0	5.98	1.40	ceramic 1	trip at rcc panel 6, biased windward (1 trip, 0.0035 in)
6853	26	3.0	37.6	0.0	5.98	1.40	ceramic 1	trip at rcc panel 6, biased leeward (1 trip, 0.0035 in)
6853	27	2.9	37.5	0.0	5.98	1.40	ceramic 1	trip at rcc panel 6, biased windward (1 trip, 0.0065 in)
6853	28	3.0	37.6	0.0	5.98	1.40	ceramic 1	"full" ablt (10 trips along wing le)
6853	29	3.0	37.6	0.0	5.98	1.40	ceramic 1	"full" ablt (10 trips along wing le, 2 fwd)
6853	31	3.0	37.6	0.0	5.98	1.40	ceramic 1	baseline - ceramic 1, repeat; Re/ft = 3.0e6
6853	33	2.1	37.5	0.0	5.96	1.40	steel 1	baseline - steel 1; Re/ft = 2.0e6
6853	34	3.0	37.8	0.0	5.98	1.40	steel 1	baseline - steel 1; Re/ft = 3.0e6
6853	36	2.0	37.5	0.0	5.96	1.40	steel 1	open wheel well, L/H = 3.8, Re/ft = 2.0e6
6853	37	3.0	37.8	0.0	5.98	1.40	steel 1	open wheel well, L/H = 3.8, Re/ft = 3.0e6
6853	39	3.0	37.8	0.0	5.98	1.40	steel 1	open wheel well, L/H = 6.4, Re/ft = 3.0e6
6853	41	3.0	37.8	0.0	5.98	1.40	steel 1	open wheel well, L/H = 17.5, Re/ft = 3.0e6
6853	42	2.1	37.5	0.0	5.97	1.40	steel 1	open wheel well, L/H = 17.5, Re/ft = 2.0e6
6853	44	3.0	37.8	0.1	5.98	1.40	steel 1	open wheel well w/ door; L/H = 3.8
6853	46	3.0	37.9	0.1	5.98	1.40	steel 1	open wheel well w/ door and gear; L/H = 3.8
6853	48	3.0	37.8	0.0	5.98	1.40	steel 1	open wheel well w/ gear; L/H = 3.8
6853	49	3.0	37.8	0.0	5.98	1.40	steel 1	baseline - steel 1, repeat; Re/ft = 3.0e6
6853	51	3.0	37.6	0.0	5.98	1.40	ceramic 1	missing rcc panel 6
6853	52	3.0	37.6	0.0	5.98	1.40	ceramic 1	gouge in MLG door
6853	53	3.0	37.6	0.0	5.98	1.40	ceramic 1	holes through carrier panels 6, 9, 12, 16
6853	54	3.0	37.6	0.0	5.98	1.40	ceramic 1	baseline - ceramic 1, repeat; Re/ft = 3.0e6
6853	55	0.0	37.8	0.7	5.97	1.40	steel 1	baseline - steel 1; Re/ft = 3.0e6; beta = 0.7
6853	57	3.0	37.8	0.7	5.97	1.40	steel 1	open wheel well, L/H = 3.8; beta = 0.7
6853	58	3.0	37.8	0.7	5.98	1.40	steel 1	open wheel well w/ gear; L/H = 3.8; beta = 0.7
6853	59	3.0	37.9	0.8	5.98	1.40	steel 1	open wheel well w/ door + gear; L/H = 3.8; beta = 0.7
6853	60	3.0	37.8	0.7	5.98	1.40	steel 1	open wheel well w/ door; L/H = 3.8; beta = 0.7
6853	61	3.0	37.9	-0.8	5.98	1.40	steel 1	open wheel well w/ door + gear; L/H = 3.8; beta = -0.8
6853	62	3.0	37.8	-0.8	5.98	1.40	steel 1	open wheel well w/ door; L/H = 3.8; beta = -0.8
6853	63	3.0	37.8	-0.9	5.98	1.40	steel 1	baseline - steel 1; beta = -0.8

Table 4.7-1 Test LaRC 6853-Mach 6 Air Hypersonic Wind Tunnel Facility - STS-107 Investigation

Test	Run	Re/ft	Alpha	Beta	Mach	Gamma	Model	Configuration
144	10	0.46	38.1	0.0	5.93	1.22	steel 1	baseline - steel 1
144	11	0.46	40.2	0.0	5.90	1.21	steel 1	baseline - steel 1, repeat
144	12	0.45	42.2	0.0	5.89	1.21	steel 1	baseline - steel 1, repeat
144	13	0.44	38.2	0.0	5.95	1.22	steel 1	baseline - steel 1, repeat
144	14	0.45	40.2	0.0	5.93	1.22	steel 1	open wheel well, L/H = 3.8
144	16	0.45	42.2	0.0	5.91	1.21	steel 1	open wheel well, L/H = 17.5
144	17	0.45	38.2	0.0	5.90	1.21	steel 1	open wheel well w/ door and gear; L/H = 3.8
144	18	0.44	40.2	0.0	5.89	1.21	steel 1	open wheel well w/ door; L/H = 3.8
144	19	0.46	42.2	0.0	5.94	1.22	steel 1	open wheel well w/ gear; L/H = 3.8
144	20	0.45	38.2	0.0	5.93	1.22	steel 1	open wheel well, L/H = 6.4
144	28	0.15	40.0	0.0	6.00	1.23	steel 1	baseline - steel 1; Re/ft = 0.15
144	29	0.41	40.2	0.0	5.88	1.21	steel 1	baseline - steel 1, repeat
144	43	0.47	37.2	0.0	5.96	1.22	ceramic 1	baseline - ceramic 1
144	44	0.45	40.1	0.0	5.94	1.22	ceramic 1	baseline - ceramic 1, repeat
144	45	0.47	42.2	0.0	5.94	1.22	ceramic 1	baseline - ceramic 1, repeat
144	47	0.47	40.1	0.0	5.92	1.22	ceramic 1	missing rcc panel 9
144	48	0.45	40.1	0.0	5.90	1.21	ceramic 1	missing rcc panels 6 and 9
144	49	0.46	40.2	0.0	5.90	1.21	ceramic 1	missing rcc panel 6
144	50	0.44	40.1	0.0	5.89	1.21	ceramic 1	baseline - ceramic 1, repeat
144	51	0.47	38.0	0.0	5.94	1.22	ceramic 1	missing rcc panel 6, repeat
144	52	0.47	40.1	0.0	5.93	1.22	ceramic 1	missing rcc panels 6 and 7
144	54	0.44	37.7	0.0	5.91	1.21	ceramic 2	baseline - ceramic 2
144	55	0.47	39.8	0.0	5.95	1.22	ceramic 2	baseline - ceramic 2, repeat
144	56	0.46	41.8	0.0	5.93	1.21	ceramic 2	baseline - ceramic 2, repeat
144	58	0.48	40.0	0.0	5.96	1.22	ceramic 2	missing rcc panel 4
144	59	0.48	40.0	0.0	5.95	1.22	ceramic 2	missing rcc panels 2 and 4
144	60	0.45	40.0	0.0	5.92	1.22	ceramic 2	missing rcc panel 2
144	61	0.46	40.3	0.0	5.90	1.21	ceramic 1	missing rcc panels 5, 6, and 7
144	62	0.45	40.0	0.0	5.89	1.21	ceramic 4	baseline - ceramic 4
144	64	0.45	37.9	0.0	5.89	1.21	ceramic 4	baseline - ceramic 4, repeat
144	65	0.47	42.0	0.0	5.94	1.22	ceramic 4	baseline - ceramic 4, repeat
144	66	0.47	40.2	0.0	5.93	1.22	ceramic 4	missing rcc panel 10
144	67	0.46	40.2	0.0	5.91	1.21	ceramic 4	missing rcc panels 10 and 12
144	68	0.46	40.2	0.0	5.90	1.21	ceramic 4	missing rcc panel 12
144	69	0.46	40.3	0.0	5.90	1.21	ceramic 1	missing rcc panels 5, 6, 7, and 8
144	70	0.45	40.4	0.0	5.89	1.21	ceramic 1	baseline - ceramic 1, repeat
144	71	0.47	40.3	0.0	5.94	1.22	ceramic 1	missing rcc panel 9, repeat
144	72	0.46	40.3	0.1	5.93	1.22	ceramic 1	missing rcc panels 5, 6, 7, 8, and 9
144	73	0.46	40.2	0.0	5.91	1.21	ceramic 4	missing rcc panels 9 and 10
144	74	0.46	40.2	0.0	5.90	1.21	ceramic 4	missing rcc panels 9 and 10, repeat
144	75	0.45	40.2	0.0	5.88	1.21	ceramic 4	missing rcc panels 9, 10 and 12
144	76	0.46	39.8	0.0	5.89	1.21	ceramic 2	baseline - ceramic 2, repeat
144	77	0.47	39.8	0.0	5.94	1.22	ceramic 2	hole through carrier panel 6
144	78	0.46	40.0	0.0	5.93	1.22	ceramic 2	hole through carrier panel 9
144	79	0.46	40.0	0.0	5.91	1.21	ceramic 2	hole through carrier panel 12
144	80	0.45	37.7	0.0	5.90	1.21	ceramic 2	baseline - ceramic 2, repeat
144	81	0.45	41.9	0.0	5.89	1.21	ceramic 2	baseline - ceramic 2, repeat
144	82	0.45	38.0	0.0	5.88	1.21	ceramic 1	baseline - ceramic 1, repeat
144	83	0.47	40.1	0.0	5.94	1.22	ceramic 1	baseline - ceramic 1, repeat
144	84	0.46	40.0	0.0	5.92	1.22	ceramic 2	missing rcc panel 4, repeat
144	85	0.46	40.0	0.1	5.91	1.21	ceramic 2	missing rcc panels 2 and 4, repeat
144	86	0.45	40.2	0.1	5.90	1.21	ceramic 4	missing rcc panels 9, 10, 11 and 12
144	88	0.27	37.3	0.0	5.92	1.22	ceramic 5	baseline - ceramic model 5; Re/ft = 0.26e6
144	89	0.44	37.8	0.0	5.87	1.21	ceramic 5	baseline - ceramic model 5; Re/ft = 0.46e6
144	90	0.30	39.3	0.0	6.00	1.23	ceramic 5	baseline - ceramic model 5, repeat; Re/ft = 0.26e6
144	91	0.46	39.9	0.0	5.93	1.22	ceramic 5	baseline - ceramic model 5, repeat; Re/ft = 0.46e6
144	92	0.28	39.3	0.0	5.96	1.22	ceramic 5	baseline - ceramic model 5, repeat; Re/ft = 0.26e6
144	93	0.45	39.9	0.0	5.90	1.21	ceramic 5	baseline - ceramic model 5, repeat; Re/ft = 0.46e6
144	94	0.27	41.4	0.0	5.92	1.22	ceramic 5	baseline - ceramic model 5, repeat; Re/ft = 0.26e6
144	95	0.44	42.0	0.0	5.87	1.21	ceramic 5	baseline - ceramic model 5, repeat; Re/ft = 0.46e6
144	96	0.27	41.3	0.0	5.98	1.23	ceramic 5	baseline - ceramic model 5, repeat; Re/ft = 0.26e6
144	97	0.45	41.9	0.0	5.92	1.22	ceramic 5	baseline - ceramic model 5, repeat; Re/ft = 0.46e6
144	98	0.27	39.5	0.0	5.94	1.22	ceramic 5	missing rcc panel 9; Re/ft = 0.26e6
144	99	0.45	40.1	0.1	5.89	1.21	ceramic 5	missing rcc panel 9; Re/ft = 0.46e6
144	100	0.28	39.5	0.0	5.94	1.22	ceramic 5	missing rcc panels 6 and 9; Re/ft = 0.26e6
144	101	0.45	40.1	0.1	5.87	1.21	ceramic 5	missing rcc panels 6 and 9; Re/ft = 0.46e6
144	102	0.46	39.9	0.0	5.89	1.21	ceramic 5	baseline - ceramic model 5, repeat; Re/ft = 0.46e6
144	103	0.47	40.0	0.0	5.94	1.22	ceramic 5	missing rcc panel 8, right wing
144	104	0.46	39.9	0.0	5.92	1.22	ceramic 5	baseline - ceramic model 5, repeat; Re/ft = 0.46e6
144	105	0.46	40.1	0.0	5.90	1.21	ceramic 5	missing rcc panel 5, right wing
144	106	0.46	39.9	1.1	5.90	1.21	ceramic 5	baseline - ceramic model 5; Re/ft = 0.46e6; beta = 1

Table 4.7-2 Test LaRC 144 - CF4 Hypersonic Wind Tunnel Facility - STS-107 Investigation

Test	Run	Re/ft	Alpha	Beta	Mach	Gamma	Model	Configuration
148	13	0.45	38.2	0.0	5.91	1.21	ceramic A	baseline - ceramic A, repeat
148	14	0.47	38.1	0.0	5.95	1.22	ceramic A	single windward groove, L/H = 10.0
148	15	0.47	38.1	0.0	5.92	1.22	ceramic A	single windward groove, L/H = 18.9
148	16	0.46	38.1	0.0	5.91	1.21	ceramic A	single windward groove, L/H = 27.8
148	17	0.45	38.4	0.0	5.90	1.21	ceramic C	baseline - ceramic C
148	19	0.46	38.4	0.0	5.90	1.21	ceramic C	baseline - ceramic C
148	20	0.43	38.4	0.0	5.88	1.21	ceramic C	missing lower rcc 9
148	21	0.47	38.4	0.0	5.93	1.22	ceramic C	missing lower rcc 7
148	22	0.46	38.4	0.0	5.92	1.22	ceramic C	baseline - ceramic C, repeat
148	23	0.46	38.1	0.0	5.92	1.22	ceramic A	double windward groove, L/H = 27.8; missing rcc 9
148	24	0.46	38.1	0.0	5.91	1.21	ceramic A	double windward groove, L/H = 27.8
148	25	0.46	38.2	0.0	5.90	1.21	ceramic A	double windward groove, L/H = 18.9
148	26	0.47	38.1	0.0	5.95	1.22	ceramic A	double windward groove, L/H = 18.9, repeat
148	27	0.45	38.1	0.0	5.92	1.22	ceramic A	double windward groove, L/H = 27.8; missing rcc 9, repeat
148	28	0.47	38.2	0.0	5.92	1.22	ceramic A	double windward groove, L/H = 27.8, repeat
148	29	0.45	38.1	0.0	5.89	1.21	ceramic A	baseline - ceramic A, repeat
148	30	0.46	38.2	0.0	5.89	1.21	ceramic A	missing rcc panel 9
148	31	0.45	38.0	0.0	5.95	1.22	ceramic A	baseline - ceramic A, repeat
148	32	0.46	38.1	0.0	5.93	1.22	ceramic A	single windward groove, L/H = 27.8; missing rcc 9
148	34	0.45	38.3	0.0	5.91	1.21	ceramic B	baseline - ceramic B
148	35	0.45	38.3	0.0	5.90	1.21	ceramic B	baseline - ceramic B, repeat
148	36	0.44	38.4	0.0	5.89	1.21	ceramic B	missing lower rcc panel 4
148	37	0.47	38.3	0.0	5.95	1.22	ceramic B	missing lower rcc panel 4, repeat
148	38	0.43	38.2	0.0	5.92	1.22	ceramic B	missing lower rcc panel 6
148	39	0.44	38.2	0.0	5.90	1.21	ceramic B	missing lower rcc panel 6, repeat
148	40	0.43	38.3	0.0	5.89	1.21	ceramic B	missing lower rcc panel 8
148	41	0.44	38.3	0.0	5.89	1.21	ceramic B	missing lower rcc panel 8, repeat
148	43	0.42	38.4	0.0	5.89	1.21	ceramic 5	baseline - ceramic 5
148	44	0.46	38.4	0.0	5.94	1.22	ceramic 5	missing rcc panel 9
148	45	0.45	38.4	0.0	5.92	1.22	ceramic 5	missing rcc panel 9, repeat
148	46	0.44	38.4	0.0	5.92	1.22	ceramic 5	baseline - ceramic 5
148	47	0.34	38.0	0.0	5.94	1.22	ceramic B	missing lower rcc panel 8; Re/ft = 0.35e6
148	48	0.33	37.9	0.0	5.92	1.22	ceramic B	missing lower rcc panel 8, with through hole; Re/ft = 0.35e6
148	49	0.32	37.9	0.0	5.90	1.21	ceramic B	baseline - ceramic B; Re/ft = 0.35e6
148	50	0.20	37.5	0.0	5.97	1.23	ceramic C	baseline - ceramic C; Re/ft = 0.20e6
148	51	0.33	38.0	0.0	5.91	1.21	ceramic C	baseline - ceramic C; Re/ft = 0.35e6
148	52	0.33	38.1	0.0	5.90	1.21	ceramic C	missing lower rcc panel 5
148	53	0.32	38.1	0.0	5.88	1.21	ceramic C	missing lower rcc panel 5, repeat
148	54	0.32	38.1	0.0	5.88	1.21	ceramic C	baseline - ceramic C, repeat; Re/ft = 0.35e6
148	55	0.31	38.1	0.0	5.87	1.21	ceramic C	missing lower rcc panel 7
148	57	0.21	37.8	0.0	5.99	1.23	ceramic 2	simulated leeside venting (fence); Re/ft = 0.20
148	61	0.45	38.5	0.0	5.90	1.21	ceramic 5	baseline - ceramic 5, tail removed
148	62	0.46	38.5	0.0	5.90	1.21	ceramic 5	baseline - ceramic 5, tail removed
148	63	0.47	38.5	0.0	5.95	1.22	ceramic 5	missing rcc panel 9, tail removed
148	64	0.45	38.5	0.0	5.92	1.22	ceramic 5	missing rcc panel 9, tail removed, repeat
148	65	0.44	38.1	0.0	5.90	1.21	ceramic A	triple windward groove, L/H = 27.8
148	67	0.45	38.2	0.0	5.89	1.21	ceramic A	triple windward groove, L/H = 22.5; faired aft edge
148	68	0.47	38.0	0.0	5.95	1.22	ceramic A	triple windward groove, L/H = 27.8, missing rcc 9
148	69	0.46	38.1	0.0	5.93	1.22	ceramic A	triple windward groove, L/H = 27.8, missing rcc 9, repeat
148	70	0.45	38.2	0.0	5.91	1.21	ceramic B	missing lower rcc panel 8, with through slot
148	75	0.20	37.8	0.0	5.98	1.23	ceramic 2	simulated leeside venting (fence); Re/ft = 0.20
148	76	0.46	37.8	0.1	5.92	1.22	ceramic 2	simulated leeside venting (fence); Re/ft = 0.46
148	81	0.20	40.0	0.0	6.01	1.24	ceramic 2	simulated leeside venting (fence), missing rcc 9; Re/ft = 0.20
148	82	0.43	40.0	0.0	5.89	1.21	ceramic 2	simulated leeside venting (fence), missing rcc 9; Re/ft = 0.46
148	86	0.50	40.2	0.0	5.98	1.23	sla D	leeside vent
148	87	0.48	40.2	0.0	5.95	1.22	sla D	leeside vent w/ windward cavity
148	88	0.46	40.2	0.0	5.93	1.22	sla D	leeside vent w/ missing T-seal (8/9)
148	89	0.17	40.2	0.0	5.90	1.21	sla D	leeside vent w/ missing T-seal (8/9); Re/ft = 0.17
148	90	0.44	40.3	0.0	5.88	1.21	sla D	leeside vent (sealed) w/ windward cavity
148	91	0.47	40.3	0.0	5.95	1.22	sla D	leeside vent (sealed) w/ windward cavity, repeat
148	92	0.47	40.3	0.0	5.94	1.22	sla D	leeside vent w/ windward cavity

Table 4.7-3 Test LaRC 148 - CF4 Hypersonic Wind Tunnel Facility - STS-107 Investigation

4.7.4 FELISA Inviscid CFD - Comments and Additional Analysis

The work presented in Section 4.3.2, Damage Assessment Using Computational Fluid Dynamics, summarized the delta aerodynamics produced by numerous damage scenarios. This section contains supporting computations that verified some of the assumptions used in the analysis and a discussion of how convergence is assessed.

4.7.4.1 Flow Solver Convergence

Two criteria are used in assessing convergence of a FELISA solution. The methodology in FELISA preserves total enthalpy, and thus the maximum and minimum total enthalpies are tracked. Since the primary utilization of FELISA is to compute aerodynamic loads, their convergence is also evaluated. Figure 4.7-3 shows the typical set of plots that are evaluated to assess convergence. Even though the residual is still dropping, the aerodynamic loads and the enthalpies have converged to a steady state. For many of the damage scenarios evaluated, the solver did not converge to a steady state solution. This is not unexpected given the types of damage (particularly the WLE damage) being evaluated. The convergence history of the loads for the baseline and the damaged configuration were co-plotted, to determine if the oscillation of the aerodynamic loads was larger than the delta aerodynamics. Figure 4.7-4 shows the aerodynamic loads convergence for a damaged (windward surface depression) and a baseline solution, where the damaged solution has reached a steady state. Figure 4.7-5 shows the same plot for a damaged solution (half panel 9 with upper carrier panel removed) that shows definite oscillations in the loads. The oscillations, however are small compared to the difference between the damaged and the baseline. The practical implication of the unsteady nature of many of the computations is that there is an bound on the delta aerodynamics, and that the idea that it is the trend of many computations that is important in the analysis of these damage scenarios.

4.7.4.2 Comparison of Absolute Aerodynamics for Flight, CF4, and Mach 6 Air

All of the delta aerodynamic analysis described in Section 4.3.2 was based on the assumption that even if the total aerodynamics did not compare exactly with the 'true' aerodynamics, the delta aerodynamics for the damaged configurations would compare well with the 'true' delta aerodynamics due to damage. Indeed, when the delta aerodynamics for wind tunnel, inviscid flight, viscous flight, and even Mach 6 perfect gas air simulations were compared, the trends gave a consistent picture. Figure 4.7-6 shows the total aerodynamics plotted against time from EI for the baseline and missing RCC panel 6+7 at flight conditions, and the baseline and missing RCC panel 6 for CF4 and Mach 6 air conditions. This figure shows that the difference between the flight, CF4, and Mach 6 air aerodynamics is much larger than the deltas between the baseline and the damaged aerodynamics for a given configuration.

4.7.4.3 Aerodynamics for Full (360°) Configurations, Baseline and Damaged

In order to assess the impact of using half body configurations for the delta aerodynamics, a set of computations was made with a full configuration, with an undamaged right side, and a missing RCC panel 9 on the left. The asymmetric aerodynamics (side force, rolling and yawing moments) are shown in Figure 4.7-7(a), and the symmetric loads (axial and normal force, and pitching moment) in Figure 4.7-7(b), plotted against sideslip. The half body aerodynamics (at $\beta=0^\circ$) are shown, and indicate that there is little difference between the full and half-body aerodynamics.

4.7.4.4 Systematic Angle of Attack and Mach number Effect in Delta Aerodynamics

The delta aerodynamics presented in Figure 4.3-42 show the missing panel aerodynamics for a range of flight conditions, which have varying Mach and angle of attack. Several computations were run to isolate the Mach number and the angle of attack effect in the delta aerodynamics, for the missing RCC panels 6+7 configuration. Figure 4.7-8 shows the delta aerodynamics plotted against Mach number (which is opposite in trend from time from EI) for an angle of attack of 40° . Only the delta yawing moment showed a strong trend, decreasing with increasing Mach number. The delta

rolling and pitching moments showed a very shallow trend toward positive with increasing Mach number. Figure 4.7-9 shows the aerodynamics and delta aerodynamics plotted against angle of attack, for a constant Mach number of 20.2 (CFD condition 4). While the typical trends with angle of attack are observed in the symmetric aerodynamics (normal force in particular), the delta aerodynamics show are not affected by angle of attack,

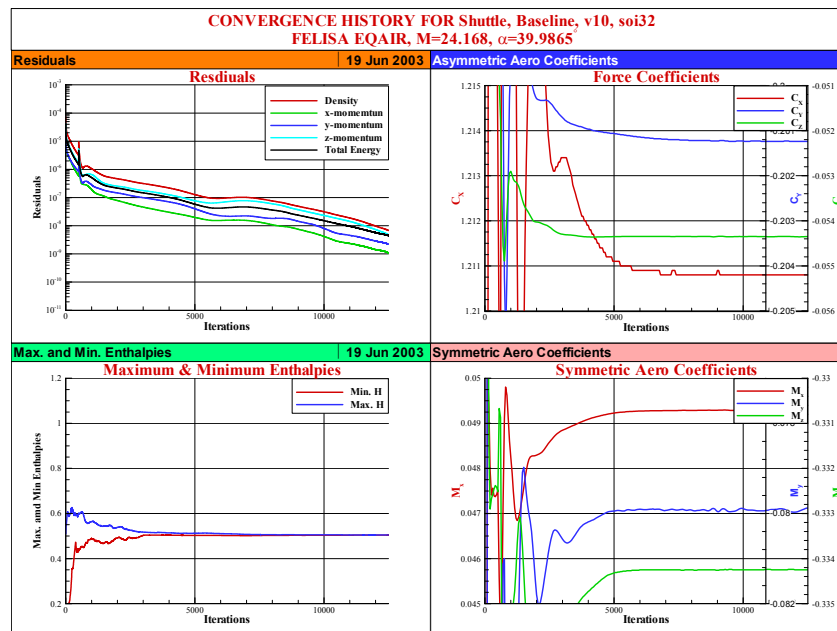


Figure 4.7-3 Typical Convergence History Plots from FELISA

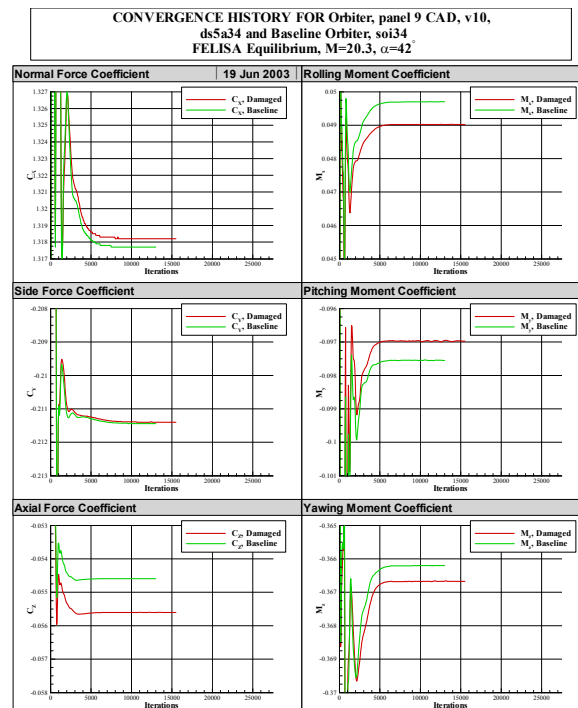


Figure 4.7-4 Aerodynamic Force and Moment Convergence for Steady Solution

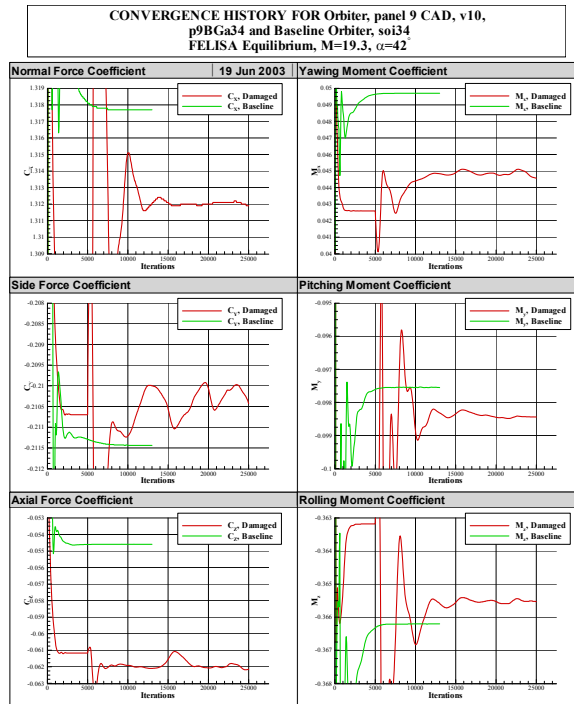


Figure 4.7-5 Aerodynamic Force and Moment Convergence for Oscillating Solution

FELISA Prediction of Aerodynamic Coefficients for Flight and Wind Tunnel Conditions, $\alpha = 40^\circ$

- At this scale, effect of missing panel small except in axial direction at
- Flight cases are for panels removed, CF_4 and Mach 6 are for panel 6 only.
- CF_4 doesn't match flight, but is closer than Mach

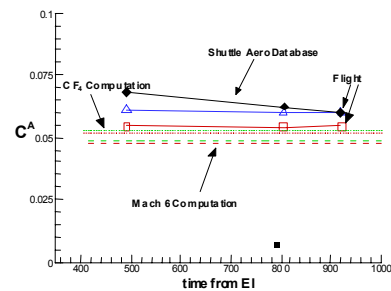
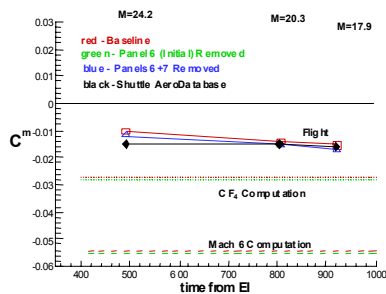
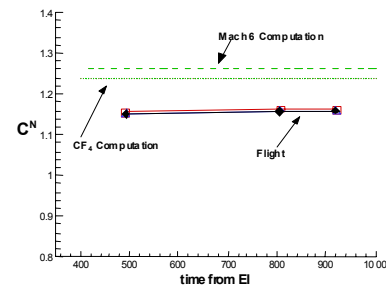
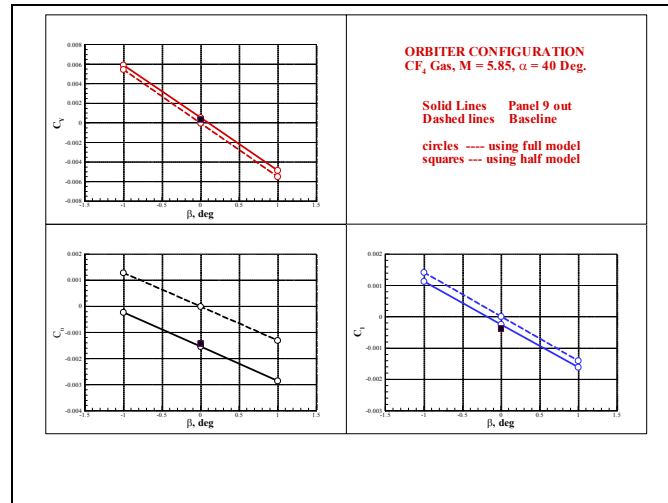
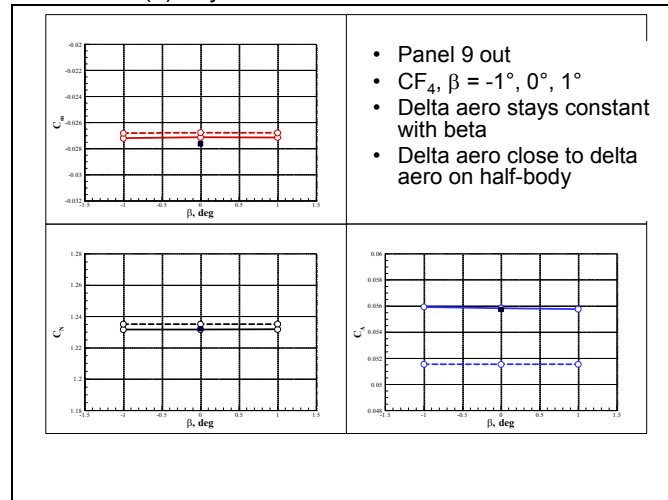


Figure 4.7-6 Comparison of Total Aerodynamics for Flight, CF₄, & Mach 6 WT Conditions



(a) Asymmetric Forces and Moments



(b) Symmetric Forces and Moments

Figure 4.7-7 Forces and Moments for Baseline and Missing RCC Panel 9 for Range of Sideslip Angles

**Effect of Mach Number, Hence
Flow Chemistry, on
Aerodynamic Coefficients and
Deltas , $\alpha = 40^\circ$**

- Pitch shows an increase with Mach, normal force a slight decrease
- Delta pitch flat, delta rolls shows slight increase, yaw shows significant decrease. Helps explain discrepancies between CF4 and flight computations.

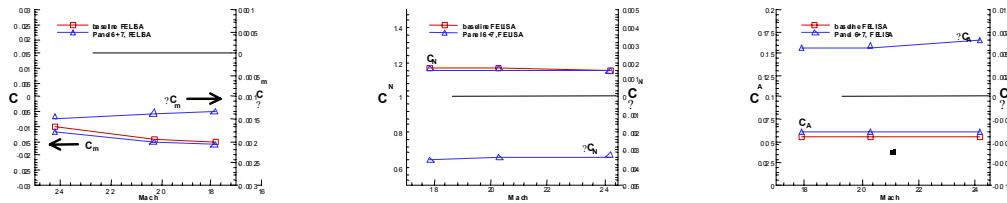
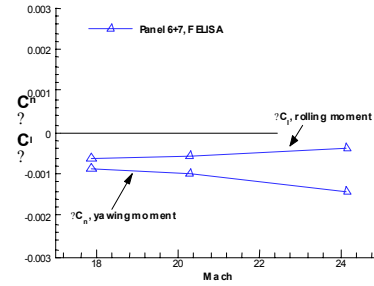


Figure 4.7-8 Effect of Mach Number on Delta Aerodynamics

**Effect of Angle of Attack on
Aerodynamic Coefficients and
Deltas
FELISA, $M = 20.3$**

- Forces and moments show typical trends with alpha
- Deltas have no significant trends for symmetric or asymmetric loads

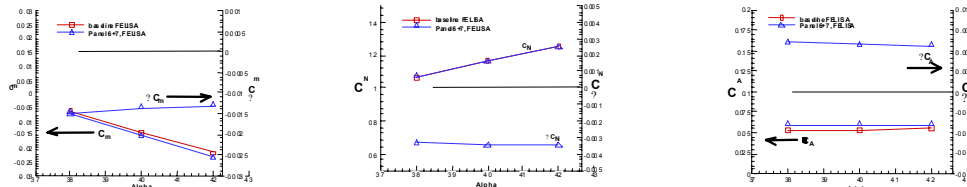
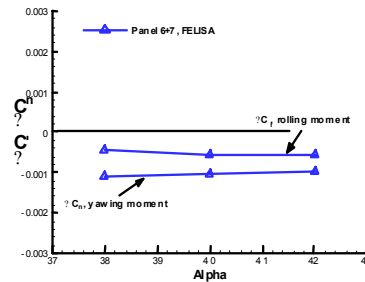


Figure 4.7-9 Effect of Angle of Attack on Delta Aerodynamics

4.7.5 OVERFLOW CFD Analysis of Leeside Flow field Interactions

4.7.5.1 Brief CFD Intro / Application Description

Missing RCC panel Navier Stokes solutions were done with the OVERFLOW code. Delta aero increments were extracted and the flow fields were analyzed for differences between missing panel solutions and the nominal configuration. Delta aero increments were obtained, including component aero from the wing, fuselage, and tail. The simulations were done to compare with the LaRC Mach 6 air tunnel. The wind tunnel model scale was 0.0075 of the full-scale orbiter corresponding to a vehicle length of approximately 9.678". The free stream conditions for the test and analysis were Mach = 5.96 at a $Re / ft = 2.976$ Million and $T_{inf} = 112.27$ R.

4.7.5.2 Configurations Analyzed

Three configurations were analyzed: baseline (no damage), panel 6 missing (original Karen Bibb geometry), and panel 9 missing. The grids were obtained from the External Aerothermal group's common grid for the nominal configuration (Aerothermodynamics Section 5.2.4.2). The common grid was modified to have overset boundaries in place of block zonal. The panel 6 and panel 9 grids were then created to match the resolution of the common grid in the missing panel region. The only difference between the grid systems was the addition of the missing panel grids. Figure 4.7-10 shows the surface grid for panel 9. The original grids were run for half the vehicle (without a VT). After evaluating the solutions, the flow field around the tail was desired so the symmetric grids were copied into both halves of the vehicle and combined to create the full geometry. The vertical tail, including the SILTS pod was added to the overset grid system. The missing panel grids didn't change, although only the RCC panel 9 missing configuration was computed on the vertical tail grid system.

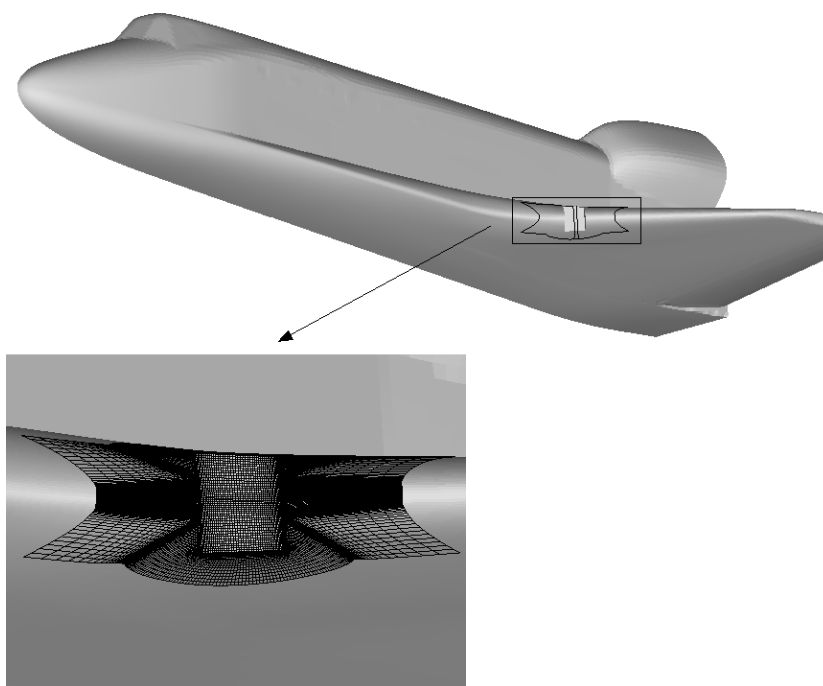


Figure 4.7-10 Surface Grid of a Missing RCC panel 9

4.7.5.3 Delta Aerodynamic Results

Table 4.7-4 shows the results for the original grid system (no VT). The delta aero increments in roll and yaw were very small for panel 6 removed.

	Cl	Cm	Cn
p6	0.09209	-0.00918	0.01287
p9	0.09156	-0.00881	0.01230
clean	0.09205	-0.00869	0.01302
Delta (p6 - clean)	0.00003	-0.00050	-0.00015
Delta (p9 - clean)	-0.00050	-0.00012	-0.00071

Table 4.7-4 Delta Aero Increments - Original grid system (no vertical tail)

The solutions done for the full grid system (baseline and the missing panel 9) with the vertical tail included gave similar delta aero as the original grid system without the tail. Table 4.7-5 shows these results.

	Cl	Cm	Cn
p9	-0.00034	-0.00615	-0.00043
clean	0.00001	-0.00623	-0.00002
Delta (p9 - clean)	-0.00035	0.00008	-0.00040

Table 4.7-5 Delta Aero Increments - Full grid system (w/vertical tail)

To better understand the source of the delta aero, the aero results were broken into the fuselage, wing, and vertical tail components. Table 4.7-6 shows these aero components. The fuselage and tail increments are very small in comparison to the wing increments. This points to the wing having the largest affect on the delta aero increments.

(p9 - clean)	ΔC_l	ΔC_m	ΔC_n
FUSELAGE	0.000016	-0.000046	-0.000022
WING	-0.000355	0.000159	-0.000418
TAIL	-0.000010	-0.000041	0.000039
TOTAL	-0.000348	0.000084	-0.000403

Table 4.7-6 Delta Aero Increments (component breakdown) - Full grid system

4.7.5.4 Observations – Missing RCC Panels (Original Grid System)

Figure 4.7-11 shows the surface C_p for the baseline configuration. Figure 4.7-12 and Figure 4.7-13 show the surface C_p for the panels 6 and 9 removed, respectively. The black dots on the figures represent several of the flight temperature measurement gage locations.

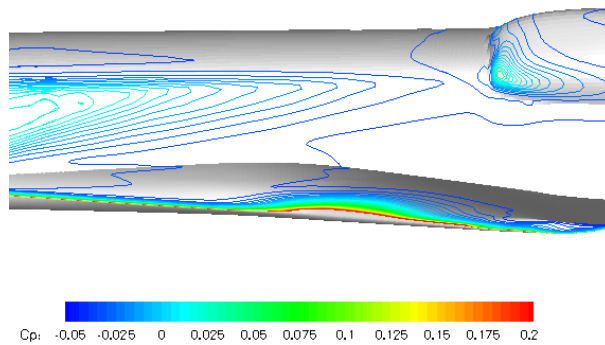


Figure 4.7-11 Surface Pressure (Cp) Baseline (no damage) Configuration.

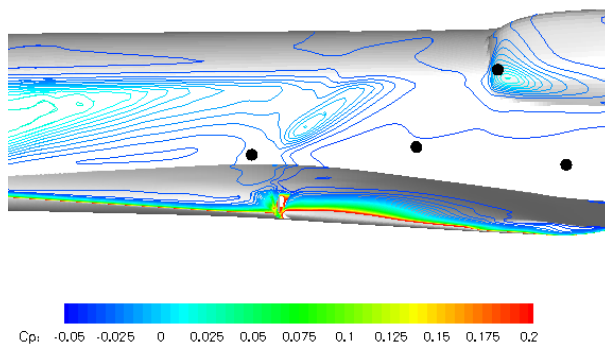


Figure 4.7-12 Surface Pressure (Cp) – Missing RCC Panel 6

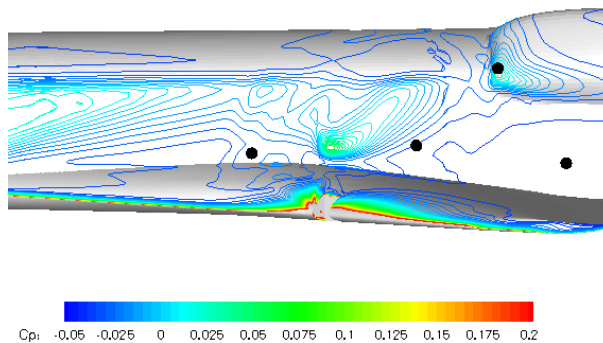


Figure 4.7-13 Surface Pressure (C_p) – Missing RCC panel 9

The interaction between the flow coming through the panel and the fuselage is very apparent for the panel 9 missing case. This impingement is much stronger with panel 9 missing than with panel 6 missing.

4.7.5.5 Observations – Missing RCC Panels (Full Grid System)

To further investigate the leeside interaction, the surface pressures on the vertical tail were analyzed to provide more information on tail pressure increments. Figure 4.7-14 shows the delta pressure coefficient (C_p panel 9 missing – nominal configuration) on the tail. It is evident from this figure the flow field on the tail is disturbed, but the maximum delta C_p values are on the order of 0.01, representing a very small change.

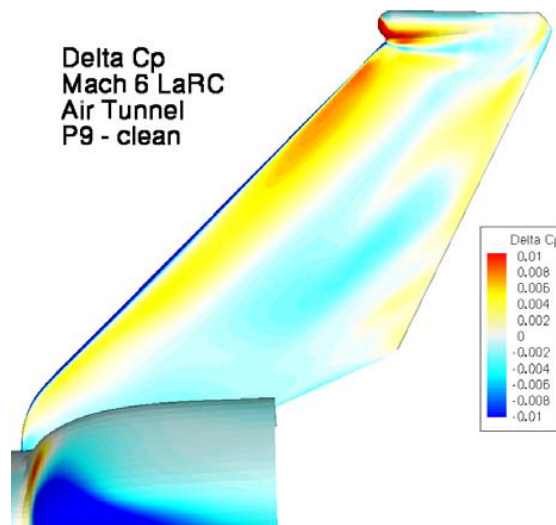


Figure 4.7-14 Delta Pressure (C_p) – Vertical Tail Surface (P9 – Baseline)

Figure 4.7-15 shows surface streamlines ($k = 3$ surface) for both the baseline configuration and the panel 9 missing. The largest difference between the 2 configurations is the flow on the lower part of the tail. The direction of the flow in this region changed directions.

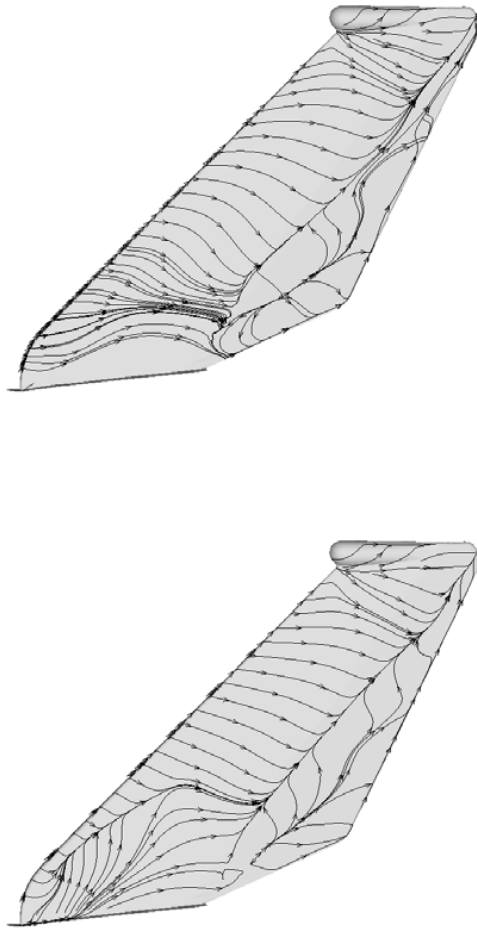


Figure 4.7-15 Surface Streamlines – Baseline and Panel 9 Configurations

The flow field on the leeside of the vehicle is directly affected by the vortex that emanates from the intersection of the wing and the fuselage (strake). Figure 4.7-16 represents this vortex by using volume ribbons. The vortex starting from the left strake never crosses the centerline of the vehicle for the baseline configuration. This is not the case for the missing panel 9 configuration. The vortex is disturbed towards the leading edge of the wing and is then pushed across the pitch plane in front of the tail. This dramatically affects the flow field on the leeside.

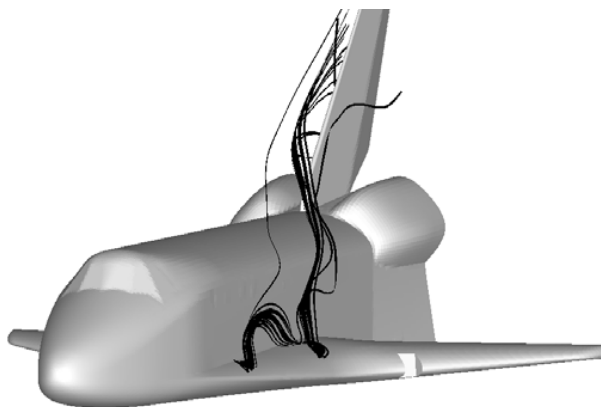
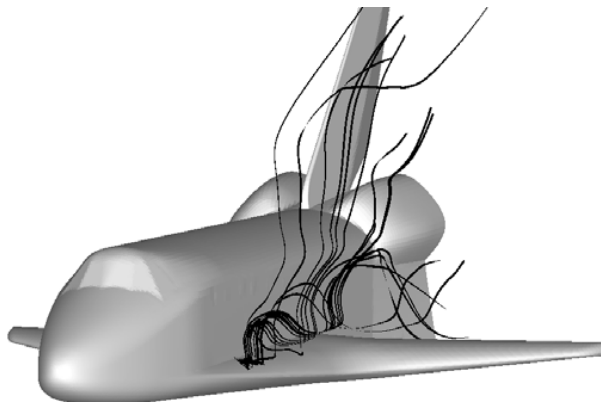


Figure 4.7-16 Volume Ribbons Emanating From the Strake - Baseline & RCC Panel 9 Missing

Based on the volume ribbon patterns, a delta pressure (C_p) plot (similar to Figure 4.7-14) was made showing the leeside of the vehicle, including the tail. Figure 4.7-17 shows this delta C_p plot. The figure shows that the flow on the port and starboard side of the tail is disturbed.

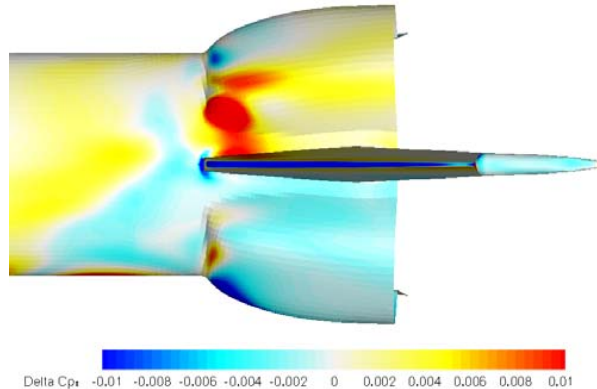


Figure 4.7-17 Delta Pressure (Cp) On the Vertical Tail Surface (P9 – Baseline).

4.7.5.6 Conclusions

The delta aerodynamic increments predicted by the OVERFLOW analysis at Mach 6 tunnel conditions are consistent with test measurements and other sources for Panel 6 or Panel 9 missing. Although the analysis of the tail flow field and the delta pressure coefficient demonstrate differences in the flow field, the delta aero increment from the tail was very small (an order of magnitude less than the increments from the wing).

4.7.6 Aerodynamic Investigation using CART3D CFD Analysis

4.7.6.1 Introduction

CART3D is a high fidelity, inviscid analysis package that uses adaptively refined Cartesian grids to discretize the volume around a defined surface geometry. It is used for conceptual and preliminary aerodynamic design and enables rapid CFD analysis on complex geometries.

4.7.6.2 STS-107 CART3D Case Definition

All the cases were completed at wind tunnel conditions of Mach 6 and 40-degrees angle of attack (corresponding to the LaRC Mach 6 air wind tunnel, Table 4.3-5).

4.7.6.3 Configurations Analyzed

In support of the STS-107 Investigation, different damage scenarios have been analyzed to try and reproduce the aerodynamics observed during Columbia's final flight. These damage scenarios were produced using two different geometries, one without a vertical tail and one including the tail. Karen Bibb, LaRC supplied the grids used to represent the baseline surface geometries. The LaRC GEOLAB defined the WLE RCC panel cutouts used to produce the different damaged configurations analyzed. Figure 4.7-18a shows the clean geometry without the vertical tail, and Figure 4.7-18b shows the clean geometry with the tail. The surface grid for the initial geometry without the vertical tail had a low resolution grid on the leeside, especially in the OMS pod region. Nominally, the resolution is appropriate because at hypersonic conditions, there are not significant aerodynamic interactions and flow features on the leeside of the vehicle. Since the initial analysis focused on WLE damage, this grid was sufficient to resolve the wing surface pressures. Once the analysis shifted to focus on the effects on the OMS pod and tail, the more refined surface grid with the vertical tail was required to ensure the leeside surface pressures were adequately resolved.

There were fourteen damage configurations analyzed using CART3D (listed in Table 4.7-7). Initial analysis focused on WLE damage. The first five configurations analyzed were for entire WLE RCC panels missing on the geometry without a vertical tail. The five configurations analyzed were: RCC 6 missing, RCC 9 missing, RCC 6 and 7 missing, RCC 5-7 missing, and RCC 1-7 missing. Figure 4.7-19 shows RCC 9 missing and an outline of RCC panels 1-7. Note that to model a missing RCC panel in this analysis, solid sidewalls in the cavity were included as a simplification over the actual geometry with an open channel between the RCC and the WLE spar. Additionally, the missing geometry accounts for removal of only the RCC panel and not the carrier panel geometry. Therefore, the back wall surface is approximately 4 to 6 inches forward of the WLE spar.

Based on debris forensics that suggested WLE damage could not include entire panels missing, partial RCC panel damage configurations were addressed. The next four cases analyzed were the lower (or windward half) of the RCC panel missing as well as a missing T-Seal. Three half-panel damage cases were computed: half of RCC 7 missing, half of RCC 8 missing, and half of RCC 9 missing. The T-Seal case was for T-Seal 9 removed, resulting in an open slot or gap between RCC panels 8 and 9. All four damaged configurations were analyzed using the geometry without the vertical tail.

Damage progression cases were analyzed next in an attempt to understand the sensitivity of the delta aerodynamics to increased levels of damage and further investigate leeside interaction effects. The final five cases were computed on the more refined (increased resolution) surface grid for the geometry with the vertical tail. The five cases were: half of RCC 7 missing, half of RCC 8 and all of RCC 9 missing, half of RCC 8 and hole #1 through the wing, lower (windward surface) carrier panel 8 and hole #2 through the wing, and half of RCC 8 and hole #2 through the wing. Hole #1 is the width of RCC 8, 20-inches long and is oriented directly behind RCC 8 funning inboard and aft. Hole #2 is 46-inches long, 28-inches wide and oriented behind RCC 9 and 10, running inboard and aft. Figure 4.7-20 thru Figure 4.7-25 show the holes and missing parts of the RCC and carrier panel.

4.7.6.4 Delta Aerodynamic Results

Table 4.7-7 lists the values of the aerodynamic coefficients for the clean configurations (with & without vertical tail) and the resulting delta values for the damaged configurations analyzed.

	Axial force (+ Aft)	Side force (+ Right)	Normal force (+ Up)	Rolling Moment (+ Right Wing down)	Pitching Moment (+ Nose Up)	Yawing Moment (+ Nose to the Right)
	Delta CA	Delta CY	Delta CN	Delta CI	Delta Cm	Delta Cn
Without Vertical Tail						
Clean	0.05100	0.14983	1.26233	0.18748	-0.06117	0.02718
Panel 6	0.00115	0.00096	-0.00126	-0.00017	-0.00032	-0.00026
Panel 9	0.00202	0.00036	-0.00193	-0.00030	-0.00028	-0.00074
Panels 6-7	0.00255	0.00116	-0.00259	-0.00037	-0.00056	-0.00056
Panels 5-7	0.00336	0.00127	-0.00306	-0.00041	-0.00085	-0.00084
Panels 1-7	0.00358	0.00096	-0.00501	-0.00069	-0.00150	-0.00099
Half 7	-0.00023	0.00039	-0.00374	-0.00007	-0.00283	-0.00008
half 8	-0.00019	0.00046	-0.00394	-0.00013	-0.00263	-0.00011
Half 9	-0.00006	0.00032	-0.00371	-0.00005	-0.00281	-0.00012
T-Seal 9	-0.00024	0.00051	-0.00423	-0.00017	-0.00242	-0.00001
With Vertical Tail						
Clean	0.05125	0.14347	1.25942	0.18578	-0.06233	0.03068
Half 7	0.00021	0.00023	-0.00013	-0.00001	0.00003	-0.00010
Half 8 Full 9	0.00421	0.00159	-0.00454	-0.00067	-0.00028	-0.00156
Half 8 & Hole #1	0.00026	-0.00095	-0.00023	-0.00017	-0.00019	0.00025
Carrier Panel 8 & Hole #2	-0.00002	0.00004	-0.00036	0.00003	-0.00014	-0.00002
Half 8 & Hole #2	0.00061	0.00056	-0.00145	-0.00023	0.00037	-0.00024

Table 4.7-7 CART3D CFD Analysis - Results by Configuration - Delta Aero Coefficients

During latter portion (after EI + 700 sec) of the STS-107 entry flight, Columbia demonstrated a negative delta yaw and a positive delta roll when compared to a nominal entry trajectory. Most of the damage configurations analyzed by CART3D show a negative delta yaw and a negative delta roll, which corresponds to the earlier portion (before EI + 600 sec) of STS-107 entry. The windward half of RCC 8 missing with hole #1 in the wing configuration shows a negative delta roll and a positive delta yaw, a pattern not seen in flight. The windward carrier panel 8 missing with hole #2 in the wing configuration shows a positive delta roll and a negative delta yaw, but the deltas are relatively small.

Figure 4.7-27a shows the surface pressure in terms of pressure coefficient (C_p) on the leeward side of the shuttle for the clean configuration. Figure 4.7-27b through Figure 4.7-29 show the C_p on the leeward side for the complete RCC panel removed damaged configurations. Notice the increase in pressure on the side of fuselage near the region of augmented heating recorded by onboard instrumentation. For these Mach 6 computations on this lower grid resolution system, none of the whole RCC panel out cases affects the pressure on the OMS pod or the area around the base of the tail.

The results from the half RCC missing configurations however do show an increase in the pressure on the OMS Pod. Figure 4.7-29 shows the surface pressure distribution on the OMS Pod for the clean configuration. Figure 4.7-31 and Figure 4.7-32a show the surface pressure distribution on the OMS Pod for the half-panel missing cases, and Figure 4.7-32b is for the missing T-Seal. For half of RCC 7 and half of RCC 8, the pressure on the forward section of the OMS Pod increases. The pressure also increases for the missing T-Seal case, and there is a slight change for the half of RCC 9 missing case. Although there were no OMS pod surface pressure measurements, recovered OMS pod debris indicates significant impact damage most likely attributed from flow through the WLE damage. These cases would support the observation that the initial damage was inboard of RCC 9 as the pressure change on the OMS pod decreases as the damage moves outboard.

The five configurations with the tail were run to evaluate the pressure impact on the tail and the OMS Pod as a possible source for the change in extracted rolling moment after EI + 600 sec. Figure 4.7-33 shows the surface pressure distribution on the tail and OMS Pod for the clean configuration. Figure 4.7-33 through Figure 4.7-36 show the surface pressure distribution on the tail and OMS Pod for the five damage configurations. The half of RCC 8 and all of RCC 9 case had the largest overall impact on the C_p distribution. There was an increase on the tail, OMS Pod and the side of the fuselage. Both Hole #2 cases showed significant impact on the tail and the OMS Pod. Half of RCC 8 and hole #1 increased the pressure on the side of the fuselage. However, it decreased the pressure on the OMS pod and tail because of the orientation of the hole with respect to RCC panel 8. The results indicate only a small amount of interaction with relatively low changes in pressure over a limited area of the vertical tail and OMS pod. Based on these and other results it was concluded that the leeside flow interaction with the vertical tail and OMS pod was not the primary source for the trend change in extracted rolling moment.

4.7.6.5 Observations

The complete loss of an RCC panel matches the early off-nominal flight trends, but does not match the trends later in flight. Additionally complete RCC panel loss increases the pressure only on the side of the fuselage, consistent with other side fuselage observations, but does not impact the vertical tail region (at the computed Mach 6 condition). However, the loss of the windward half of RCC panels 7 and 8 redirects the flow onto the OMS pod and tail area, which increases the pressure in those areas. These increases are not large enough to produce the delta roll and delta yaw trends seen in flight, but are consistent with debris forensics and elevated heating rates observed on the OMS pod

One of the most influential damage configurations is a hole through the wing. The effect on the OMS pod and tail area is driven by the orientation of the hole with respect to the flow field and alignment of the fuselage. The delta aerodynamics for these cases is more consistent with early flight trends.

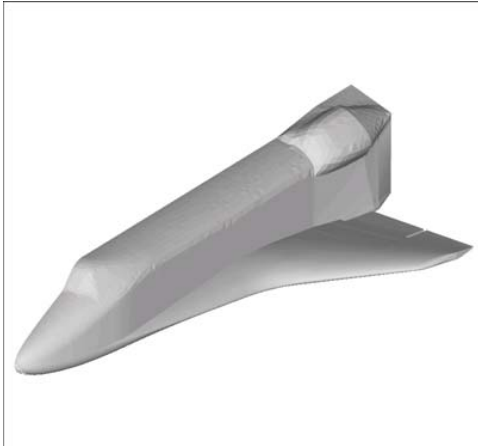


Figure 4.7-18a&b Baseline Clean Geometry (a) – no Vertical Tail & (b) with Vertical Tail

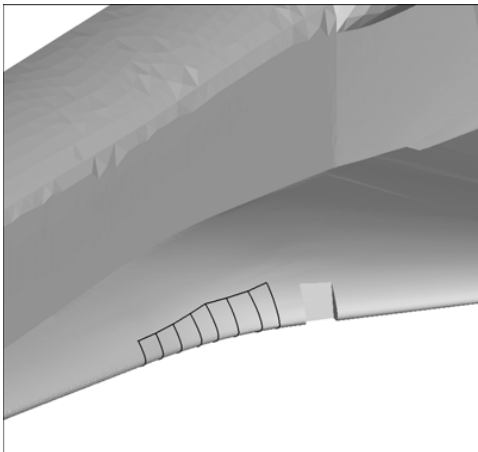


Figure 4.7-19 Missing RCC 9 with Outline of RCC 1 thru 7

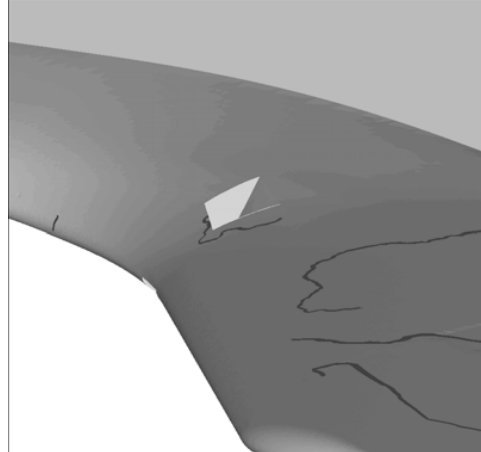


Figure 4.7-20 Windward View – Missing Lower Half of RCC 8 w/Hole #1 thru Wing

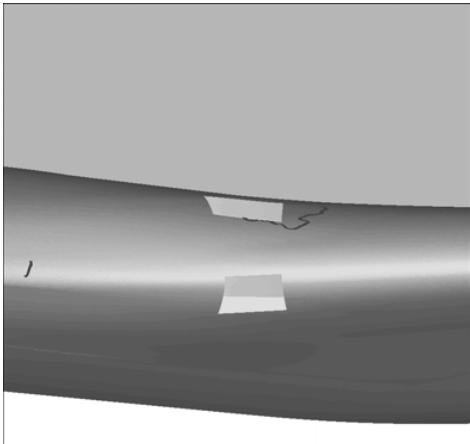


Figure 4.7-21 Front View – Missing Lower Half of RCC 8 w/Hole #1 thru Wing

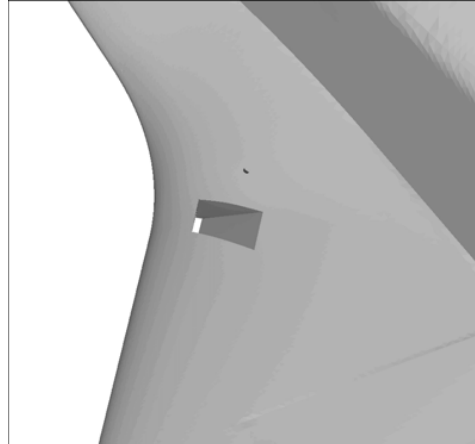


Figure 4.7-22 Windward View - Carrier Panel 8 Missing and Hole #2 in Wing

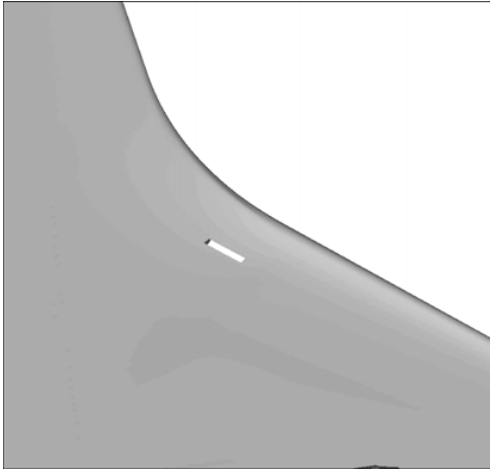


Figure 4.7-23 Windward View - Lower Carrier Panel 8 Missing and Hole #2 through Wing

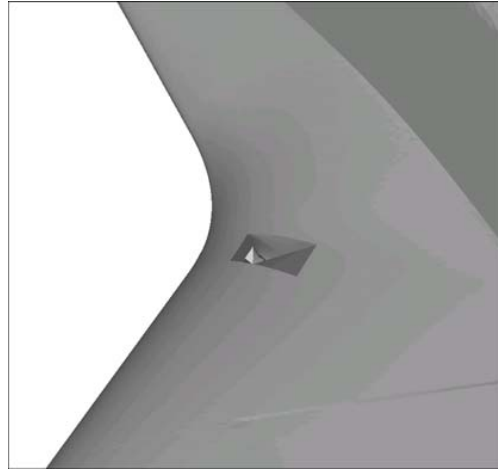


Figure 4.7-24 Leeward View - Lower Half of RCC 8 Missing and Hole #2 through Wing

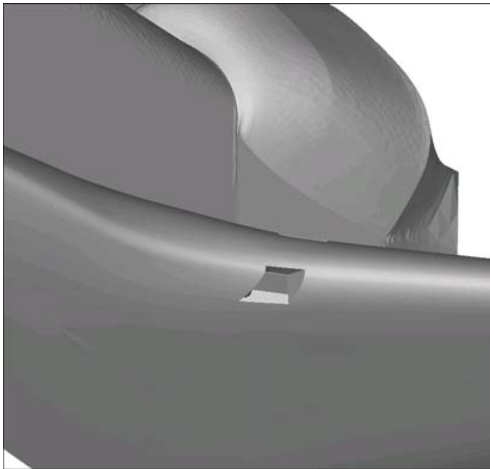


Figure 4.7-25 Windward View - Lower Half of RCC 8 Missing and Hole #2 Through Wing

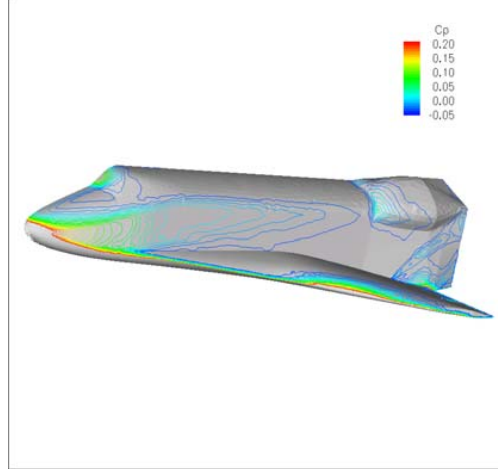


Figure 4.7-26 Surface Pressure (Cp) – Baseline Configuration

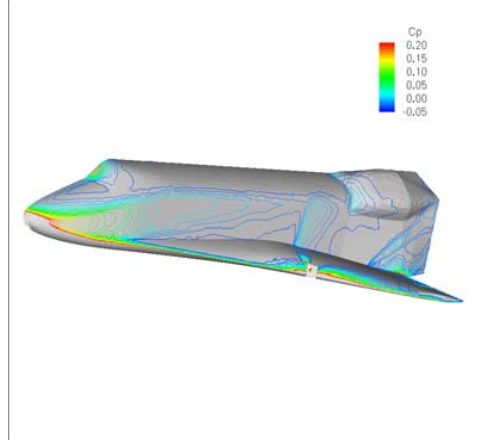
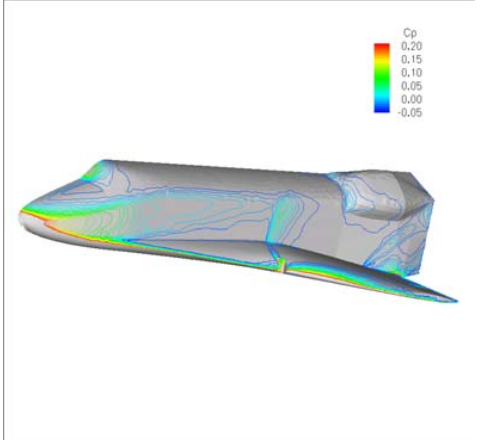


Figure 4.7-27a&b - Surface Pressure (Cp) – (a) Missing Panel 6 & (b) Missing Panel 9

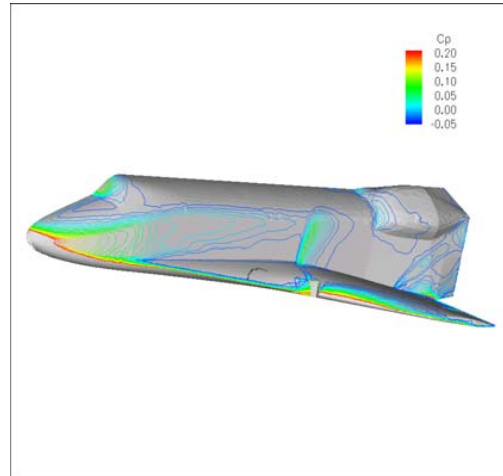
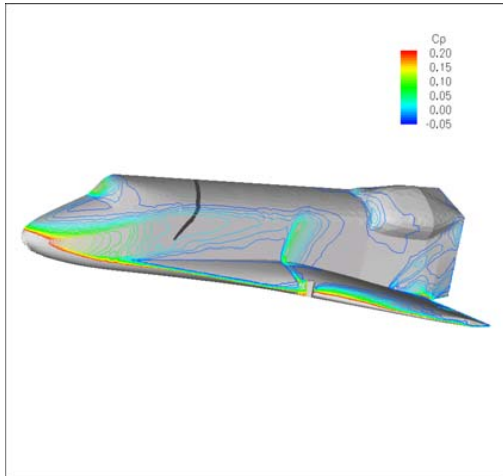


Figure 4.7-28a&b - Surface Pressure (C_p) - (a) Missing RCC Panels 6&7 & (b) Missing 5-7

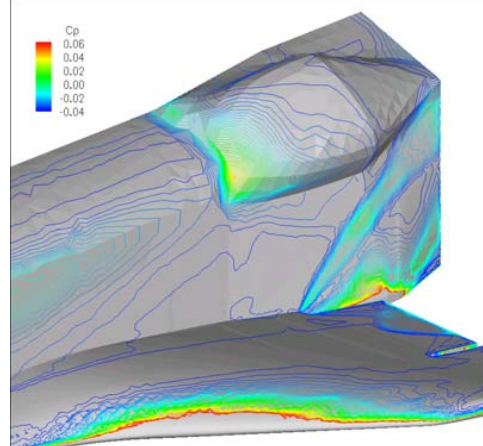
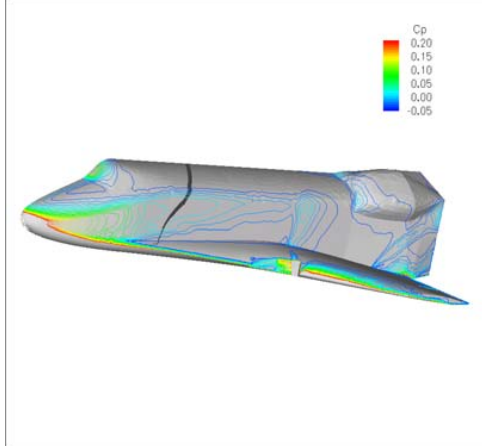


Figure 4.7-29 Surface Pressure (C_p) - Missing RCC Panels 1 through 7

Figure 4.7-30 Surface Pressure (C_p) - Baseline Configuration (OMS Pod)

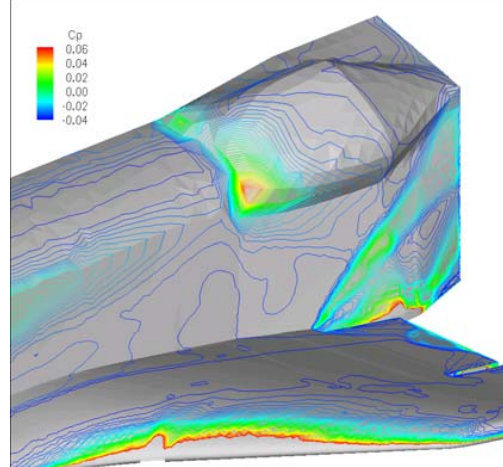
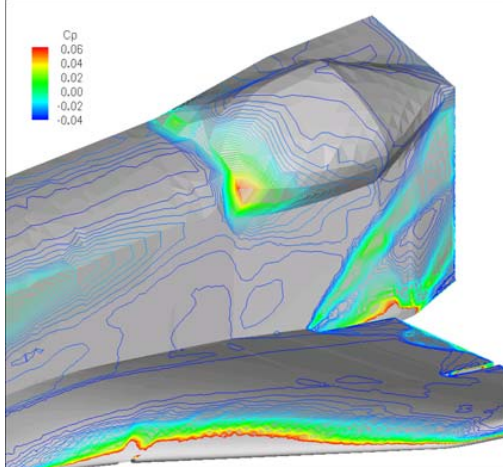


Figure 4.7-31a&b - Surface Pressure (C_p) - (a) Lower Half of RCC 7 & (b) Lower Half RCC 8

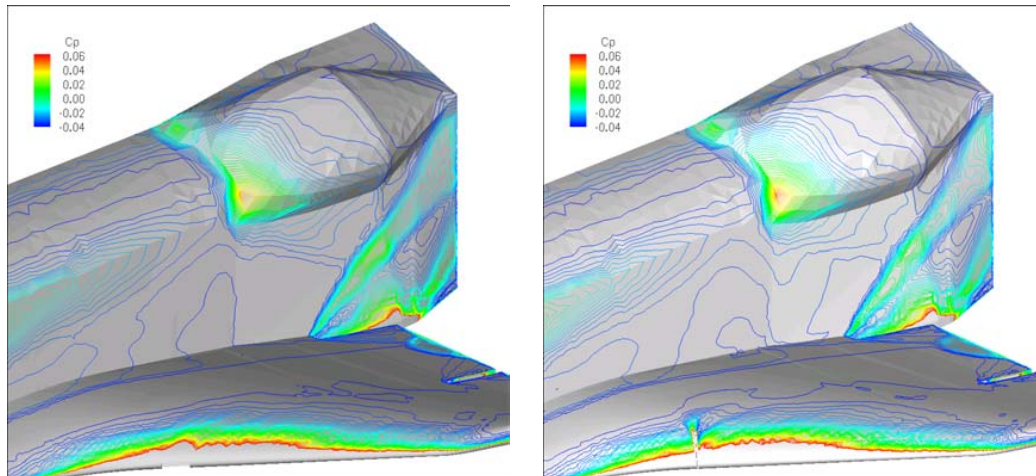


Figure 4.7-32a&b Surface Pressure (C_p) - Missing Lower Half RCC 9 & (b) Missing T-Seal 9

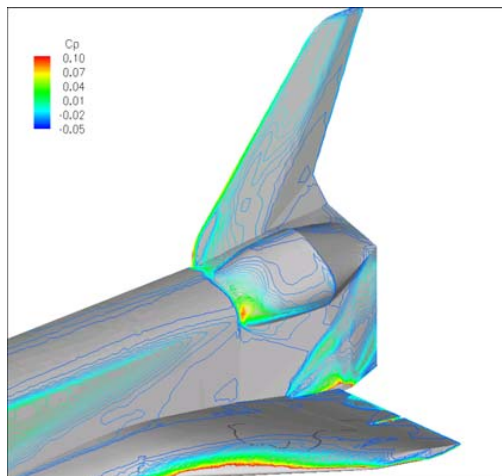


Figure 4.7-33 Surface Pressure (C_p) - Baseline Configuration (OMS & VT)

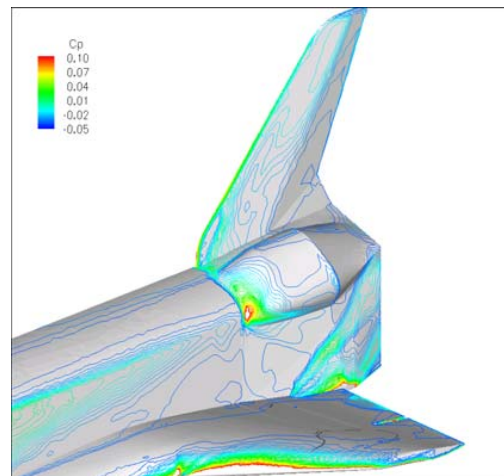


Figure 4.7-34 Surface Pressure (C_p) - Lower Half of RCC 7 Missing

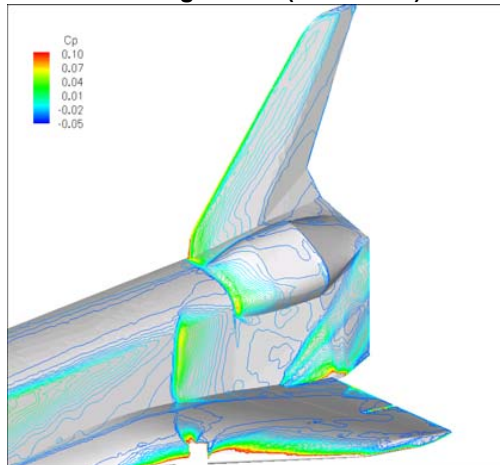
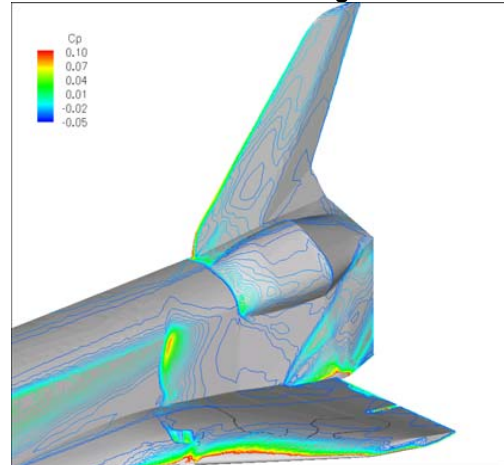
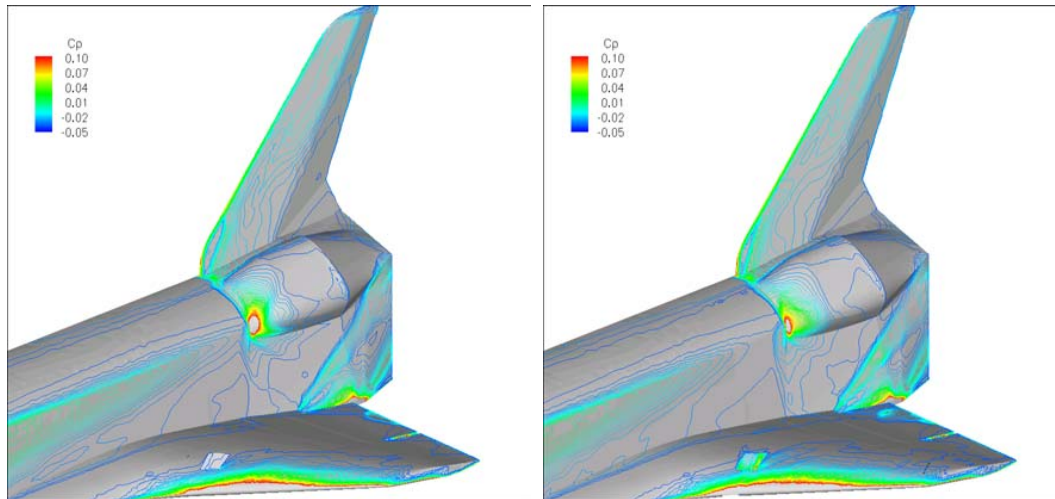


Figure 4.7-35a&b Surface Pressure (C_p) - (a) Missing Lower Half of RCC 8+ all of RCC 9 (b) Missing Lower Half of RCC 8 + Hole No. 1 through Wing





4.7.7 Aerodynamic Investigation using USA CFD Analysis

Boeing-Huntington Beach completed a CFD analysis of a damaged orbiter configuration (missing RCC Panel 6) using their USA Navier-Stokes solver at flight conditions.

4.7.7.1 USA Description

The unified solution algorithm (USA) code is a very versatile flow solver that can be used to compute numerical solutions to a large class of aerodynamic and aerothermodynamic problems by solving the Euler or Reynolds averaged Navier-Stokes (RANS) equations. The discretization is of TVD formulation using finite volume framework. Various Riemann solvers can be used with the preferred one being the modified Lax-Freidrichs scheme. A multi-zonal structural grid bookkeeping method facilitates the treatment of complex geometric topologies. A real gas approach based on a finite rate chemistry formulation can be coupled or uncoupled with the fluid dynamics to treat reacting and non-reacting gaseous species. In this work, the approximate factorization scheme using the implicit time marching option was used. The simulations were speeded up using grid-sequencing. The convergence of flow simulations were confirmed by monitoring the time history of surface results.

4.7.7.2 STS 107 CFD case definition

This analysis was done to quantify the effect on the force and moment coefficients due to the removal of the leading edge panel number 6. The cavity was modeled without any representation of the actual exposed interior components of the wing leading edge. The geometry represents the initial panel 6 definition. As detailed in Section 4.3.2.3.2 this is somewhat less than the full panel 6 geometry.

Configurations analyzed

There were two real gas CFD cases considered under this effort. The first one consisted of analysis of the intact vehicle and the second was for vehicle with RCC panel 6 missing. Flight conditions consisted of free stream Mach 18 and angle of attack of 40 degrees. Equilibrium air assumptions were utilized to handle this Mach number. A third case with perfect gas assumption was also conducted for the baseline geometry.

4.7.7.3 Delta Aerodynamic results

CASE	Geometry	Chemistry	CA	CN	CLM	CLL	CLN
OADB	OADB	-	0.06284	1.1598	-0.01667	0	0
1	Baseline	Real Gas/Equilibrium	0.06861	1.1158	-0.01297	0	0
2	"	Perfect gas	0.06439	1.201	-0.04693	0	0
3	RCC#6 Off	Real Gas/Equilibrium	0.069	1.1587	-0.0248	-0.0004	-0.0015

4.7.7.4 Observations/Conclusions

The analysis were carried out using an orbiter half model. The rolling moment and yawing moments were estimated from two half model solutions with the assumption of flow being essentially axial along the symmetry plane. The magnitude of these numbers were of the same order as the error band for the solution convergence and hence not highly reliable.

4.7.8 CFD Tools:

4.7.8.1 FELISA Inviscid Mesh Generation and Flow Solver

Computations of the present study were performed using the FELISA unstructured grid software. This software package consists of a set of computer codes for unstructured grid generation, and the simulation of three-dimensional steady inviscid flows using unstructured tetrahedral grids.

The mesh generation process starts with the definition of a geometry. The computational domain must be a watertight solid. The solid can be developed within a solid modeling CAD package (i.e., Unigraphics or Pro-Engineer), a geometry preprocessor such as GridTool, or by hand. For all of the FELISA work on the Columbia Accident Investigation, the baseline and damaged geometry models were developed within GridTool, with the starting baseline geometry as the structured grid developed at LaRC several years ago using a 1997 Orbiter CAD model. (A solid model based on the 2003 Orbiter CAD model was developed for use with FELISA, but it came available in the middle of the investigation, and the decision was made to continue using the original model.) The second step in the mesh generation process is to graphically define the spacing functions, which determine local mesh size, within either GridTool or GridEx. (GridEx is a mesh generation package under development at LaRC, and has the option of using the FELISA mesh generator). The mesh generation takes place in 2 steps. The surface is triangulated with either the FELISA-SURFACE code, or within the GridEx tool. Generation of the tetrahedral volume mesh is performed using the FELISA-3D_mesh code. Both surface and volume grids are essentially isotropic with little or no stretching. Once the baseline geometry and the mesh spacing were defined for the flight and CF4 conditions, producing a mesh for a new damage scenario only took a couple of hours of preparation work, and 4-8 hours of computer time. Mesh sizes for the damage scenario cases ranged from 2.5 to 5.5 million nodes, up to 30 million tetrahedral elements.

Two flow solvers are available with FELISA—one applicable for transonic flows, and the other for hypersonic flows. The hypersonic flow solver has options for perfect gas, equilibrium air, CF4, CO2, and several other gases (including Mars, Neptune, and Titan atmosphere) in equilibrium. This solver also has the capability of solving chemical non-equilibrium flow, and real gas (chemical and thermal non-equilibrium) flow. This software package has been used extensively for inviscid computations for X-34, X-33, X-37, Mars landers, and also for the Space Shuttle Orbiter at high angles of attack (see Ref. 1). The hypersonic flow solver with the equilibrium air and with the CF4 options was used for the present computations. The solvers are parallelized using MPI for rapid computations. For this investigation, the code was run both a local cluster of PC's with up to 24 processors, and on the NAS Origin 3000 system, 'chapman', with up to 64 processors. Wall clock time for obtaining a converged solution ranged from 8 – 24 hours, and depended on mesh size and the complexity of the damage scenario.

Post-processors such as the aerodynamic analysis routine are part of the software package. More information on FELISA software may be found in Ref. 2. A description of the hypersonic flow solver may be found in Ref. 3.

1. R. K. Prabhu: "Inviscid Flow Computations of the Shuttle Orbiter for Mach 10 and 15 and Angles of Attack 40 to 60 Degrees," NASA/CR-2001-211267, December 2001.

2. J. Peiro, J. Peraire, and K. Morgan: "FELISA System Reference Manual and User's Guide," University College Swansea Report, 1993.

3. K. L. Bibb, J. Peraire, and C. J. Riley: "Hypersonic Flow Computations on Unstructured Meshes," AIAA Paper 97-0625, January 1997.

4.7.8.2 Overflow

OVERFLOW is a structured (overset) grid, Navier-Stokes flow solver. It uses a finite-difference formulation, with flow quantities stored at the grid nodes. OVERFLOW has central- and Roe upwind-difference options, and uses a diagonalized, implicit approximate factorization scheme for the time advance. Local time stepping, multigrid and grid sequencing are used to accelerate convergence to a steady state. In this study, 2nd-order central differencing with Jameson-type 2nd/4th-order scalar dissipation is used. Thin-layer viscous terms are computed in wall-normal directions by default.

References:

D.C. Jespersen, T.H. Pulliam, and P.G. Buning, "Recent Enhancements to OVERFLOW," AIAA-97-0644, AIAA 35th Aerospace Sciences Meeting, Reno, NV, Jan. 1997.
<http://science.nas.nasa.gov/~jesperse/papers/aiaa97-0644.ps.Z>

P.G. Buning, D.C. Jespersen, T.H. Pulliam, G.H. Klopfer, W.M. Chan, J.P. Slotnick, S.E. Krist, and K.J. Renze, "OVERFLOW User's Manual, Version 1.8s," NASA Langley Research Center, Nov. 2000.

4.7.8.3 CART3D

CART3D is a high fidelity inviscid analysis package developed at NASA Ames Research Center. The geometry required is represented as a closed, watertight, triangulated surface. From this triangulated surface, CART3D produces the volume mesh. The volume mesh is a topologically unstructured, adaptively refined, Cartesian mesh produced around the geometry. The user can control the initial mesh division, the number of refinement levels, and specify certain regions for more cell refinement to develop a useable volume mesh. Using the volume mesh, CART3D uses a domain-decomposition, scalable, multi-level solver to solve the inviscid flow Euler equations.

For more information, visit the CART3D home page at <http://people.nas.nasa.gov/~aftosmis/cart3d/cart3Dhome.html>

4.7.8.4 GASP

The GASP Real-Gas Navier-Stokes code was the primary code for solutions accomplished at Ames Research Center. This code originated as a commercially available code developed at AeroSoft, Inc (ref ARC1), but has been modified at ARC to enhance both capability and robustness specifically for hypersonic reentry applications (ref ARC2, ARC3, ARC4).

The GASP Reynolds Averaged Navier-Stokes code is a three-dimensional (3D) finite-volume code. Upwind flux options exist for this code, but for the present solutions the van Leer (ref ARC5) inviscid flux formulation was applied in all three directions. A formally 3rd order upwind-biased MUSCL scheme combined with min-mod limiter is selected to provide higher order accuracy. Experience at ARC with this code has indicated that wall normal spacing is sufficient to obtain accurate heat transfer with the Van Leer flux formulation and 3rd order accuracy provided the wall node Cell Reynolds number is kept below a value of 5. For most of the calculations provided in the present work the wall node Cell Reynolds number is approximately 1, which yields the best results in convergence and accuracy. Time advancement to steady state is accomplished with either a 2D Approximate Factorization, AF2, in the nominal cross-flow plane with planar relaxation in the streamwise direction, or, alternatively, with a point-Jacobi algorithm with inner iterations. Experience at ARC has shown that these two time-advancement schemes as implemented in GASP are nearly identical in convergence, robustness and speed.

The 5-species finite reaction rate model for dissociating air of Park (ref ARC6) was used in these calculations using GASP. In this chemistry model, air is composed primarily of molecular nitrogen, N₂, and molecular oxygen, O₂, with the possibility of dissociation at high temperature into atomic nitrogen, N, and atomic oxygen, O, followed by formation of NO. For the high Mach number, high altitude portion of a low Earth orbit reentry trajectory as considered herein, the molecular oxygen, O₂, present in the atmosphere will almost entirely dissociate into atomic oxygen, O, upon encountering the bow shock. However, N₂ will undergo but slight dissociation with lesser amounts of N and NO formed. The reaction rates are typically slow enough that little recombination occurs for hypersonic flows prior to the exit boundary except for that due to the catalytic effect of certain thermal protection surface materials.

The real-gas air chemistry has an important effect on the hypersonic flow about the orbiter by altering the shock location since energy is required to dissociate the molecular oxygen through the shock, the temperature and density rise through the shock are not as great as would otherwise occur for a perfect gas thereby reducing the effective gamma for the real gas in the shock relations. A further real-gas effect is that chemical energy is released at the shuttle surface due to recombination of O to O₂ as a consequence of the catalytic behavior of the RCG shuttle tile material. This catalytic wall effect yields a higher heating rate to the wall than for non-catalytic materials.

Species transport properties are calculated using Blottner relations with mixture properties calculated using Eucken relations. See ref ARC1 for further details.

Stewart (ref ARC7) characterized the surface catalytic recombination of air due to various thermal protection system insulation materials including RCG as used on the windward side of the shuttle orbiter. RCG and other

catalytic materials act to enhance the rate of recombination of atomic oxygen into molecular oxygen and of atomic nitrogen into molecular nitrogen. Molecular NO is assumed to experience no catalytic effect. In the process, additional thermal energy is released to the wall due to the chemical reaction occurring at the surface.

The primary wall boundary condition used for these shuttle calculations is that of radiative equilibrium combined with the above RCG catalytic behavior. In this viscous wall boundary condition, there is an assumption that the radiative heat transfer from the wall exactly balances the thermal energy transfer to the wall due to convective heat transfer combined with energy release to the wall due to the surface catalytic chemical reaction. The radiative equilibrium boundary condition requires the simultaneous solution of 4 species equations (molecular NO is not considered catalytic) combined with an equation for the energy balance, all of which are written at the wall node. To then solve this wall boundary condition for each Navier-Stokes solver iteration, a Newton-Raphson method achieves quadratic convergence.

Additional boundary conditions used include conventional point-to-point zonal boundaries, adiabatic viscous wall, free-stream, and a specified back-pressure outflow boundary condition. Point-wise boundary conditions can be specified optionally for any of the 6 faces of each grid block and were used for the vented cavity panel 9 solutions.

Most of the solutions delivered were laminar throughout the solution domain. However, some eddy-viscosity turbulence models calculations were conducted to establish approximate turbulence heating enhancements and for validation purposes. Turbulence models implemented into this code include the Baldwin-Lomax algebraic model of Baldwin-Lomax (Ref ARC7) and the 2-eq SST/K-Omega turbulence model of Menter(Ref ARC8). These models have compressibility corrections suitable for hypersonic flows and have been validated for heat transfer in hypersonic strong interactions as implemented in the ARC version of the GASP code(see Ref ARC3). A means for specification of turbulence transition is implemented in the code, but is not used for the present work.

The GASP code was run initially on a serial processor computer (Intel 2 GHz XEON processor running RedHat Linux v 7.3). These early runs were for fully catalytic solid surface rather than RCG on grids of approximately 3/4 million grid points and took 96 hours. To improve throughput, subsequent work was moved to the NAS parallel-processing cluster, chapman, which is based on up to 1024 SGI Origin O3K cpus. For the parallel processor runs, the grids were decomposed into as many as 48 grid blocks each of which was then run on a separate SGI processor in the NAS chapman cluster. With grids of 1.9 million grid points, the chapman parallel processor runs took approximately 48 hours.

Convergence criterion was based on examination of residual history, temperature and pressure history for selected surface points during the entire iteration sequence, and when convergence was nearly complete examination of delta T and delta P surface plots separated by 50 to 200 iterations. Typically the L2 residual would drop by 5 orders of magnitude and the selected surface temperatures and pressures would become constant. The delta T and delta P surface plots were facilitated by the gasptools package written by D. Prabhu and M. Wright of Ames and which is based on perl scripts making use of the GASP print utility and the Tecplot plotting package. Typically the delta T surface plots were examined for constant temperature within 5 degrees over the entire shuttle surface. Some of the damage cases exhibited some oscillation of approximately a 10 degree K magnitude which was deemed acceptable inasmuch as there existed a physical basis.

4.7.8.5 USA

The unified solution algorithm (USA) code is a very versatile flow solver that can be used to compute numerical solutions to a large class of aerodynamic and aerothermodynamic problems by solving the Euler or Reynolds averaged Navier-Stokes (RANS) equations. The discretization is of TVD formulation using finite volume framework. Various Riemann solvers can be used with the preferred one being the modified Lax-Freidrichs scheme. A multi-zonal structural grid bookkeeping method facilitates the treatment of complex geometric topologies. A real gas approach based on a finite rate chemistry formulation can be coupled or uncoupled with the fluid dynamics to treat reacting and non-reacting gaseous species. In this work, the approximate factorization scheme using the implicit time marching option was used. The simulations were speeded up using grid-sequencing. The convergence of flow simulations were confirmed by monitoring the time history of surface results.

5 AEROTHERMODYNAMICS

5.1 Introduction

5.1.1 Team Objective

The objective of the aerothermodynamics team was to define local and acreage predicted heating environments of the Orbiter for nominal and damaged configurations in support of the Columbia accident investigation. These environments were used to explain the anomalies in the flight data and were provided to the thermal structures team in support of various thermal analyses, Figure 5.1.3-1.

5.1.2 Aerothermodynamics Overview –Orbiter Perspective

The discipline of aerothermodynamics as applied to the Orbiter principally refers to the aerodynamically induced heating of the vehicle during high speed flight. Significant aerodynamic heating occurs at Mach numbers of 2 and above. For the Orbiter, the highest heating is observed during re-entry from orbit as it descends into the earth's atmosphere traveling at Mach numbers greater than 25.

The heating is a result of the conversion of Orbiter kinetic energy into thermal energy. As the Orbiter passes through the atmosphere at high Mach numbers a shock wave is formed in front of the vehicle, called the bow shock. The bow shock processes convert the kinetic energy into thermal energy by reducing the air speed while tremendously increasing its temperature. Just behind the shock wave, the air can reach temperatures as high as 10,000° F. At these temperatures, the majority of the molecules that make up air, N₂ and O₂, dissociate into their respective atomic constituents. Such dissociated gases are termed high temperature gases. After passing through the bow shock, the heated dissociated gas flows around the vehicle, and thus the energy of the gas will be convectively transferred to heat the surface. Because this heating is extreme during re-entry, a thermal protection system (TPS) is required.

In order to determine the rate at which the heat is transferred to the surface of a vehicle, the flow physics that the vehicle will encounter must be understood, i.e., bow shocks, wing shocks, shock interactions, surface boundary layers and boundary layer state (laminar, transitional, or turbulent), shock-boundary layer interactions, and boundary layer separation and reattachment zones. The heat transfer rate will be a function of the vehicle geometry, its orientation to the flow, the surface temperature of the vehicle, the trajectory being flown through the atmosphere, and the TPS properties. Lastly, at Mach numbers greater than about 5, in a regime called hypersonic, chemical reactions in the air due to the energy exchange are significant. These reactions not only affect the heating of the vehicle but also its aerodynamics.

Flow chemistry affects the shock waves, pressure distributions, and heating distribution around the vehicle. As mentioned previously, at the speeds of Orbiter atmospheric re-entry, all of the molecular oxygen and most of the molecular nitrogen dissociate into their atomic forms via an endothermic reaction. This dissociation occurs due to the heating caused by the initial bow shock. The flow chemistry within this dissociated region may be considered in either a chemical equilibrium or non-equilibrium state, which also has an effect on the heat transfer rate. Determining the state depends upon the speed of the chemical reactions compared with the speed of the vehicle. It is during the phase of re-entry in which the dissociated region of the flow is also in a chemically non-equilibrium state that interaction of the dissociated gas with the TPS surface material properties can have a significant impact on the amount of heat being transferred to the vehicle. Surfaces that are non-catalytic inhibit the recombination of atomic nitrogen and oxygen and thus minimize the amount of heat transfer, whereas fully catalytic surfaces maximize the heat being transferred from the gas to the surface. In the case of the Orbiter TPS, both the tiles and leading edge materials are considered partially catalytic and are closer to non-catalytic than fully catalytic. This low partial catalytic property was designed into the TPS system to reduce the amount of chemical recombination energy transferred to the surface.

All of these issues must be considered when providing heating environments to be used in follow-on analyses. For a more thorough discussion on aerothermodynamics and high temperature gas dynamics, please refer to the works of Bertin and Anderson.

5.1.3 Approach to Determining Required Environments

As mentioned, there are many factors that need to be understood in order to determine Orbiter heating environments. Most of the previous work on determining these environments focused on a nominal Orbiter configuration during the TPS design and certification. Determining the environments for a damaged Orbiter is a more difficult problem. First, the size, shape, and location of the original and progressing damage are unknown. Second, because the damage exposes internal structure and permits external gases to enter internal cavities, the problem becomes a mixed internal-external flow problem. Finally, the problem is further complicated by the fact that as the damage to the Orbiter progressed, both the external and internal geometry changed, and the free stream conditions were also continuously changing.

During the design and operation of the Orbiter, and the design of more advanced vehicles since, numerous tools and testing techniques have been developed, and they were applied in support of this investigation. These tools include engineering methods using simplified geometries (e.g., spheres for nose caps, cylinders for wing leading edges), computational fluid dynamics (CFD), direct simulation Monte Carlo techniques (DSMC), and wind tunnel testing along with the associated instrumentation. The certified Orbiter heating model was also used as the benchmark for the Orbiter external heating environment as well as existing computational and testing data. This certified heating model is described in Section 5.2.2. The tools and techniques utilized for the certified Orbiter heating model were applied to nominal configurations with as-designed outer mold line (OML) geometry lines. There have been very limited pre-accident studies involving heating of the internal structure as a result of a penetration in the TPS. Those particular studies dealt with micrometeoroid penetrations and not the larger scale damage being considered as the root cause of the Columbia accident. The consideration of large scale damage to the Orbiter represented a new area of engineering analysis, especially for the determination of the internal heating environments.

In order to provide the external and internal heating environments needed for the investigation, a team of engineers and scientists from government, industry, and academia was formed. Two sub-teams were then formed - one focusing on external heating environments and the other on internal heating environments. The team decided that the damage configurations to be assessed were to be treated as static or at most quasi-static, in order to reduce the complexity of the analyses being performed. Also, it was recognized that since there was no time for a formal verification process of the environments being provided, the use of engineering best practices, multiple solution sources, and team review of the data would be sufficient. The idea was that the data were to be used in support of determining the plausibility of a given scenario and not to define the exact environments, because the exact configuration of the damage would never be known.

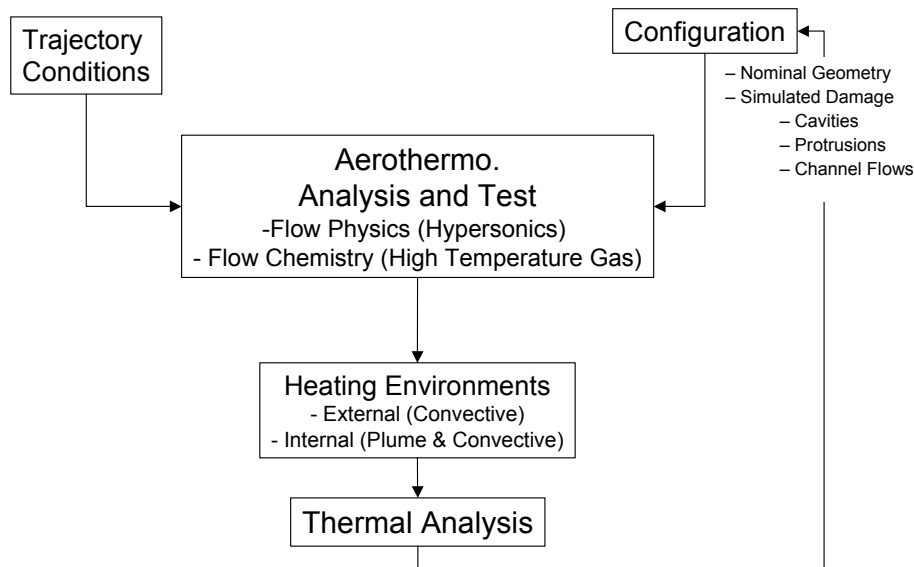


Figure 5.1.3-1 Aerothermodynamics Analysis Process

5.2 Orbiter External Aerothermodynamic Environments (Nominal & Damaged Configurations)

External aerothermodynamic environments for both nominal and damaged Orbiter configurations were needed for several aspects of the investigation. These include assessing the flight data using the aerothermodynamic results directly, qualitatively and/or quantitatively, or as input to the internal environments and thermal analysis teams. This section will review the relevant STS-107 flight data pertaining to the external environment and the working scenario, provide background on the certified Orbiter entry heating methodology, present the results from wind tunnel testing and computational analyses, and, finally, apply those data to the working scenario issues described in this section.

5.2.1 Orbiter OML/Skin Flight Data Observations

During the STS-107 re-entry, several off-nominal sensor readings on the Orbiter OML were recorded on the recovered Modular Auxiliary Data System (MADS) recorder. Also, several Orbiter Instrumentation (OI) sensors on the inner structure showed off nominal readings. Although there were a significant number of other off-nominal sensor readings in the MADS and OI data, those discussed in this section are pertinent relative to the external flow field and how they relate to the working scenario. The specific sensors to be discussed in this section include the surface thermocouples (T/Cs) on the left side fuselage and left OMS pod, the temperature sensors on the chin panel expansion seal, vacuum vent nozzle, water dump nozzle, and a surface T/C just behind the RCC Panel 9 and Panel 10 interface. Although not Orbiter flight data, the Kirtland photo image will be discussed in this section as it potentially shows a damaged Orbiter configuration.

5.2.1.1 Side Fuselage and OMS Pod

From the data available via the OI system, three measurements on the side fuselage indicated off nominal increased heating responses compared with previous flight data. The most significant of these increased heating responses was from V34T1106A, the location of which is shown in Figure 5.2.1-1. On the MADS there were 11 out of 14 surface T/Cs that indicated off-nominal response during the STS-107 re-entry prior to LOS. Those sensors showed both increased and reduced heating effects on the left side fuselage and OMS pod (locations depicted in Figure 5.2.1-1), as compared with previous flight data. Figure 5.2.1-2a – f show examples of these comparisons. The reduced heating was noted on the forward portion of the OMS pod and two sensors on the side fuselage-payload bay door area and began as early as 49:49 GMT (EI+340 sec). It is noteworthy that during this early part of the STS-107 flight, between 49:49 GMT (EI+340 sec) and about 52:09 GMT (EI+480 sec), only off-nominal low heating rates were

observed in any of the available side fuselage or OMS pod sensor data. Between 52:39 (EI+510 sec) and 53:09 GMT (EI+540 sec) the heating began to increase above the nominal range at various gauge locations compared with previous flights. This heating increase began with two measurements on the forward part of the OMS pod, V07T9978 and V07T9976. The different onset times for off nominal increased heating at the various gauge locations are a significant indicator of damage progression occurring on the Orbiter, Figure 5.2.1-1 and Figure 5.2.1-3.

An analysis was performed to back out the relative decrease or increase in heating that was observed. Since these were surface T/C's, an radiation equilibrium wall condition assumption can be made such that

$$\frac{\dot{q}_{STS-}}{\dot{q}_{Nominal}} \cong \frac{T_{STS-}^4}{T^4}.$$

In this relation, \dot{q} is the heat transfer rate and T is the surface temperature in degrees Rankine. Using an average over previous flight data as a nominal value, a ratio of the disturbed to nominal heating was obtained. For all the sensors that experienced reduced heating during the early portion of the flight, before 52:09 GMT (EI+480 sec), the ratio of heating ranged from 0.6 to 0.8. The sensors on the OMS pod that showed reduced heating experienced heating ratios of 0.6 to 0.7 compared with previous flights. During the segment of the flight where off-nominal higher heating rates were observed, after 52:09 GMT (EI+480 sec), the heating ratios across several sensors on the side fuselage and OMS pod varied from 1.7 to 5.2.

A close examination of the temperature response of V07T9220 indicates at least two significant events during the period between 52:39 GMT (EI+510 sec) and 57:19 GMT (EI+850 sec), Figure 5.2.1-4. Observed debris events were co-plotted on the side fuselage and OMS pod data to investigate any correlation to the observed temperature increases, Figure 5.2.1-5, Figure 5.2.1-6, and Figure 5.2.1-7. The data for these gauges indicate that significant external changes were occurring on the Orbiter even before the first debris event was observed. Other flight data indicate that the wing spar had already been breached by the time the increased heating on the OMS pod was experienced. However, debris events 5 and 6 (with the flash) stand out as correlating well with changes in the slope of the temperature response. These data indicate a progression of damage on the wing that resulted from initial damage in the panel 5 through 9 region.

Finally, a check on the surface emittance of tiles recovered from the OMS pod region was performed to assess whether or not surface contamination could be the cause of the observed temperature response. If the heating environment were nominal, then the emittance of the TPS would have had to decrease to 0.3 from the nominal 0.85 value in order to match the temperature response, Figure 5.2.1-8. The emittance of these post-accident tiles was measured at NASA KSC and was shown to be nearly the same as a pristine tile. Therefore, the side fuselage and OMS pod measurements are believed to be accurate indicators of the reduced and increased heating.

5.2.1.2 Wing Surface T/C V07T9666A

V07T9666A is a surface T/C located on the lower wing immediately aft of the panel 9 / 10 interface, Figure 5.2.1-9. The data, Figure 5.2.1-10, indicate that this sensor begins to show an off-nominal behavior at 50:19 GMT (EI+370 sec). This start of off-nominal time is 30 seconds after the start of decreased heating recorded on the side fuselage and OMS pod. As can be seen in the figure, there were other flights in which an off-nominal temperature behavior can be observed for this T/C. However, the earlier off-nominal responses for the T/C are not of similar signature to the data seen for STS-107. No proven explanation can be provided for the previous off-nominal flight data but one theory is that the T/C temperature is demonstrating a sensitivity to the shock interaction. Shock interaction regions are areas within the flow field where two or more strong shock structures intersect. For the Orbiter, a very strong shock interaction occurs between the bow shock and wing shock, resulting in locally higher heating and pressure. In fact, the very high heating experienced on the Orbiter wing leading edge, in the region where the wing transitions from the strake section to the main wing section, results directly from the bow-

shock/wing-shock interaction. The heating produced by such an interaction can be very localized, implying very large surface heating gradients in the immediate vicinity of the interaction. The precise location of this interaction is a function of many variables related to high-speed aeroheating environments, and even small changes in these variables can cause significant changes in the actual position of the shock-shock interaction and hence the underlying heating experienced at the surface. No further discussion will be provided in this report on the off-nominal low data, but this information was noted here for completeness. The off-nominal high readings for STS-107 continue until the V07T9666A T/C fails at approximately 52:25 GMT (EI+496 sec).

The off-nominal trend for the V07T966A instrument occurs prior to any of the debris events that were observed, so no correlation can be made to observed debris. However, as was noted previously, instrumentation inside of the WLE and along the wing spar, i.e. V09T9910A, V12G9921A, V12G9169A, indicated that heating was already occurring in the WLE cavity when the off-nominal temperature at V07T9666A was noted. Thus, the temperature response of this gauge potentially indicates a worsening condition either inside the WLE cavity or at the original damage site itself.

5.2.1.3 Chin Panel and Vacuum Vent / Water Supply Dump Nozzles

Four additional temperature measurements indicated off-nominal behavior on the vehicle. However, these were located more forward on the fuselage than the sensors previously discussed. Additionally, these instruments are not surface thermocouples, but are instead Resistance Temperature Devices (RTDs) which were typically attached to structural elements of the Orbiter. The first of these was one of two RTDs located on the Nose Cap/Chin Panel expansion seal, Figure 5.2.1-11. The other three were located on the left side of the Orbiter; one associated with the vacuum vent nozzle and the other two with the water supply dump nozzle located just above the waste water dump nozzle, Figure 5.2.1-12.

The chin panel sensor, V09T9889A, was the first of these sensors to indicate off-nominal trends at 52:09 GMT (EI+480 sec) but it recovers to the "nominal" slope by 52:49 GMT (EI+520 sec), Figure 5.2.1-13. Note that V09T9880A, only 23 inches away on the centerline, did not show this off-nominal signature. Also in Figure 5.2.1-13, the vacuum vent, V62T0551A, and water supply dump nozzles temperature sensors, V62T0440A & 0439A (not shown), indicate similar behavior albeit at a slightly different start time of 52:32 GMT (EI+503 sec). However, the vacuum vent RTD recovered to the previous slope at 52:47 GMT (EI+518 sec), prior to the water supply nozzle RTD at 52:55 GMT (EI+526 sec). The slope of the temperature curves seen by these sensors essentially doubles between times 52:32 GMT (EI+503 sec) and 52:52 GMT (EI+523 sec). These vent nozzle temperature rise rate increases equate to an additional heat transfer rate of approximately 0.038 BTU/sec (40 Watts). Note that the nozzle temperatures were recorded via downlink on the OI system, and that off-nominal measurements were bounded by communication dropouts. The data dropouts were two of several unexplained communication blackouts (as noted by the gaps in the downlink data) that occurred prior to LOS.

As has been mentioned, the responses from these forward fuselage sensors are unusual in that their readings return to their nominal trends after a short period of off-nominal response. However, it is noted that the RTD response of the waste water dump nozzle, V62T0519A, located seven inches below the supply nozzle, V62T0520A, showed no indication of off-nominal response during the entire entry. Lastly, there was a surface T/C, V07T9522A, located just aft of and above the vent nozzle group that showed nominal behavior for the entire entry except for a sharp decrease in the data over one cycle. These data along with the observed debris data have been co-plotted in Figure 5.2.1-14. As can be seen, no clear relationship can be observed between the debris events and response of the sensors that performed nominally. Although not shown, the response of the chin panel gauge does coincide with the estimated time of the wing spar breach (see Section 6 for further details).

5.2.1.4 Kirtland Photo

As the Orbiter was passing over the Albuquerque, New Mexico area, images of the Orbiter were obtained from the Kirtland AFB Starfire Optical Range. Figure 5.2.1-15 shows the principle image of the set. Although a thorough analysis of the images was made (see Image Analysis Team Report), no direct evidence of damage to the Orbiter could be discerned. However, damage to the Orbiter, especially the WLE, could be inferred from the anomalous bulges noted on the left wing. The principle source of light

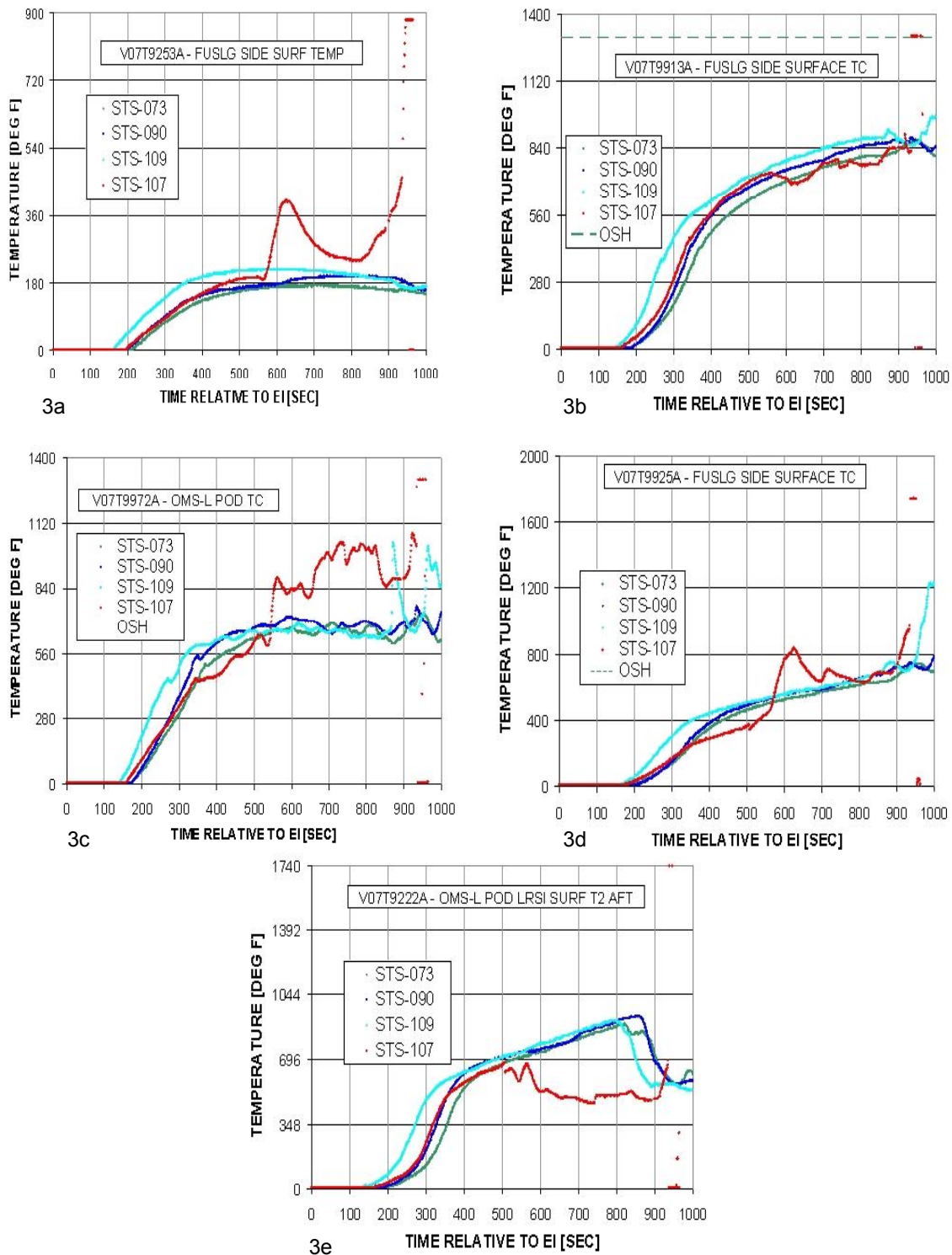


Figure 5.2.1-2a – 3e STS-107 Orbiter Side Fuselage and OMS Pod temperature comparisons with previous flights of Columbia.

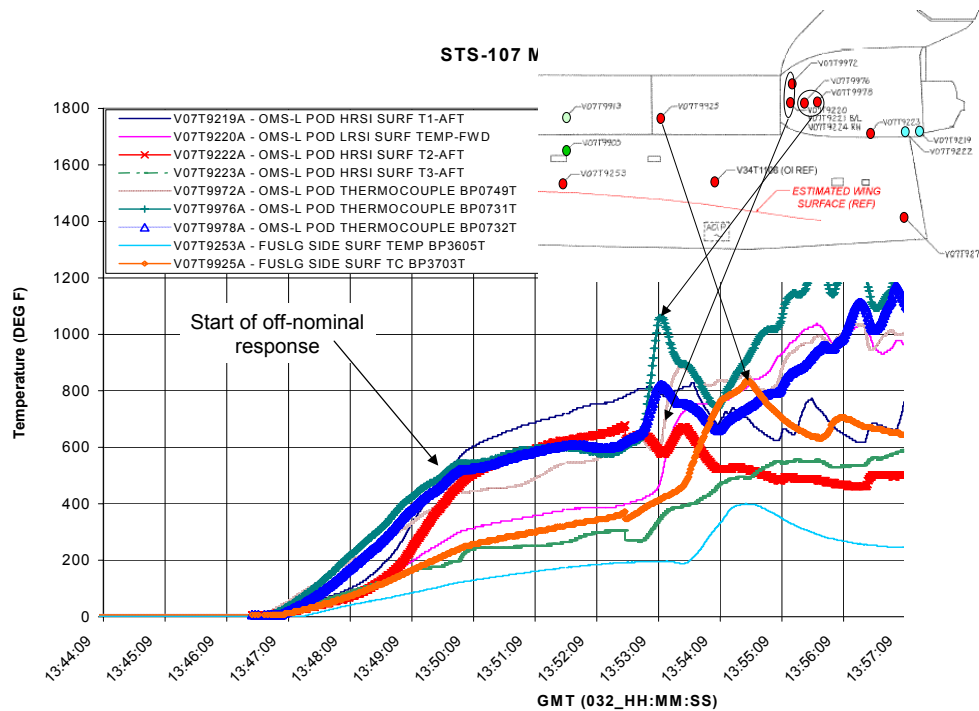


Figure 5.2.1-3 Left Side Fuselage and OMS Pod Off-Nominal Responses Indicate Aft to Forward Progression of Increased Heating

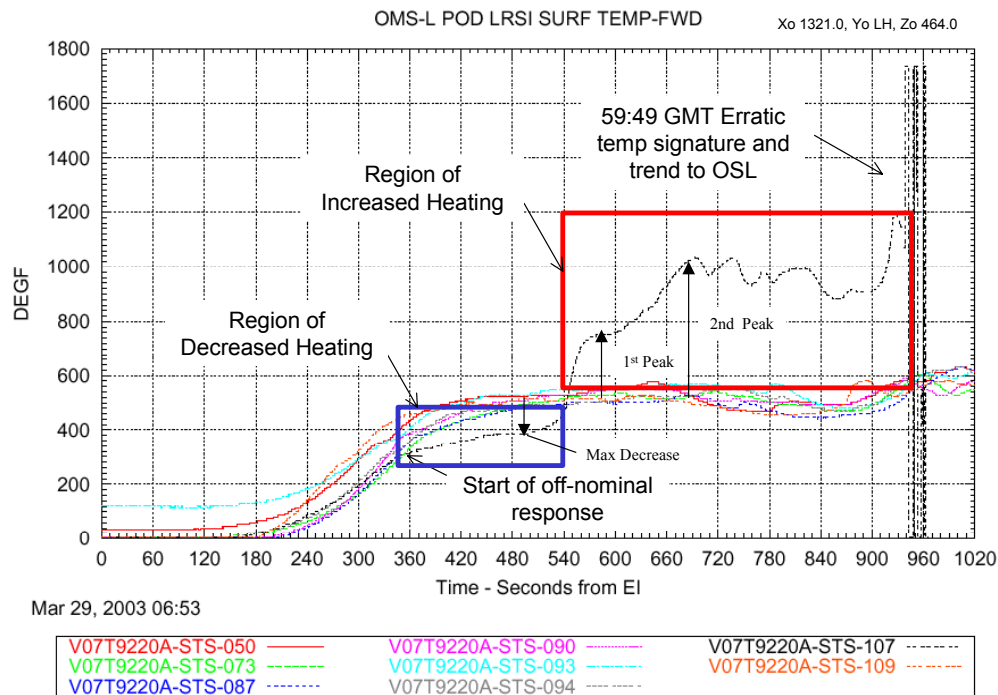


Figure 5.2.1-4 An example of Left OMS Pod temperature response that indicates at least two significant events during the period of increased heating

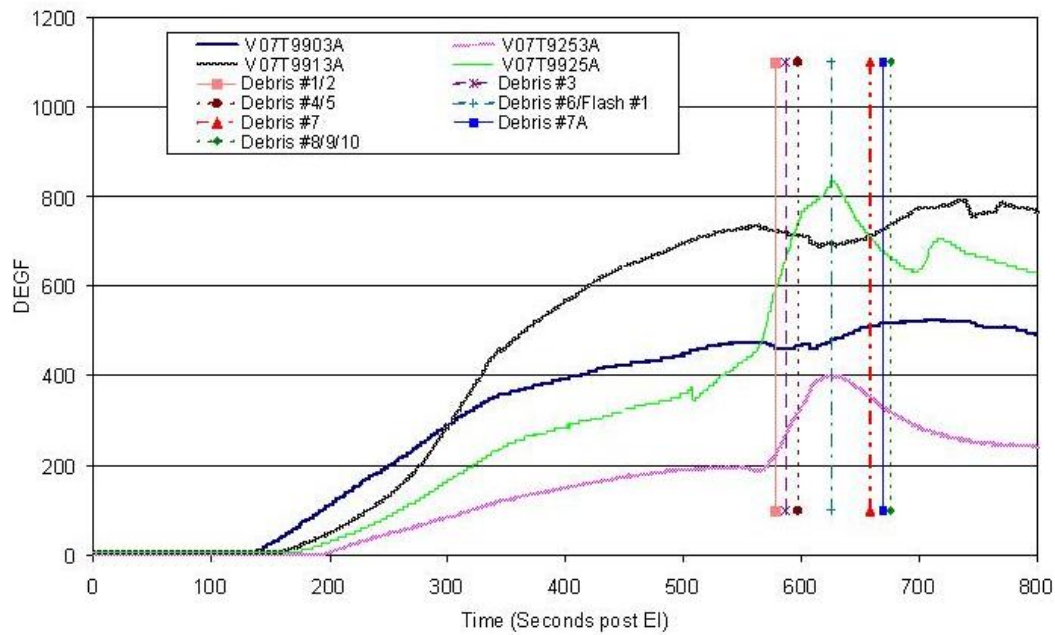


Figure 5.2.1-5 Mid Fuselage and Aft-Left Side Payload Bay Surface T/Cs response along with Debris Events 1 through 10

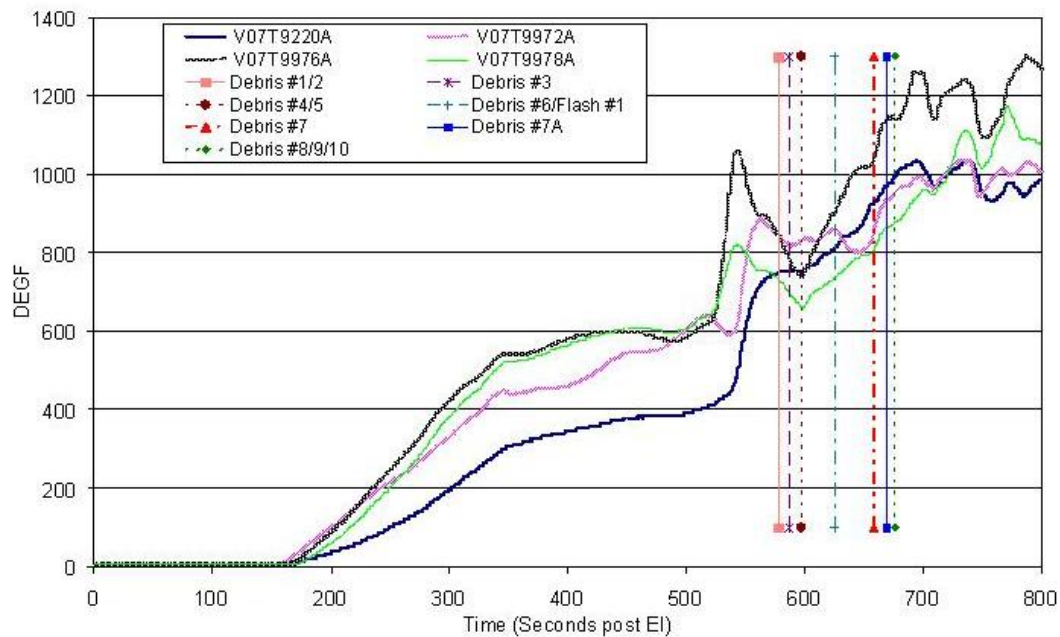


Figure 5.2.1-6 Forward Left OMS Pod Surface T/C responses along with Debris Events 1 through 10

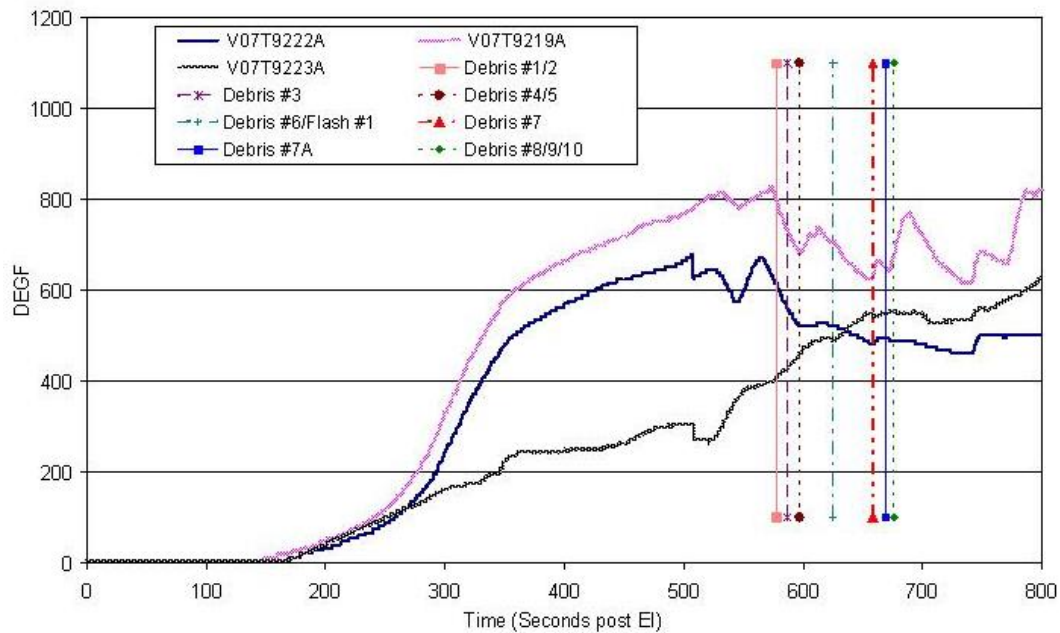


Figure 5.2.1-7 Mid and Aft Left OMS Pod Surface T/C responses along with Debris Events 1 through 10

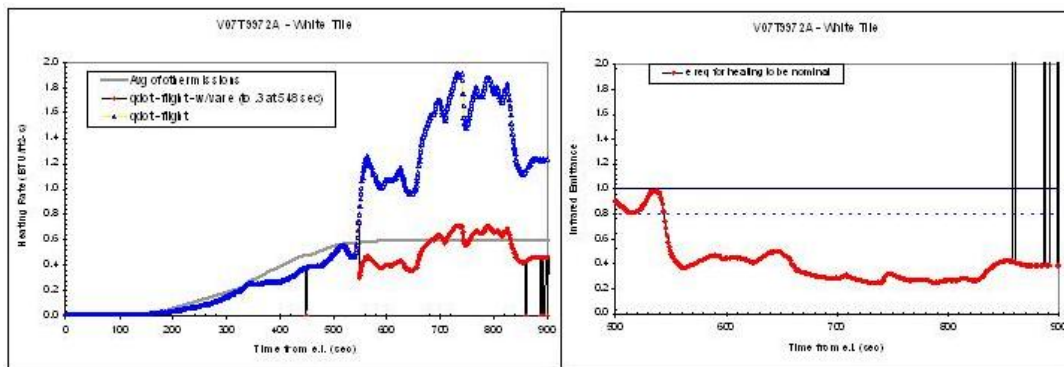
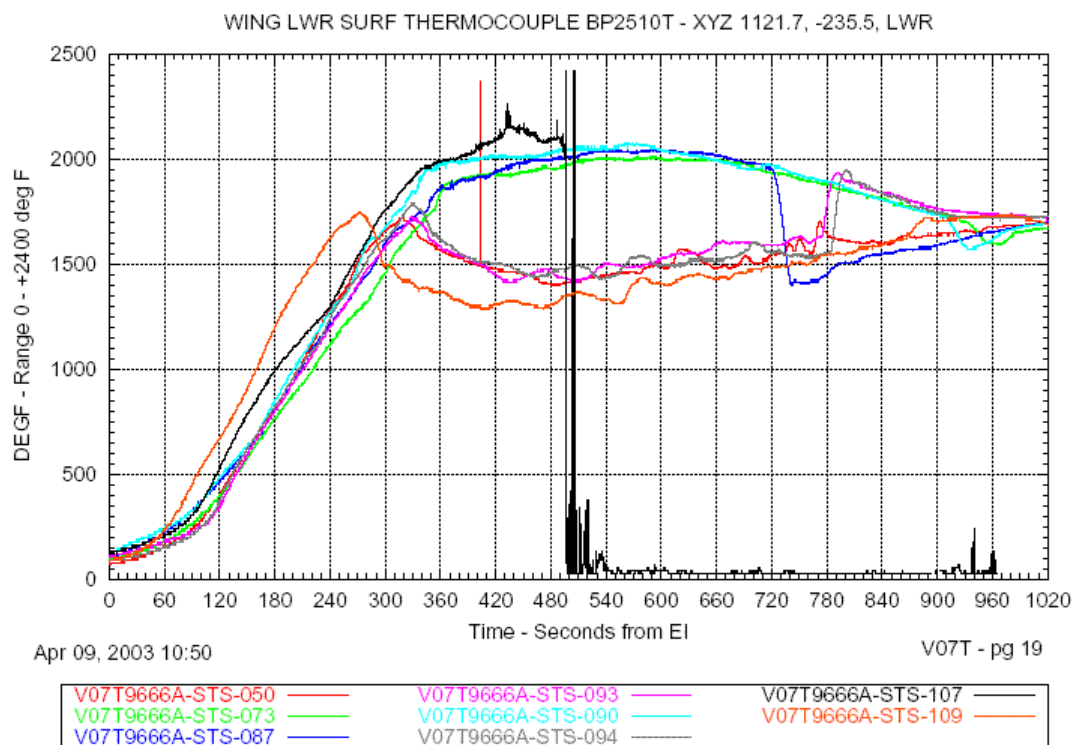


Figure 5.2.1-8 Emittance change needed to return inferred heating rates to previous flight average



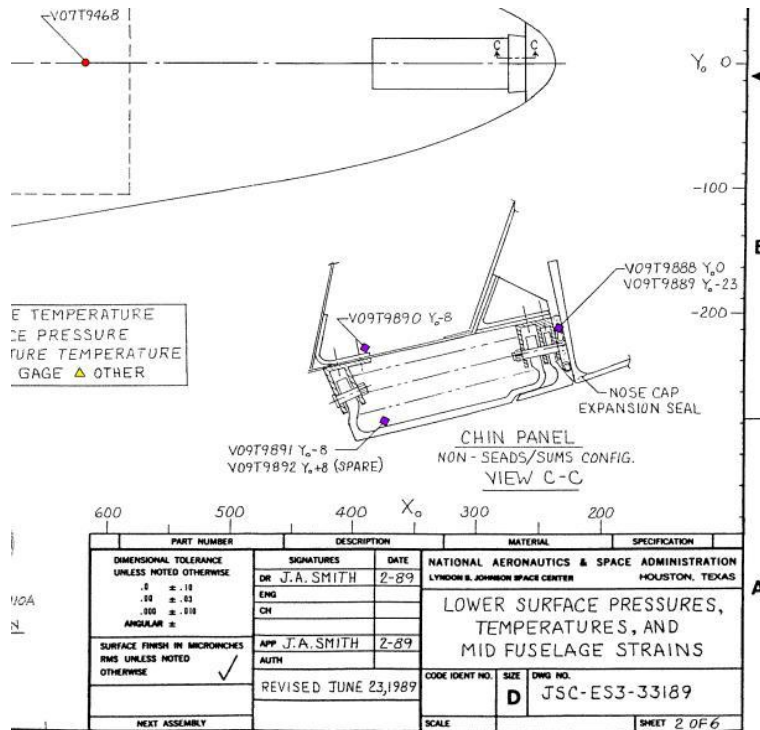


Figure 5.2.1-11 Nose Cap / Chin Panel Expansion Seal Instrument Locations

Figure 5.2.1-12

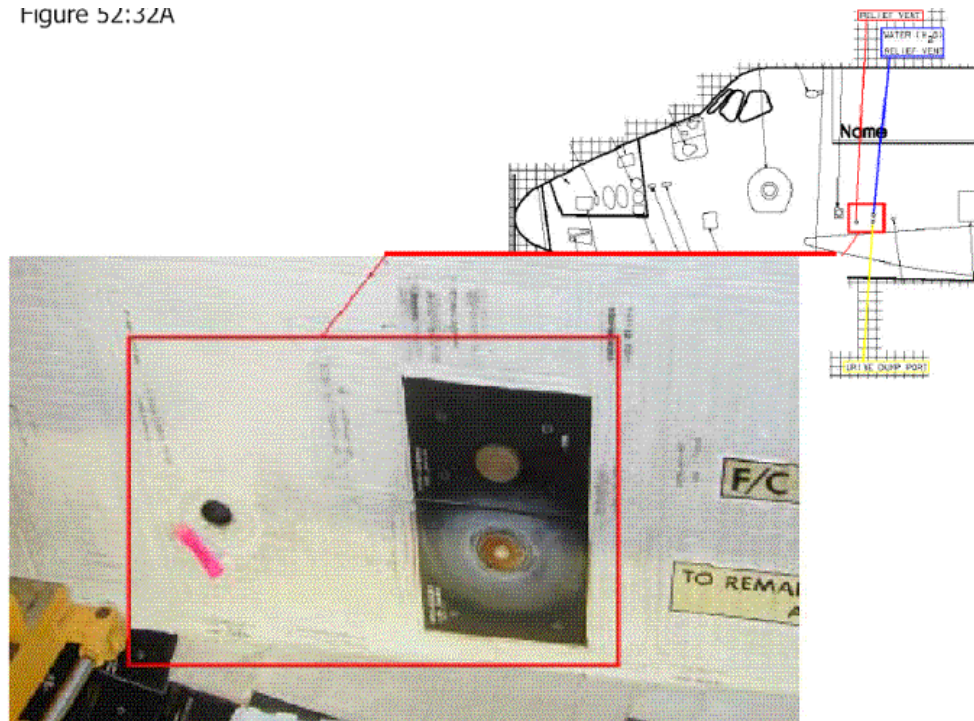


Figure 5.2.1-12 Vacuum Vent and Water Dump Nozzle Locations

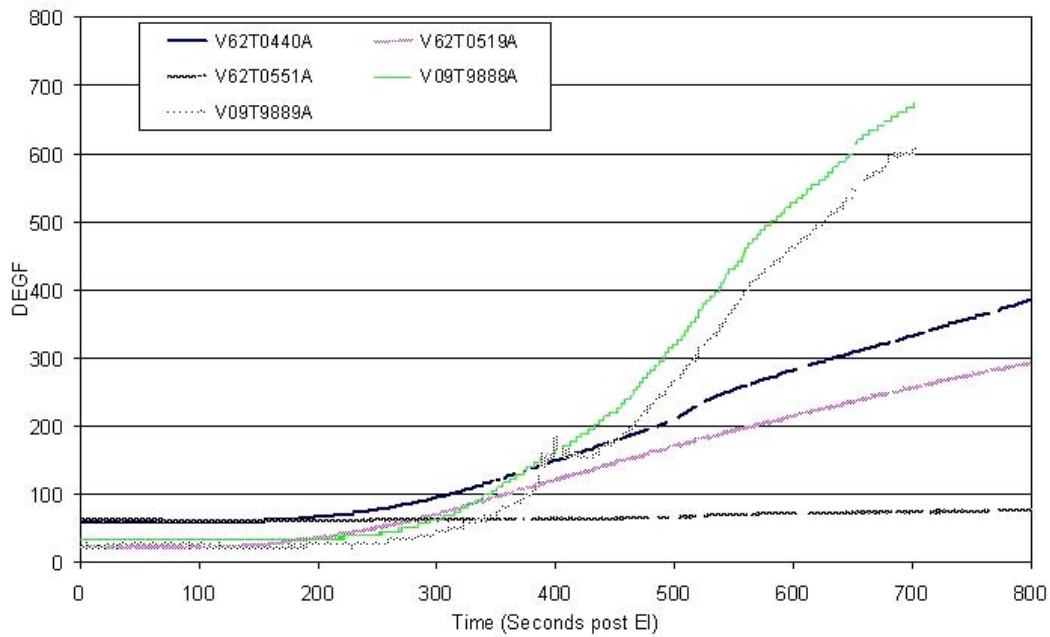


Figure 5.2.1-13 Chin Panel (V09T9880A and V09T9889A), Vacuum Vent (V62T0551A), Water Supply Dump Nozzle (V62T0440A), and Water Waste Dump Nozzle (V62T0519A)

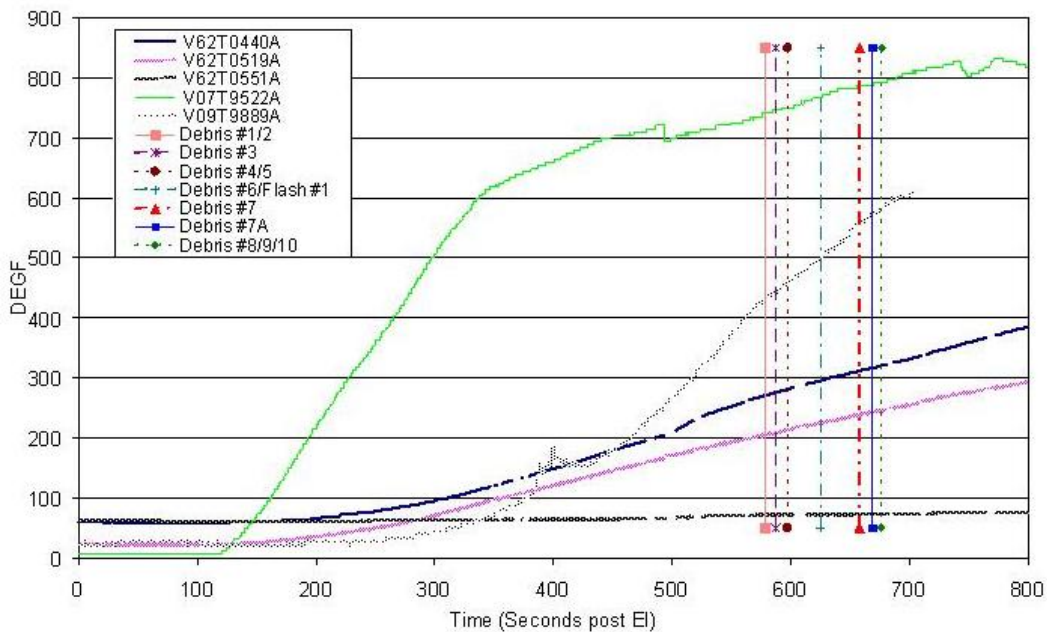


Figure 5.2.1-14 Chin Panel, Vent Nozzles, and local Surface T/C data plotted along with Debris Events 1 through 10.

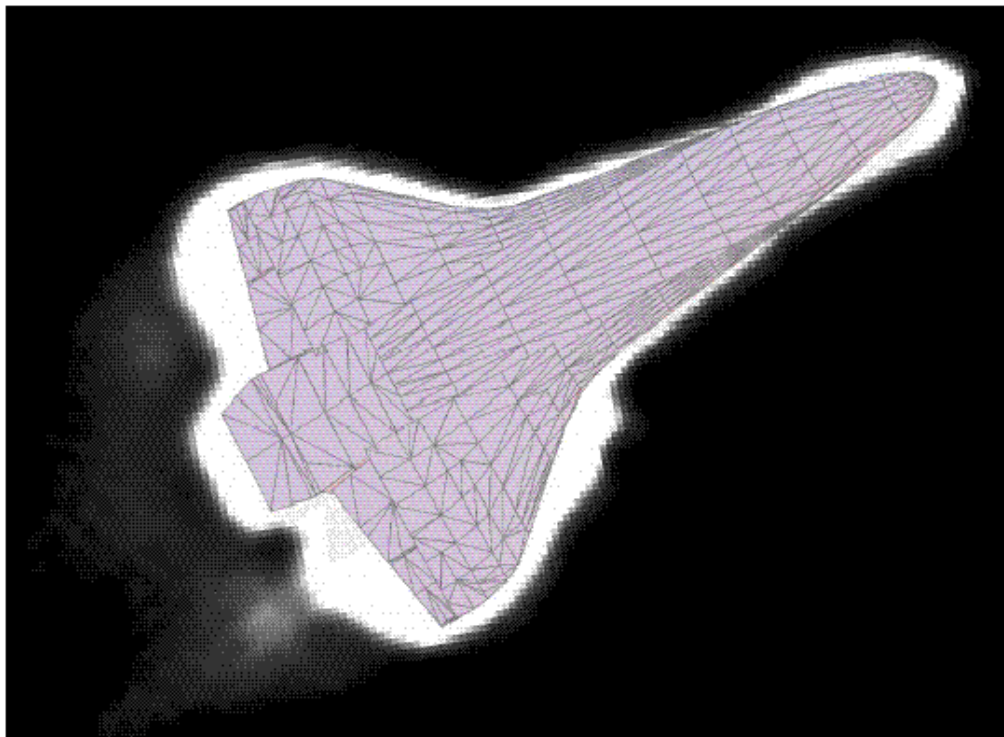


Figure 5.2.1-15 Kirtland AFB image taken at 13:57:14 GMT. Image has been enhanced and an Orbiter wire frame overlaid. View is of windward side of the Orbiter. Orbiter was in a left wing down roll attitude when this image was obtained.

5.2.2 Orbiter Certified Body Point Heating Methodology

5.2.2.1 Background on Body Point Heating Model Development

Entry aerodynamic heating of the Shuttle Orbiter is a result of the flow of air at high speed over the Orbiter. Friction between the air filaments as they stream over the orbiter surface, and compression near the stagnation regions of the nose and leading edges, convert kinetic energy of motion into heat. This heated gas environment envelops the Orbiter during its critical re-entry phase of flight.

Aerodynamic heating rates are influenced by all properties of the flow field as well as conditions at the body surface. In the external flow, the density, velocity, pressure, streamline pattern, and chemical composition must all be determined before heating calculations can be performed accurately.

The approach used for the development of Shuttle aerodynamic heating prediction methodology was to draw upon a vast knowledge available in the literature and combine it with Shuttle Orbiter wind tunnel data and Orbiter flight test data.

Use of wind tunnel data was strongly emphasized in the development of a heating prediction methodology. Where wind tunnel data were not available, analytical methods were used. It was the design philosophy (Figure 5.2.2-1) that, by proper use of wind tunnel data and analytical methods and by identifying and accounting for uncertainties in a logical manner, a minimum risk approach to the aerothermodynamic design of the Orbiter, without unnecessary conservatism, would be achieved. A nominal fairing/interpretation of wind tunnel data was used to develop the methodology. Verification of these methods was based on flow field solutions and data from developmental flight tests (OFT). A detailed description of the Orbiter entry heating prediction methods and database can be found in Rockwell International Document STS 83-0948 (1988).

5.2.2.2 Body Point Heating for Nose Cap, Wing Leading, Main Landing Gear Door

The basic approach for the Orbiter acreage is to break down the Orbiter into simple geometric shapes: sphere, cylinder, cones and wedges (Figure 5.2.2-2). These Simple Geometric Shapes (SGS) are correlated with wind tunnel data and adjusted to a nominal fit of the data. The SGS are then extrapolated to flight, while the adjustment factor is held constant. The adjustment factor accounts for Orbiter location, angle of attack, and Reynolds number variation. This approach works well for the Orbiter lower surfaces.

5.2.2.2.1 Fuselage Lower Surface (Nose Cap, Main Landing Gear Door)

The fuselage lower surface was divided into regions of both blunt body and slender body flows (Figure 5.2.2-3). The region of slender body flows was designated to be where the change in slope of the local velocity went to zero.

The bluntness of the Orbiter nose affects the downstream heating rate by altering the surface pressure distribution and by increasing the entropy of the flow at the boundary layer edge. For a cone, this bluntness causes the pressure to increase for a distance of one or two nose radii to a value greater than that for a sharp cone.

In the blunt body flow region, heat transfer film coefficients from wind tunnel data ratioed to reference sphere heat transfer values were applied to flight conditions adjusted by a slender body transfer factor. The reference sphere heating values were computed by the Fay & Riddell (1958) stagnation heating formulation with a variable Lewis number term. The heating distribution around the orbiter stagnation point at a 40° angle of attack is shown in Figure 5.2.2-4.

At the stagnation point in the sonic flow zone, the slender body adjustment factors have a value of 1.0 and increase to the slender body value of 1.6 at $X/L = 0.208$ for α equal to 30°. For angle of attack greater than 30°, the slender body interaction zone is held constant at $X/L = 0.20$, although the adjustment factor is allowed to vary (Figure 5.2.2-5).

The slender body adjustment factors were determined by ratioing laminar flat plate theory values at flight to those at wind tunnel conditions. This resulted in the blunt to slender body transfer distribution of Figure 5.2.2-6.

The blunt body flow region is characterized by high pressure gradients, which, in the axial direction can be approximated by a Newtonian-Prandtl Meyer expansion (Figure 5.2.2-7), while the heat transfer can be approximated for wind tunnel conditions with a Cohen and Beckwith (1961) similar solution (Figure 5.2.2-8).

In the slender body region, a system was developed to modify Eckert's flat plate theory for streamline divergence by a series of factors as shown in Figure 5.2.2-9. Streamline patterns were obtained from oil flow data. To do this, wind tunnel data were compared with SGS using a nominal fit of the data, and laminar factors (LAMFACs) were developed. These laminar factors were allowed to vary with angle of attack. The LAMFACs were correlated with two angles of attack (α_{REF}) selected as reference conditions (1,2). Slopes of the LAMFAC (designated: Q_{SLOPE}) were developed about these two alphas, and reference laminar factors were established. This resulted in an angle of attack variation in equation form:

$$ALFAC = 1 + \frac{(\alpha - \alpha_{REF}) * Q_{SLOPE}}{LAMFAC_{REF}}$$

The SGS was adjusted by the product of ALFAC * LAMFAC_{REF} to account for divergence. The assumption was made that both ALFAC and LAMFAC developed in the wind tunnel at $\gamma = 1.4$ and basically Mach 8 had the same variations and magnitude under flight conditions. An example of the variation in LAMFAC with angle of attack can be found in Figure 5.2.2-10 through Figure 5.2.2-12 for the lower surface body point 1600. Figure 5.2.2-11 shows the variation of wind tunnel test data and flat plate theory with angle of attack. When this information was converted to LAMFAC, the distribution in Figure 5.2.2-12 was obtained.

The origin of the flow used in the flat plate calculation was assumed to be at $X/L = 0$. When applied to points aft of $X/L = 0.2$, the small variation in angle of attack on stagnation point movement would be negligible in the wetted flow length. Forward of $X/L = 0.2$ (blunt body) the flow length did not fit directly into heating methodologies (heating ratios), although it is still of importance to boundary layer transition calculations.

Spalding and Chi (1964) turbulent flat plate values were adjusted using turbulent factors which were developed along similar patterns to the laminar factors. Turbulent factors also vary with angle of attack and body location and correlate similarly to the laminar factor equation.

Laminar factors were generally based on wind tunnel data from test OH39, OH49B and OH50B having model scales of 0.0175 and 0.04.

The existence of chemical non-equilibrium in the shock layer during much of the Orbiter's entry trajectory, coupled with the relatively non-catalytic behavior of the TPS materials, necessitate an additional correction to laminar equilibrium heating values on the nose cap and lower surface. This adjustment is in the form of a catalytic heating parameter (η) inferred from flight data:

$$(q_{wall})_{catalytic} = h_{eq} (i_r - i_w - \eta i_d)$$

where h_{eq} is the equilibrium heat transfer coefficient, i_r is recovery enthalpy, i_w is the wall enthalpy and i_d is dissociation enthalpy. Here, $\eta = 0$ implies equilibrium heating and $\eta = 1$ is equivalent to non-catalytic wall heating.

The catalytic resistance coefficient, η , is developed from a recombination rate constant dependent on surface recombination efficiency and gas properties at the surface. Thermocouple data from STS-2, STS-3 and STS-5 were used to determine the numerical form of the temperature dependent recombination

efficiency. Detailed discussion of the non-catalytic heating approach and correlation technique is presented in Miller (1984).

5.2.2.2.2 Wing Leading Edge Heating Methodology

In the philosophy of simple geometric theories, the wing leading edge would be thought of as a swept cylinder. However, there are several features that move this approach to only a starting solution for the problem. First, an airfoil attached to the leading edge affects the shock shape and thereby affects the effective radius of the cylinder. Second, the intersection of the bow shock with the leading edge shock (Figure 5.2.2-13) produces several features as discussed in various sources. The shuttle wing leading edge shock region was interpreted to experience a type V interference pattern (Figure 5.2.2-14). This type of shock interaction results in a new shock that strikes the leading edge at about 55% semi-span (dependent on angle of attack) and disturbs the wing lower surface. Also formed is a jet shear layer that strikes the outboard section of the wing, scrubbing both the upper and lower surfaces.

Based on wind tunnel data from wind tunnel test OH66, the effective radius variation with angle of attack was developed (Figure 5.2.2-15). By using this curve along with the modified swept cylinder equation, the effect of shock impingement can be determined (Figure 5.2.2-16). This figure represents the effect of shock impingement at 55% semi-span. Therefore, as the shock position moves with angle of attack, the maximum heating footprint moves leading to a maximum heating at the 55% semi-span between 35 and 40 degrees angle of attack. At the other angles of attack, maximum heating would occur at a different span-wise location.

Wind tunnel data applied directly to flight were used. Data were applied in terms of film coefficients (local to reference sphere ratio) as a function of angle of attack and leading edge location. For span locations where no data existed, the modified swept cylinder was used.

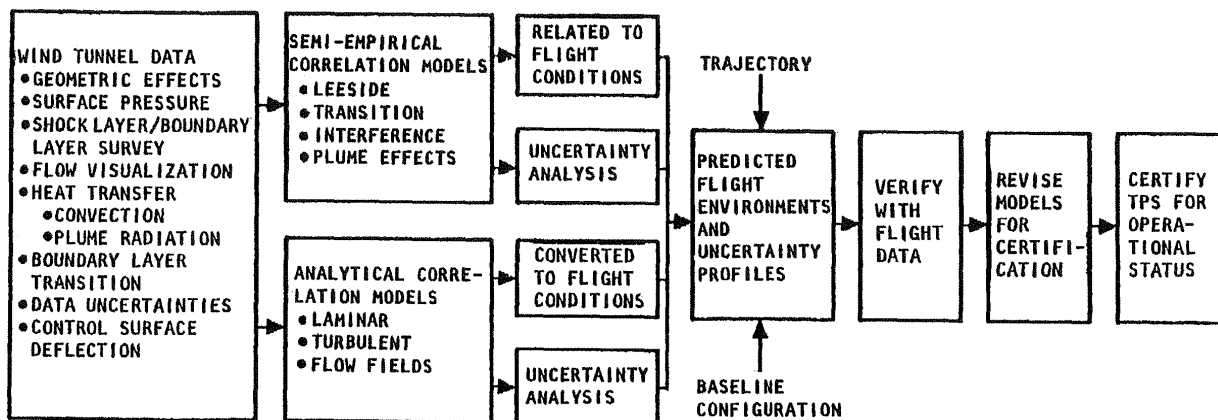


Figure 5.2.2-1 Orbiter Entry Heating Design and Certification Logic

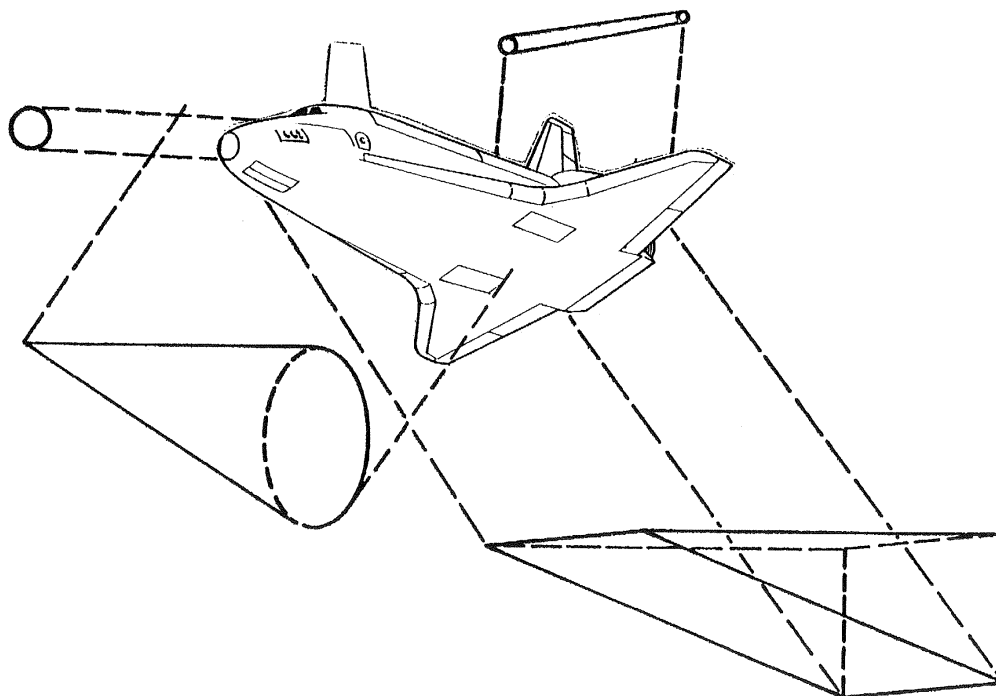


Figure 5.2.2-2 Simple Geometric Modeling (SGS)

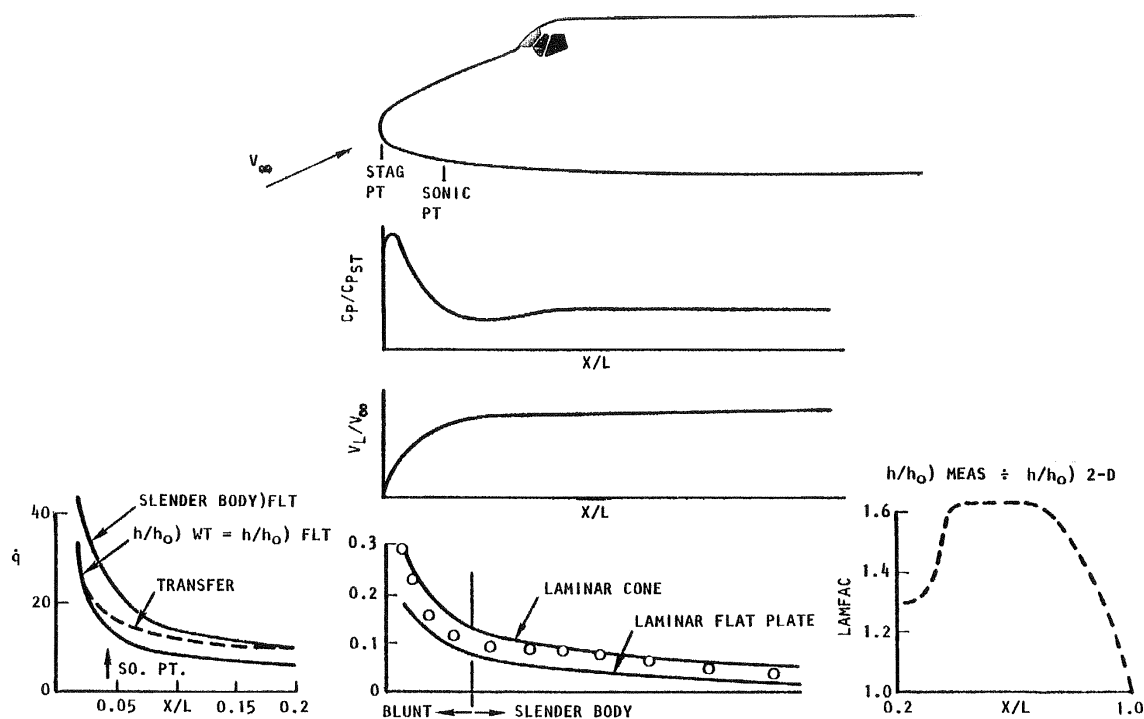


Figure 5.2.2-3 Fuselage Lower Surface Heating Extrapolation to Flight

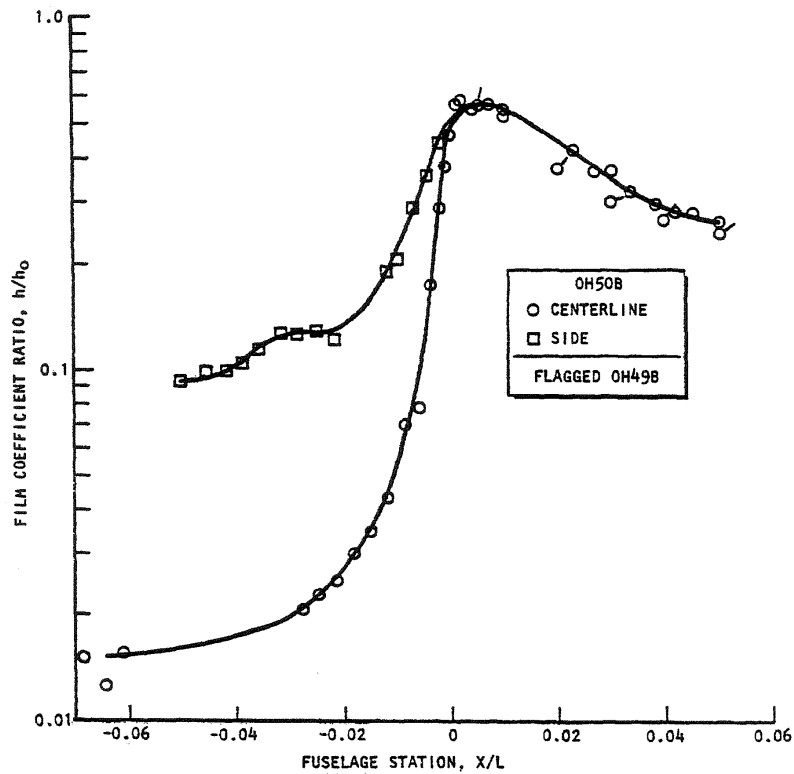


Figure 5.2.2-4 Heating Distribution Around the Orbiter Stagnation Point at Alpha = 40°

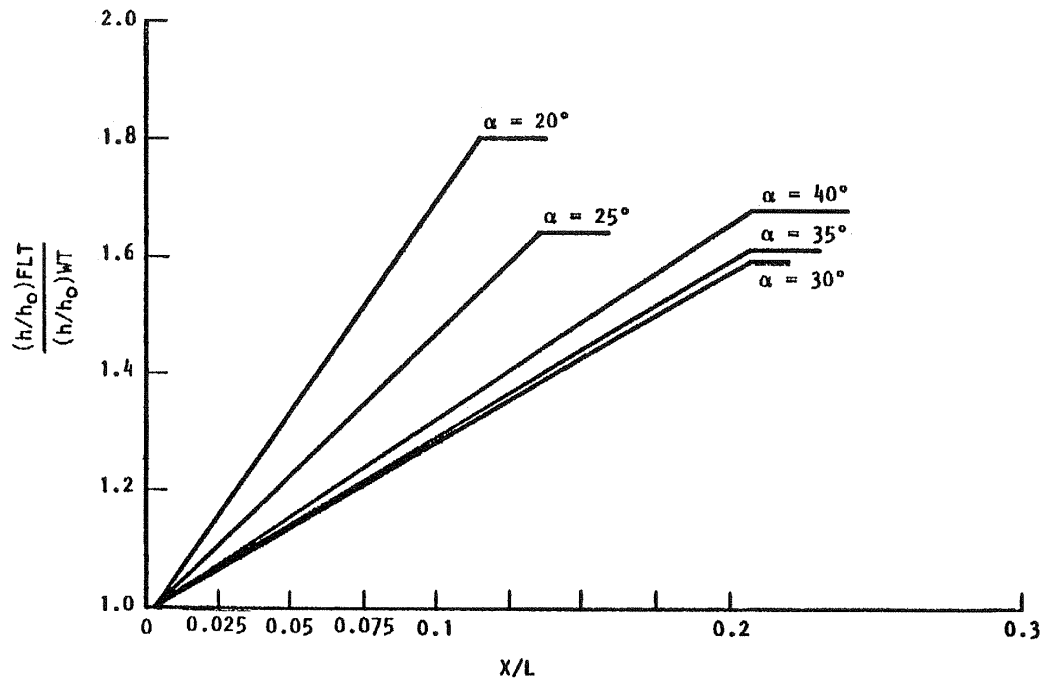


Figure 5.2.2-5 Wind Tunnel to Flight Scaling

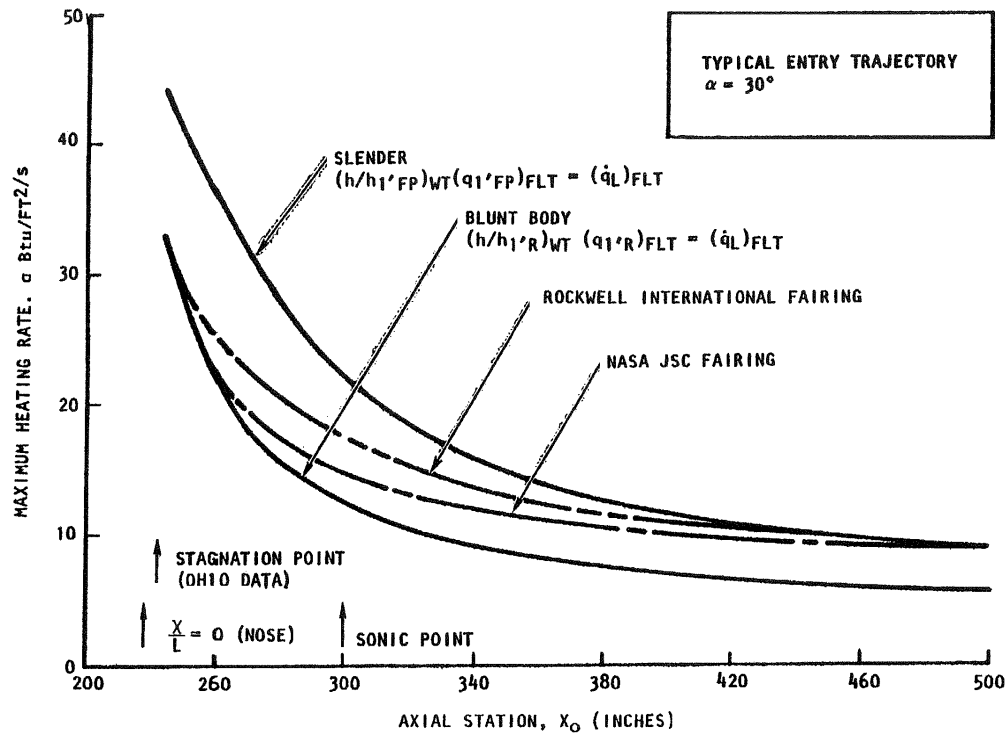


Figure 5.2.2-6 Blunt-Body-to-Slender Body Transfer Determination

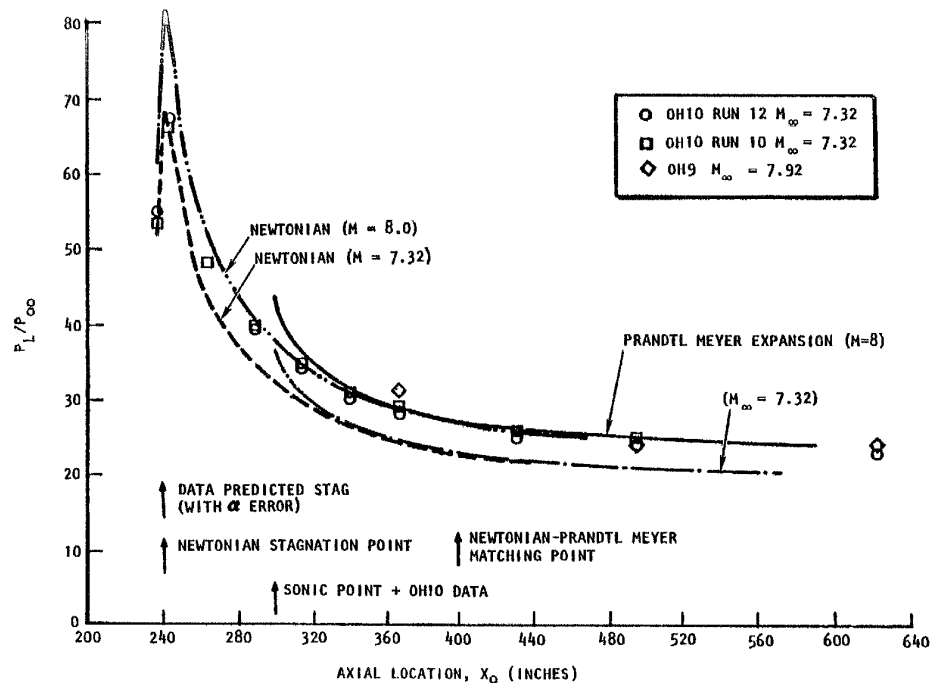


Figure 5.2.2-7 Forebody Pressure Modeling Under Wind Tunnel Conditions ($\alpha = 30^\circ$)

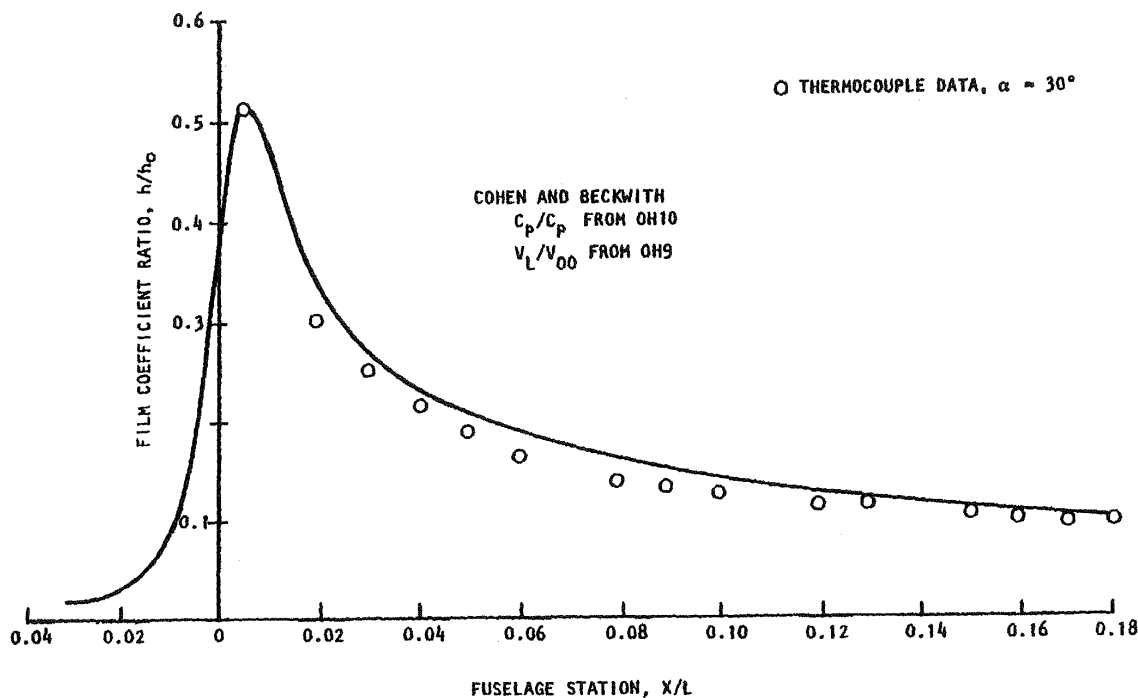
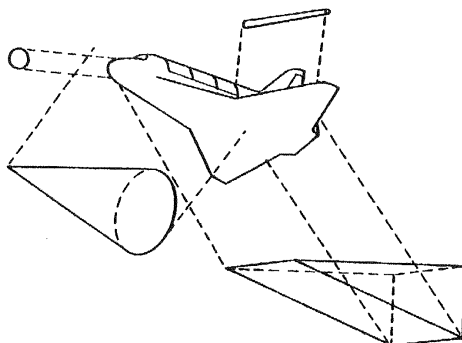


Figure 5.2.2-8 Cohen and Beckwith Modeling of Fuselage Forebody

REPRESENTATIVE FLOW MODELS



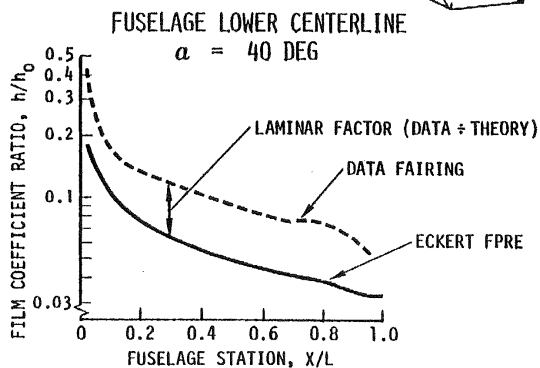
LAMINAR FLAT PLATE – ECKERT H*

$$h_{FP}^* = \frac{0.332 (\rho^* \mu^*)^{\frac{1}{2}} (V_L)^{\frac{1}{2}} (32.16)}{(X)^{\frac{1}{2}} (P_R)^{\frac{2}{3}}}$$

h_{FP} WIND TUNNEL : INPUT PERFECT GAS PROPERTIES

h_{FP} FLIGHT : INPUT FLIGHT PROPERTIES

$\therefore h)_{FLT} = h_{FP})_{FLT} \cdot (\text{LAMINAR FACTOR})$



$\frac{X}{L}$	LAMINAR FACTOR $\alpha = 40 \text{ DEG}$
0.2	1.71
0.3	1.86
0.4	1.95
0.5	1.88
0.6	1.82
0.7	1.81
0.8	1.93
0.9	1.83
1.0	1.31

Figure 5.2.2-9 Orbiter Lower Surface Methodology, Slender Body Approach

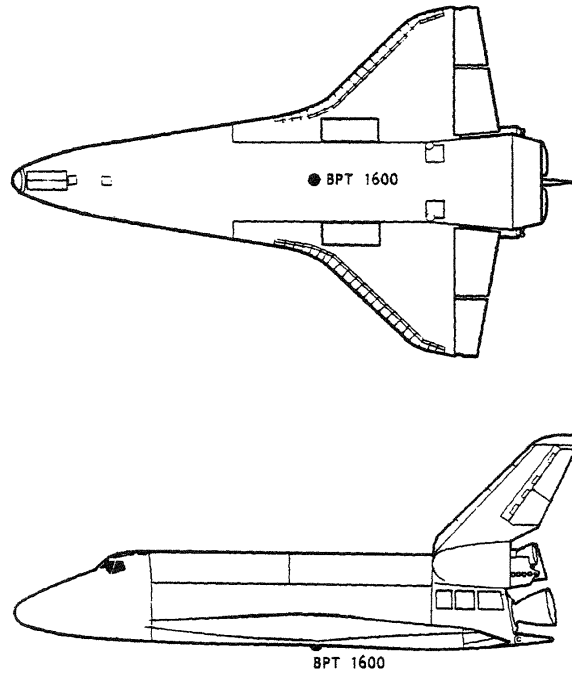


Figure 5.2.2-10 Typical Lower Surface Location

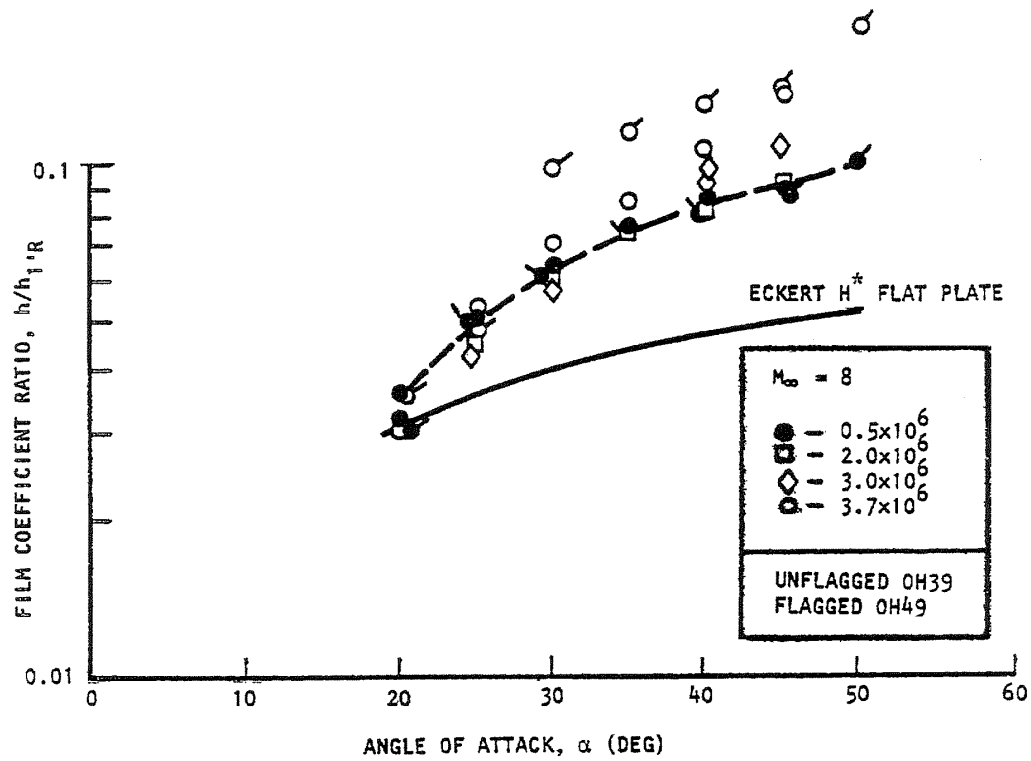


Figure 5.2.2-11 Local Heating Variation With Angle of Attack on Fuselage Lower Surface Centerline at X/L = 0.6

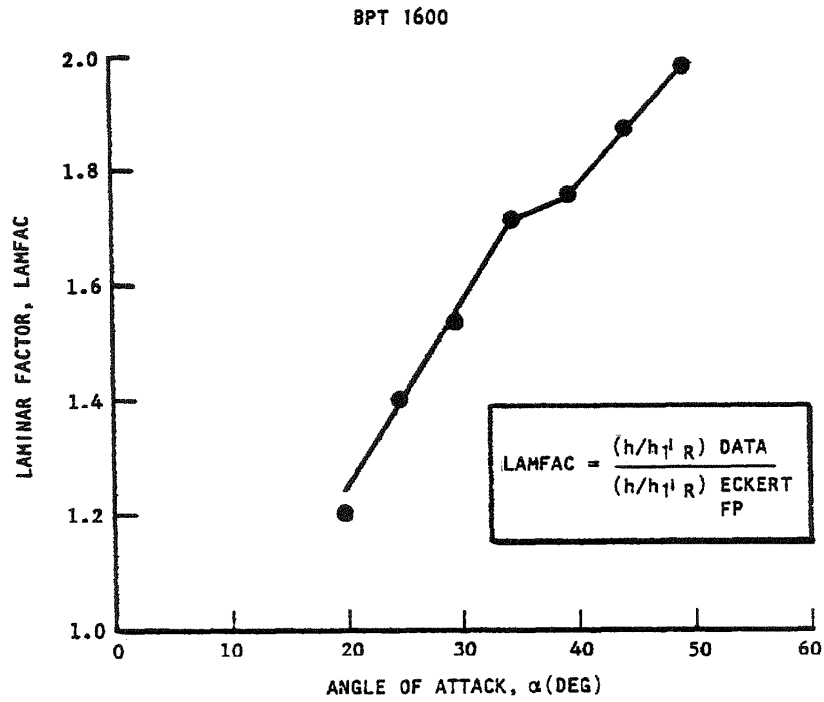


Figure 5.2.2-12 Fuselage Lower Surface Centerline Laminar Factor Laminar Variation With Angle of Attack

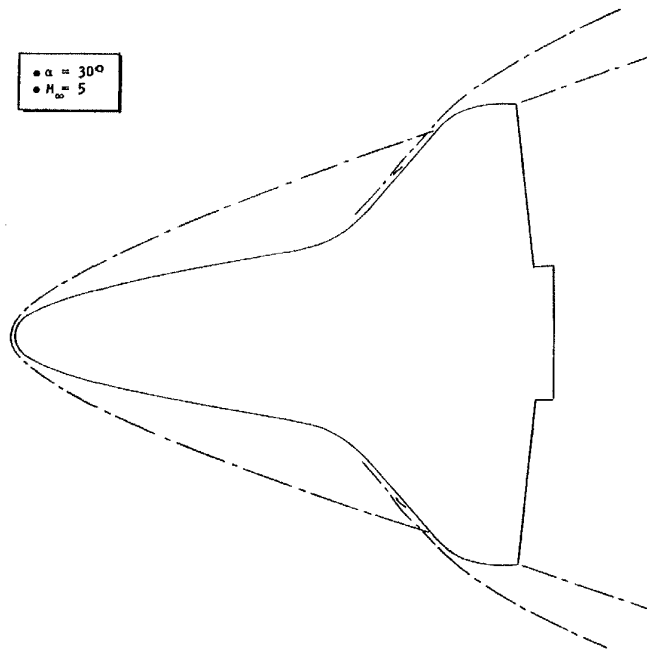


Figure 5.2.2-13 Shock Patterns Based on Wind Tunnel Shadowgraph

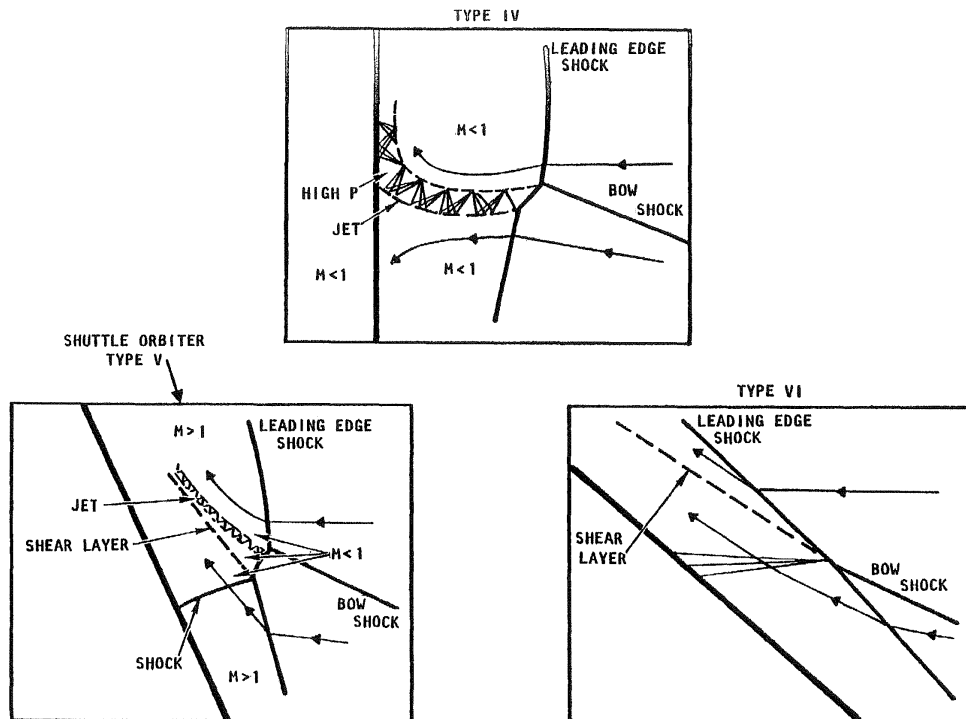


Figure 5.2.2-14 Variation in Shock Impingement Patterns

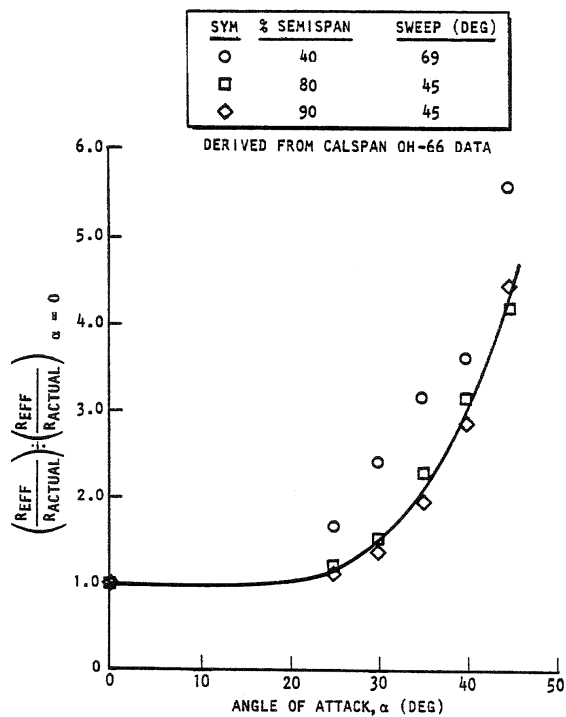


Figure 5.2.2-15 Angle of Attack Effect on Leading Edge Effective Radius

$$\text{SHOCK EFFECT} = \frac{R_{\text{EFF}}}{R_{\text{ACTUAL}}} \left(\text{FIGURE 1-107} \div \frac{R_{\text{EFF}}}{R_{\text{ACTUAL}}} \right) 55\% \text{ SEMISPAN}$$

DERIVED FROM CALSPAN OH-66 DATA

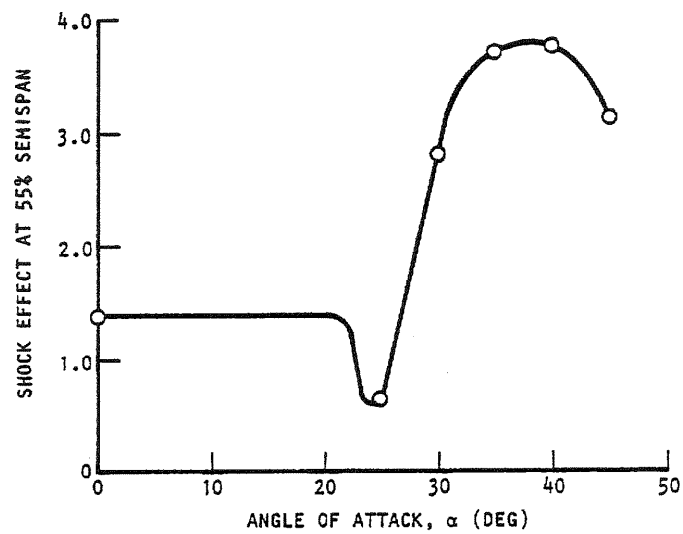


Figure 5.2.2-16 Angle of Attack Effect on Shock Impingement Effects

5.2.3 Wind Tunnel Testing

The purpose of this section is to describe the hypersonic aerothermodynamic wind-tunnel program conducted at the NASA Langley Research Center in support of the STS-107 accident investigation. The primary objective of the testing was to provide information regarding surface heating characteristics on scaled Orbiter models with surface perturbations to simulate various forms of localized damage to the thermal protection system (TPS). With very limited flight information available during the first weeks after the loss of STS 107, initial experimental testing covered a broad spectrum of TPS damage. As the investigation developed, increasing emphasis was placed on obtaining test data consistent with the subsequent body of recovered debris and extracted Orbiter OEX flight recorder data. Presentation of all heating test data associated with TPS damage, particularly that associated with early scenarios, has not been attempted in this section; emphasis has instead been placed on the data relevant to the working scenario involving damage to RCC panels 5-9.

Presently, the NASA has three active hypersonic wind tunnels (collectively referred to as the Langley Aerothermodynamics Laboratory) in the NASA LaRC inventory of ground-based facilities for hypersonic aerodynamic and aero-heating testing. Two facilities, the NASA LaRC 20-Inch Mach 6 Air and the 20-Inch Mach 6 CF₄ Tunnels, were utilized to characterize both heating and aerodynamic effects associated with damage scenarios. The high run productivity of the Mach 6 air tunnel was essential for assessments of damage scenarios involving large numbers of geometric parametrics. This initial screening capability was ideal for establishing test priorities and optimizing use of the more appropriate Mach 6 CF₄ tunnel. In addition, the wind tunnel results helped to focus application of higher fidelity CFD tools for damage simulations at flight conditions. Testing was not pursued in other facilities because appropriate testing techniques to perform rapid simultaneous aerodynamic and global aero-heating measurements on the Orbiter configuration were not available. Other NASA high enthalpy facilities or shock tunnels outside of NASA, while capable of generating high velocity/enthalpy conditions, were not amenable to the quick, parametric screening necessary for an investigation of this scope. The characterization of leeward flow fields in shock tunnels would also present challenges due to extremely short run times.

Documentation of global surface heat transfer, complimentary surface streamline patterns, and shock shapes are provided in this section for various simulated damage scenarios. Test parametrics include angles of attack from 38 to 42 deg, sideslip angles of ± 1 deg, unit Reynolds numbers from 0.05×10^6 to 6.5×10^6 /ft, and normal shock density ratios of 5 (Mach 6 air) and 12 (Mach 6 CF₄). The model scale utilized in these studies was 0.0075 (approximately 10 inches).

5.2.3.1 Mach 6 Air and Mach 6 CF₄ Applicability Flight

Aeroheating events leading to the loss of Columbia occurred during hypervelocity entry at low Reynolds numbers and high Mach number (25 to 18) and enthalpy levels. This complex flight environment is characterized by the excitation of energy modes in the gas as it passes through the bow shock wave of the Orbiter. At high enthalpy conditions, high temperature effects result in dissociation, recombination, and ionization of the air, and these in turn dictate changes in the shock layer flow. An effect with large impacts on the flow field is the reduction of the ratio of specific heats (herein referred to as γ) relative to a non-reacting perfect gas. In hypervelocity flight, decreases in γ within the windward and leeward Orbiter flow field result in increases in the density ratio across shock waves. The change in density ratio produces differences in shock layer structure including shock inclination and standoff distances and hence, shock interaction locations. Larger degrees of flow compression and expansion can exist relative to a non-reacting gas and these changes have been shown to directly influence Orbiter aerodynamics. While it is recognized that a nominal Orbiter entry environment cannot be duplicated in any one ground-based facility, aeroheating effects due to localized damage are first and foremost the result of flow physics or fluid dynamic phenomena (e.g., boundary layer/shear layer transition, shock-shock and shock-boundary layer interaction, flow separation-reattachment) associated with a given vehicle geometry, attitude, and flight condition. High temperature chemistry effects at high flow enthalpy levels "alter" the aerodynamic or aeroheating characteristics due to flow physics, but do not add new flow physics phenomena or delete any.

Testing in the perfect gas environment of a Mach 6 air tunnel captures all pertinent flow physics phenomena but does not provide information as to how the results may be influenced by flow chemistry. To address the effects of flow chemistry, the experimental test program was designed to take advantage of the simulation capability of the 20-Inch Mach 6 CF₄ Tunnel. Orbiter damage scenarios were first screened in the Mach 6 air tunnel for aerodynamic and aerothermodynamic consistency; the most promising were then tested in the CF₄ tunnel. This conventional-type (as opposed to impulse-type) low enthalpy hypersonic tunnel has relatively long run times and avoids complex chemistry typically associated with high enthalpy facilities. Modeling of the effects of flow chemistry that occur at the actual flight conditions is accomplished by using a heavier-than-air test gas that exhibits a low ratio of specific heats and a correspondingly high normal shock density ratio characteristic of air at reacting hypersonic conditions. In conjunction with the Mach 6 air tunnel, this CF₄ tunnel provides the capability to test at the same free-stream Mach and Reynolds numbers, but at two values of density ratio (approximately 5 in air and 12 in CF₄). The Mach 6 CF₄ density ratio of 12 is relatively close to the values of 15-18 encountered near Orbiter re-entry peak. Thus, generating large density ratio values simulates many of the aerodynamic and aeroheating effects associated with a high temperature gas. Synergistic tests of the Orbiter in these facilities led Miller (1982) to conclude that the effects of density ratio on the non-dimensional windward surface heating at hypersonic entry angles of attack were small.

Prior to the application of CFD with complex reacting chemistry air, perfect-gas engineering codes were used quite successfully to predict aerodynamic/aero-heating characteristics at hypervelocity conditions where the effects of flow chemistry were significant. This was accomplished via modifications to the perfect gas equations by the introduction of an effective gamma to "account" for high temperature effects. The effective gamma (herein referred as γ_{eff}) was based on the normal-shock density ratio value and the free-stream Mach number (for Mach numbers > 10) at re-entry conditions. Thus, one method to bridge between perfect air and heavy gas hypersonic wind tunnels and flight is through the use of an effective gamma. Brauckmann (1995) used gamma defined as local enthalpy divided by internal energy to successfully characterize the STS-1 pitch-up anomaly by relating Orbiter aerodynamic measurements made in the CF₄ tunnel to flight predictions. For the Orbiter at flight Mach numbers above 18, γ_{eff} is approximately 1.11. In the Mach 6 CF₄ and air tunnels, the value is 1.13 and 1.40, respectively. A close agreement between flight prediction and measured windward bow shock inclination and standoff distance is shown in Figure 5.2.3-1. In addition, there is general agreement between the flight and Mach 6 CF₄ tunnel conditions for predicted pressure coefficients and non-dimensional heating distributions (and wing bow shock interaction locations) on the Orbiter windward surface (Figure 5.2.3-2). These two observations imply very good ground-based simulation capability of the Orbiter windward flow field.

Compressibility (Mach number) effects were not addressed explicitly via testing in the two facilities. However, during hypervelocity/hypersonic entry the Orbiter is at relatively high angles of attack and thus the local Mach number over a majority of the windward surface is supersonic (typically between 2 and 3). For blunt to moderately blunt configurations such as the Orbiter at entry angles-of-attack, aerodynamic characteristics are essentially independent of Mach number. In terms of viscous simulation in the continuum (Reynolds number) regime, the flight free stream Reynolds number based on vehicle length was below 0.5×10^6 up to the point of the first measured off-nominal heating event on the side fuselage and OMS pod regions. The free stream Reynolds number for STS-107 had increased to approximately 2.4×10^6 at loss of signal near M=18. In the Mach 6 air testing, Reynolds number based on model length was varied between 0.3×10^6 and 6.5×10^6 , and the majority of testing occurred at 2.4×10^6 . The length Reynolds number in the Mach 6 CF₄ tunnel was varied between 0.05×10^6 and 0.55×10^6 with most of the testing at 0.4×10^6 . These Mach 6 CF₄ conditions are more representative of the flight conditions prior to loss of signal (higher altitude and Mach number). In the design of wind tunnel experiments, local conditions are often more appropriate when, for example, boundary layer correlations are sought. For the Orbiter at M=18 in flight, the edge Mach number at X/L=0.6 is approximately 3 with a post normal shock Reynolds number of 0.4×10^6 (Bouslog, 1995). The corresponding conditions for the Mach 6 air tunnel (at X/L=0.6) are 2.3 and 0.42×10^6 , respectively. During a nominal Orbiter entry at Mach numbers greater than 18, the windward (Bouslog, 1995) and leeward (Throckmorton, 1995) flows are laminar. Wall-to-total temperature ratio was 0.60 and 0.45 for the air and CF₄ tunnels, respectively. Flight wall-to-total temperature ratio for the Orbiter near Mach 18 at flight conditions is generally within the range of 0.2 to 0.3.

In terms of facility limitations, it is recognized that acoustic disturbances are inherent for any hypersonic ground-based facility having a turbulent boundary layer on the nozzle wall. This fact may promote transition in an attached or separated wall boundary layer earlier than may occur in flight. Surface roughness related transition data provided to the investigation for correlation purposes were based upon a fully effective roughness criterion, whereby turbulence is initiated immediately downstream of the roughness element site. When vehicle surface roughness is present (a typical boundary layer transition bypass), it is generally accepted within the transition community that facility noise from conventional tunnels has little effect on transition as long as roughness heights are large enough to be considered effective.

One of the largest unknowns associated with the ground-based testing performed as part of the STS-107 investigation is the extrapolation to flight of wind tunnel based leeside flow field characteristics. Data derived from conventional air facilities regarding leeward flow separation, reattachment, transition of separated or attached leeward flow, and leeward vortex interactions all present significant scaling issues as discussed by Haney (1995). Historically, the CF₄ tunnel has not been heavily utilized for characterization of separated, leeward (or wake) flows. Rather, it has been used for aerodynamic studies associated with blunt planetary entry configurations where the inviscid forebody flow is primarily governed by the normal shock density ratio (Jones, 1969). If, in hypervelocity flight, the Orbiter leeside flow is non-reacting or frozen due to the rapid flow expansion around the leading edge, it is quite possible that the CF₄ simulation (with a free-stream $\gamma=1.22$) will provide a rather good representation of coupled leeside flow physics and flow chemistry. It will be equally important in the future to determine how well CFD can accurately capture the “challenging” leeside flow physics (e.g., flow separation/reattachment, vortical flow) at wind tunnel conditions before the complexity of flow chemistry at flight conditions is introduced. In Mach 6 CF₄ results for the Orbiter, it has been observed that the spatial location of maximum OMS pod heating is closer to the location observed in flight (i.e., the high temperature black tile on the flight vehicle) relative to that inferred from test results in Mach 6 air. It is suggested by these observations that perturbations to the nominal leeward flow field from certain damage scenarios may also be better represented by the Mach 6 CF₄ tests (as opposed to Mach 6 air) as the disturbances generally originate from the windward surface.

5.2.3.2 Orbiter Configurations Tested

Baseline Orbiter Models

More than 70 cast ceramic models of the Orbiter configuration were manufactured as part of the investigation and they all share a common construction technique. Initially, during the first weeks of the investigation, existing ceramic 0.0075 scale models of the Orbiter from a prior NASA JSC/LARC collaboration (Berry, 2002) were utilized. The expansive scope of aeroheating testing needed for the investigation, however, required additional models to be fabricated. To accomplish this quickly, a pre-existing epoxy based mold constructed from the 0.0075 scale metallic force & moment model (used during the early phases of the aerodynamic testing-see Section 4.3.1) was used to slip cast each new ceramic model. A magnesia ceramic was used to backfill the ceramic shells, thus providing strength and support to the base mounted sting support structure. Ceramic models used during simultaneous aerodynamic and aeroheating tests were constructed in a similar fashion, but were modified to accept a six-component balance. An overview of model fabrication used exclusively for thermal testing is shown in Figure 5.2.3-3. In order to obtain accurate heat-transfer data with the phosphor or IR technique, the ceramic models are cast with a material having low thermal diffusivity and well-defined, uniform, isotropic thermal properties. The phosphor coatings typically do not require refurbishment between runs in the wind tunnel and have been measured to be approximately 0.001 inch thick. Details concerning the model fabrication technique and phosphor coating can be found in Buck (1993, 2000). Fiducial marks were placed on the model side fuselage surface at the locations for RTDs V34T1106A and V09T1724A (Orbiter coordinates provided by NASA JSC) and axial stations X/L= 0.25, 0.50, 0.75, and 0.90. These fiducial marks were used to assist in more accurately determining spatial locations of surface heating features.

Modified Orbiter Models

Damage to the Orbiter was simulated on the ceramic models in several ways and was driven by the leading scenario(s) at the time of testing. Initial modifications to the model surface involved placing discrete protuberances at strategic locations on the windward surface (e.g., left main landing gear door) and along the left wing leading edge (along individual RCC or adjacent carrier panels). Subsequent

modeling of damage scenarios was more intrusive and involved machining cavities or holes through the wing. Damage in the form of a completely missing isolated RCC panel 6 was initially attempted with hand tools and later with milling operations. The approximate locations of RCC panels, carrier panels, and TPS damage for these early tests were taken from technical drawings of the TPS layout (Joels, 1982) and transferred to the model surface via transparency. A higher fidelity, more systematic approach to characterizing wing leading edge damage was undertaken and involved construction of 13 models (see Figure 5.2.3-3) each with an individual missing RCC panel (1-13). RCC panel and adjacent upper and lower carrier panel locations were provided in the form of a CAD file. These locations were transferred to the model as discrete points via the surface verification laboratory at NASA LaRC. Additional models were constructed to characterize thermal effects associated with multiple missing RCC panels, partially missing panels (with and without vent paths down the RCC channel or to the leeside) on the wing upper surface, and missing T-seals. The leading edge channel formed by the Orbiter RCC panels was not captured with the ceramic models. Thus, removal of an RCC panel or T-seal yielded solid walls and hence no lateral pressure relief.

Simulation of leading edge damage with a leading edge channel (lateral pressure relief) similar to the flight vehicle required a unique approach to model construction. A solid model CAD file (1997 definition-see sec 5.2.3.2) was modified to approximate the volume of the RCC channel (Figure 5.2.3-4). A rapid prototyping technique was used to “grow” a resin stereolithography (SLA) model. Thermal protection of the resin model was provided for by application of a ceramic coating to the resin model. Qualitative thermal imaging was accomplished via the phosphor thermography technique. To characterize the thermal effects associated with RCC channel venting to the leeside, a similar approach was taken. A resin model was internally modified (see Figure 5.2.3-5) to blow CF_4 or nitrogen gas through a continuous 0.01-inch vent gap along the upper wing near the RCC/carrier panel interface.

5.2.3.3 Results for Mach 6 Air

Wing Leading Edge Discontinuities

The sensitivity of global aeroheating distributions on the windward and side fuselage surfaces to several forms of simulated RCC panel 6 damage is summarized in Figure 5.2.3-6 and Figure 5.2.3-7, respectively. These results, obtained using IR thermography, all correspond to the same model residence time in the flow and indicate local areas of increased surface temperature relative to the nominal configuration. The typical surface protuberances placed along the wing leading edge would correspond to a 13-inch x 13-inch full scale surface raised 0.5-inch above the nominal outer mold line. While shown to be effective at promoting boundary layer transition on the windward surface, the raised disturbances along the leading edge did not produce temperature augmentations on the side fuselage at these Mach 6 air conditions. The temperature image corresponding to run 47 in Figure 5.2.3-7 was the first direct experimental evidence that simulated RCC panel damage in the form of a “notch” could produce a localized heating anomaly on the Orbiter side fuselage.

Missing Wing RCC Panel Survey

The sensitivity of Orbiter side fuselage surface heating to simulated RCC panel damage for completely missing individual panels is summarized in Figure 5.2.3-8. At the time of testing, the body of recovered debris did not refute the possibility of entire RCC panels missing and it was felt that this form of damage would be easier to model computationally. Higher fidelity, parametric removal of individual leading edge RCC panels 1-13 was undertaken to characterize the location and magnitude of the heating disturbance on the side fuselage. The results were obtained using phosphor thermography and indicate local areas of increased surface heating relative to the nominal wing leading edge. Global heating distributions are presented in terms of the ratio of enthalpy-based heat-transfer coefficients h/h_{REF} , where h_{REF} corresponds to the Fay and Riddell (1958) predicted sphere stagnation-point heating with a 1-ft radius at flight scale (i.e., radius equal to 0.09-inches at wind tunnel scale). Unless noted otherwise, a constant maximum color value of 0.25 was selected for data presentation to maintain consistency when viewing or comparing images. On the contour scale, the colors tending towards red indicate areas of higher heating (temperatures) while the colors towards blue represent areas of lower heating.

A localized heating disturbance on the side fuselage (Figure 5.2.3-8) was evident for all panel locations RCC (1-13). Although the heating magnitudes associated with the disturbance were generally insensitive to the location of the missing panel, the inclination of the heating pattern on the side fuselage was

dependent on the span-wise location of the RCC damage. The nearly vertical side fuselage heating footprint associated with missing RCC panel 1 approached a nearly horizontal orientation (parallel to the Orbiter reference waterline) as the systematic removal of individual RCC panels progressed outboard to missing RCC panel 12. A missing RCC panel at the location of the Mach 6 air wing/bow shock interaction (RCC panel 12) did not result in abrupt changes to the side fuselage heating footprint in terms of location or magnitude. In addition, no large location or magnitude changes to the surface heating associated with missing RCC panel 12 were observed for small changes in angle-of-attack (Figure 5.2.3-9), sideslip (Figure 5.2.3-10), or a factor of 4 increase in Reynolds number (Figure 5.2.3-11). Heating images taken from above the model (Figure 5.2.3-12) indicated that disturbances created from wing leading edge damage could produce leeward flow field perturbations strong enough to reduce the OMS pod heating for missing RCC inboard of panel 9. In contrast, local heating augmentations to the forward face of the OMS pod were measured for missing $9 \leq \text{RCC panel} \leq 11$. Comparison of Schlieren images revealed the local shock structure complexity associated with missing RCC panel 8 (Figure 5.2.3-13) relative to a baseline undamaged wing leading edge (Figure 5.2.3-14).

Holes Through Wing

Limited parametric studies of simulated damage in the form of a wing breach from the windward surface to the leeward surface were attempted in this facility and were primarily associated with aerodynamic testing (see Section 4.3.1). Initially, circular holes dimensionally consistent with the width of a carrier panel (approximately 4 inches full scale) were placed at the interfaces for carrier panels 5, 9, 12, and 16. The holes were found to force boundary layer transition on the windward surface to the damage site. The model and IR setup for the aerodynamic tests at this point in time precluded imaging the side fuselage. Since the model also incorporated damage in the form of missing RCC panel 6, it is believed that effects (if any) from the carrier panel holes would have been dominated by the disturbance from the missing RCC panel.

TPS damage in the form of a much larger breach through the wing was attempted, but the side fuselage heating measurements were considered qualitative due to compromised phosphor coatings on the models that were used. The holes were orientated normal to the wing chord and were located near the left main landing gear door. One hole location was approximately located at the center of the forward bulkhead ($X=1040$ -inches in Orbiter coordinates) and the second location was near the center of the outboard bulkhead ($Y=167$ -inches in Orbiter coordinates). At each location, the wing hole diameter was systematically changed from 0.0625 to 0.125 and 0.25-inch at wind tunnel scale (8.3, 16.7, and 33.3-inch full scale). While the compromised phosphor coating considerably degraded the image quality, it was evident that no change in side surface heating was apparent for any tested combination of location or diameter.

Aerothermodynamics Associated with Asymmetric Boundary Layer Transition

Boundary layer transition on the Orbiter during re-entry is known to introduce small changes in the aerodynamics of the vehicle. Thus, in order to assess the sensitivity of Orbiter aerodynamics to several forms of simulated damage, damage resulting in boundary layer transition was evaluated. The surface heating results complementing the companion aerodynamic tests (see Section 4.3.1) were obtained using IR thermography. The results indicated several surface protuberances (corresponding to a 6-inch x 6-inch full scale surface raised 0.5 to 1-inch above the nominal outer mold line) placed along the wing leading edge would effectively promote Asymmetric Boundary Layer Transition (ABLT) on the windward surface. As mentioned in Section 4.0, the corresponding aerodynamic data provided the first direct evidence that while ABLT could produce measurable aerodynamic increments consistent with the Orbiter ABLT model for flight, the trends were inconsistent with STS-107 flight data.

5.2.3.4 Results for Mach 6 CF₄

Windward Surface Protuberances

A limited data set was obtained in the Mach 6 CF₄ tunnel to determine (1) if the Orbiter windward surface boundary layer could be forced turbulent with discrete isolated roughness, and (2) if the results were positive, could they be mapped onto a previously developed Orbiter boundary layer transition correlation developed in the Mach 6 air tunnel (Berry, 2002). The forced boundary layer transition results are summarized in Figure 5.2.3-15. Surface protuberances were placed on the windward centerline near X/L of 0.26. This location corresponds to the location of a protuberance observed on flight STS-73 which

resulted in an “early” high Mach number (approximately 19) boundary layer transition event. The protuberances correspond to a 6 x 6-inch full scale surface raised approximately 0.5, 0.9, and 1.5-inch above the nominal outer mold line. Boundary layer edge conditions were computed with a method consistent with the Mach 6 air correlation and yielded protuberance height-to-boundary layer thickness ratio (k/δ) values of 0.2 to 1.75. The discrete data points in Figure 5.2.3-15 correspond to laminar, incipient and effective roughness and these Mach 6 CF₄ data are compared with previously correlated Mach 6 air perfect gas results (solid curves). This limited data set represents the first discrete roughness boundary layer transition data on the Orbiter acquired in the Mach 6 CF₄ facility. Because complicated effects interact to produce boundary layer transition, and a comprehensive study could not be carried out (due to time constraints) of how the current limited Mach 6 CF₄ data set relates to the previously developed correlation of Berry (2002) for Mach 6 air, assessments of boundary layer transition for STS-107 utilized the previously developed correlation.

Missing Wing RCC Panel Survey

The sensitivity of side fuselage heating distributions to RCC panel damage in the Mach 6 CF₄ facility for completely missing panels is summarized in Figure 5.2.3-16. At the time of this testing, the body of recovered wing debris suggested that loss of an entire RCC panel was not likely, except for RCC panel 9. Higher fidelity, parametric removal of individual leading edge RCC panels (1-13) was pursued to characterize the location and magnitude of the heating disturbance on the side fuselage and to compare with the Mach 6 air results. Similar to the previously obtained Mach 6 air data, the CF₄ results were obtained using phosphor thermography and indicate local areas of increased surface heating relative to the nominal configuration. As discussed previously, global heating distributions are presented in terms of the ratio of enthalpy-based heat-transfer coefficients h/h_{REF} , and unless noted otherwise, a constant color bar maximum value of 0.25 was selected with colors tending towards red indicative of areas of higher heating (temperatures).

A localized heating disturbance on the side fuselage (Figure 5.2.3-16) was evident for all RCC panel locations (1-13). The relationship of the heating pattern inclination on the side fuselage to missing panel span-wise location was different from that observed for Mach 6 air. The local disturbance in the Mach 6 CF₄ facility was “directed” at the OMS pod, resulting in heating augmentations to the forward face of the OMS pod for missing panel $1 \leq RCC \leq 10$ (in contrast to heating reductions in Mach 6 air). Similar to the Mach 6 air trends, however, heating magnitudes associated with the disturbance on the side fuselage were generally insensitive to the location of the missing panel. A missing RCC panel at the location of the wing/bow shock interaction for Mach 6 CF₄ (RCC panel 9) did not result in abrupt location or magnitude changes to the side fuselage heating footprint. Similar to the observation in Mach 6 air results, the side fuselage heating footprint approached a nearly horizontal orientation (parallel to the Orbiter reference waterline) as the systematic removal of individual RCC panels progressed outboard. No significant Reynolds number effects were observed for TPS damage in the form of missing RCC panels. Based upon the Mach 6 air results, no Mach 6 CF₄ heating sensitivity studies were attempted for angle-of-attack and sideslip.

The leading edge channel formed by the wing spar and RCC panels on the flight vehicle was not captured with the solid ceramic models. Removal of an individual RCC panel by a milling machine yielded solid walls and hence, no lateral pressure relief. Limited tests on ceramic-coated resin models with a leading edge channel were conducted to investigate this. Characterization of any differences in the leeside flow field associated with a missing RCC panel and lateral pressure relief along the wing leading edge was felt necessary. Although qualitative in terms of heating magnitudes, the comparison of side fuselage heating patterns associated with an open and closed leading edge channel (Figure 5.2.3-17) suggests that the local heating disturbance propagates further forward (i.e., further upstream) when the damaged cavity is allowed to vent down the RCC channel.

Partial RCC Panel Damage

As the debris recovery effort drew to a close, the body of evidence indicated that partially damaged RCC panels (as opposed to entirely missing panels) was likely. Sensitivity of the Orbiter side fuselage heating associated with several forms of RCC panel 9 damage are shown in Figure 5.2.3-18. At this wing leading edge location only a missing T-seal or a completely missing RCC panel lead to off-nominal heating disturbances on the side fuselage or OMS pod. The missing T-seal was located at the RCC 8/9 interface and was sized to simulate a gap taken from the leading edge back to the wing spar. The gap width was

approximately 1.3-inch full scale, which corresponds roughly to the correct width for a removed T-seal. In contrast to the completely missing RCC panel, the missing T-seal disturbance did not indicate any off nominal side fuselage heating and affected only the lower side surface of the OMS pod.

The various forms of lower RCC panel 9 damage did not result in side fuselage/OMS pod off nominal heating (Figure 5.2.3-18). However, this was not the case for all wing leading edge locations, as shown in Figure 5.2.3-19. The test results indicated that the extent of RCC panel damage in relation to the wing leading edge attachment line largely determines if the disturbance is "swept" to the leeside. Qualitative heating images associated with the companion force and moment tests indicated the threshold for disturbances propagated to the leeside from half RCC panel damage was between RCC 5 and 6 (see Section 4.3.1, Figure 4.3.16). In other words, half RCC panel damage at panels 1 to 4 produced fuselage side heating disturbances in the Mach 6 CF₄ facility, whereas half RCC panel damage outboard of panel 5 did not.

Holes Through Wing

Limited parametric studies for simulated damage in the form of a breach from the wing windward surface to the leeward surface were attempted in the Mach 6 CF₄ facility for dedicated aero-heating tests. Wing hole parametrics were primarily associated with the simultaneous aerodynamic/aero-heating testing (see sec 4.3.1). Similar to the Mach 6 air results discussed previously, holes through the wing (located at the center of carrier panels 6, 9, 12) were found to increase heating on the windward surface, a characteristic of boundary layer transition. With regard to the dedicated aeroheating tests, an early qualitative result with a single circular hole placed at the RCC/carrier panel 5/6 interface did not result in off-nominal heating to the side fuselage/OMS pod (Figure 5.2.3-20). Heating associated with missing RCC panel 6 is shown for comparison. The hole was orientated normal to the wing chord with the diameter dimensionally consistent with the width of a carrier panel.

Venting from Discrete Locations along Wing Upper Surface with RCC Panel Damage

Qualitative heating images associated with the companion force and moment tests indicated that disturbance propagation to the side fuselage with partial RCC panel damage (the lower surface missing) for panels outboard of RCC 5 was possible. In order to investigate a partial panel damage case that might lead to leeside heating effects, the stagnated flow in the damaged panel region was allowed to vent via a carrier panel slot (see Sec 4.3.1). This experimental evidence coupled with a developing understanding of recovered Columbia debris prompted an effort to qualitatively characterize the possible influence of mass addition on the leeside flow field. The ceramic-coated resin models that possessed a wing leading edge channel were further modified to include venting paths to the leeward surface. The total estimated venting area was first computed per unit panel; a series of circular holes with the per panel vent area were drilled into the leading edge channel near each RCC/carrier panel interface. The channel was allowed to pressurize via damage in the form of a completely missing RCC panel 9. No attempt was made to measure local pressure or mass flow rate along the wing leading edge. The qualitative data presented in Figure 5.2.3-21 reveals little effect of this venting via circular holes on side fuselage heating patterns. Since the model also incorporated damage in the form of missing RCC panel 9, it is believed that effects (if any) from the discrete carrier panel venting holes were dominated by the disturbance from the missing RCC panel.

Venting from Continuous Gap Along Upper Wing Surface with/without RCC Panel Damage

To isolate possible venting effects from major RCC damage that dominates the leeward flow field, qualitative tests were first conducted on a ceramic-coated resin model with an undamaged leading edge. In contrast to the previous resin model with discrete holes, new resin models with a continuous 0.01-inch wide vent gap running along the upper wing RCC/carrier panel interface were fabricated (see Figure 5.2.3-5). The gap width on the model was a limitation of the manufacturing process and is approximately a factor of 10 larger than the actual vent gap width at model scale. Gaseous CF₄ was fed to the gap internally via a free-stream flow field pitot tube and allowed to vent to the leeside through the gap. A pressure measurement inside the wing provided a pressure measurement for the flow being fed into the RCC channel. The internal gap pressure measurement divided by the computed surface pressure exceeded a factor of 2, indicating the flow was sonic at the gap (surface pressure predictions at wind tunnel conditions provided by methods detailed in Section 5.2.4). The qualitative data presented in Figure 5.2.3-22 suggests that mass addition (venting) to the leeside via this continuous vent gap behind RCC 1 to 22 forces wing flow separation and leeside flow field perturbations, resulting in off-nominal low

heating on both the side fuselage and the OMS pod. The maximum contour ratio of enthalpy-based heat-transfer coefficients h/h_{REF} , was changed to 0.10 for the leeward planform image to provide more detail associated with the heating patterns ($h/h_{REF} = 0.25$ for the side fuselage images).

Having demonstrated leeside flow field perturbations from venting, attempts at controlling mass flow rates using gaseous nitrogen were made. As with the previous CF_4 venting study, the qualitative heating tests were conducted on a ceramic-coated resin model with an undamaged leading edge. The objective of these tests was to correlate the off nominal low side fuselage/OMS pod heating using a local jet momentum to free-stream momentum ratio. The form of the momentum ratio was based on previous work by Stone and Cary (1972), and Zukoski and Spaid (1964). The experimental results shown in Figure 5.2.3-23 at two free-stream Reynolds numbers reveal off-nominal low side fuselage heating for momentum ratios > 0.35 , and OMS pod heating reductions for momentum ratios > 0.80 . These momentum ratios were determined by assuming sonic orifice conditions. The maximum contour ratio of enthalpy-based heat-transfer coefficients h/h_{REF} , was changed to 0.10 for these side fuselage images to provide more detail associated with the heating patterns. These results provide experimental data suggesting that a threshold scaling parameter ratio of about 0.3 or greater is required to cause side fuselage effects, and a threshold value of 0.5 or greater is required for OMS pod effects.

To conclude the wing venting characterization study, a cavity near the lower surface carrier panel of RCC panel 8 was machined into the previously tested resin model (Figure 5.2.3-24) permitting the wing leading edge channel to pressurize and vent to the wing leeward surface along the gap. The initial wing hole-to-vent gap area ratio was approximately 0.5. It has been previously shown that lower half panel RCC damage at this location (RCC panel 8) does not affect leeside heating, whereas the lower RCC panel damage shown in Figure 5.2.3-24 produces leeside heating effects. Similar to the previous venting scenarios, regions of off-nominal low heating were evident on the side fuselage/OMS pod as shown in Figure 5.2.3-24. In this image, the maximum contour ratio of enthalpy-based heat-transfer coefficients h/h_{REF} , was changed to 0.10 for the leeward planform image to provide more detail associated with the heating patterns ($h/h_{REF} = 0.25$ for the side fuselage images). Increasing the wing hole-to-vent gap area ratio to approximately 1 produced similar effects (not shown) on the off nominal heating.

5.2.3.5 General Experimental Observations

Description of Leeside Flow

The purpose of this section is to provide a brief overview of the Orbiter leeside flow field and to provide insight into how some of the RCC damage scenarios may have affected the side fuselage/OMS pod heating. An interpretation of the Orbiter leeside flow, Figure 5.2.3-25, taken from Baranowski (1983), captures the complexity of the three-dimensional flow structures that affect the Orbiter's leeward surfaces Figure 5.2.3-25 (a). The leeside is dominated by regions of strong flow expansions, flow separation/reattachment (which may be laminar, transitional, or turbulent), shock interactions, and vortical flow. For these reasons, the leeward flow field is highly sensitive to compressibility and viscous effects, and may be chemically frozen.

Flow features in the upper payload bay area with angles-of-attack less than 35 deg, are thought to be dominated by a vortex pair that interact along the centerline, Figure 5.2.3-25 (b, c, and d-1). At angles-of-attack between 35 and 45 deg, this vortex pair moves off the surface as depicted in Figure 5.2.3-25 (1d-2). Below this primary vortex pair a "quasi" boundary layer forms within which secondary or tertiary embedded vortices can develop. The so-called "vortex" scrubbing often used to describe the heating along the Orbiter side fuselage is, in actuality, reattachment of flow that has separated from the upper wing surface. It is this complex system of separated /re-circulating flow that is potentially perturbed by disturbances emanating from wing leading edge damage. Baranowski (1983), writes "...properties in the upper fuselage vortices are likely to be influenced by flow originating along the strake [wing] leading edge and impinging on the side fuselage." It is reasonable to assume that wing damage which alters the leading edge flow separation characteristics could have first-order effects on side fuselage/OMS pod heating.

Leeside Flow with Wing Leading Edge Damage

The effects of a missing RCC panel on Orbiter leeside flow as inferred from surface heating and corresponding streamline patterns are shown in Figure 5.2.3-26. Flow separation from the wing upper

surface and subsequent reattachment on the side fuselage as described by Baranowski (1983) is apparent from the surface oil flow streamline patterns. Locally displaced flow separations/reattachments (inferred from streamline patterns) are shown in Figure 5.2.3-26. Displacement of the embedded wing shock(s) as depicted in Figure 5.2.3-25 (1d-2) is also probable. It is believed that a jet-like plume originating from the wing leading edge damage is responsible for the observed heating augmentations. Until computational predictions demonstrate the ability to accurately capture the complex surface phenomenon (i.e., leeside wing separation, reattachment for both damaged and undamaged leading edges) as shown in Figure 5.2.3-26, the nature of the perturbed off-surface leeside flow remains speculative.

Off-Nominal Leeside Heating Trends

Side fuselage/OMS pod heating augmentations and reductions resulting from various damage scenarios have been identified from the ground-based tests. However, the off-nominal heating disturbances inferred from the experimental data were highly localized. In addition, the exact damage to Columbia is unknown and time dependent. These two factors are strong indicators that comparisons of wind tunnel derived augmentation/reduction factors to flight thermocouple and RTD magnitudes be performed with prudence.

The heating data presented in Figure 5.2.3-22 through Figure 5.2.3-24 suggest that in the absence of major leading edge damage (that tends to dominate the leeward flow field and results in *both* off-nominal high and low heating), mass addition via a degraded upper surface vent slot along the RCC 1-22/carrier panel interface can produce off-nominal low heating on both the side fuselage and OMS pod. As the heating data measurements were made on resin models, they are considered qualitative. However, it was determined that the side fuselage areas indicated in Figure 5.2.3-22 showed heating reductions of approximately 65% to 75% of the nominal surface heating. In terms of momentum ratio, a threshold for leeside venting effects was experimentally determined and should be correlated against flow field predictions involving both leading edge damage and leeside venting. However, the experimental data do suggest that a momentum ratio of at least approximately 0.3 is required to provide changes in leeside heating on the Orbiter.

Side fuselage heating augmentations associated with missing RCC panels were found to range from 2 to 12. In Mach 6 air, no changes to the surface heating associated with missing RCC panel 12 were observed for small changes in angle-of-attack (Figure 5.2.3-9), sideslip (Figure 5.2.3-10), or a factor of 4 increase in Reynolds number (Figure 5.2.3-11). Similar to the Mach 6 air trends, side fuselage heating peak magnitudes associated with missing RCC panels in Mach 6 CF₄ were generally insensitive to the location of the missing panel as shown Figure 5.2.3-16.

The test results in both facilities indicate that missing RCC panel damage outboard of RCC panel 10 leads to the heating footprint becomes nearly horizontal to the Orbiter reference waterline. In this orientation, the disturbance would act much like a "fluid fence" and would effectively prevent flow from flowing up through the elevon/fuselage gap to impinge on the lower aft corner of the OMS pod such as occurs with a nominal configuration (Haney, 1995).

Effect of Normal Shock Density Ratio on Heating Patterns

Side fuselage localized heating disturbances for normal shock density ratios of approximately 5 ($\gamma_{\text{eff}} = 1.4$) and 12 ($\gamma_{\text{eff}} = 1.13$) are contrasted in Figure 5.2.3-27 for individual missing RCC panels (1, 5, and 9). It has been noted earlier that for a missing RCC panel inboard of panel 10, the local heating disturbance on the side fuselage was more inclined from vertical in Mach 6 CF₄ than in Mach 6 air. That effect results in heating augmentations to the forward face of the OMS pod (see also Figure 5.2.3-16). For CF₄, it is speculated that local differences in γ on the leeside contribute to leading edge separation differences on the upper surface of the wing. It is not unreasonable to assume that differences in the wing embedded shock structure associated with air and CF₄ for a missing RCC panel would affect the flow to the leeside in a contrasting manner. Stronger flow expansions characteristic of a lower γ would imply larger flow turning angles as the separated flow off the wing is swept aft. If in flight, the Orbiter leeside flow is non-reacting or frozen due to the rapid flow expansion around the leading edge, it is quite possible that the Mach 6 CF₄ simulation (with a value of freestream γ limited to 1.22) provides a better representation than Mach 6 air ($\gamma = 1.4$) of coupled leeside flow physics and chemistry associated with hypervelocity flight.

Detailed computational and experimental studies of this topic would be required to address this question more comprehensively. However, at this time, the maturity of CFD to contribute significantly to a better characterization of the leeside flow field and γ effects is an open topic of discussion.

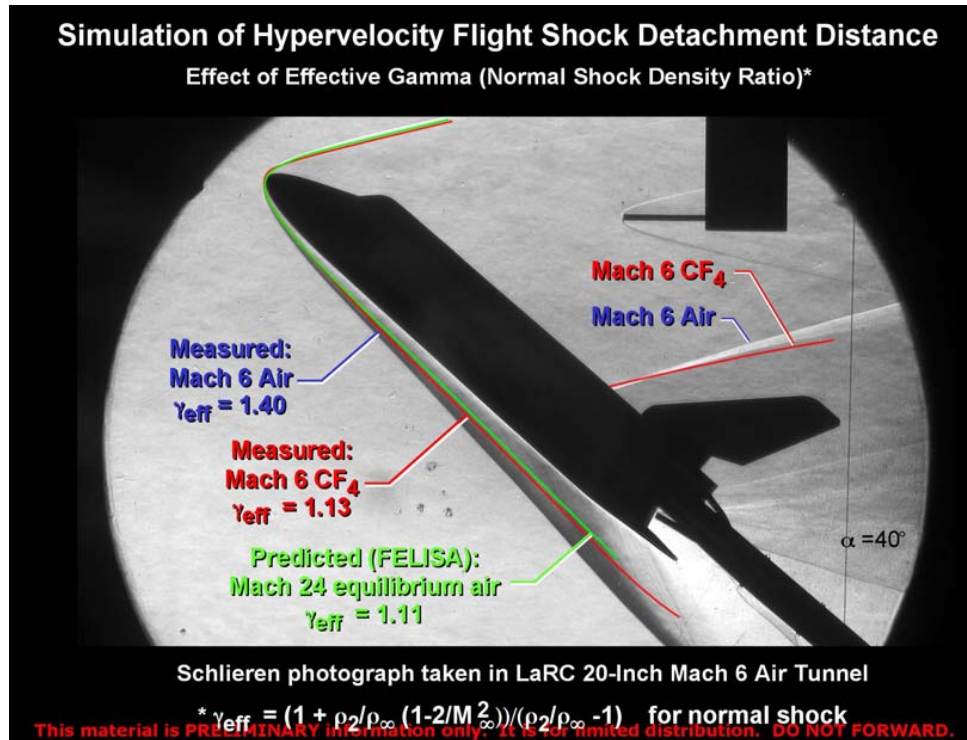


Figure 5.2.3-1 Simulation of Hypervelocity Flight Shock Detachment Distance

LAURA Prediction of Orbiter Surface Pressure and Heating

Comparison of Mach 24 Flight to CF₄ Wind Tunnel Condition

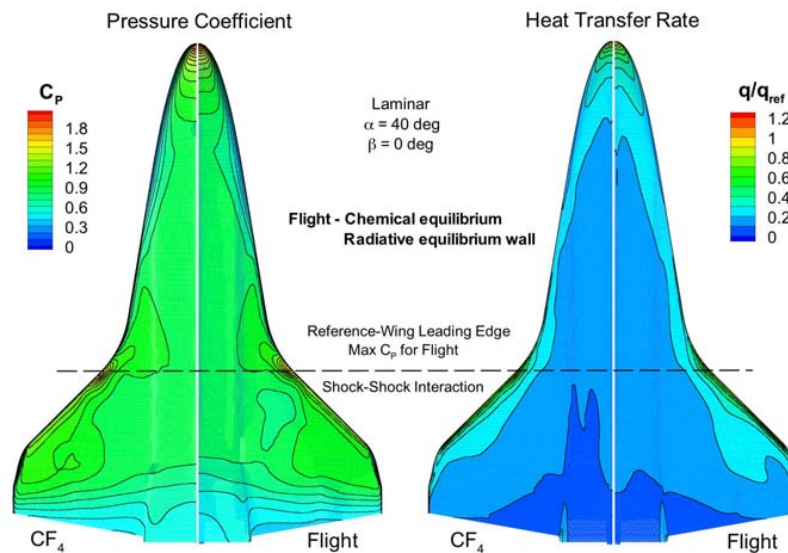
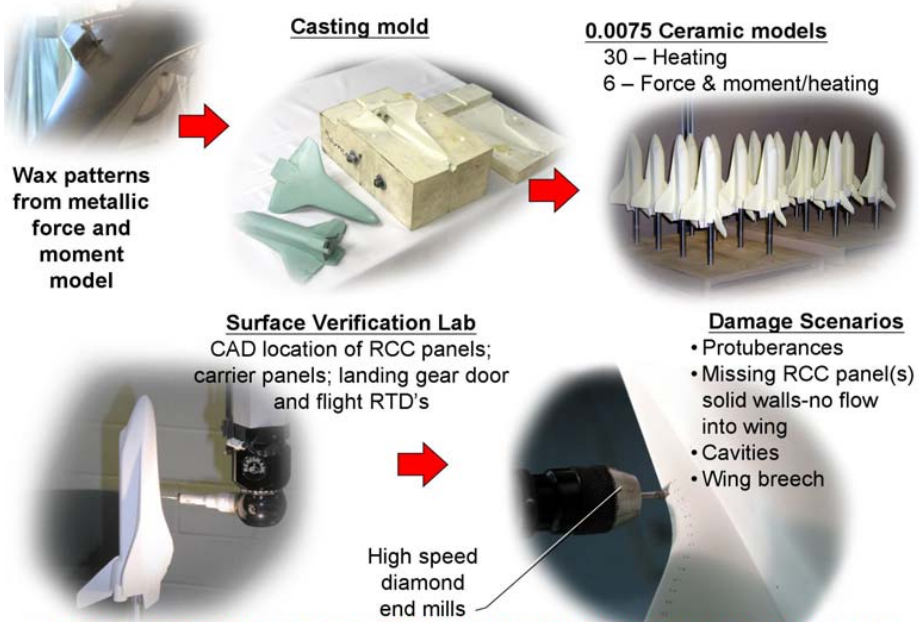


Figure 5.2.3-2 LaRC LAURA solutions of Orbiter windward surface pressure and heat flux

Overview of Orbiter Wind Tunnel Model Fabrication



This material is PRELIMINARY information only. It is for limited distribution. DO NOT FORWARD.

Figure 5.2.3-3 Ceramic model fabrication process

Fabrication of Shuttle Orbiter Wind Tunnel Model With Wing RCC Channel

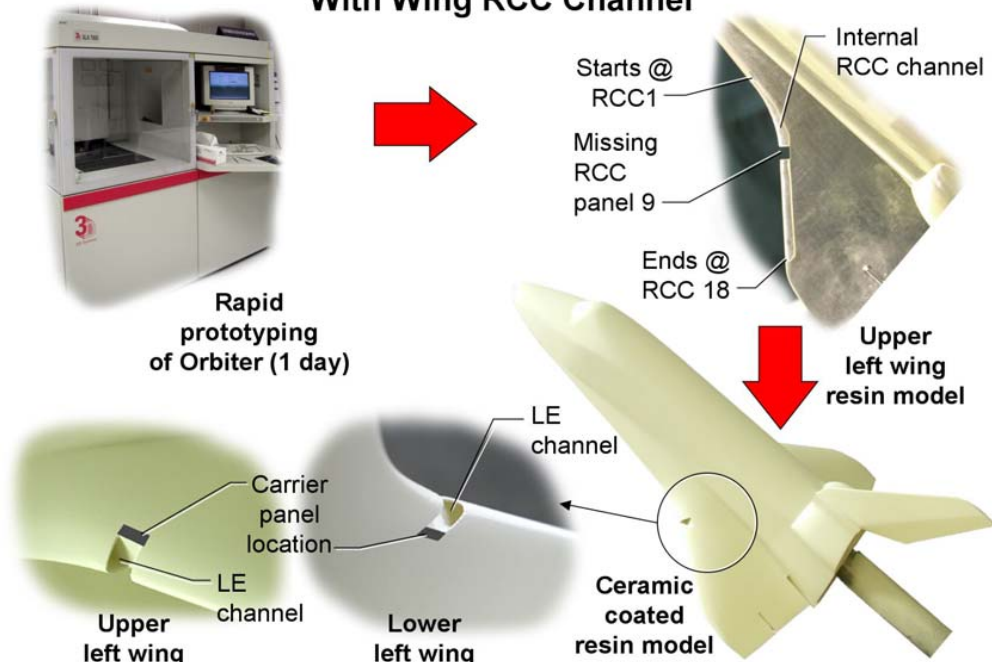


Figure 5.2.3-4 SLA model fabrication process of Orbiter with WLE cavity

Fabrication of Shuttle Orbiter Wind Tunnel Model With Vent Gap Along Wing Leading Edge

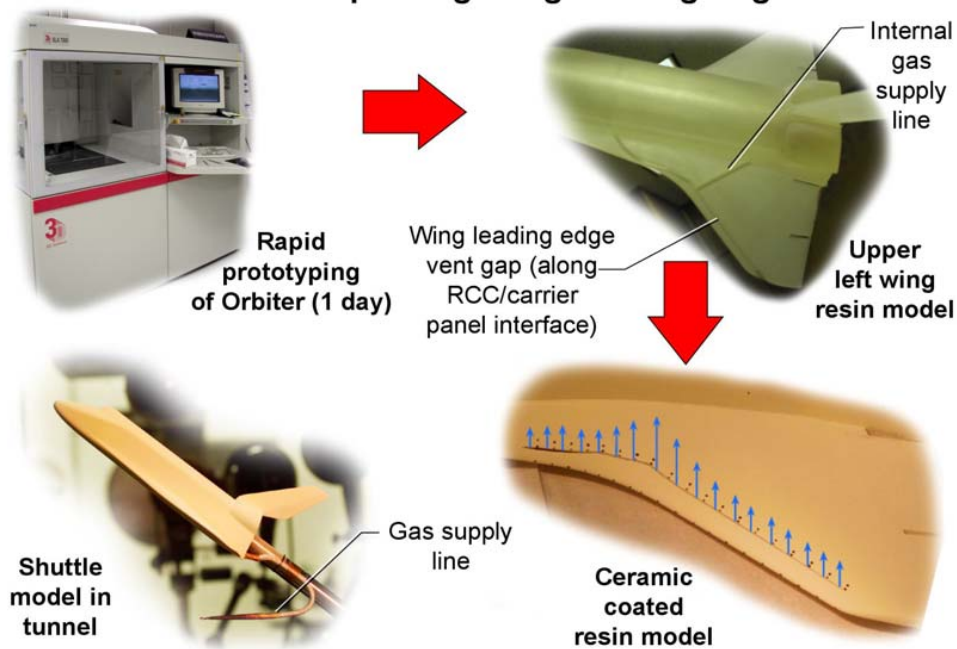


Figure 5.2.3-5 SLA fabrication process of Orbiter with WLE vented cavity and gas supply line

Effect of RCC Panel #6 L.E. Surface Discontinuity on Orbiter Windward Thermal Mapping

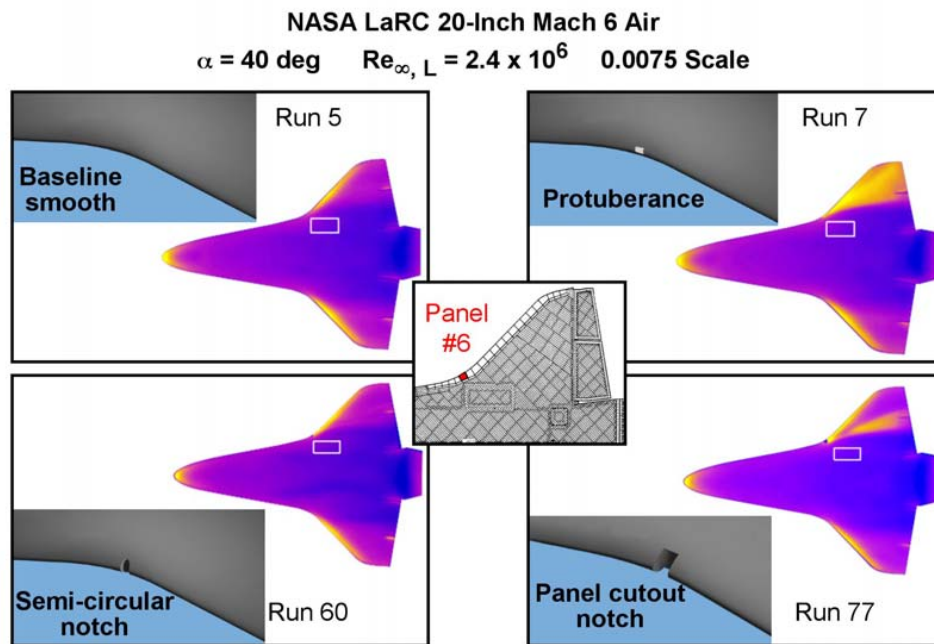


Figure 5.2.3-6 Effect of RCC Panel 6 surface discontinuity, windward view

Effect of RCC Panel #6 L.E. Surface Discontinuity on Orbiter Mid Fuselage Thermal Mapping

NASA LaRC 20-Inch Mach 6 Air
 $\alpha = 40 \text{ deg}$ $Re_{\infty, L} = 2.4 \times 10^6$ 0.0075 Scale

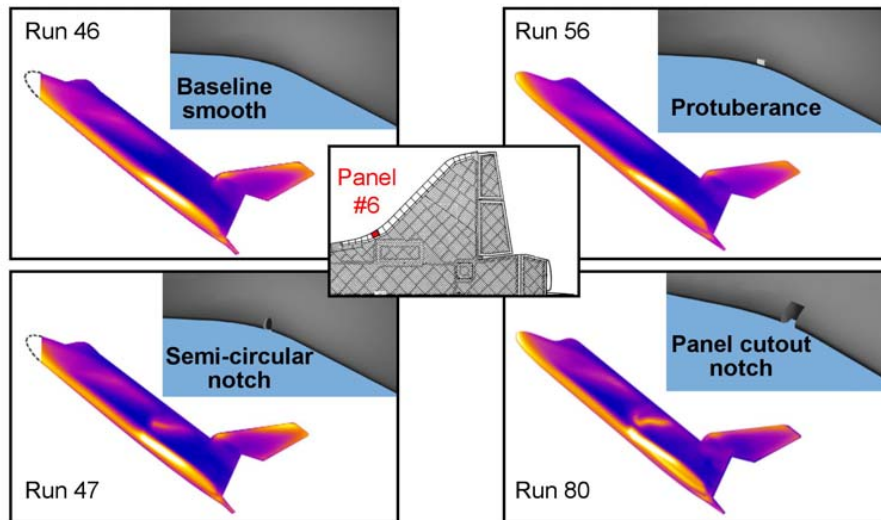


Figure 5.2.3-7 Effect of RCC Panel 6 surface discontinuity, side fuselage view

Complex Leeward Flowfield Associated with Orbiter Leading Edge Damage

Mach 6 Air $\gamma_{\text{eff}} = 1.4$ $\alpha = 40 \text{ deg}$ $Re_{\infty, L} = 2.4 \times 10^6$ $\beta = 0 \text{ deg}$

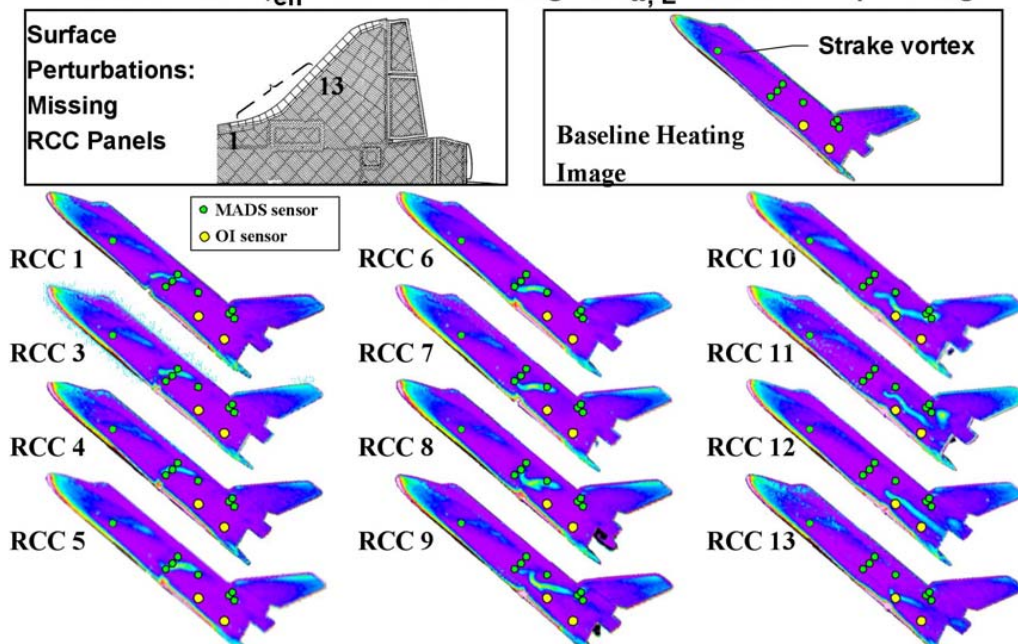
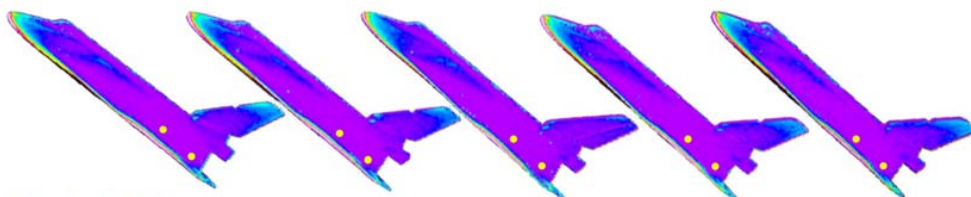


Figure 5.2.3-8 Mach 6 Air results of full RCC panel removed

Effect of Angle-of-Attack on Side-Fuselage Heating Patterns Associated With Missing RCC Panel Near Shock Interaction

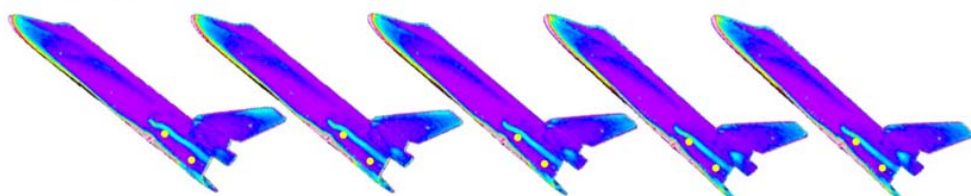
Mach 6 Air $\gamma_{\text{eff}} = 1.4$ $\alpha = 40 \text{ deg}$ $Re_{\infty, L} = 2.4 \times 10^6$ $\beta = 0 \text{ deg}$

Baseline



Missing RCC

panel #12 (Wing/bow shock interaction location perfect gas M = 6 air)



$\alpha = 38 \text{ deg}$

39 deg

40 deg

41 deg

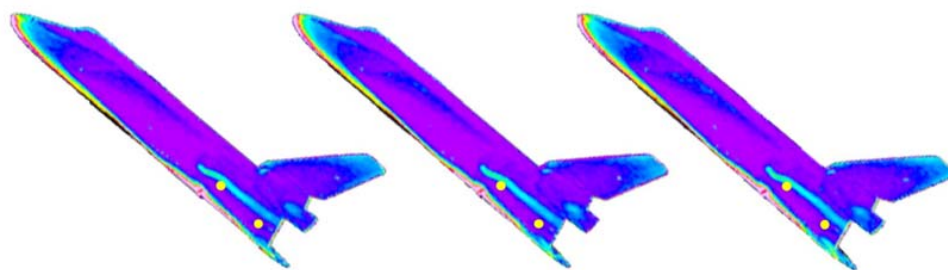
42 deg

No large location or magnitude changes associated with side-fuselage heating

Figure 5.2.3-9 Assessment of the effect of angle of attack on side fuselage heating

Effect of Sideslip on Side-Fuselage Heating Patterns Associated With Missing RCC Panel Near Shock Interaction

Mach 6 Air $\gamma_{\text{eff}} = 1.4$ $\alpha = 40 \text{ deg}$ $Re_{\infty, L} = 2.4 \times 10^6$



$\beta = +1 \text{ deg}$

0 deg

-1 deg

No large location or magnitude changes associated with side-fuselage heating

Figure 5.2.3-10 Assessment of the effect of angle of sideslip on side fuselage heating

Effect of Reynolds Number on Side-Fuselage Heating Patterns Associated With Missing RCC Panel Near Shock Interaction

Mach 6 Air $\gamma_{\text{eff}} = 1.4$ $\alpha = 40$ deg $\beta = 0$ deg

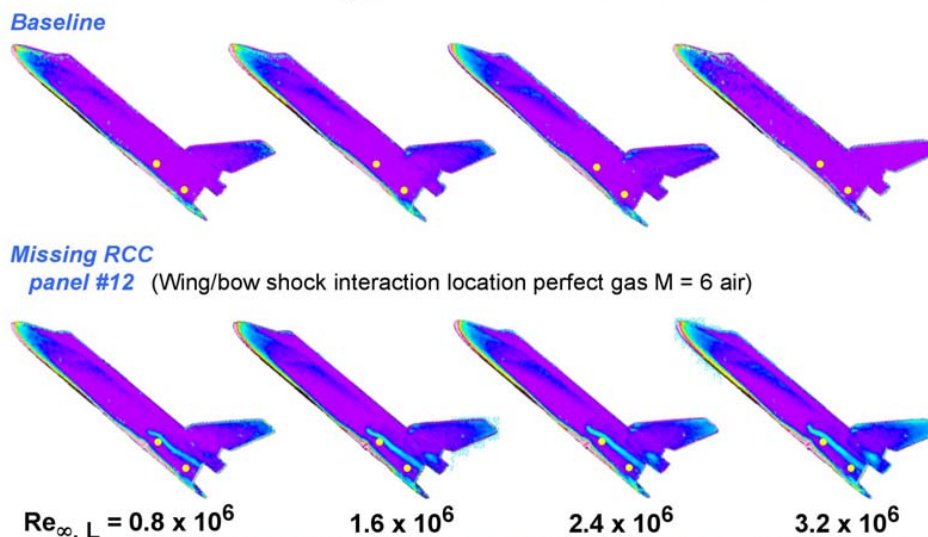


Figure 5.2.3-11 Assessment of the effect of Reynolds Number on side fuselage heating

Effect of Missing RCC Panel on Orbiter Leeside Flowfield as Inferred From Surface Heating Patterns

Mach 6 Air $\gamma_{\text{eff}} = 1.4$ $\alpha = 40$ deg $Re_{\infty, L} = 2.4 \times 10^6$ $\beta = 0$ deg

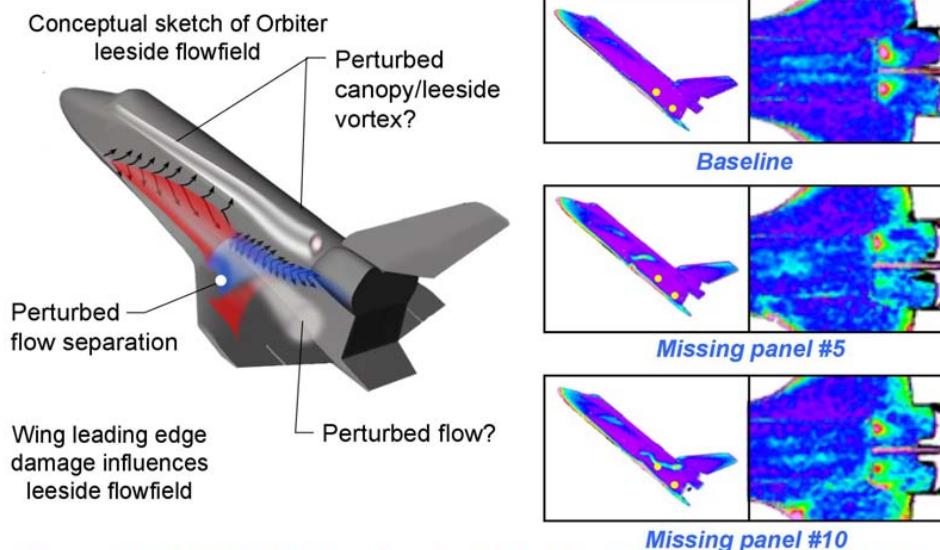


Figure 5.2.3-12 Orbiter leeside flow field changes as a result of WLE damage

Orbiter Leeside Heating and Corresponding Shock Pattern

Mach 6 Air $\gamma_{\text{eff}} = 1.4$ $\alpha = 40$ deg $Re_{\infty, L} = 2.4 \times 10^6$ $\beta = 0$ deg

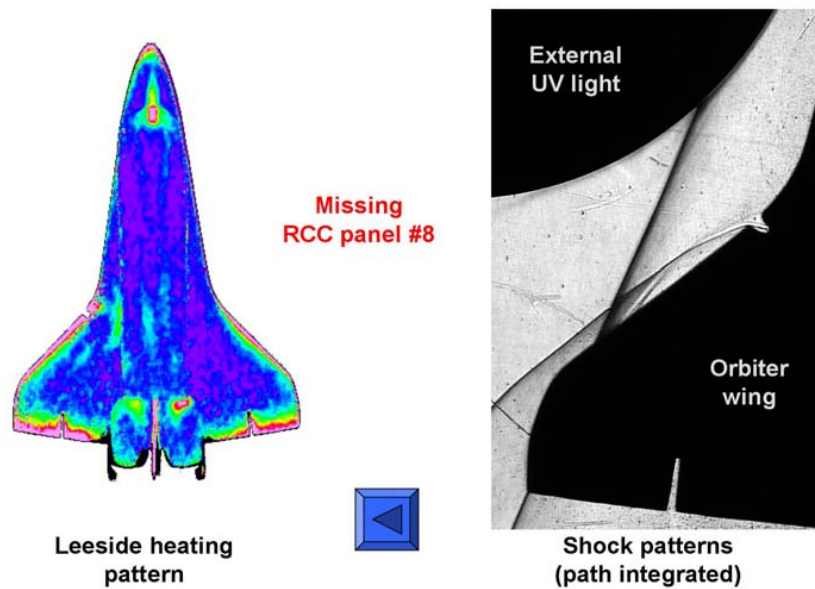


Figure 5.2.3-13 RCC Panel 8 Removed leeside heating and shock pattern

Orbiter Leeside Heating and Corresponding Shock Pattern

Mach 6 Air $\gamma_{\text{eff}} = 1.4$ $\alpha = 40$ deg $Re_{\infty, L} = 2.4 \times 10^6$ $\beta = 0$ deg

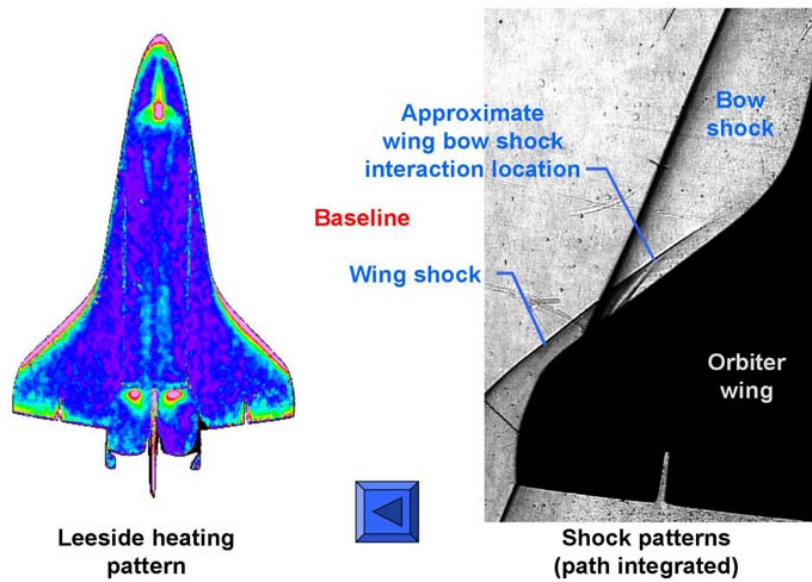


Figure 5.2.3-14 Baseline leeside heating and shock pattern

Roughness Induced Transition on Shuttle Orbiter

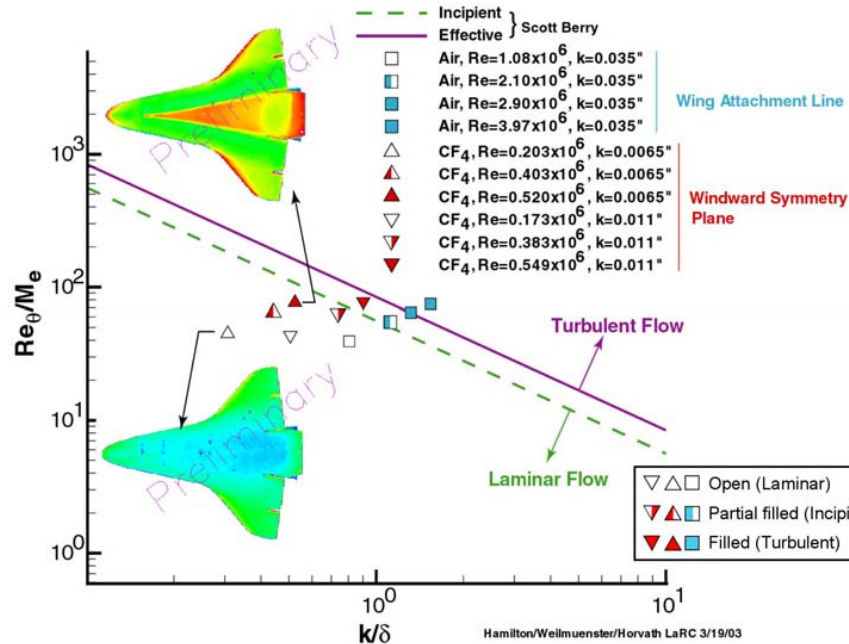


Figure 5.2.3-15 Roughness induced transition on the Orbiter. Berry correlation as compared to wind tunnel test results in both Mach 6 Air and Mach 6 CF₄

Complex Leeward Flowfield Associated with Orbiter Leading Edge Damage

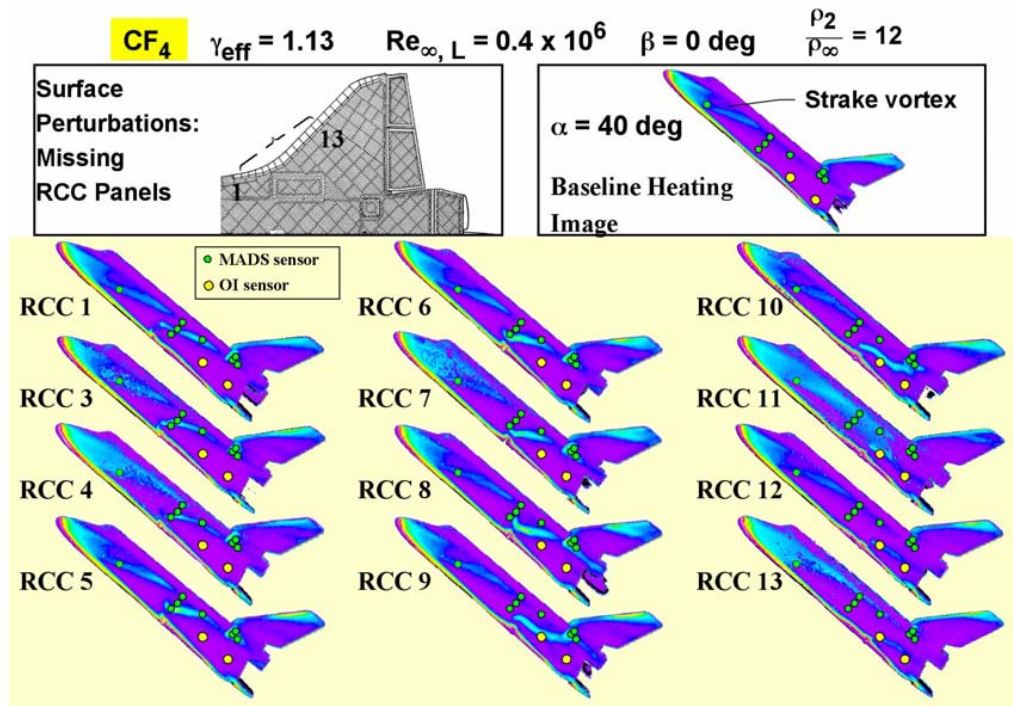


Figure 5.2.3-16 Mach 6 CF₄ results for full RCC panels removed

Sensitivity of Orbiter Side Fuselage Thermal Mapping Pattern to Open/Closed Leading Edge RCC Channel

$$CF_4 \quad \gamma_{\text{eff}} = 1.13 \quad \alpha = 40 \text{ deg} \quad Re_{\infty, L} = 0.4 \times 10^6 \quad \beta = 0 \text{ deg} \quad \frac{p_2}{p_{\infty}} = 12$$

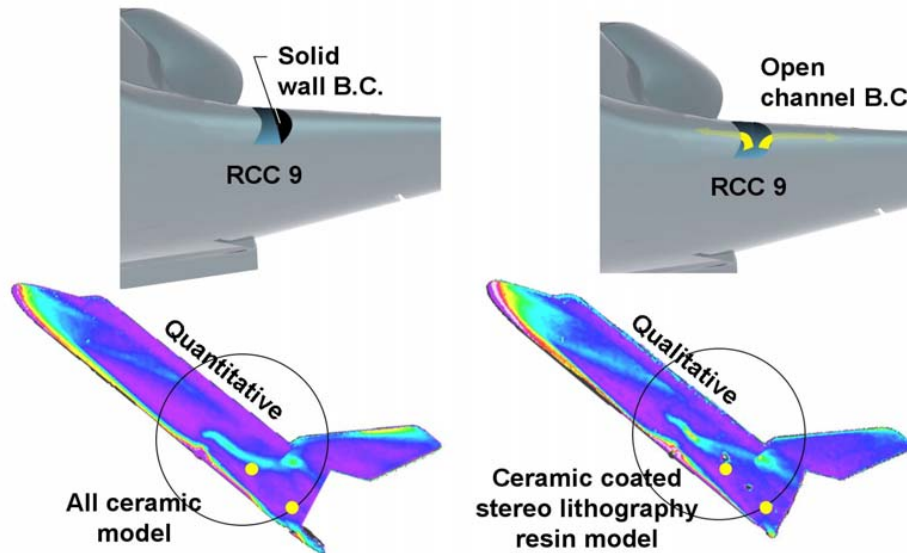


Figure 5.2.3-17 Effect of closed versus opened WLE cavity on side fuselage heating footprint

Sensitivity of Orbiter Side Fuselage Heating to Partially Damaged RCC Panel 9

$$CF_4 \quad \gamma_{\text{eff}} = 1.13 \quad \alpha = 40 \text{ deg} \quad Re_{\infty, L} = 0.4 \times 10^6 \quad \beta = 0 \text{ deg} \quad \frac{p_2}{p_{\infty}} = 12$$

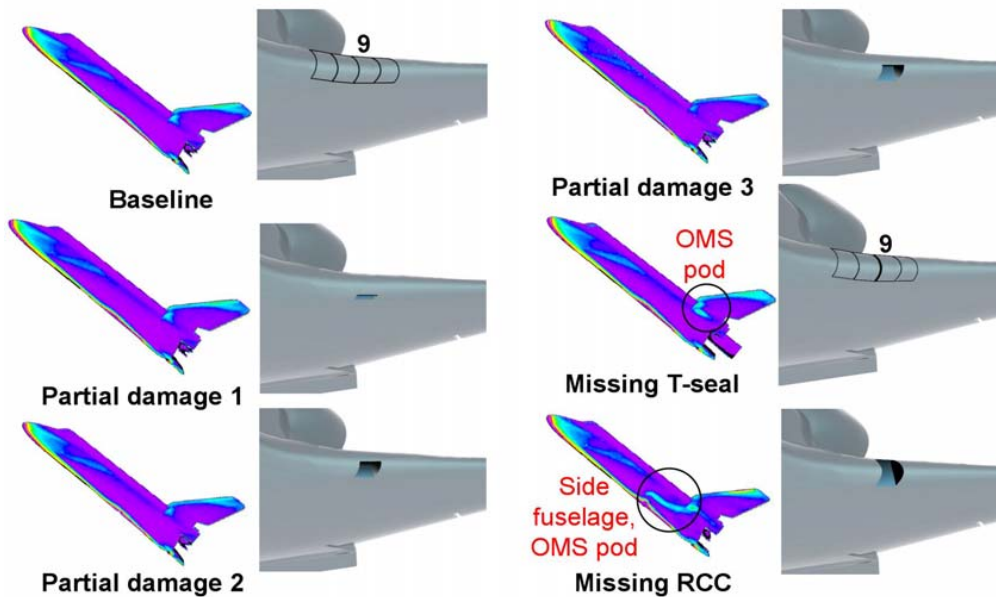


Figure 5.2.3-18 Effect of various types of panel 9 damage on side fuselage heating

Sensitivity of Orbiter Side Fuselage Thermal Patterns to Partially Damaged RCC Panels

CF_4 $\gamma_{eff} = 1.13$ $\alpha = 40 \text{ deg}$ $Re_{\infty, L} = 0.4 \times 10^6$ $\beta = 0 \text{ deg}$ $\frac{p_2}{p_{\infty}} = 12$

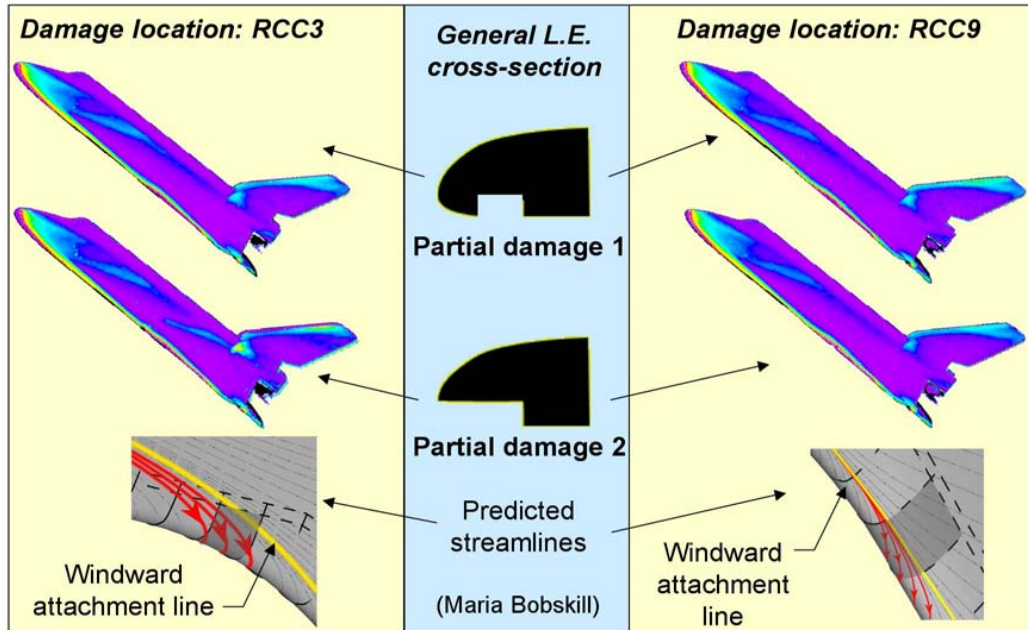
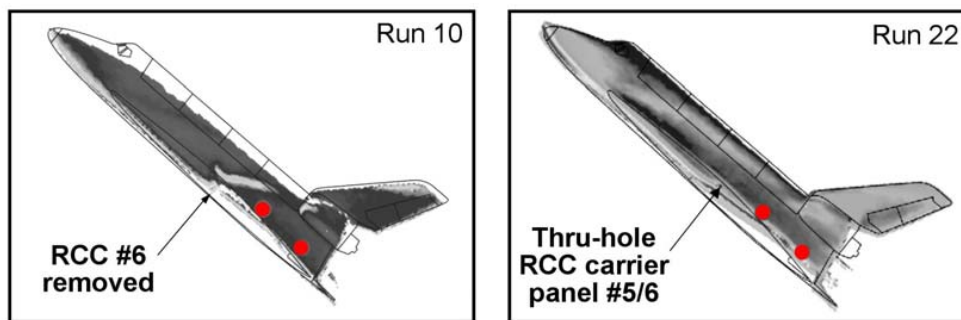


Figure 5.2.3-19 Partial panel damage assessment

Effect of RCC Panel L.E. Surface Discontinuity on Orbiter Mid Fuselage Thermal Mapping

NASA LaRC CF_4

$\alpha = 40 \text{ deg}$ $Re_{\infty, L} = 0.45 \times 10^6$ $\gamma_2 = 1.15$ 0.0075 Scale



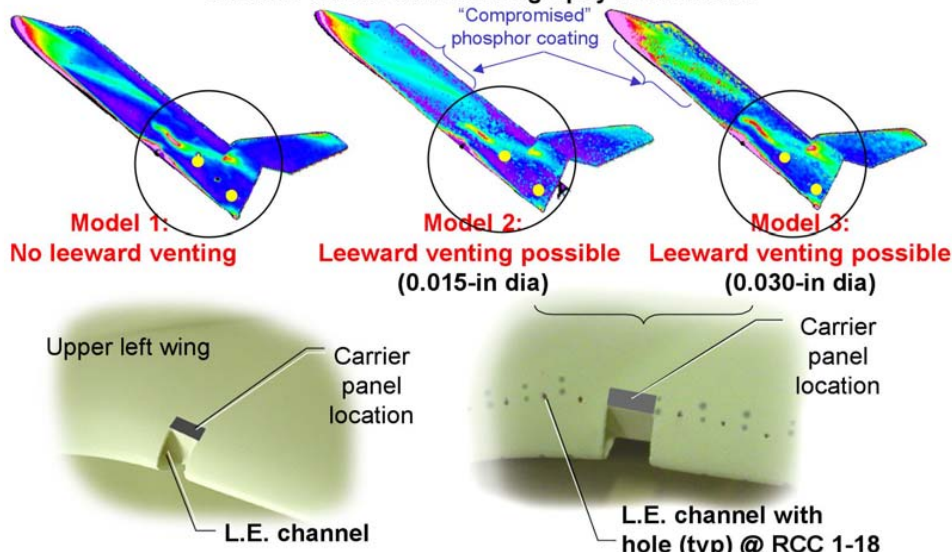
Note grayscale level change between runs

Figure 5.2.3-20 Hole through the wing assessment

Sensitivity of Orbiter Side Fuselage Thermal Mapping Pattern to Leading Edge RCC Channel Venting

CF_4 $\gamma_{eff} = 1.13$ $\alpha = 40$ deg $Re_{\infty, L} = 0.4 \times 10^6$ $\beta = 0$ deg $\frac{p_2}{p_{\infty}} = 12$

Ceramic coated stereo lithography resin model



• Qualitatively, no major leeside differences vented vs. unvented

Figure 5.2.3-21 Initial assessment of venting with panel 9 missing and WLE cavity

Sensitivity of Orbiter Side Fuselage/OMS Pod Heating Patterns to Gas Venting Along Wing Leeside Vent Gap

CF_4 $\gamma_{eff} = 1.13$ $\frac{p_2}{p_{\infty}} = 12$ $Re_{\infty, L} = 0.4 \times 10^6$ $\alpha = 40$ deg $\beta = 0$ deg

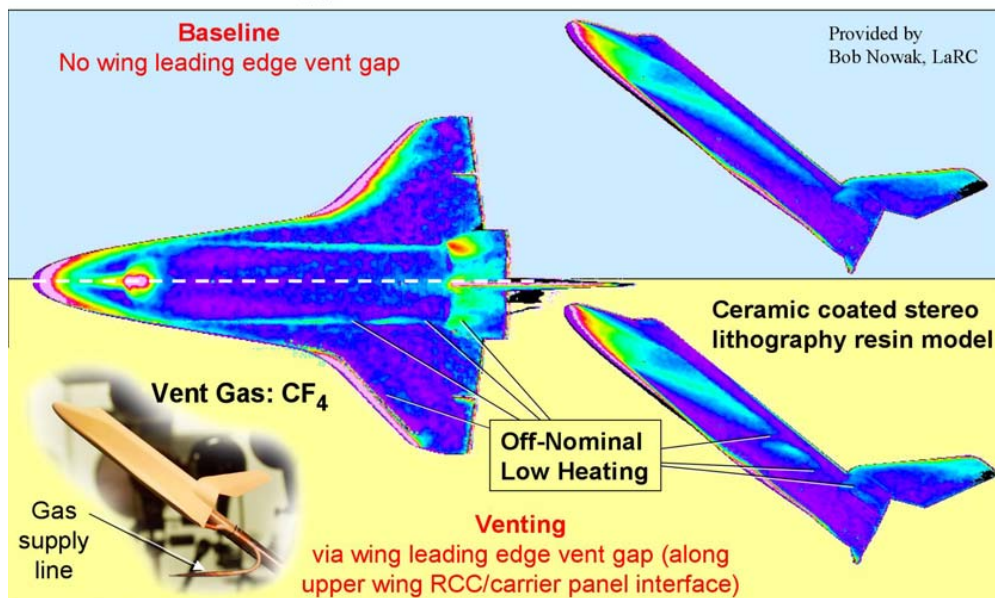
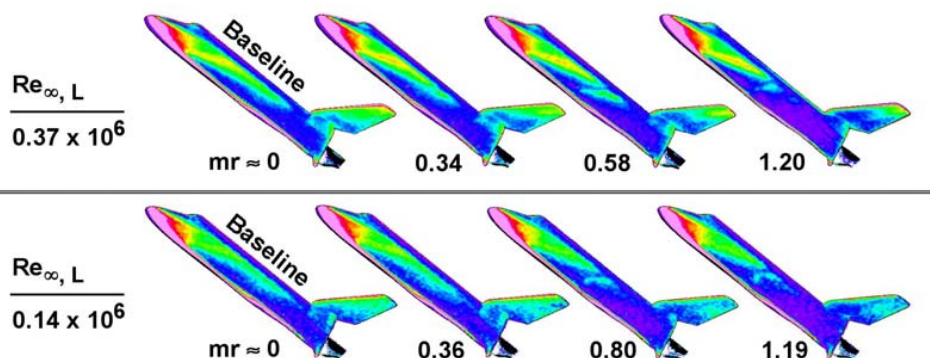


Figure 5.2.3-22 Effect of venting from a WLE cavity with leeside vents; gas supply was from a pitot probe in the flow field

Sensitivity of Orbiter Side Fuselage/OMS Pod Heating Patterns to Gas Venting Along Wing Leaside Vent Gap

$$CF_4 \quad \gamma_{\text{eff}} = 1.13 \quad \frac{\rho_2}{\rho_\infty} = 12 \quad \alpha = 40 \text{ deg} \quad \beta = 0 \text{ deg}$$

Vent Gas: Nitrogen



Wing leeside venting results in off-nominal low side fuselage/OMS pod heating
• No effect of venting for $mr < 0.35$

$$mr = \frac{\rho_{\text{vent}} (V_{\text{vent}})^2}{\rho_\infty (V_\infty)^2}$$

Figure 5.2.3-23 Reynolds Number and Momentum Ratio variation effects on side fuselage heating; gas supply from regulated GN2

Sensitivity of Orbiter Side Fuselage/OMS Pod Heating Patterns to Gas Venting Along Wing Leaside Vent Gap

$$CF_4 \quad \gamma_{\text{eff}} = 1.13 \quad \frac{\rho_2}{\rho_\infty} = 12 \quad Re_{\infty, L} = 0.4 \times 10^6 \quad \alpha = 40 \text{ deg} \quad \beta = 0 \text{ deg}$$

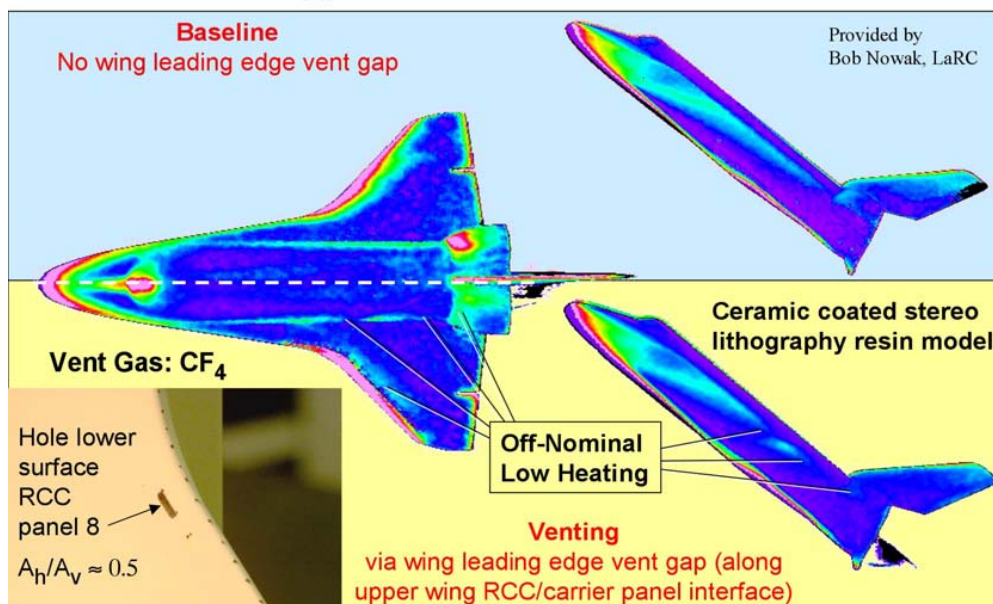


Figure 5.2.3-24 Effect of flow from windward damage through leeside vent on side fuselage heating

Orbiter Leeside Flow Physics

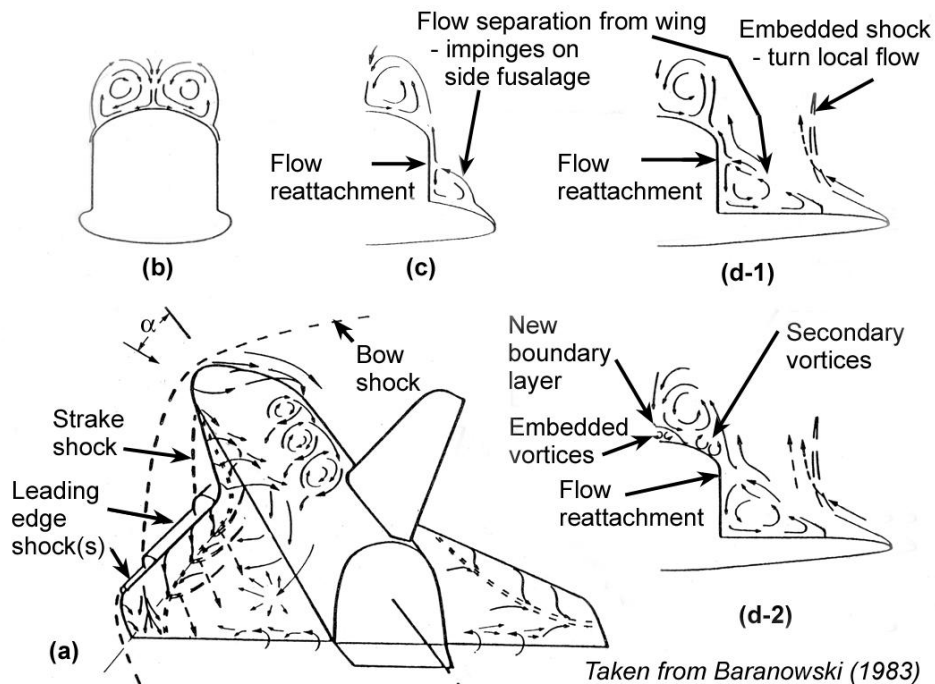


Figure 5.2.3-25 Orbiter Leeside Flow Physics

Effect of Missing RCC Panel on Orbiter Leeside Flowfield as Inferred From Surface Heating And Streamline Patterns

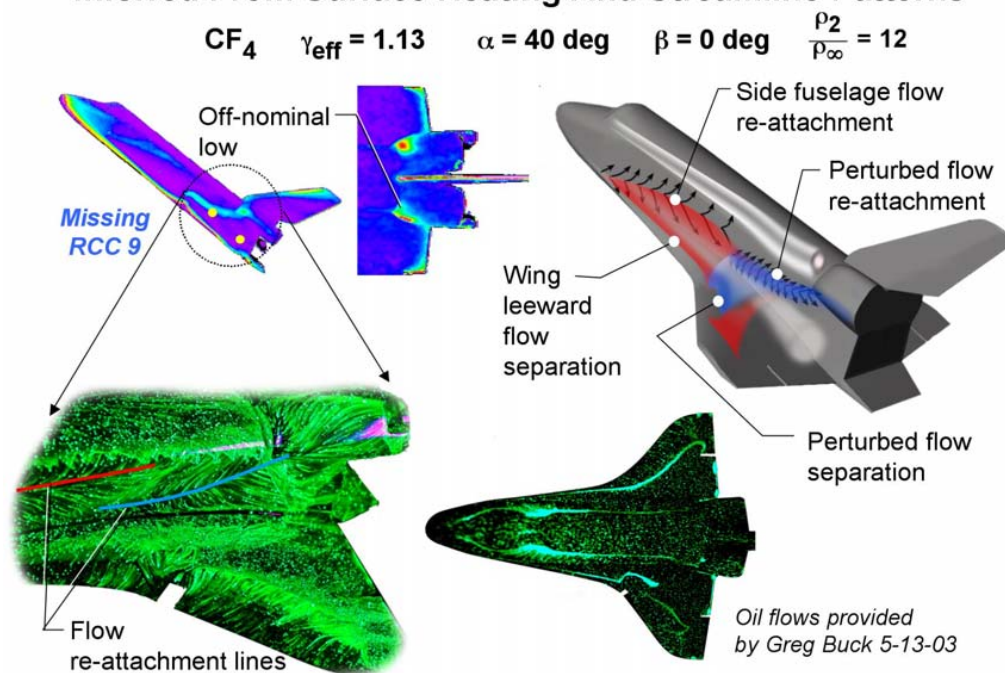


Figure 5.2.3-26 Phosphor Oil Flow showing leeside surface flow separation

Comparison of Orbiter Side Fuselage Heating Patterns Associated With Missing RCC Panels

$M_\infty = 6$ $\alpha = 40$ deg $\beta = 0$ deg

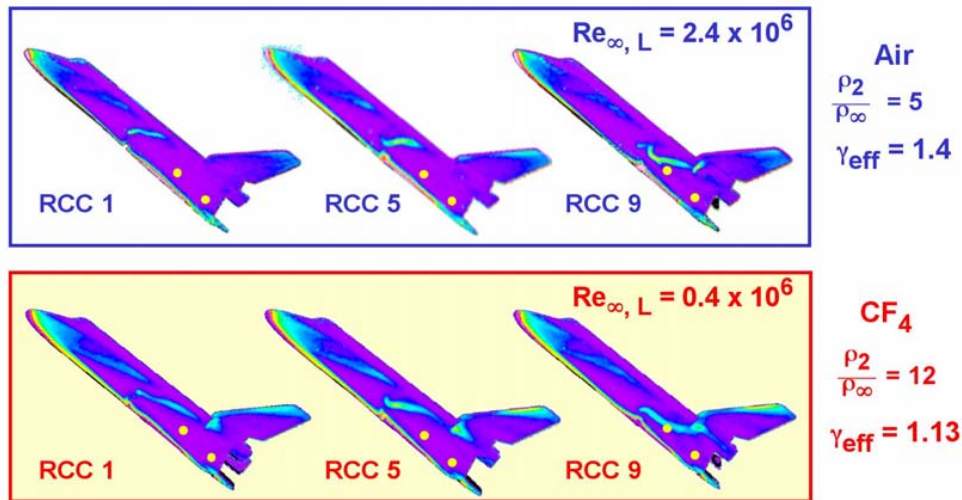


Figure 5.2.3-27 Comparison of Orbiter Side Fuselage Heating Patterns Associated with Missing RCC Panels

5.2.4 Computational Fluid Dynamics (CFD) and Direct Simulation Monte Carlo (DSMC)

5.2.4.1 Introduction for CFD and DSMC

Investigations of the Orbiter's external flow field encompassed several aspects of numerical analyses, from the high altitude rarefied regime to the lower altitude continuum regime. Since no ground-based facility can reproduce the Orbiter environments during hypervelocity re-entry conditions, the use of numerical simulations to understand the flow field at flight conditions was critical during the investigation. The analyses goals were primarily focused on two topics, providing nominal external flow field information supporting localized engineering analyses, and damaged configuration solutions to investigate changes in the aerodynamic and aerothermodynamic characteristics of the Orbiter. Because the magnitude of these analyses is daunting, a parallel effort across several organizations was required. The Navier-Stokes tools employed in the continuum regime analyses included GASP, LAURA, OVERFLOW, SACCARA and USA. The Direct Simulation Monte Carlo (DSMC) tools utilized in the rarefied regime included DAC and ICARUS. More details on each of the tools can be found in the Appendices.

Several concerns affected how the effort was approached, and effective utilization of the array of organizations and tools required the team to follow a staged route in the generation of the External Environments. Concerns with how the effort was approached center around aspects of validation and calibration of the numerical results. Information provided from STS-107 OI data highlighted the idea that significant efforts would be required to assess Orbiter leeside heating environments, yet no extensive leeside calibration effort has ever been performed with Orbiter flight data. In addition, concerns also exist about the validity of numerical simulations for damaged leading edge geometries. In light of these concerns, many leeside environment aspects and the damaged leading edge environment aspects from the numerical solutions must be viewed with an appropriate perspective. The perspective to take is that the solutions relied on established best practices at the time of the investigation. However, they are in essence uncalibrated for the leeside flow field and/or damaged leading edge configurations. Some effort was undertaken to assess the accuracy of the solutions by performing a comparison with STS-2 flight-derived surface temperatures and heat flux. Further information from that study is included in Section 5.2.4.3 (CFD/DSMC Validation). In addition, a study was initiated to characterize our ability to model the hypersonic leeside Orbiter flow field at wind tunnel conditions. Further information from that study is also included in Section 5.2.4.3 (CFD/DSMC Validation). Despite the concerns above about perspective and calibration, it is important to point out that the simulations can still provide much insight into the flow field characteristics and physical mechanisms at work on the Orbiter leeside. Also, an approach of using the results more in an engineering sense than in an absolute quantitative or scientific sense is what will drive interpretations of the CFD and DSMC numerical results to be presented in later sections.

As mentioned above, effectively utilizing the External Environment team's assets (tools, people and computers) to develop relevant CFD solutions required the use of a staged route. The first step in this staged route involved relying on established best practices to generate a suite of initial solutions on the undamaged Orbiter configuration with grid systems that were already available. However, the existing CFD grid systems from the various contributing organizations were markedly different in their intended purpose, resolution and even their Orbiter geometry representation. Thus, while these initial solutions were being generated for STS-107-specific re-entry conditions, an effort was undertaken to standardize the team on a single Orbiter CAD definition and generate a Common Baseline grid system that could be used to generate an extended set of solutions for both nominal and damage scenario configurations. Further information on this common grid generation effort can be found in Section 5.4.2 (Grid Development). Because of the difference in resolution requirements between DSMC and Navier-Stokes solutions, the Common Baseline grid developed for the Navier-Stokes studies was inappropriate for the DSMC analyses. For this reason, the decision was made to use a heritage DSMC Orbiter surface grid that has been shown to agree well with Orbiter aerodynamic flight data in previous studies. Later, as our understanding of the available flight data grew and was affected by a rapid and dynamic environment of investigation, the External Environments team simulations took on three distinct aspects. These aspects are nominal solution environments, to be covered in Section 5.2.4.4, providing damaged leading edge simulations, covered in Section 5.2.4.5, and providing simulations on other damage configurations that supported the effort to focus down to the Working Scenario. Those additional efforts will not be covered in any detail in this report, however.

5.2.4.2 Grid Development

Many aspects of numerical analyses are driven as much by process requirements as the particular physical modeling assumptions. In the simulation of hypersonic or hypervelocity flow fields, local changes in surface definition or grid density can affect the flow field results. These localized changes can be difficult to attribute specifically to either the surface definition or differences in results obtained by different tools and/or users. In order to move beyond discrepancies generated by differences in surface definition or grid resolution among the various numerical tools, an effort was undertaken to standardize the Aerodynamics and Aerothermodynamics teams on a common surface definition. In addition, the External Environments team standardized their Navier-Stokes simulations on a Common Baseline grid system. However, the DSMC simulations did not utilize the Common Baseline grid system. The Common Baseline grid developed for the External Environments Navier-Stokes studies was inappropriate for the DSMC analysis because of the resolution of the surface geometry. Over-discretization of the surface reduces the sampling count used to convert the microscopic events simulated by DSMC into macroscopic properties, thus increasing the statistical noise. Therefore, for the DSMC calculations, the decision was made to use a heritage DSMC Orbiter surface grid that has been shown to agree well with actual Orbiter flight data in previous studies. Efforts to standardize the Aerodynamics and Aerothermodynamics teams on a specific CAD definition are described in this section. In addition, details on the CAD definition developed as a standard for the Aerodynamics and Aerothermodynamics teams are provided. Also included is an overview of the Common Baseline grid system utilized by the External Environments team.

A majority of the viscous flow simulations performed for the Space Shuttle Orbiter Columbia accident investigation utilized structured volume grids. Structured grids are comprised of a logical or computational domain, characterized by three mutually orthogonal curvilinear coordinate directions. The orthogonal coordinates, in combination with a mapping that dictates how the points are placed on the surface of the vehicle, describe a vehicle to be analyzed. The mapping is referred to as a topology. It links the physical domain where the vehicle is typically described with Cartesian coordinates such as (x,y,z), to the computational domain where the coordinates are typically (i,j,k) and form a cube. In a structured grid, the most important issues to be addressed are the integrity of the outer mold lines that define the surface of the vehicle, the topology, and the quality of the grid with respect to the viscous flow solver to be used. Each of these issues will be discussed within the context of presenting our overall grid generation approach.

Initial computations performed by NASA (ARC, LaRC, and JSC), Boeing, and SNL made use of existing surface and volume grids for viscous flow simulations. The geometry description in use by most organizations prior to the STS-107 investigation was a version of the Shuttle Orbiter developed by Mississippi State University, under contract to NASA-JSC in 1997. This geometry, referred to as the '97 definition, had several problematic regions on the vehicle, including an abnormally thick leading edge in the region of wing crank, and improperly modeled geometry at the wing tip/aileron junction. At the time of the accident, however, Navier-Stokes grids from the various organizations based on the '97 definition were the most accurate available. Thus, these initial meshes were used to commence computational fluid dynamic (CFD) simulations.

Despite inaccuracies in the '97 definition, NASA –LaRC developed a damaged RCC panel 6 geometry on that database. The volume grid was a modified version of an existing single-block volume grid, originally consisting of more than 9 million points. The damaged panel 6 geometry was estimated from existing Space Shuttle Orbiter Experimentation (OEX) documents. The surface and volumes of the previously existing grid system were modified to accommodate a damaged panel utilizing the “embedded” O-grid technique, and a new volume grid of 18 blocks and more than 18 million points was developed. This definition of panel 6 damage, referred to as the panel 6 “notch” grid, was used in many different computations performed at LaRC, Boeing, SNL, and JSC. It was so-named because the length of the missing RCC panel 6 was one half of the actual panel; hence it was a mere notch in the wing leading edge. Owing to its early availability, the panel 6 “notch” definition was used for many of the initial damaged RCC computations. In addition, the generation of a volume grid on this early geometry definition provided extremely valuable insights towards developing structured volume grids for all subsequent leading edge damage scenarios.

In parallel with the CFD calculations that began on the pre-existing meshes, a new effort was initiated by the External Environments team to develop a common baseline grid. Following several discussions with representatives from all groups, an embedded O-grid topology was chosen. The embedded O-grid topology provides flexibility, enabling accurate computation of various damage scenarios with significantly reduced volume grid regeneration. As shown in Figure 5.2.4-1, there are three possible structured grid topologies. Each topology is so-named because of its structure; the O-grid looks like an O, and similarly for the C- and H-grids.

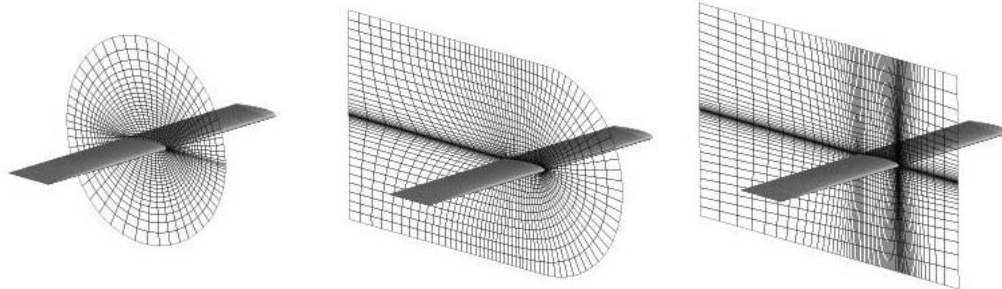
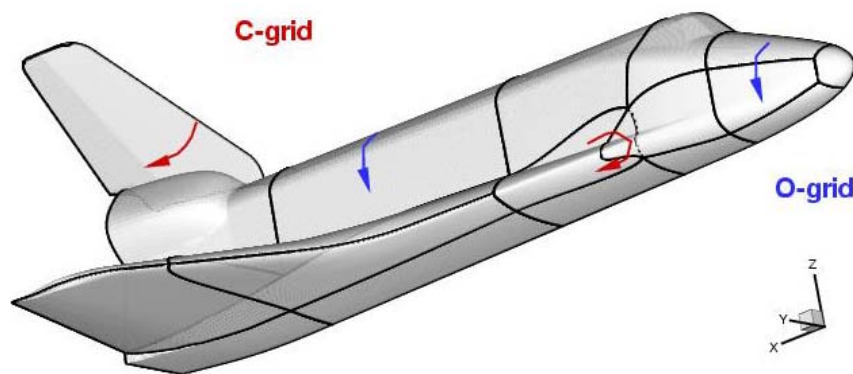


Figure 5.2.4-1 O-, C-, and H-grid topologies

For the common baseline grid, an O-grid wrapping around the entire vehicle from the top to the bottom was used as a starting point. The wings were then isolated topologically with C-grids so that grid resolution along the span of the wings would be completely independent of the main O-grid that wraps around the vehicle, as shown in Figure 5.2.4-3. This topology was chosen specifically because it permits blocks on the wing within the



**Figure 5.2.4-2
Figure 5.2.4-3 Common grid baseline topology**

C-grid to be removed and replaced with an “embedded” O-grid, thus focusing grid points to a damaged leading edge area by altering the spacing and clustering.

Common baseline grid development began with the creation of a smooth outer mold line (OML) version that could be used to benchmark all the flow solvers from the various organizations. As noted previously, initial computations used the '97 OML definition for the grid systems. The '97 geometry definition had several accuracy issues, mentioned above, that needed to be addressed. These issues led to the development of a new, more accurate geometry description from computer-aided design (CAD) data provided by NASA -JSC to NASA-LaRC and ARC. The geometric description provided by NASA-JSC was not a complete geometry, as it had several regions where surfaces describing the wing and fuselage were not sealed. This produced holes where a grid could not be generated. Thus, the CAD representation was slightly modified to ensure that a solid model could be mathematically described with the data provided by NASA-JSC. To ensure a good solid model, the CAD representation was modified by filling in the “holes” and smoothing over gaps between the control surfaces and the respective hinge lines. In addition, the control surfaces were positioned based on initial STS-107 flight data. The resulting

surface definition became the '03-definition of the Space Shuttle Orbiter and it was utilized for the common baseline grid generation.

The process used in the common baseline grid generation, as well as many of the subsequent surface and volume grids used for viscous flow simulations is shown in Figure 5.2.4-4.

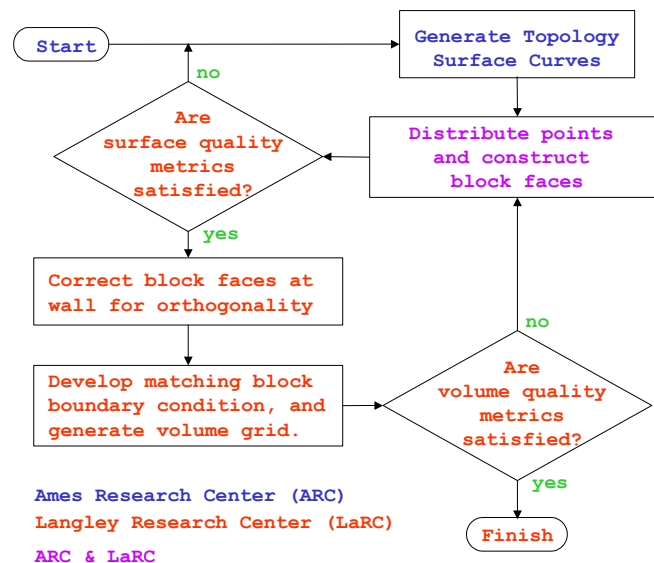


Figure 5.2.4-4 Grid generation process with ARC and LaRC

The first step in generating the common baseline grid system was the development of the basic grid topology. After the topology was developed, the next step involved the detailed generation of the surface meshes over the entire OML of the Orbiter. Next, initial block faces for all of the non-surface faces that defined the volume grid boundaries were created to produce a complete first sketch of the entire mesh. After these initial surfaces were constructed, the surface grids and initial block faces were evaluated for overall grid quality. Modifications were then made to ensure orthogonality of the grid lines emanating from the wall and to ensure that the grid metrics could be satisfied for grid stretching. Once an acceptable quality was reached for the OML surface and block interfaces, an initial volume grid was generated. Newly developed technologies were developed by LaRC to ensure slope continuity across matching block boundaries, producing superior grids that could meet grid quality metrics requirements established by the team. These requirements will be discussed in more detail later in this sub-section.

The primary grid generation software used at NASA-ARC was the GridGen software from Pointwise Inc., while NASA-LaRC utilized a combination of GridGen, the Volume Grid Manipulator (VGM), and the Three-Dimensional Grids about Anything using Poisson's Equations with upgrades from Ames and Langley (3DGRAPE/AL) for grid generation. NASA-LaRC also used the CFD Analyzer software from AMTEC Engineering Inc. for grid quality evaluations. The GridGen software was used to develop the initial surface grids by constructing grid lines on the baseline IGES-format database. GridGen was also used to construct the volume grids. However, due to limitations in GridGen, the interfaces of all blocks with edges coinciding with the OML were modified with VGM. This was done to ensure that the block interfaces were locally orthogonal to the vehicle OML. After block interface modification, the VGM software was used to develop a C-II continuous boundary condition across matching block volume grids. The volume grids were then elliptically smoothed in GridGen. In some rare instances where GridGen was unable to produce a volume grid with all positive cell volumes, the 3DGRAPE/AL software was used to generate the volume grid. After GridGen smoothing, all volume grids were modified and improved with VGM to reduce grid stretching. Finally, individual organizations re-positioned the outer boundary location of the baseline common grid to closely match the bow shock location for a given flight condition. The

repositioning of the outer boundary also allowed re-stretching in the normal direction to optimize the grid distribution in the shock layer.

The development of all surface and volume grids for the damage scenarios investigated by the External Environments team used the baseline common grid as a starting point. Several complete volume grids were generated to model various damage conditions of the Shuttle Orbiter, including Missing Main Landing Gear door tiles (MLG), a forward dump valve investigation, and Missing Reinforced Carbon-Carbon (RCC) panel 6 and Missing RCC panel 9 configurations. In addition, the Aerodynamics team used this grid system for portions of their Navier-Stokes analyses. In a general sense, therefore, each grid was generated with the same process identified in Figure 5.2.4-4. Also, as the damage scenarios varied, only the wing region was modified to accommodate a given damage scenario. This is illustrated in Figure 5.2.4-5, where the wing blocks and the attached fuselage blocks (shaded yellow) are modified to accommodate a damage scenario. This figure also shows the “embedded” O-grid, which encompasses the damage site. Using this topology, the center square on the wing leading edge representing a missing RCC panel was resolved with many more grid points than in the nominal geometry grid. However, this additional grid density did not affect any other portion of the vehicle. This approach made generation of new damage scenario volume grids easier and more efficient because only the wing leading edge region blocks needed to be re-constructed. All subsequent damage scenarios were generated with this type of topology, enabling the development of several different volume grids for the Shuttle Orbiter within a two-month period. It is estimated that this procedure saved 50% of the grid generation time compared with rebuilding a new volume grid each time a different damage scenario was considered.

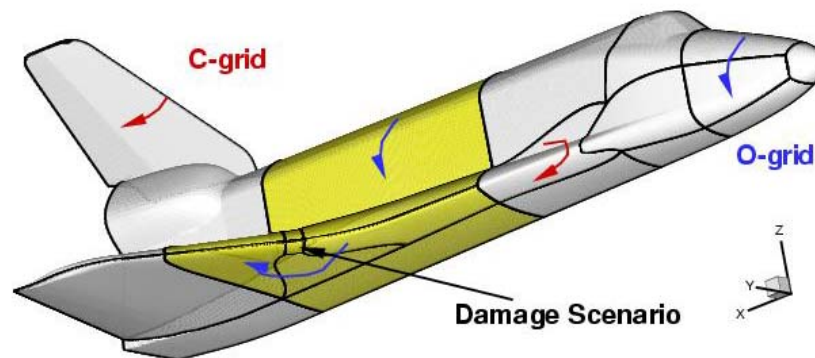


Figure 5.2.4-5 Damage scenario topology

Grid quality metrics used to assess the common baseline grid were defined based on extensive experience at NASA-LaRC in grid generation. The grid metrics used to determine the quality of the grid with respect to CFD include cell-to-cell stretching, interior and near-wall orthogonality, and cell volume. Based on previous work in structured grid generation, grid stretching should be less than a factor of 1.5 from one point to the next. Grid line orthogonality at the wall should be within 10 degrees of orthogonal, and cell volumes should be positive. These metrics are used to assess the grid quality by evaluating the maximum stretching, and minimum orthogonality, as well as the root mean square (RMS) and three-sigma values of the metrics, assuming a normal distribution. Based on anecdotal evidence obtained with the grids used for this effort, failure to adhere to reasonable limits for these metrics can result in inaccurate flow simulations. This evidence also suggests that grids with large values for these metrics will suffer from slower convergence of flow field residuals. Tabulated in Table 5.2.4-1 are the grid metrics for the common baseline grid, generated with the previously identified software and process. Note that the ξ -direction is streamwise from nose to tail, the η -direction is from top of the vehicle to the bottom, and the ζ -direction is from the wall to the outer bow-shock within the flow field. These directions represent the three mutually orthogonal computational coordinates that are used in the mapping of the grid to the geometry, using the topologies described. The common baseline grid contains nearly 3.5 million points and 20 blocks, and was suitable for computations by all viscous-flow CFD software used by the team.

Table 5.2.4-1 Baseline common grid quality metrics

	Minimum	Average $\pm 3\sigma$	Maximum
I-Stretching (ξ)	1.000	1.048 \pm 0.132	2.775
J-Stretching (η)	1.000	1.015 \pm 0.132	2.775
K-Stretching (ζ)	1.000	1.013 \pm 0.075	1.763
J-K Orthogonality (ξ)	0.018	0.671 \pm 0.708	1.000
I-K Orthogonality (η)	0.042	0.729 \pm 0.621	1.000
I-J Orthogonality (ζ)	0.023	0.836 \pm 0.528	1.000

Additional Comments on Damage Scenario Meshes

Using the embedded-O mesh topology, the exterior grid resolution is focused toward the damage location. As previously noted, separate external meshes were created for the RCC panel 6 and panel 9 cases. The missing panel meshes allow the flexibility to assess a wide range of damage at a specific panel location. The inner perimeter of the focused embedded-O follows the OML at the RCC panel of interest. The External Environments team utilized two different topologies to investigate the damaged RCC panel parametrics. One group utilized a simple H-mesh interior for the missing RCC cavity. This topology required that Navier-Stokes spacing was achieved, tangential to the OML surface in the radial direction, as the external embedded-O mesh approached the perimeter of the damage location. The cavity itself is modeled with a simple H-topology that has Navier-Stokes spacing against each block face. The internal topology is broken out into a series of H blocks to permit various or progressive damage scenarios to be considered. For example the interior of an RCC panel removed cavity had separate H-grids for the carrier panels the RCC panel and the RCC channel interior. Each internal block maintained Navier-Stokes spacing against each of its six faces such that once the mesh was constructed any combination of upper/lower carrier panel and/or RCC panel could be computed without any re-gridding or re-stretching.

The second mesh topology used for damage scenarios employed a double-O mesh topology interior for the missing RCC cavity. While this topology required the creation of seven internal cavity blocks to ensure that Navier-Stokes clustering was obtained against all interior faces of the cavity, it did not require the Navier-Stokes clustering of the exterior grid except in the traditional normal direction. The inside of the cavity for the second option is constructed with a central H-mesh that is enclosed on six sides by unique blocks. Each of the surrounding six blocks has Navier-Stokes spacing against a single outward facing block face. This topology completely isolates the Navier-Stokes spacing, used against each of the interior walls, from propagating outside of the cavity region. However, the topology also requires interior cavity meshes (not the external mesh) to be constructed independently for the upper and lower panel out cases. Figure 5.2.4-6 shows a cut through the double-O interior mesh topology for the full panel 6 removed case. Similar interior mesh configurations were constructed for the full panel 9 out geometry and the two half panel out geometries.

For each damage grid option, the exterior mesh is built in two halves corresponding to upper and lower halves of the Orbiter, and is split at the wing leading edge water line. This split construction permits a missing upper half panel, a missing lower half panel, or a complete panel missing to be simulated from a single grid system. Furthermore, for each option the exterior meshes were clustered against all OML surfaces with Navier-Stokes spacing to meet a cell Reynolds number of approximately 1. Even the H-block that extends from the OML surface of the damage location to the outer boundary (present for both damage scenario topologies) has the same Navier-Stokes spacing. This exterior mesh construction, for either option, allows the various damage configurations such as smooth OML, half panel out and full panel out to be computed with changes only to the interior cavity mesh boundary conditions.

Both options allowed the region of the damaged RCC panel that vents into the leading edge channel to be modeled with an outflow boundary condition. The first option, with a simple H mesh interior to the cavity, was chosen for the LAURA simulations. It allowed the flexibility to easily re-distribute the grid to

satisfy a surface grid spacing criterion. However, this capability also resulted in a larger grid system due to the competing requirements of Navier-Stokes spacing in the radial/tangential direction along the perimeter of the damage location and the less than 1.5 point-to-point stretching ratio. The only way to meet both demands was to increase the number of points within the external common grid topology. The second option allowed the flexibility to model various damage scenarios using a single external grid system that could have considerably fewer points since there were no demands on Navier-Stokes spacing in the tangential/radial direction, but this flexibility was obtained at the expense of a topologically more complex internal cavity grid system and the need to have independent internal cavity meshes for either half- or full panel out scenarios. The two topologies are depicted in Figure 5.2.4-6 and Figure 5.2.4-7. Both topologies were utilized for the damaged RCC panel parametrics considered, and the various simulations performed with GASP and LAURA will be described in more detail in the damage scenario description of the CFD results.

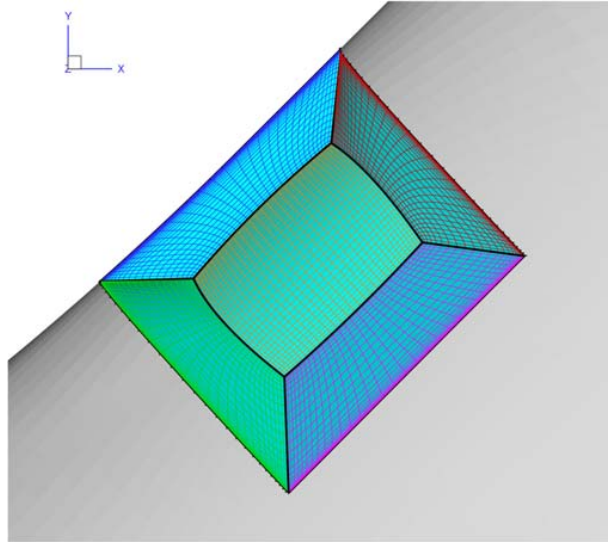


Figure 5.2.4-6 Cut through full panel out interior cavity mesh for GASP simulations

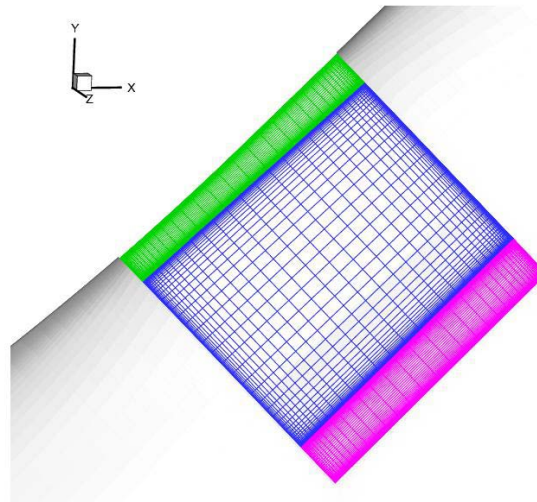


Figure 5.2.4-7 Cut through full panel out cavity mesh for LAURA Panel 9 simulation

5.2.4.3 CFD/DSMC Verification for the Orbiter Configuration

In order to determine laminar and turbulent heating rates and surface temperature uncertainty bands for the primary Navier-Stokes solvers used in the investigation, researchers from Boeing Huntington Beach, NASA-ARC, and NASA-LaRC computed Navier-Stokes CFD solutions to compare against STS-2 flight data at three trajectory points, two laminar and one turbulent. Results from this study are provided in the following section. The CFD codes USA, LAURA, and GASP were used for the simulations by the Boeing-Huntington Beach, NASA-LaRC, and NASA-ARC groups, respectively, and are described in Section 5.6. Since this work was done prior to the completion of the common CFD grid, the grids available to each group at the time of STS-107 were used. They did not include body flap or elevon deflections and had been constructed primarily to capture windward side heating.

In order to make a comparison with flight data, three STS-2 trajectory points were simulated using the free-stream conditions shown in Table 5.2.4-2. The Mach 24 point was selected to approximate the conditions at the start of the peak heating region on the STS-107 trajectory. The Mach 18 point was selected to approximate the point on the STS-107 trajectory for which good GPS data were available. The Mach 7 point was selected to provide a turbulent comparison case.

Table 5.2.4-2 Freestream conditions for STS-2 computations

<u>Case</u>	<u>M</u>	<u>V</u>	<u>ρ</u>	<u>T</u>	<u>alt.</u>	<u>Re/L</u>
		<u>(m/s)</u>	<u>(kg/m³)</u>	<u>(K)</u>	<u>(km)</u>	<u>(1/m)</u>
t = 75260 s	24.3	6920.0	5.7500E-05	202.00	72.400	28439
t = 75950 s	18.1	5617.0	1.6260E-04	240.60	64.400	56430
t = 76310 s	7.7	2486.0	1.9130E-03	256.90	45.070	278700

<u>Case</u>	<u>M</u>	<u>V</u>	<u>ρ</u>	<u>T</u>	<u>alt.</u>	<u>Re/L</u>
		<u>(ft/s)</u>	<u>(slug/ft³)</u>	<u>(R)</u>	<u>(ft)</u>	<u>(1/ft)</u>
t = 75260 s	24.3	22714.0	1.1152E-07	363.29	237670	8822
t = 75950 s	18.1	18430.0	3.1558E-07	433.07	211440	17958
t = 76310 s	7.7	8156.0	3.7094E-06	462.56	147870	88576

Comparisons between the computed and flight derived surface heat transfer rate data provide an additional measure of confidence in the numerical simulations at flight conditions. The results of these comparisons using the experimental data derived by Throckmorton and Hartung are discussed in the following paragraphs. Additionally, code-to-code comparisons are presented for predicted surface pressures. All calculations were made with a 5 species nonequilibrium chemistry model assuming thermal equilibrium. A radiative equilibrium wall boundary condition with the emissivity set to 0.90 was used. The RCG catalysis model from Stewart was used for the entire vehicle for each of the solvers. In the case of the Mach 7 condition, NASA-LaRC used the Cebecchi-Smith turbulence model, while NASA-ARC used the Baldwin-Lomax turbulence model.

Mach 24 Results

Figure 5.2.4-8 shows STS-2 flight data for surface heat flux plotted over the computed results for the windward side of the orbiter. The two tiles covered with a catalytic coating are indicated in the figure. The GASP and LAURA results are in general agreement, and the comparison with the data is good. The solutions are not expected to match the data in the body flap region since neither Ames nor Langley modeled the actual body flap deflection in their solutions.

Figure 5.2.4-9 gives a more quantitative comparison of the results along the windward centerline. The comparison between both predictions and the flight data is excellent for the non-catalytic locations

upstream of the body flap. A fully-catalytic GASP solution is also shown in Figure 5.2.4-9. The prediction matches the data at the downstream catalytic tile, but under-predicts the heating at the upstream catalytic tile. This under-prediction is not surprising since the computation is not modeling the physical situation of a catalytic tile surrounded by non-catalytic tiles. The heating on the isolated catalytic tile downstream of non-catalytic tiles should be higher than the heating at the same location downstream of catalytic tiles. The higher heating can be attributed to higher atomic species mass fractions in the boundary layer. The atomic species exist in higher quantities for the non-catalytic upstream tiles case because a lower-catalytic surface suppresses recombination of the atomic constituents. Thus, for an isolated catalytic tile in the vicinity of non-catalytic tiles, more atomic species exist in the approaching boundary layer, providing more potential for catalytic heat transfer.

The heating rate uncertainty, defined as the difference of the computed and flight derived heating rates divided by the flight derived heating rate, is shown in Figure 5.2.4-10 at every measurement location. The same data are also presented in Figure 5.2.4-11 as a function of axial co-ordinate down the Orbiter.

Figure 5.2.4-12 shows the computed heat transfer rates from GASP and LAURA on a slice through the Orbiter at a location of $X = 1215$ in Orbiter coordinates, which passes just downstream of the main landing gear (MLG) door. The agreement between the two codes on the wind side and around the wing leading edge is quite good. On the leeward side, the results differ by as much as 100%, although this is not surprising since neither grid was optimized to capture leeward heating. In fact, the grid used for the GASP calculations is particularly coarse. The Z-location of RTD V34T1106 is indicated in the figure.

The heating results for a slice at $Y = 167$ in are shown in Figure 5.2.4-13. This slice is along the outboard edge of the MLG. On the wind side, the predictions of the two codes are within 10% of each other, and the heating rates on the WLE are within 2%. Figure 5.2.4-14 shows the predicted heating rates along the WLE. The codes are in good agreement except in the downstream region where the LAURA heating rates are about 30% higher than the GASP heating rates. Given the difference in grid resolution between the two solutions, a difference of 30% is not unreasonable. In addition, the shock-shock interaction region is a particularly difficult feature to resolve numerically. Because of this and the fact that a comprehensive calibration study using Orbiter wing leading edge heating flight data has not been performed, questions remain about what is required to obtain an accurate flight prediction.

The comparison of windward centerline pressure predicted by GASP and LAURA is shown in Figure 5.2.4-15. The two codes give similar answers, except for the wiggles in the GASP solution between $0.3 < X/L < 0.5$. These wiggles are caused by waves in the surface geometry used to create the GASP grid. Later comparisons for STS-107 cases computed on the common grid showed good agreement between the GASP and LAURA results.

Mach 18 Results

The results for Mach 18 are similar to the results for Mach 24. Figure 5.2.4-16 shows the computed and flight derived surface heat transfer rates on the windward side of the Orbiter. Figure 5.2.4-17 shows a comparison between the CFD predictions and the flight data on the windward centerline. Figure 5.2.4-18 and Figure 5.2.4-19 show the uncertainties in the computed data. The off-centerline results show the same trends as in the Mach 24 case. GASP and LAURA agree within about 10% of each other on the wind side, but differ on the lee side due to the differences in the grids.

Mach 7 Results

Figure 5.2.4-20 shows the computed and measured heat transfer rates for the Mach 7 turbulent trajectory point. In GASP the Baldwin-Lomax model was turned on at $X/L = 0.4$. In LAURA, the Cebecchi-Smith turbulence model was turned on at $X/L = 0.3$. The flight data indicates transition in the region $0.3 < X/L < 0.5$. The GASP computation predicts higher heating than the LAURA computation. The higher heating in GASP can be seen clearly in Figure 5.2.4-21 where results on the windward centerline are presented. Figure 5.2.4-22 and Figure 5.2.4-23 show the uncertainties in the computed data.

Summary of STS-2 Surface Heating Comparisons

The agreement among the CFD codes utilized in this comparison to STS-2 flight derived heat flux data is generally very good considering that different codes and different meshes were used. There are some windward oscillations in the GASP solutions due to waviness in the surface grid. In addition, differences between the results from LAURA and GASP are apparent on the lee side. However, as mentioned previously, the grids were not tailored to capture leeside heating, and it is likely that lack of grid resolution is the reason for the differences among the codes. Only a comprehensive calibration study of leeside flow heating environments on the Orbiter can establish whether differences in leeside heating between the two solvers are due to grid resolution.

Table 5.2.4-3 shows the standard deviation of the computed heat transfer rates from the flight data for the windward surface gauges upstream of the body flap and elevons, forward of $X = 1433.2$ in. The laminar results are within about 15% of the data, while the turbulent results are within 30% of the data. The poorer than expected comparison with the turbulent results could be due to the fact that the radiative equilibrium assumption at the wall may not be valid. The flight data do show differences of up to 20% between the inferred radiative equilibrium heat fluxes and convective heat fluxes, suggesting that the surface is not in radiative equilibrium.

Table 5.2.4-3 Standard deviation of heating results

	LAURA	GASP	USA
M=24 Laminar	12.50%	12.60%	N/A
M=18 Laminar	11.20%	15.30%	N/A
M=7 Turbulent	27.70%	27.20%	N/A

Comparisons of Computed and Measured Surface Streamlines at Wind Tunnel Conditions

The simulation of leeside flows with computational fluid dynamics is a challenging endeavor, and the inclusion of leading edge damage parametrics into the activity makes the effort even more difficult. Most activities for the simulation of hypersonic flow fields have focused on the windward regions where surface heating drives the selection of thermal protection systems. In the case of the Space Shuttle Orbiter, no comprehensive leeside flow field calibration study has ever been performed. Because of this lack of historical base, the leeside results included in this report need to be looked at from an engineering perspective, as mentioned in Section 5.2.4.1. In order to provide some information on the quality of the leeside flow field results from the CFD simulations, LAURA computations were performed to simulate a wind tunnel experiment in the LaRC Mach 6 CF_4 wind tunnel. The computation was performed using the thin layer formulation of the Navier-Stokes equations assuming laminar flow and vibrational equilibrium. The grid used for these computations had 2 million cells, most of which were devoted to the vehicle windward side, and was derived from the '97 geometry definitions. The grid covered the leeward side and windward side of the vehicle but did not extend into the wake. The model scale for the computations was 0.75%. The angle of attack was 40 degrees and the sideslip angle was 0 degrees. A constant wall temperature boundary condition of 300 K was assumed, and the Mach 6 CF_4 CFD computation was run with the following free-stream conditions:

Mach = 5.902
Velocity = 889.84 m/s
Density = 1.9417×10^{-2} kg/m³
Temperature = 198.38 K
Reynolds Number = 0.44 million/ft

The CF_4 wind tunnel experiment, run at 40 degrees angle of attack, had the following free-stream conditions:

Mach = 5.94
Velocity = 880 m/s
Density = 1.97×10^{-2} kg/m³
Temperature = 190 K
Reynolds Number = 0.47 million/ft

The two sets of conditions are very similar, but are not an exact match because the CFD conditions were chosen before the wind tunnel experiment was performed. However, these free stream conditions are considered similar enough to provide a valid comparison. Computed and measured streamlines on the lee side of the vehicle are shown in Figure 5.2.4-24. The experimental streamlines, shown in the top of the figure, were obtained from post-run images using an oil flow technique. The lower images are computed surface streamlines from the LAURA simulation at the wind tunnel conditions listed above. While differences, possibly due to grid resolution, are observed in the computed and measured locations of the strake vortex separation line on the aft portion of the wing leeside, the code predicted the separation and reattachment line locations of the strake and canopy vortices. In general, good agreement was observed in this first comparison of leeside surface streamlines between the viscous solver LAURA and CF₄ wind tunnel measurements. The level of agreement in the streamline patterns between the experimental and numerical results demonstrates the confidence level that can be expected for the leeside flow simulation. Certain aspects of the flow field show quite reasonable agreement, e.g., the separation and reattachment locations on the fuselage and inboard wing regions, while others show less agreement, e.g., the outboard region of the wing leeside. The LAURA simulation was obtained using best practices available at the time of the accident, which do not include an a priori knowledge of what is necessary and sufficient to model the lee side of the Orbiter flow field. This statement is true for both wind tunnel and flight conditions. These results reinforce the statement made in Section 5.2.4.1 and reiterated here. Critical insight can be gained into the flow field characteristics and physical mechanisms at work on the Orbiter leeside. But, an approach towards interpreting the results more in an engineering sense than a scientific sense must be used for any of the leeside numerical results in this report because an established practice for obtaining accurate Orbiter leeside simulations is not known at this time.

Comments on DSMC Verification

A comparison of DSMC heating results with STS-2 flight data was also considered. After reviewing the available STS-2 data from Throckmorton and Hartung, it was decided that a comparison could not be made with the DSMC methodology. This was because the surface thermocouple data available showed little or no temperature response at the higher altitudes where it is reasonable to employ the DSMC method. Therefore, it was determined that an aerodynamic comparison previously made between STS-62 flight data and DSMC results would serve as verification that the surface geometry selected was acceptable to use for the DSMC analysis work done to support this investigation. More information on that study can be found in Boyles (2003). The Orbiter surface geometry used in the study by Boyles was also used for the 350,000 ft altitude DSMC solution performed for the STS-107 investigation, and the 300,000 ft altitude DSMC solution utilized a slightly finer resolution Orbiter definition. In addition to the conclusion to rely on the aerodynamic study as sufficient calibration for the STS-107 investigation, the judgment was made to accept the heating results obtained using the best practices available at the time of the accident. Therefore, to date, no comprehensive comparison has been made of DSMC heating results for the Orbiter at rarefied re-entry conditions.

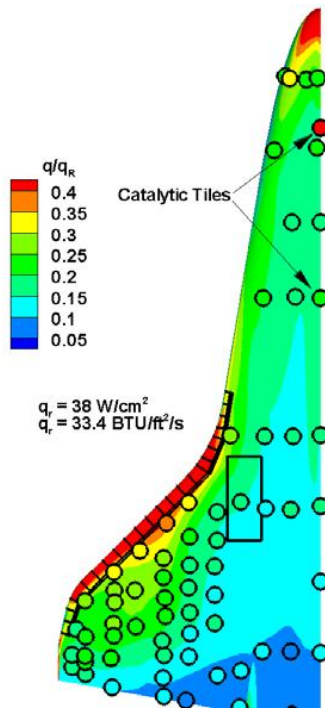
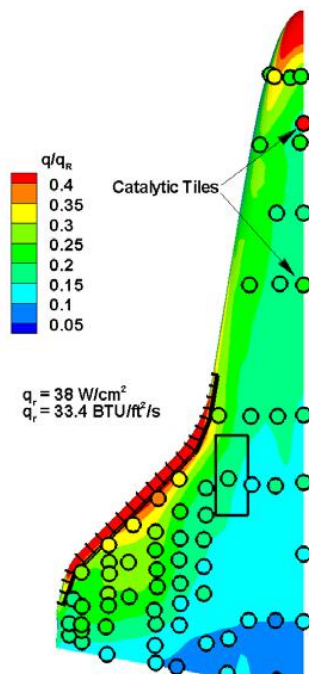


Figure 5.2.4-8 Windward surface temperature predictions from GASP and LAURA compared with flight data at Mach 24. Experimental data are plotted inside the circular symbols. The symbol size is made larger than the measurement extent to aid visualization of the data.

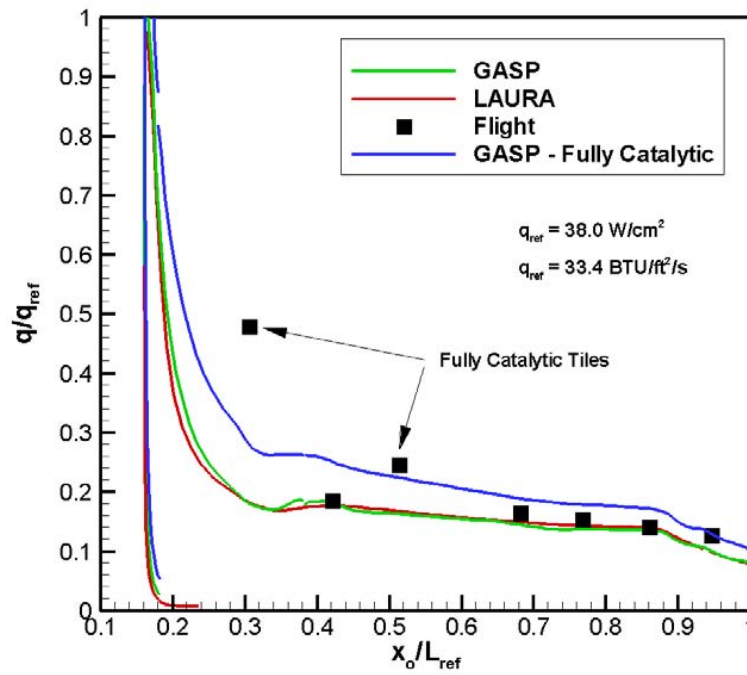


Figure 5.2.4-9 Windward centerline heat transfer rate for Mach 24. $L_{ref} = 37.24 \text{ m} = 1466 \text{ in}$

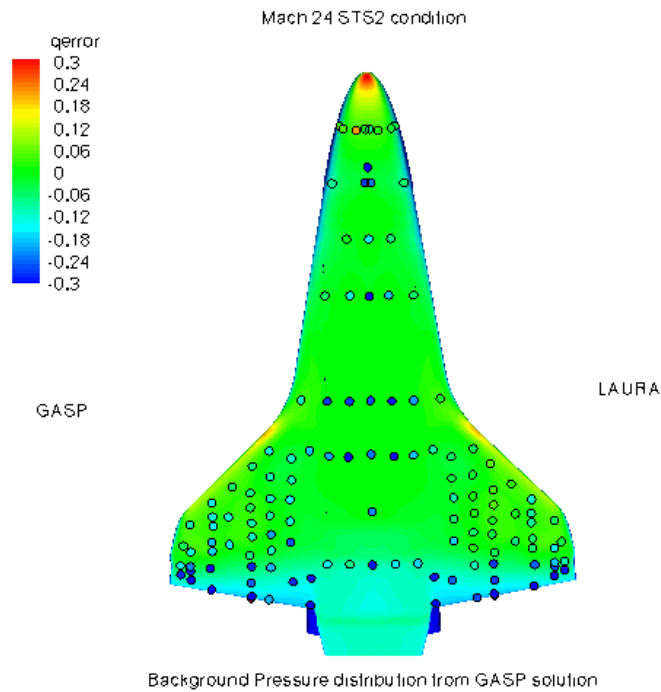


Figure 5.2.4-10 Windward heating rate uncertainty at Mach 24 plotted over pressure contours
 $q_{error} = (q_{cfd} - q_{flight})/q_{flight}$

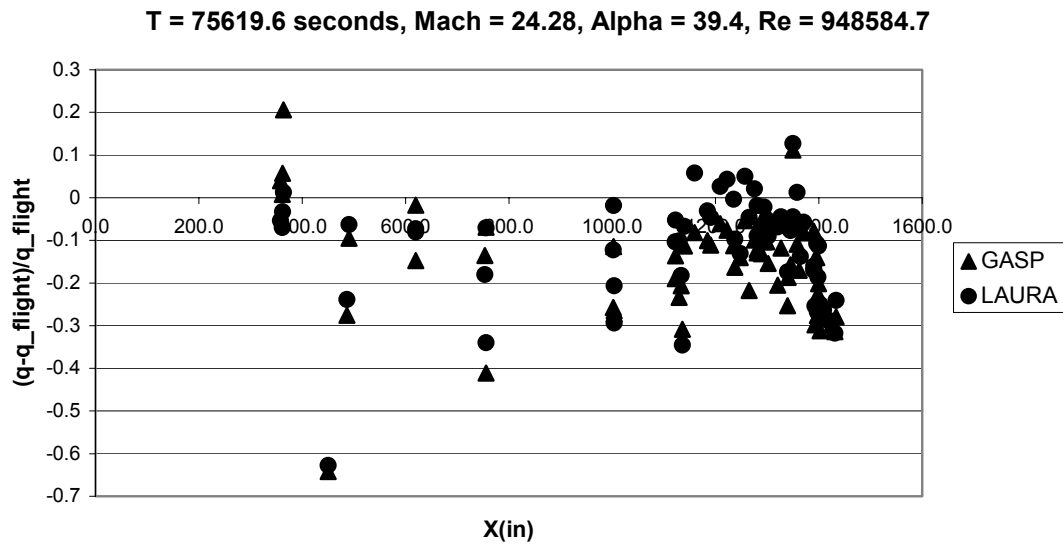


Figure 5.2.4-11 Heating rate uncertainty at Mach 24 as a function axial distance along the orbiter

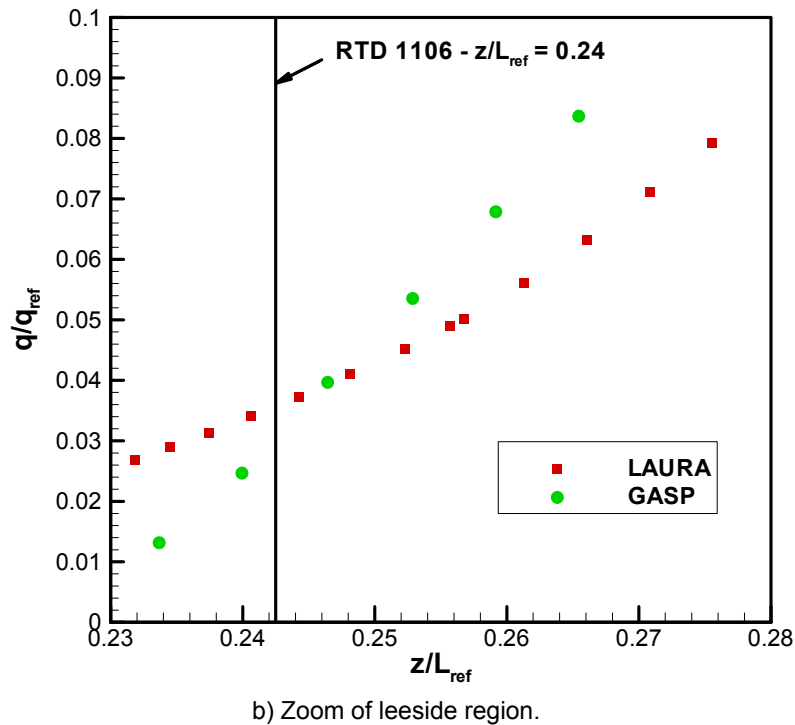
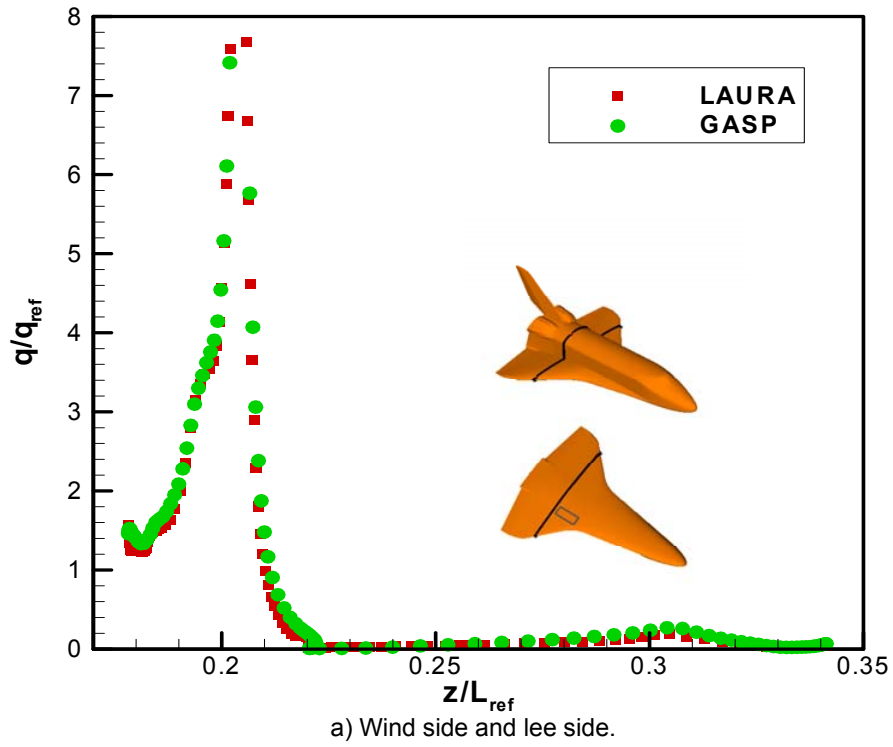


Figure 5.2.4-12 Comparison of GASP and LAURA heat transfer rates along a cut at X = 1215 in. The location of the MLG is shown in the inset. $q_{ref} = 3.55 \text{ W/cm}^2 = 3.13 \text{ BTU/ft}^2/\text{s}$. $L_{ref} = 37.24 \text{ m} = 1466 \text{ in}$.

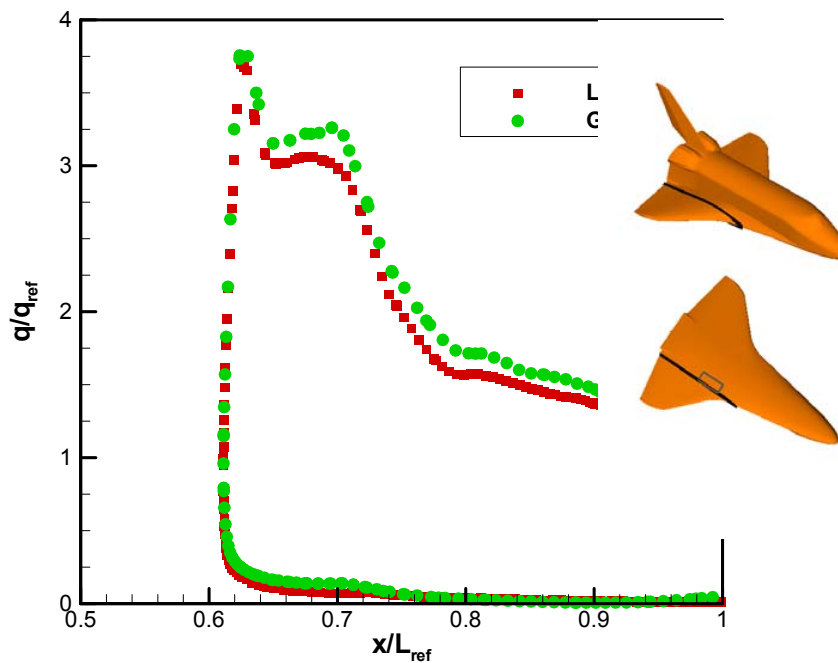


Figure 5.2.4-13 Comparison of GASP and LAURA heat transfer rates along a cut at $Y = 167$ in. The MLG location MLG is shown in the inset. $q_{ref} = 3.55 \text{ W/cm}^2 = 3.13 \text{ BTU/ft}^2/\text{s}$. $L_{ref} = 37.24 \text{ m} = 1466 \text{ in.}$

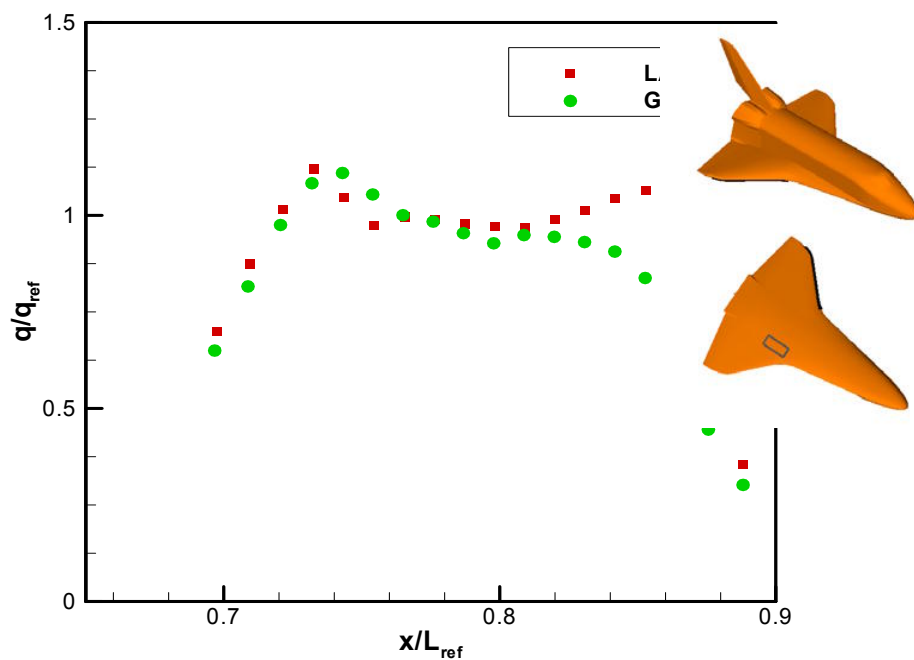


Figure 5.2.4-14 Comparison of GASP and LAURA heat transfer rates along the wing leading edge. $q_{ref} = 37.8 \text{ W/cm}^2 = 33.2 \text{ BTU/ft}^2/\text{s}$. $L_{ref} = 37.24 \text{ m} = 1466 \text{ in.}$

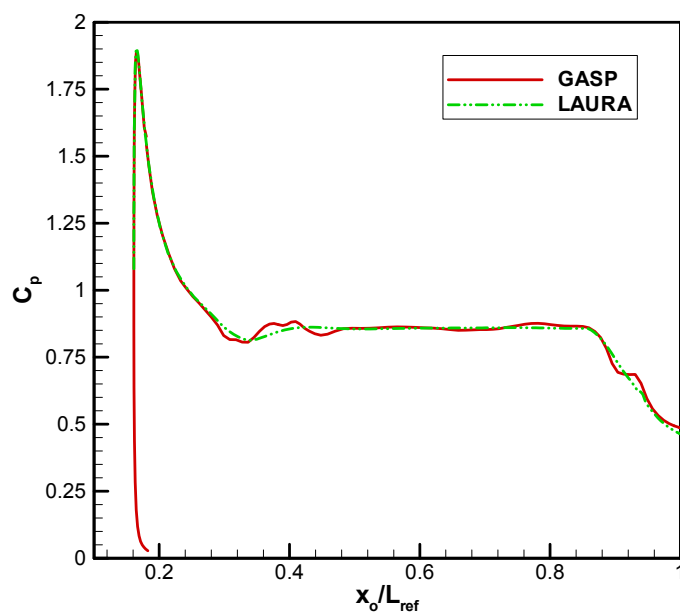


Figure 5.2.4-15 Computed windward centerline pressure distributions from GASP and LAURA.
 $L_{ref} = 37.24 \text{ m} = 1466 \text{ in.}$

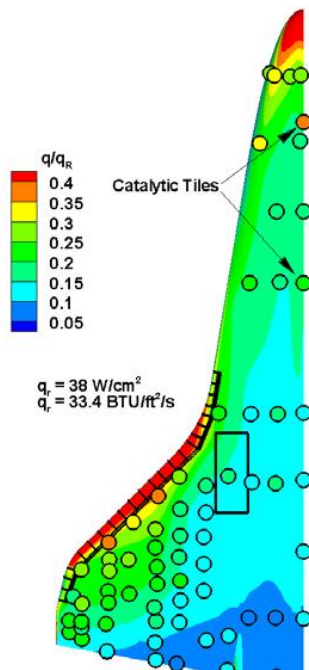
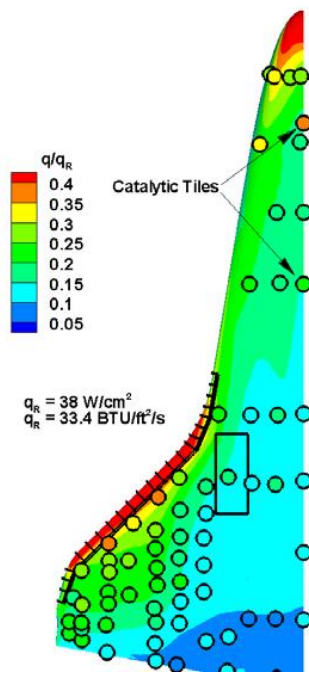


Figure 5.2.4-16 Windward surface temperature predictions from GASP and LAURA compared with flight data at Mach 18. Experimental data are plotted inside the circular symbols. The symbol size is made larger than the measurement extent to aid visualization of the data.

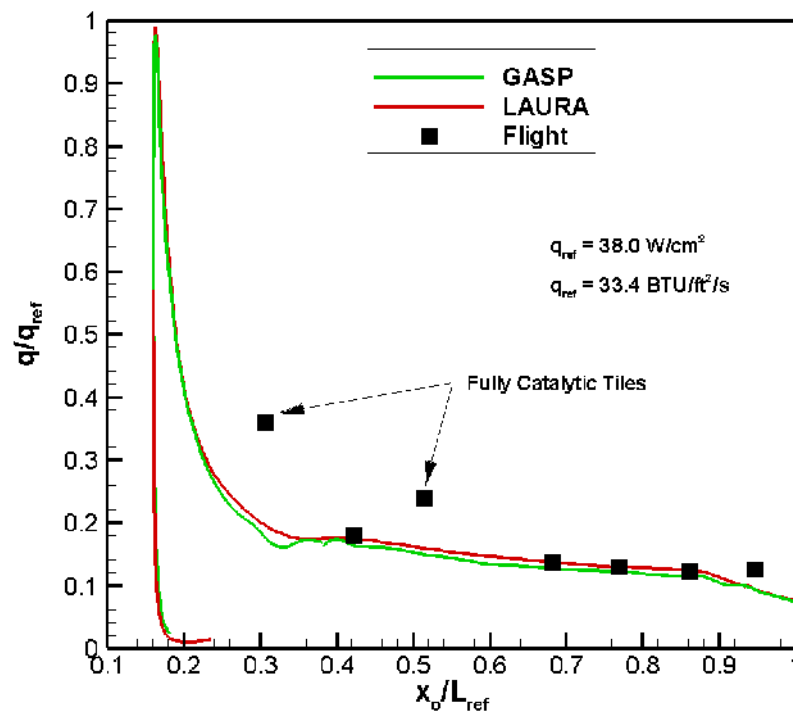


Figure 5.2.4-17 Windward centerline heat transfer rate for Mach 18. $L_{ref} = 37.24 \text{ m} = 1466 \text{ in.}$

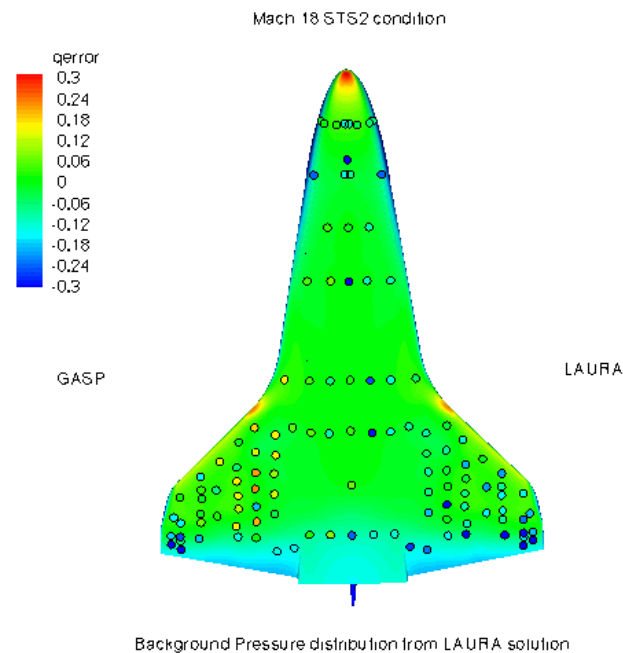


Figure 5.2.4-18 Windward heating rate uncertainty at Mach 18 plotted over pressure contours
 $q_{error} = (q_{cfd} - q_{flight})/q_{flight}$

T = 75949.6, Mach = 18.06, alpha = 41.2, Re = 1930932

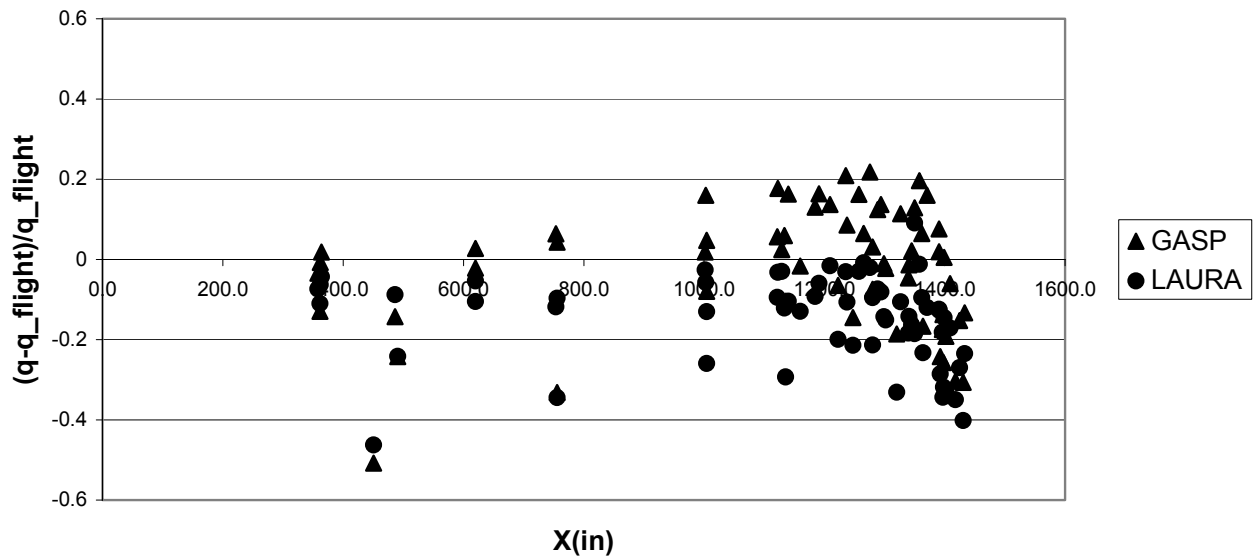


Figure 5.2.4-19 Heating rate uncertainty at Mach 18 as a function axial distance along the orbiter